SIMULTANEOUS BIAXIAL STRETCHING OF ISOTACTIC POLYPROPYLENE FILMS IN THE PARTLY MOLTEN STATE

by

Ludovic Capt

Department of Chemical Engineering
McGill University, Montreal, Canada

A Thesis Submitted to McGill University in Partial Fulfillment
of the Requirements for the Degree of Doctor of Philosophy

April 2003

National Library
of Canada

Acquisitions and
Bibliographic Services

395 Wellington Street
Ottawa ON K1A 0N4
Canada

Bibliothèque nationale
du Canada

Acquisisitons et
services bibliographiques

395, rue Wellington
Ottawa ON K1A 0N4
Canada

Your file Votre référence
ISBN: 0-612-88433-3
Our file Notre référence
ISBN: 0-612-88433-3

ABSTRACT

This thesis presents a detailed study of the simultaneous biaxial stretching of isotactic polypropylene (iPP) films in the partly molten state. Four commercial grades of isotactic PP (PP1 – PP4) were investigated. The first three resins differed principally in isotacticity levels, which were 94.8%, 98.6%, and 99.5%, and the fourth resin had molecular weight and isotacticity levels similar to those of PP2, but differed in crystallization behavior. The four iPP resins were extruded and cast under similar conditions. The severity of the cooling was varied for PP4. The cast films were stretched on the laboratory film stretcher, that simulates closely the stretching conditions encountered in the industrial tenter-frame stretching process. The morphology of the cast films and the final stretched films was characterized by differential scanning calorimetry and wide-angle X-ray diffraction. The reflection technique was used for the X-ray measurements. Finally, the mechanical and optical properties of the films were determined, and the results were correlated with the film morphology and orientation. The effects of drawing temperature, stretching ratio, strain rate, initial morphology, and chain tacticity on deformation behavior, stretched film morphology, and end-film properties were studied, and correlations were sought.

Simultaneous equibiaxial stretching was found to be homogeneous for sufficiently high deformation rates ($\dot{\varepsilon}_H > 0.1\ \mathrm{s}^{-1}$). The stiffness and the thermal stability of the crystallites played an important role in deformation behavior. In fact, the biaxial yield stress showed linear dependence on the crystallite size. Upon simultaneous equibiaxial deformation, crystallinity and especially orientation increased, while crystallite size decreased. The isotacticity content was found to influence greatly the thermal stability of the initial morphology. Increasing isotacticity leads to an increase in DSC melting peak temperature of the initial morphology, overall stress of deformation, and in the final crystallinity, orientation, elastic modulus, and tensile strength of the end film. Finally, it was concluded that the crystalline phase, that melts during preheating prior to stretching forms a "structured melt" phase. The amount of structured melt is related to the tensile strength at break of the end film. Finally, it was showed that an optimal gloss is obtained, if the cast film is stretched about 15°C below its melting point.

RÉSUMÉ

L'objectif de ce travail résidait dans l'étude de l'étirage simultané biaxial de films de polypropylène isotactique à l'état partiellement fondu. Quatre résines (PP1 – PP4) de polypropylène isotactique ont été étudiées. Les trois premières résines avaient leur taux d'isotacticité comme principale différence. La quatrième résine avait une masse moléculaire et un taux d'isotacticité similaires à PP2, mais avait un comportement à la cristallisation différent. Les quatre résines ont été extrudées et mises en forme de films « cast » dans des conditions identiques. De plus, la sévérité du refroidissement a été variée dans le cas de PP4. Les films «cast» ont été biétirés avec un banc d'étirage qui simule étroitement les conditions d'étirage rencontrées sur une ligne de production d'extrusion biétirage à plat (procédé « tenter »). La morphologie des films «cast» et des films biétirés a été caractérisée par calorimétrie et diffraction aux rayons X. Les mesures aux rayons X ont été effectués en réflexion. Finalement, les propriétés mécaniques et optiques des films ont été évaluées, et les résultats ont été corrélés avec la morphologie et l'orientation des films. Les effets de la température et l'élongation d'étirage, de la vitesse de déformation, de la morphologie initiale, et del'isotacticité sur le comportement à la déformation, sur la morphologie de l'état étiré, et sur les propriétés des films ont été étudiés, et des corrélations ont été cherchées.

Il a été trouvé que si la vitesse de déformation est suffisamment élevée ($\dot{\varepsilon}_H > 0.1$ s^{-1}), l'étirage simultané biaxial est homogène. La rigidité et la stabilité thermique des cristallites jouent un rôle important dans le comportement à la déformation. En effet, le seuil d'écoulement biaxial dépend linéairement de la taille des cristallites. Le taux de cristallinité, et particulièrement l'orientation augmente, tandis que la taille des cristallites décroît en augmentant le biétirage. Il a été trouvé que le taux d'isotacticité influence considérablement la stabilité thermique de la morphologie initiale. En augmentant le taux d'isotacticité, la stabilité thermique de la morphologie initiale, la contrainte globale de déformation, la cristallinité, l'orientation, le module élastique, et la résistance à la tension du film biétiré sont augmentés. Finalement, il a été conclu que les cristallites peu thermiquement stable qui fondent pendant le préchauffage avant l'étirage forment un « état fondu structuré ». La quantité de cette phase fondu structurée a été trouvée reliée à la résistance à la tension du film final.

A la mémoire de mon grand-père Pierrot
et à mes parents

ACKNOWLEDGEMENT

I wish to express my deepest appreciation to my research supervisor, Prof. Musa R. Kamal, for the guidance and encouragement received throughout this project. I also would like to also to express my utmost gratitude for the invaluable support and guidance from Prof. Münstedt throughout the time I spent at the Institute of Polymer Materials of the University Erlangen - Nuremberg. I also extend my thanks to the Bavarian Research Foundation, the Natural Sciences and Engineering Research Council of Canada, and Nova Chemicals for financial support. I am particularly grateful to the Bavarian Research Foundation for the fellowship that made it possible for me to carry out the experimental work at the Institute of Polymer Materials.

Furthermore, we would like to thank the following:

- Mr. Stefan Rettenberger for his scientific, logistic, and language help and his moral support throughout the project.
- Mr. Marko Heyder for the incredible amount of valuable work he carried out on the laboratory film stretcher and other difficult measurements.
- Brückner Maschinenbau GmbH (Siegsdorf, Germany) for providing the raw materials, preparing the initial cast films, and characterizing the mechanical and optical properties of the stretched films.
- Prof. K. Stopperka, Mr J. Sänze, and Dr. M. Wolf from Brückner for the valuable discussions and Mr. S. Sieber for the technical support with the laboratory stretcher.
- The technicians at the Institute in Erlangen for their professional and friendly help for all the valuable measurements and for the technical support.
- The colleagues at the Institute in Erlangen for their enriching discussion about different topics of polymer science.
- Mrs. Beate Huckemann and Mr Maussner from Siemens AG for very kindly letting me carry out my own pole figure measurements.

Finally, I would like to express my love to my parents for their patience and constant encouragement.

Table of Content

Abstract ii
Résumé iii
Acknowledgments v
Table of Content vi
List of Figures xiii
List of Tables xxi

CHAPTER 1 INTRODUCTION 1

CHAPTER 2 TECHNICAL BACKGROUND AND LITERATURE REVIEW 4
2.1 - Polypropylene 5
  2.1.1 - Introduction 5
  2.1.2 - Stereochemistry of Polypropylene 5
    2.1.2.1 - Introduction to Stereochemistry of Polypropylene 5
    2.1.2.2 - Stereochemistry and Crystallinity 6
  2.1.3 - Crystal Structures of Isotactic Polypropylene 7
  2.1.4 - Lamellar Structures of Isotactic Polypropylene 9
  2.1.5 - Spherulitic Structures of Isotactic Polypropylene 11
  2.1.6 - Melting Behavior of Isotactic Polypropylene 12
    2.1.6.1 - Equilibrium Melting Temperature 12
    2.1.6.2 - Peak Multiplication on Melting of iPP 13
2.2 - Film Processing 15
  2.2.1 - General Principle 15
  2.2.2 - Biaxially Oriented PP Film Processes 16
    2.2.2.1 - Double-Bubble Film Process 16
    2.2.2.2 - Tenter-Frame Process 16
  2.2.3 - Tenter-Frame Stretching Processes 17
    2.2.3.1 - General Principles 17
    2.2.3.2 - Cast Film Extrusion 19

2.2.3.3 - Preheating 20
2.2.3.4 - Sequential Tenter-Frame Stretching 21
2.2.3.5 - Simultaneous Tenter-Frame Biaxial Stretching 21
2.2.3.6 - Heat Setting 22
2.3 - Biaxial Orientation and Texture 23
2.3.1 - Introduction to Orientation 23
2.3.1.1 - Achieving Orientation 23
2.3.1.2 - Achieving Biaxial Orientation 24
2.3.2 - Defining Molecular Orientation and Texture 25
2.3.2.1 - Defining Molecular Orientation 25
2.3.2.2 - Defining Texture for Polymers 27
2.3.3 - Characterization of Biaxial Orientation 28
2.4 - Deformation Mechanisms and Morphology of Polypropylene 29
2.4.1 - Macroscopic Deformation Behavior 29
2.4.2 - Structural Deformation Mechanisms 30
2.4.2.1 - Structural Models for Cold Drawing 31
2.4.2.2 - Deformation Mechanisms of Semicrystalline Polymers 32
2.4.2.3 - Cavitation during yielding 33
2.4.2.4 - Structural Models for the Oriented Fibrous Structure 33
2.4.2.5 - Ultradrawability 34
2.4.2.6 - Peculiarities of the Deformation Mechanisms of iPP 34
2.4.3 - Drawing in the Partly Molten State 35
2.4.4 - Effect of Initial Morphology on Deformation and Morphology 36
2.4.4.1 - Effect of Initial Morphology on Deformation 36
2.4.4.2 - Effect of Initial Morphology on Oriented Morphology 37
References of Chapter 2 38

CHAPTER 3 OBJECTIVES 48

CHAPTER 4 EXPERIMENTAL 50
4.1 - Materials and Cast Film Preparation 50

- 4.1.1 - Materials 50
- 4.1.2 - Preparation of the Initial Film Morphology 52
  - 4.1.2.1 - Preparation of the Cast Films 52
  - 4.1.2.2 - Preparation of the Preheated Cast Films 54
  - 4.1.2.3 - Preparation of the Annealed Cast Films 54

4.2 - Characterization Techniques 55

- 4.2.1 - Wide-Angle X-Ray Diffraction 55
  - 4.2.1.1 - Principles of X-Ray Diffraction 55
  - 4.2.1.2 - Wide-Angle X-Ray Diffractometer 56
  - 4.2.1.3 - Analysis of X-Ray Diffraction Data 57
- 4.2.2 - Wide Angle X-Ray Diffraction Pole Figures 62
  - 4.2.2.1 - Principle 62
  - 4.2.2.2 - Pole Figure Measurements 63
  - 4.2.2.3 - Pole Figure Data Analysis 63
- 4.2.3 - Fourier Transform Infrared (FTIR) – Infrared Dichroism 64
  - 4.2.3.1 - Principle 64
  - 4.2.3.2 - Experimental Details 65
  - 4.2.3.3 - Data Analysis 66
  - 4.2.3.4 - Comparison of the orientation characterization techniques 68
- 4.2.4 - Thermal Analysis (Differential Scanning Calorimeter) 68
  - 4.2.4.1 - Experimental Procedures 69
- 4.2.4.2 - Sample Preparation 69
- 4.2.4.3 - DSC Curve Analysis 69
- 4.2.5 - Polarized Light Microscopy 71
- 4.2.6 - Film End-Use Properties 71
- 4.2.7 - Stress Optical Analysis 72

4.3 - Biaxial Film Stretcher 74

- 4.3.1 - General Description 74
- 4.3.2 - Description of a Stretching Experiment 77
- 4.3.3 - Evaluation of Reproducibility 78

References of Chapter 4 81

CHAPTER 5 INITIAL FILM MORPHOLOGY **84**

5.1 - Effect of Chain Tacticity on Initial Film Morphology 84

5.1.1 - Results and Discussion 84

5.1.2 - Conclusions 88

5.2 - Effects of Casting Conditions on Initial Film Morphology 89

5.2.1 - Results and Discussion 89

5.2.2 - Conclusions 94

5.3 - Effect of High Temperature Thermal Treatment on Initial Film Morphology 95

5.3.1 - Effect of Annealing on Initial Film Morphology 95

5.3.1.1 - Results 95

5.3.1.2 - Discussion 98

5.3.2 - Effect of Preheating on Initial Film Morphology 101

5.3.2.1 - Effect of Preheating Temperature on Initial Film Morphology 102

5.3.2.2 - Effect of Preheating on The CF1 – CF4 Cast Films 104

5.4 - Summary 106

References of Chapter 5 107

CHAPTER 6 SIMULTANEOUS BIAXIAL DEFORMATION BEHAVIOR OF POLYPROPYLENE FILMS **110**

6.1 - Homogeneity of the Simultaneous Biaxial Deformation 110

6.1.1 - General Definition of Homogeneous Deformation 110

6.1.2 - Homogeneity of the Equibiaxial Deformation 111

6.1.3 - Evolution of the Macroscopic Biaxial Deformation 112

6.1.4 - Discussion 115

6.2 - Effect of Stretching Conditions on Biaxial Deformation Behavior 115

6.2.1 - Effect of Drawing Temperature on Biaxial Deformation Behavior 116

6.2.2 - Effect of Strain Rate on Biaxial Deformation Behavior 120

6.2.3 - Conclusions 121

6.3 - Effect of Initial Morphology on Biaxial Deformation Behavior 122

6.3.1 - Effect of Melt-Crystallized Morphology on Deformation Behavior 122

6.3.2 - Effect of Annealed Morphology on Deformation Behavior 124
6.3.3 - Discussion 127
6.3.3.1 - Relations between the structural factors of initial film morphology and the level of yield stress 128
6.3.3.2 - Relation between the structural factors of initial film morphology and deformation homogeneity 129
6.3.4 - Conclusions 131
6.4 - Effect of Chain Tacticity on Biaxial Deformation Behavior 132
6.4.1 - Results 132
6.5 - Summary 136
References of Chapter 6 137

CHAPTER 7 MORPHOLOGY DEVELOPMENT DURING SIMULTANEOUS BIAXIAL STRETCHING 140

7.1 - Effects of Stretching Conditions on the Equibiaxially Stretched Film Morphology 140
7.1.1 - Effects of Drawing Temperature and Stretching Ratio on the Equibiaxially Stretched Film Morphology 140
7.1.1.1 - Results and Discussion 140
7.1.1.2 - Conclusions 149
7.1.2 - Effect of Strain rate on the Equibiaxially Stretched Film Morphology 150
7.1.2.1 - Results 150
7.1.2.2 - Discussion and Conclusions 151
7.1.3 - Effect of Deformation Type on the Biaxially Stretched Film Morphology 153
7.2 - Effect of Initial Film Morphology on the Equibiaxially Stretched Film Morphology 154
7.2.1 - Melt-Crystallized Cast Films 154
7.2.2 - Annealed Cast Films 157
7.2.3 - Conclusions 161
7.3 - Effect of Chain Tacticity on the Equibiaxially Stretched Film Morphology 161
7.3.1 - Results 162

7.3.2 - Discussion and Conclusions 164
7.4 - Summary 168
References of Chapter 7 170

CHAPTER 8 END-FILM PROPERTIES AND STRUCTURE-PROPERTY RELATIONSHIPS 172

8.1 - Effects of Stretching Conditions on End-Film Properties 172
8.1.1 - Effect of Area Stretching Ratio on End-Film Properties 173
8.1.2 - Effect of Drawing Temperature on End-Film Properties 175
8.1.3 - Effect of Strain Rate on Film Properties 177
8.2 - Effect of Initial Film Morphology on End-Film Properties 179
8.3 - Effect of Chain Tacticity on End-Film Properties 181
8.4 - Correlations between Film Morphology and End-Film Properties 186
8.4.1 - Mechanical properties 186
8.4.2 - Optical properties 189
References of Chapter 8 190

CHAPTER 9 SUMMARY 191
CHAPTER 10 CONCLUSIONS & ORIGINAL CONTRIBUTIONS 197

APPENDICES A1

CONTENT OF APPENDICES A2

APPENDIX A COMPLEMENT OF CHAPTER 4 A3
A.1 - Wide-Angle X-Ray Diffraction A-3
A.1.1 - Principles A-3
A.1.2 - Measurement Techniques A-6
A.1.3 - Wide-Angle X-Ray Diffractometer A-7
A.1.4 - Analysis of X-Ray Diffraction Data A-8
A.1.5 - Measurement Reproducibility A-18

A.2 - Wide Angle X-Ray Diffraction Pole Figures A-20

  A.2.1 - Principle A-20

  A.2.2 - Pole Figure Measurements A-21

  A.2.3 - Pole Figure Data Analysis A-23

A.3 - Measurement of the Isotacticity Index A-26

  A.3.1 - Principle A-26

  A.3.2 - Experimental Procedure A-26

APPENDIX B COMPLEMENT OF CHAPTER 5 B-1

  Surface Morphology of the Cast Films B-1

APPENDIX C COMPLEMENT OF CHAPTER 7 C-1

C.1 - Effect of Stretching Conditions on Biaxially Stretched Morphology C-1

  C.1.1 - Effect of Stretching Temperature and Strain Ratio on Stretched Morphology C-1

  C.1.2 - Effect of Stain Rate on Equibiaxially Stretched Morphology C-2

C.2 - Effect of Initial Morphology on Biaxially Stretched Morphology C-3

C.3 - Effect of Chain Tacticity on Equibiaxially Stretched Morphology C-5

C.4 - Effect of Deformation Type on the Equibiaxially Stretched Film Morphology C-7

  C.4.1 - Effect on Crystalline Texture - Results and Discussion C-7

  C.4.2 - Effect on Film Morphology - Results and Discussion C-11

  C.4.3 - Conclusions C-16

APPENDIX D COMPLEMENT OF CHAPTER 8 D-1

D.1 - Effect of Stretching Ratio on the End-Film Properties for the PP2 Cast Film D-1

D.2 - Effect of Drawing Temperature on the End-Film Properties for the PP1 Cast Film D-2

D.3 - Effect of Drawing Temperature on the End-Film Properties for the PP2 Cast Film D-3

D.4 - Effect of Drawing Temperature on the End-Film Properties for the PP3 Cast Film D-4

D.5 - Effect of Strain Rate on the End-Film Properties for the PP2 Cast Film D-5

D.6 - Effect of Initial Morphology on the End-Film Properties for the PP2 Cast Film D-6

List of Figures

Figure 2-1 *Schematic of the stereochemical configurations of polypropylene: (a) isotactic PP, (b) syndiotactic PP, and (c) atactic PP (○ = methyl group; ● = carbon group)* *6*

Figure 2-2 *Schematic illustration of the monoclinic unit cell (left) and of the helical chain conformation (right) of isotactic polypropylene (· = C atom, · = methyl group; a, b, and c are the unit cell dimensions) [Documentation, 2000 #558]* *8*

Figure 2-3 *Schematic of the lamellar branching morphology of iPP at the (a) lamellar level and at the (b) spherulitic level (T = tangential; R = radial; a* = main growth direction)* *10*

Figure 2-4 *Formation of the different types of iPP spherulites during isothermal and non-isothermal crystallization(14); Symbol notation can be found in text* *11*

Figure 2-5 *Schematic of a sequential biaxial tenter-frame stretching process; (a) extrusion line, (b) casting unit, (c) MD orientation unit, (d) preheating zone, (e) TD orientation unit, (f) heat setting zone, with cooling zone, (g) pull roll unit, and (h) winding unit* *17*

Figure 2-6 *Schematic of the LISIM© technology. (a) clip chains, (b) linear-motor-controlled clip* *18*

Figure 2-7 *Schematic of the cast film process(61) a: slit die; b: chill roll; c: air knife; d: film; 1: roll zone; 2: median zone; 3: air zone* *19*

Figure 2-8 *Definition of the types of orientation with l being the stretching ratio* *24*

Figure 2-9 *Definition of orientation (a) in terms of Euler angles and (b) in terms of the angles q i,J* *25*

Figure 2-10 *Schematic representation of the relation between tensile deformation behavior and thickness uniformity; with elastic deformation along (AB), necking at (B), neck propagation along (BC), and onset of strain hardening at (C)* *30*

Figure 2-11 *Schematic adapted from Zhang et al.(90) showing the different deformation mechanisms operative in semicrystalline polymers; (a) original lamellar structure, (b) lamellar separation, (c) interlamellar shear, (d) lamellar stack rotation, (e) fine chain slip, (f) coarse chain slip or lamellar fragmentation, and (g) lamellar fragmentation coupled with cavitation* *32*

Figure 2-12 *Schematic of the (010) [001] crystallographic slip system* *35*

Figure 4-1 *Molecular weight distributions of the main three linear homopolymers obtained by gel permeation chromatography (GPC)* *51*

Figure 4-2 *Chill roll / water bath unit of the cast film process* *53*

Figure 4-3 *Schematic of (a) the monoclinic space lattice of the a crystal form of iPP showing the three main diffraction planes (110), (040), and (130) and (b) the (040) diffraction plane and the corresponding apparent crystallite size at the lamellar scale* *56*

Figure 4-4 *Example of the multi-peak fitting procedure and the constructed amorphous halo for an isotropic iPP sample* *59*

Figure 4-5 *Schematic of the in-plane orientation of (040) crystal planes* *61*

Figure 4-6 *Experimental set-up for the tilted infrared dichroism experiments* *66*

Figure 4-7 *An example of the curve fitting for an equi-biaxially stretched PP film. The polarization is in the machine direction. The upper curve is the difference between the fitted and observed spectrum on the same scale* *67*

Figure 4-8 *Comparison of the orientation characterization results obtained from the different techniques used in this study for different resins stretched under the same conditions* *68*

Figure 4-9 *DSC curve analysis illustrating the definitions of the melting temperature (Tm), the melting enthalpy (DHf), and the onset of melting (Tom)* *70*

Figure 4-10 *DSC curve analysis illustrating the definitions for the unmolten crystallinity (UC) and the structured melt (SM) quantities* *71*

Figure 4-11 *Schematic representation of the Brückner laboratory film stretcher* *74*

Figure 4-12 *Photographs of the stretching frame* *76*

Figure 4-13 *Force vs. time for the simultaneous equibiaxial stretching of an iPP cast film.* 78

Figure 4-14 *Reproducibility of stretching experiments for the same series.* 79

Figure 4-15 *Reproducibility of a stretching series for simultaneous equibiaxial drawing experiments.* 81

Figure 5-1 *WAXD patterns measured on both sides for (a) PP1, (b) PP2, and (c) PP3. (d) Average WAXD patterns of three cast films (all curves plotted on the same intensity scale; the baselines represent the amorphous halos)* 85

Figure 5-2 *DSC melting curves of the cast films for PP1, PP2, and PP3* 87

Figure 5-3 *WAXD patterns of the CF1, CF2, CF3, and CF4 cast films (plotted on the same intensity scale; baselines represent the amorphous halos)* 90

Figure 5-4 *Polarized light microscopy images of the bulk morphology for the CF1, CF2, CF3, and CF4 cast films (the arrow shows clusters of small spherulites)* 92

Figure 5-5 *DSC melting curves of the CF1, CF2, CF3, and CF4 cast films* 93

Figure 5-6 *WAXD patterns for both sides of (a) the PP2 cast film and the specimens annealed at (b) 150°C, (c) 157°C, and (d) 160°C (dotted baselines are the amorphous halos)* 96

Figure 5-7 *DSC melting curves of the PP2 cast film and of the annealed specimens* 97

Figure 5-8 *Apparent crystallite sizes as function of X-ray crystallinity for the series of annealed samples* 99

Figure 5-9 *DSC melting curves of the PP2 cast film and the PP2-P150, and PP2-P160 preheated samples* 102

Figure 5-10 *Comparison of the average WAXD patterns between the initial and preheated morphology for the CF1, CF2, CF3, and CF4 cast films* 105

Figure 6-1 *Photographs of samples (a)&(b) and of the corresponding fringe patterns (c)&(d) of films simultaneously equibiaxially stretched up to a 2.0 x 2.0 ratio. (a)&(c) Ts= 150°C and = 0.01 s-1; (b)&(d) Ts= 155°C and = 1 s-1. (arrows in (c) indicate the local principal stress direction. Upper-left and lower-right corner high brightness is due to the light source)* 112

Figure 6-2 *Fringe patterns of PP2 samples equibiaxially stretched at 155°C with a of 0.01 s-1 (a) 1.3 x 1.3; (b) 1.5 x 1.5; and (c) 2.0 x 2.0.* 113

Figure 6-3 *Fringe patterns of PP2 samples equibiaxially stretched at 155°C with a of 1s-1 (a) 1.3 x 1.3; (b) 1.5 x 1.5; and (c) 2.0 x 2.0.* 114

Figure 6-4 *Fringe patterns of films equibiaxially stretched up to a 1.5 x 1.5 ratio with a Hencky strain rate of 1 s-1 at various temperatures (a) 140°C; (b) 150°C; (c) 155°C; (d) 160°C.* 116

Figure 6-5 *Effect of stretching temperature on the stress-strain curves for the equibiaxial deformation of the PP2 cast film* 117

Figure 6-6 *Effect of stretching temperature and stretching ratio on the film thickness profile, expressed as the normalized difference between the average thickness of the central area and that of the total area.* 119

Figure 6-7 *Effect of the strain rate on the nominal strain-stress curves. Only MD stresses are represented for specimens equibiaxially stretched at various strain rates* 121

Figure 6-8 *Effect of the initial morphology on the nominal stress-strain curves for the equibiaxial stretching at 150°C and 160°C of the melt-crystallized samples (only MD stresses are shown)* 123

Figure 6-9 *Effect of the initial morphology on the nominal stress strain curves for the equibiaxial stretching of the annealed samples (YRS = Yield Region Sharpness)* 125

Figure 6-10 *Fringe patterns of samples equibiaxially stretched up to a 1.3 x 1.3 ratio with = 1 s-1 at 150°C. (a) PP2 cast film; (b) A140, and (c) A160* 127

Figure 6-11 *Nominal stress-strain curves of the simultaneous equibiaxial stretching experiments at 150°C with a strain rate of 1 s-1 for PP1, PP2 and PP3* 133

Figure 6-12 *Fringe patterns of films simultaneously equibiaxially stretched at 150°C up to a 2 x 2 area ratio for (a) PP1, (b) PP2, and (c) PP3* 133

Figure 6-13 *Nominal stress-strain curves for samples stretched simultaneously equibiaxially at Tm – 10°C. PP1 at 150°C, PP2 at 155°C, and PP3 at 158°C.* 135

Figure 7-1 *Effect of area stretching ratio on the DSC melting behavior for the PP2 films equibiaxially stretched at 150°C* 141

Figure 7-2 *Effects of the area stretching ratio and drawing temperature on the DSC crystallinity for equibiaxially stretched PP2 films* 142

Figure 7-3 *Effect of area stretching ratio on the WAXD pattern for the PP2 films equibiaxially stretched at 150°C* 144

Figure 7-4 *Comparison between the WAXD patterns measured in reflection and transmission for a simultaneously equibiaxially stretched film* 145

Figure 7-5 *Effects of the area stretching ratio and drawing temperature on the D110 and D040 apparent crystallite sizes for equibiaxially stretched PP2 films* 146

Figure 7-6 *Effects of the area stretching ratio and drawing temperature on the (040) in-plane orientation index for equibiaxially stretched PP2 films* 148

Figure 7-13 *Effect of strain rate on the melting point for PP2 films equibiaxially stretched at 150°C up to a 4.9x4.9 area stretching ratio* 151

Figure 7-14 *Effect of strain rate on the apparent crystallite size for PP2 films equibiaxially stretched at 150°C up to a 4.9x4.9 area stretching ratio* 152

Figure 7-15 *Effect of strain rate on the (040) in-plane orientation for PP2 films equibiaxially stretched at 150°c up to a 4.9x4.9 area stretching ratio* 152

Figure 7-16 *Effect of the initial cast film crystallinity on the melting point of equibiaxially stretched films at 150°C and 160°C C (Cast film crystallinity obtained from DSC measurements)* 156

Figure 7-17 *Effect of the initial cast film crystallinity on the D040 apparent crystallite size of equibiaxially stretched films at 150°C and 160°C (Cast film crystallinity obtained from WAXD measurements)* 156

Figure 7-18 *Effect of the initial cast film crystallinity on the (040) in-plane orientation of equibiaxially stretched films at 150°C and 160°C (Cast film crystallinity obtained from WAXD measurements)* *157*

Figure 7-19 *Relation between the film thicknesses and the apparent crystallite sizes for the annealed cast films equibiaxially stretched at 150°C* *159*

Figure 7-20 *(040) in-plane orientation and <cos²q b,ND> (from infrared dichroism measurements) for the annealed cast films equibiaxially stretched at 150°C, plotted versus film thickness* *160*

Figure 7-21 *DSC melting curves of the three homopolymer resins stretched equibiaxially at 150°C up to a 4.9 x 4.9 stretching ratio* *163*

Figure 7-22 *Increase in crystallinity due to stretching versus the structured melt for the three homopolymer resins* *165*

Figure 7-23 *Increase in melting temperature due to stretching versus the molten crystallinity for the three homopolymer resins* *166*

Figure 7-24 *(040) in-plane orientation versus Tm – Ts for the three homopolymer resins* *166*

Figure 8-1 *Effect of area stretching ratio on the E-modulus and the elongation at break for the PP2 films simultaneously equibiaxially stretched at 155°C* *174*

Figure 8-2 *Effect of area stretching ratio on the tensile strength and the shrinkage for the PP2 films simultaneously equibiaxially stretched at 155°C (average values from the MD and TD results are plotted)* *174*

Figure 8-3 *Effect of area stretching ratio on Gloss and Haze for the PP2 films simultaneously equibiaxially stretched at 155°C* *175*

Figure 8-4 *Effect of stretching temperature on the E-modulus and the elongation at break for the PP2 films simultaneously equibiaxially stretched up to a 4.9 x 4.9 area stretching ratio* *176*

Figure 8-5 Effect of stretching temperature on tensile strength and shrinkage for the PP2 films simultaneously equibiaxially stretched up to a 4.9 x 4.9 area stretching ratio 176

Figure 8-6 Effect of stretching temperature on Gloss and Haze for the PP2 films simultaneously equibiaxially stretched up to a 4.9 x 4.9 area stretching ratio 177

Figure 8-7 Effect of strain rate on the E-modulus and the elongation at break for the PP2 films simultaneously equibiaxially stretched at 150°C up to a 4.9 x 4.9 area stretching ratio 178

Figure 8-8 Effect of strain rate on the tensile strength and shrinkage for the PP2 films simultaneously equibiaxially stretched at 150°C up to a 4.9 x 4.9 area stretching ratio 178

Figure 8-9 Effect of initial film morphology the tensile strength and the E-modulus for the PP4-CFx films simultaneously equibiaxially stretched at 150°C up to a 4.9 x 4.9 area stretching ratio 180

Figure 8-10 Effect of initial film morphology on Gloss and Haze for the PP2 annealed films simultaneously equibiaxially stretched at 150°C up to a 4.0 x 4.0 area stretching ratio 180

Figure 8-11 Effect of stretching temperature on the E-modulus for the PP1, PP2, and PP3 films simultaneously equibiaxially stretched up to a 4.9 x 4.9 area stretching ratio 183

Figure 8-12 Effect of stretching temperature on the shrinkage for the PP1, PP2, and PP3 films simultaneously equibiaxially stretched up to a 4.9 x 4.9 area stretching ratio 183

Figure 8-13 Tensile strength versus the amount of structured melt for the PP1, PP2, and PP3 films simultaneously equibiaxially stretched up to a 4.9 x 4.9 area stretching ratio 185

Figure 8-14 Elongation at break versus the unmolten crystallinity for the PP1, PP2, and PP3 films simultaneously equibiaxially stretched up to a 4.9 x 4.9 area stretching ratio at different temperatures 185

Figure 8-15 *Tensile strength versus the (040) in plane orientation index for a series of equibiaxially stretched films at different temperatures for the three homopolymer resins* *187*

Figure 8-16 *Elongation at break versus the (040) in-plane orientation index for a series of equibiaxially stretched films at different temperatures for the three homopolymer resins* *188*

Figure 8-17 *E-modulus versus the film crystallinity for a series of equibiaxially stretched films at different temperatures for the three homopolymer resins* *188*

List of Tables

Table 2-1 *Crystallographic data of isotactic polypropylene* 7

Table 4-1 *Molecular properties of the polypropylene resins; Isotacticity as measured by xylene solubility (XS) measurements by infrared (IR)* 52

Table 4-2 *Morphological characteristics of the raw materials* 52

Table 4-3 *Casting conditions for the various cast films* 53

Table 5-1 *Morphological characteristics of the PP1, PP2, and PP3 cast films. WAXD values are averages from both sides. (CI = crystallinity index; Dhkl = apparent crystallite size calculated from the (hkl) diffraction peak; FWHM = full width at half maximum of the melting peak; Sph. = spherulite)* 87

Table 5-2 *Morphological characteristics of the CF1, CF2, CF3, and CF4 cast films. (ksm = smectic phase index; kb = b-phase index)* 91

Table 5-3 *Morphological characteristics of the cast film and annealed specimens* 97

Table 5-4 *Morphological characteristics of the PP2 cast film and preheated samples* 103

Table 5-5 *Room temperature crystallinity (CI) and the amounts in unmolten crystalline phase (UC) and structured melt (SM) at 150°C, 160°C, and DT = 10°C for the PP1, PP2, and PP3 cast films* 104

Table 5-6 *Room temperature crystallinity (CI) and the amounts in unmolten crystalline phase (UC) and structured melt (SM) at 150°C and 160°C for the four CF1-CF4 cast films* 105

Table 6-1 *Effect of the nominal draw ratio on the local true draw ratio and film thickness for PP2 samples simultaneously equibiaxially stretched at 155°C with a Hency strain rate of 1 s-1* 115

Table 6-2 *Effect of drawing temperature on true draw ratios and film thickness for samples equibiaxially stretched up to 4.9 x 4.9 with a Hencky strain rate of 1 s-1 and where Dt = (t36 - t4)/t36* 118

Table 6-3 *Local true draw ratios, thicknesses, and thickness profile coefficient of the films stretched at 150°C up to 4.9 x 4.9 with a Hencky strain rate of a s-1 for the four PP4 melt-crystallized cast films (Δt = (t36 - t4)/t36)* 124

Table 6-4 *True draw ratios, film thicknesses, and YRS of the films stretched at 150°C up to 4.0 x 4.0 with a strain rate of 0.68 s-1 for the PP2 and annealed cast films* 126

Table 6-5 *True draw ratios, film thicknesses, and YRS of the films stretched at 150°C up to 4.0 x 4.0 for the PP1, PP2, and PP3 cast films* 134

Table 7-1 *Morphological characteristics of the PP2 annealed films equibiaxially stretched up to a 4 x 4 stretching ratio at 150°C* 157

Table 7-2 *DSC crystallinity index, melting point, crystallite size, and (040) in-plane orientation of the PP1,PP2, and PP3 film samples that were stretched at different temperatures up to a 4.9 x 4.9 stretching ratio* 163

Table 8-1 *Mechanical and optical properties of films equibiaxially stretched at different temperatures for the PP1, PP2, and PP3 resins* 182

CHAPTER 1

INTRODUCTION

The biaxially oriented polypropylene (BOPP) film industry has been one of the most dynamic and fast growing sectors of the plastics packaging industry in recent years. The use of BOPP film has grown from a small specialist market originally developed as a replacement for cellulose film, to one which has carved out whole new market applications and uses. BOPP films, due to their high stiffness, transparency and good moisture barrier properties, are routinely used as packaging material for food and non-food packaging and overwrapping films. Biaxially oriented polypropylene (BOPP) represents 58% of the world market of biaxially oriented films. Because of the 10% annual increase in the use of BOPP films during the 1990s, there was a need for faster and wider film production lines. As a result, the film stretching technology has evolved considerably in the last ten years. BOPP and biaxially oriented polyethylene terephthalate (BOPET) films are mostly produced through a sequential tenter-frame process, in which films are cold drawn in two consecutive steps in two perpendicular directions at different temperatures. However, a novel simultaneous biaxial stretching (LISIM©: Linear Motor Simultaneous Stretching Technology) process was recently developed by Brückner Maschinenbau GmbH, Germany. This technique allows the commercial production of uniform and highly oriented films, using one-step-biaxial-stretching, at high speed while minimizing energy consumption. A laboratory biaxial stretching device that simulates closely the above novel commercial tenter-frame biaxial stretching process, in terms of deformation rate and temperature homogeneity, was recently developed by Brückner.

The tenter-frame biaxial stretching process is based on the solid-phase drawing of a polymer, in which deformation of chains takes place in an elastic-plastic manner at high temperature below the melting point (T_m). Biaxial stretching differs from the other film forming processes, such as film blowing, cast film, and extrusion coating, in which film formation occurs through visco-elastic deformation of a polymer melt at relatively high temperatures, above T_m. The major difference between these two types of film forming processes is the amount of achieved orientation. More highly oriented products will be obtained for the processes in which deformation can take place in the solid state (1).

There is extensive information in the literature about the solid-phase deformation of semicrystalline polymers, especially polyethylene (PE) and isotactic polypropylene (iPP). In the past, most of the studies were concerned with the uniaxial deformation at room temperature. Recent studies have been carried out on the biaxial deformation of semicrystalline polymers, such as polyethylene terephthalate (PET), iPP, PE, polyvinyl chloride, and other more complex systems. However, few studies focused on the simultaneous biaxial stretching of iPP at temperatures close to the melting point (2-4). Furthermore, there is a lack of knowledge about the effects of the initial morphology or of the molecular structure, especially the stereoregularity of propylene polymers, on deformation.

In order to fill this gap, the present work provides a thorough study of the simultaneous biaxial stretching of isotactic polypropylene films at temperatures close to the melting point. The effects of stretching conditions, such as drawing temperature, stretching ratio, strain rate, and deformation type, on the macroscopic biaxial deformation behavior, the biaxially stretched morphology and the final properties were investigated. Special attention was given to the effects of the chain tacticity of iPP resins and the initial morphology on the different aspects of the biaxial stretching process. Because deformation takes place at temperatures close to T_m, the state and the characteristics of the partly molten morphology just before stretching are of great interest. Differential scanning calorimetry and wide-angle X-ray diffraction measurements were the main experimental techniques used to characterize the evolution of the morphology and orientation during stretching. Finally, the mechanical and optical properties of the films were determined, in order to evaluate their relationships with the biaxially stretched film morphology.

The present text is divided into 8 chapters. Chapter 2 introduces the general properties of propylene polymers, and gives a presentation of film forming, with emphasis on the biaxial tenter-frame stretching and biaxial orientation. It also reviews the models used to describe the deformation of semicrystalline polymers. Chapter 3 states the detailed objectives of the present work. Chapter 4 is subdivided into three parts. Firstly, it gives the molecular characteristics of the four commercial PP grades and the experimental conditions used to prepare and treat the initial cast films. The second part presents the different experimental techniques employed to characterize the morphology and orientation. Special attention is given to the wide angle X-ray diffraction technique. The third part of Chapter 4 gives a detailed description of the laboratory film stretcher and its measurement capabilities. Chapters 5 to 9 present and discuss the results. Chapter 5 describes the initial morphology of the cast films that were subjected to biaxial stretching and the effect of thermal treatment on these morphologies. Chapter 6 presents the equibiaxial deformation behavior of these films. The effects of stretching conditions, initial morphology, and chain tacticity are discussed. Chapter 7 discusses the same effects on the biaxially stretched film morphology. Chapter 8 presents the mechanical and optical properties of the end-film, and correlations between film morphology and final properties are discussed. Finally, Chapter 9 gives the main conclusions about the effects of stretching conditions, initial morphology, and chain tacticity on deformation behavior, film morphology, and the final film properties. Furthermore, recommendations for future work and claims to original contributions to knowledge are outlined.

References

1 - I. M. Ward, P. D. Coates and M. M. Dumoulin, Solid Phase Processing of Polymers, Hanser, Munich, (2000).

2 - W. W. Cox and E. K. Bullock. in *Polyolefins X: International Conference*, "Draw stress characterization of polypropylene for improved biaxial film processability", 397-415 (1997).

3 - H. Tanaka, T. Masuko and S. Okajima,"Studies on biaxial stretching of polypropylene film. IX. Melting behavior of biaxially stretched film in one step", J. Appl. Polym. Sci., **17**, 1715-1725 (1973).

4 - H. Tanaka and S. Okajima,"Studies on biaxial stretching of polypropylene film. XII. Effect of crystallinity on the deformation mechanism of the biaxial stretching in one step", J. Polym. Sci. Polym. Letters, **15**, 349-362 (1977).

CHAPTER 2

TECHNICAL BACKGROUND AND LITERATURE REVIEW

This chapter introduces the relevant concepts of polymer science employed in this work. The pertinent information related to the biaxial stretching of films is presented in four sections. The first one describes the significant molecular and morphological characteristics of polypropylene materials. The second section presents the fundamentals of film processing, with emphasis on the tenter-frame stretching process. The third reviews the concepts of biaxial orientation, and the last section reviews the models describing the deformation mechanisms of semicrystalline polymers. Emphasis is placed on the mechanisms involved in stretching of isotactic polypropylene

[Refs. on p. 38]

2.1 - Polypropylene

2.1.1 - Introduction

Propylene polymers were produced, before 1950, in the form of a viscous oil. The properties of this oil at room temperature did not exhibit interesting properties for industrial applications. The industrial interests in polypropylene (PP) started with the production of crystalline high molecular weight isotactic polypropylene, which was first polymerized in 1954 by Natta et al. (1), using organo-metallic catalysts based on titanium and aluminum. The development of more efficient and more sophisticated catalysts allowed the production of a wide range of PP homopolymers and random and block copolymers, with various molecular weight distributions, which could be used in numerous and versatile applications. More recently, the advent of metallocene and single-site catalysts has made it possible to control both the molecular weight distribution and the microstructure (tacticity, regioregularity, comonomer distribution) of polypropylene over a wide range.

2.1.2 - Stereochemistry of Polypropylene

2.1.2.1 - Introduction to Stereochemistry of Polypropylene

The stereochemistry of propylene polymers is controlled by the degree of branching, the regioregularity, and the stereoregularity (2). Depending on the stereo arrangement of the monomer added to the growing chain, propylene can polymerize in the isotactic, syndiotactic, or atactic form. Isotactic PP chains result from the head-to-tail addition (1-2 insertion) of propylene monomer units, for which the methyl groups always have the same configuration with respect to the polymer backbone. Syndiotactic PP results from the same head-to-tail addition of monomer units, but the methyl groups have an alternating configuration with respect to the polymer backbone. Atactic chains do not have any consistent placement of the methyl groups. Figure 2-1 shows a schematic representation of isotactic, syndiotactic, and atactic chains.

(a) Isotactic

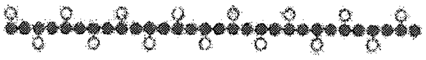

(b) Syndiotactic

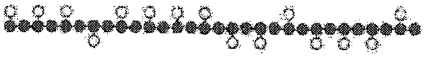

(c) Atactic

Figure 2-1 *Schematic of the stereochemical configurations of polypropylene: (a) isotactic PP, (b) syndiotactic PP, and (c) atactic PP (○ = methyl group; ● = carbon group)*

Metallocene catalysts produce polymers with a more homogeneous structure, compared to the Ziegler-Natta (ZN) catalysts. Metallocene PP has thus narrow molecular weight distribution, constant tacticity, and purely random insertion of comonomers. However, metallocene catalysts produce chain defects resulting from head-to-head or tail-to-tail addition of monomer units. This stereo defect in the chain can be detected by ^{13}C nuclear magnetic resonance (NMR) and is referred to as a 2-1 insertion defect(3). This stereo defect does not occur in the case of ZN catalysts because of steric restrictions(4).

Beyond homopolymers, there is a wide range of propylene copolymers and terpolymers, usually with ethylene and butene of two types: random and impact. Random copolymers contain a low amount (up to 6% by weight) of comonomer inserted randomly within the chain. Impact copolymers are heterophasic copolymers, which contain up to 40% of ethylene-propylene rubber (EPR) dispersed in a homopolymer matrix.

2.1.2.2 - Stereochemistry and Crystallinity

The degree of crystallinity of PP homopolymer is governed primarily by the tacticity of the polymer chain. The level of tacticity can vary greatly in isotactic or syndiotactic PP. High crystallinity requires high tacticity, which implies the presence of long, uninterrupted setereospecific sequences along the chain (2). As the tacticity is reduced, crystallinity is reduced. In the extreme case, atactic polypropylene has no crystallinity. The stereoregularity can be viewed in terms of the defect distribution along a single chain and the distribution among chains in various defect frequencies.

2.1.3 - Crystal Structures of Isotactic Polypropylene

It has long been recognized that isotactic polypropylene (iPP) can exist in several polymorphic forms, which are the α-, β-, and γ-forms and a mesomorphic or smectic form (5-7). The formation of the different forms is principally governed by crystallization conditions and molecular characteristics.

The different crystallographic symmetries of isotactic polypropylene are monoclinic (α), hexagonal (β), and orthorhombic (γ). They are all composed of chains in 3_1 helical conformation with a common repeating distance of 0.65 nm (see Figure 2-2). However, they differ in unit cell symmetry, inter-chain packing, and structural disorder. The main characteristics of the crystallographic symmetries of the three polymorphic forms of isotactic polypropylene are listed in Table 2-1.

Table 2-1 Crystallographic data of isotactic polypropylene

Crystal System (Crystal form)	**Crystal Density** [g.cm^{-3}]	**Lattice constants** [Å]				**Ref.**
		a	**b**	**c**	**angles**	
Monoclinic (α-form)	0.946	6.66	20.78	6.50	β=99.62°	(7)
Hexagonal (β-form)	0.921	19.08	-	6.49	β=120°	(7)
Orthorhombic (γ-form)	0.954	8.54	9.93	42.41	-	(8)

2.1.3.1.1 - α-Form

The α-form is the dominant and most widely occurring form encountered under normal processing conditions. Recently, it was reported that the α-form can be recrystallized and/or annealed from a less ordered α_1 form to a more ordered α_2 form (9). The minor difference between these two forms is a few tenths of one kJ/mol in terms of packing energy and is attributed to a different arrangement of the "up" and "down" helices in the crystal units. The α_1 form has a random distribution, whereas the α_2 form has a well-defined disposition of the helices (9, 10).

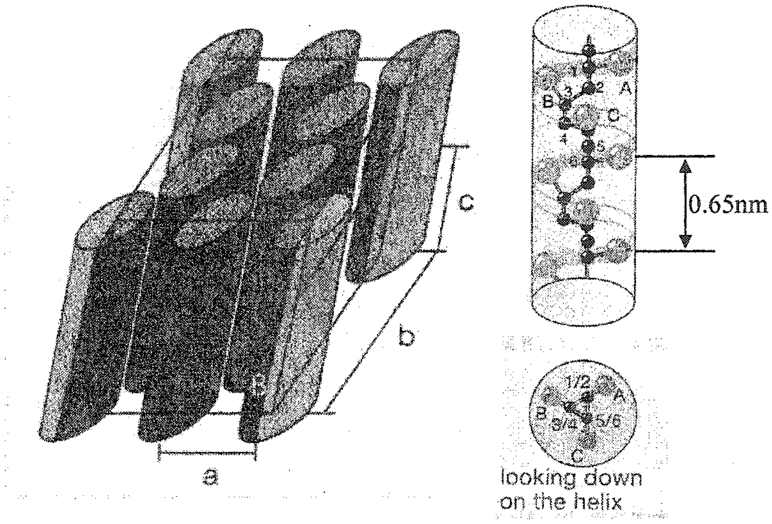

Figure 2-2 *Schematic illustration of the monoclinic unit cell (left) and of the helical chain conformation (right) of isotactic polypropylene (● = C atom, ● = methyl group; a, b, and c are the unit cell dimensions)* (11)

2.1.3.1.2 - β-Form

Interest in the β-form has increased markedly in recent years, and the application of the β-form is definitely favorable in some fields, such as film forming (12, 13). The β-form can be partially crystallized in samples mixed with other crystal forms under normal crystallization conditions. The preparation of rich or even pure β-form can be successfully achieved through crystallization in a temperature gradient, or the use of selective nucleating agents (14). Comprehensive investigations have revealed that the formation of β-iPP has an upper and lower temperature of conversion, T(αβ) and T(βα), respectively (15). The β-form is known to have a low packing density and thus numerous glide planes (16). This explains why the β-form is thermodynamically less stable than the α-form. β-iPP is transformed into α-iPP under appropriate conditions of heating (15, 17) and applied strain (18-21).

2.1.3.1.3 - γ-Form of Isotactic Polypropylene

The γ-orthorhombic structure can be produced with Ziegler-Natta-catalyzed iPP (ZN-iPP) resins by crystallization at elevated pressure above 200 MPa or utilizing low molecular weight iPP (7, 22). The γ-orthorhombic structure has also been observed when PP was copolymerized with ethylene or butene (23). Recently, it has been shown that metallocene-catalyzed iPP homopolymers can produce the γ-form at atmospheric pressure (24, 25).

2.1.3.1.4 - Smectic Phase

The mesomorphic phase is of great industrial interest, since it can be formed under rapid cooling conditions, which occur in many commercial manufacturing processes. Numerous studies have been carried out to understand the morphology of the quenched state of iPP (5, 6, 26-34). It was found that the smectic phase represents a state of order intermediate between the amorphous and crystalline states (5). It was found that the smectic phase is also composed of chains in a 3_1 helical conformation (6) and possesses a short range three-dimensional order of limited nature (27). The size and symmetry of the ordered regions have not been fully resolved and are still being argued (29-31, 33). Another significant aspect of the smectic phase is its metastability. Various studies were conducted to elucidate the formation and stability of the disordered smectic phase (32, 34-44). They indicated that the disorder can be induced either by rapid quenching from the melt or, under certain conditions, by the disruption of existing crystallites by deformation processes. It was also found that the smectic phase is stable at room temperature but is transformed to the more stable α-form either by annealing above 60-70°C (26, 28, 36) or by mechanical deformation (44).

2.1.4 - Lamellar Structures of Isotactic Polypropylene

Isotactic Polypropylene exhibits a unique tendency for lamellae to organize into a highly characteristic lamellar branching or "cross-hatching" (45-48). This feature of the morphology is observed only for the α-form. It is schematically represented in Figure 2-3. The lamellar structure of the γ-form and the smectic phase will not be presented because the former is relatively infrequent in commercial products, and the latter has not been fully resolved.

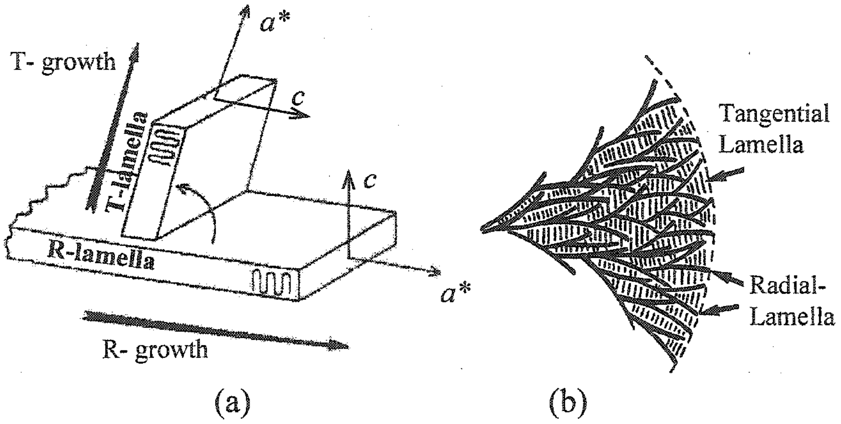

Figure 2-3 Schematic of the lamellar branching morphology of iPP at the (a) lamellar level and at the (b) spherulitic level (T = tangential; R = radial; a = main growth direction)*

The lamellar branching of α-iPP is attributed to homo-epitaxial growth of the daughter lamellae (T-lamella) on the lateral (010) crystallographic plane of the mother lamellae (R-lamella) with a constant angle (80° or 100°) (49). The preferred growth of the dominant R-lamellae has been determined to be associated with the a*-crystallographic direction (46, 49), the main growth direction. The degree of lamellar branching was reported to decrease with increasing crystallization temperature (46, 48, 50) and isotacticity (50), with some exceptions for highly structurally regular isotactic polypropylene fractions (51).

Norton and Keller(46) found that the lamellar structure of the β-form consists of broad, locally parallel stacked lamellae, just as in the spherulites of other polymers. The authors also found that the lamellae of the β-form have a propensity to twist along the radial growth direction (*a*-crystallographic axis), thus presenting a broad spread of orientation varying from *b*-axis to *c*-axis profiles.

The above peculiarities of the iPP lamellar structure have been linked to the optical classification of the iPP spherulites, as discussed below.

2.1.5 - Spherulitic Structures of Isotactic Polypropylene

Several research groups have made morphological observations of spherulitic iPP through polarized light microscopy (PLM), over a large crystallization temperature range (46-48). Depending on the birefringence of the spherulites (positive or negative, weak or strong) and if the lamella were straight or twisted, they classified the iPP spherulites into four main, distinct types: α_I, α_{II}, β_{III}, and β_{IV}. The first two types, α_I and α_{II}, consist of α-iPP spherulites that crystallize in different temperature ranges, resulting in a different level of lamellar branching and a weak birefringence. The latter two spherulite types, β_{III}, and β_{IV}, consist of β-iPP spherulites, having either radial, straight lamella (β_{III}) or twisted lamella (β_{IV}), that crystallize within certain constraints of isothermal crystallization temperature, as shown in Figure 2-4. These are characterized by a strong birefringence.

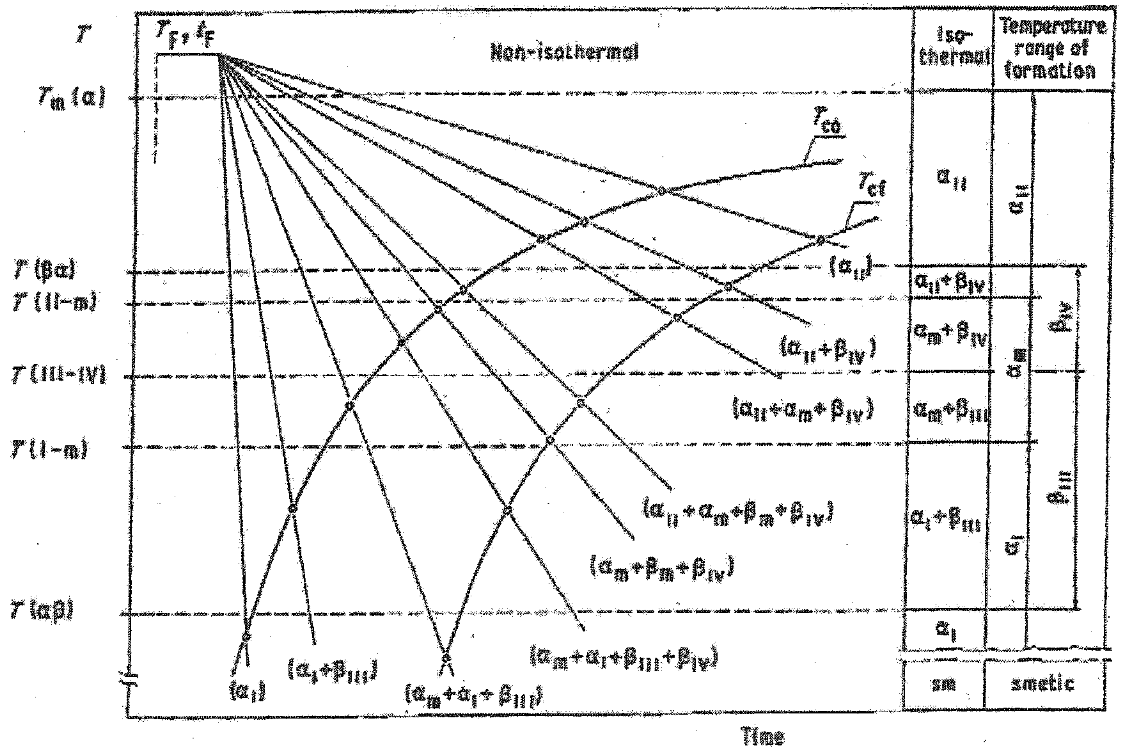

Figure 2-4 Formation of the different types of iPP spherulites during isothermal and non-isothermal crystallization(15); Symbol notation can be found in text

The formation of the different types of spherulite is governed primarily by the crystallization conditions, which is illustrated in Figure 2-4. It can be seen that, in certain temperature ranges, α_m and β_m spherulites can be formed. These were defined as mixed-type spherulites, which have no specific optical character. It can be deduced that, under non-isothermal conditions at high cooing rates, iPP crystallizes into α-spherulites and into the smectic phase. On the other hand, it crystallizes into α- and β-spherulites, if the cooling conditions are moderate.

The crystallization conditions were reported to affect the structure of the amorphous phase, i.e. the entanglement density and tie molecule fraction. A tie molecule is a chain section anchored in the crystal lattice of adjacent lamellae. Low crystallization temperatures lead to a higher entanglement density and tie molecule fraction than high temperature crystallization (52, 53). Moreover, it is suspected that the β-spherulites possess a higher density of tie molecules, compared to the α-spherulites, when crystallized under the same conditions (16).

2.1.6 - Melting Behavior of Isotactic Polypropylene

Melting of polymers is a complex process; it is highly dependent on the thermal and mechanical conditions during the formation of the crystal structure, on the thermal history of the crystalline samples, and on the testing parameters (e.g. heating rate) (54). The most common technique to follow the course of melting is calorimetry. Calorimetric melting curves can provide the melting point and the degree of crystallinity of semicrystalline polymers. In addition to the common factors affecting melting of polymers, such as molecular weight, orientation, annealing, etc…, the isotacticity and polymorphism of iPP influence greatly the melting behavior, the occurrence of multiple endotherms, and the equilibrium melting temperature (T_m^0). T_m^0 is the ratio of the change in enthalpy over the entropy change for the first order melting transition from pure crystalline polymer to pure amorphous melt.

2.1.6.1 - Equilibrium Melting Temperature

Varga (14), Phillips and Wolkowicz (2), and Bu et al. (55) reviewed the numerous studies carried out to determine the equilibrium melting temperature, T_m^0, and the heat of fusion of a 100% crystalline sample, ΔH_f^0, for α-iPP and β-iPP. Literature data were found to be quite contradictory.

Literature data for T_m^0 of high molecular weight and highly isotactic α-iPP lie between 180°C and 220°C and for ΔH_f^0 between 150 J/g and 210 J/g. Bu et al. (55) accepted the following values of 187.6 K for T_m^0 and of 207.1 J/g for ΔH_f^0. The wide range of data can be explained by the fact that, T_m , T_m^0 , and ΔH_f^0 are decreased by disturbing the regularity of the polymer chain, reducing isotacticity or randomly incorporated defects or comonomer units (14, 56). For example, the metallocene-based iPP resins possess the characteristic of the presence of homogeneously distributed 2_1 insertion defects, which are assumed to be excluded out of the lamellae. This explains the low melting behavior of the metallocene-based resins (4, 57).

For β-iPP, the determination of T_m^0 and ΔH_f^0 is disturbed by the presence of a mixed polymorphic composition and the tendency for recrystallization into α-iPP, as discussed below. The values that were determined using pure β-iPP are the most reliable. Varga (14) suggested the following values of 184 ± 5 K for T_m^0 and 113 ± 11 J/g for ΔH_f^0.

Few studies have been reported on γ-iPP because of the difficulty to prepare pure γ-iPP and due to its unstable nature. Recently, however, Bond et al. (25) were able to determine T_m^0 for the γ-orthorhombic crystal structure, using metallocene resins, and found a value of 178 ± 4 K.

2.1.6.2 - Peak Multiplication on Melting of iPP

The shape of the calorimetric melting curve, the melting profile of iPP, may contain two or more melting peaks. This may be attributed to mainly three reasons: (i) separated melting of different crystallites; (ii) different polymorphic fractions; (iii) recrystallization or transition superimposed on melting.

The melting curves of α-iPP, samples crystallized (15) or annealed (58) at different temperatures, show multiple individual peaks referring to separate melting of crystallite fractions that differ in size and perfection. Certain isothermally crystallized iPP samples can exhibit two endotherms corresponding to the melting of the two distinct R-and T- lamellae populations (51). Crystallites with differing thermal stability can also be the result of a mechanical or thermal treatment (e.g., annealing) .

Isotactic PP samples that were quenched may contain some unstable smectic phase, which is transformed into α-modification with increasing temperature (26, 28, 36). The smectic-to-α-form, solid state transition is characterized by an exotherm in differential scanning calorimetry (DSC) scans at temperatures between 65°C and 120°C (37, 39). During crystallization, conventional Ziegler-Natta-type iPP can also form some β-phase together with the α-phase. Consequently, a low temperature peak due to the melting of the β-form can be superimposed on the main melting peak of the α-modification. However, melting curves of samples containing both α- and β-form can be more complex, because of the possible recrystallization of the β-form into the α-modification (βα recrystallization) during heating (14).

Finally, PP samples, that show no other polymorphic forms (β-, γ-, smectic form) than the stable α-form, may still exhibit multiple endotherms. This can be due to melting-recrystallization-remelting processes or self-annealing / perfection of crystallites during heating (2).

2.2 - Film Processing

The present section will introduce the fundamental difference between the melt- and solid phase-based processes that are employed to produce biaxially oriented thin films. A comparison among the solid phase-based processes available to manufacture biaxially oriented polypropylene (BOPP) films is then presented. Finally, a detailed description of both sequential and simultaneous biaxial tenter-frame stretching processes is given.

2.2.1 - General Principle

In the manufacturing of large volumes of thermoplastic films, such as those made from polyethylene (PE), polypropylene (PP), polyvinyl Chloride (PVC), and polyethylene terephthalate (PET), the polymer is deformed in the melt and/or solid state. In the first case, film formation involves visco-elastic deformation of the polymer melt at relatively high temperatures, above the melting point (T_m). The cast film, film blowing, and extrusion coating processes are the main melt-based film forming processes. In the second case, for the solid-phase-based processes, deformation takes place in an elastic-plastic manner at high temperatures but below T_m , in the so called rubbery state. The tenter-frame stretching and double-bubble processes are the main film formation processes based on this deformation principle.

In film forming processes based on the solid phase, orientation is achieved in the following sequence: (i) reheating a solidified, unoriented specimen to a temperature range in which the crystalline phase is partially melted, (ii) stretching the sample into the desired shape, and (iii) cooling while the sample is still under tension, in order to freeze the orientation. In the melt-based processes, orientation is obtained by rapidly drawing the polymer melt leaving the extrusion die, while simultaneously cooling to cause solidification of the polymer.

The major difference between the two types of film forming processes is in the amount of achievable orientation. Solid phase processes produce more highly oriented products (59).

2.2.2 - Biaxially Oriented PP Film Processes

Biaxially oriented PP films can be made via two distinctly different types of processes, in which deformation takes place in the rubbery state: the double bubble (or tubular) film process and the tenter-frame (or tentering) process. The tentering process is divided further into the sequential and the simultaneous stretching methods.

2.2.2.1 - Double-Bubble Film Process

In the double-bubble process, a thick tube is extruded downwards through an annular die over a water-cooled sizing mandrel and quenched further in a water bath. This first "bubble" is then reheated to a temperature between 140°C and 160°C and is then oriented in the second "bubble" by inflation, while simultaneously being stretched in the machine direction. The film is then air cooled and wound on rolls. The capital cost of the tubular film process is lower than for the tentering process, but it produces film with a limited thickness range at low output rates (2). Film thicknesses range from 8μm to 50μm, with line outputs in the range of 100 kg/h to 550 kg/h.

2.2.2.2 - Tenter-Frame Process

The sequential and simultaneous tentering processes are employed independently in accordance with the resin characteristics. The major part of the biaxially oriented films is produced by the sequential tentering process. This method is more common for the manufacture of biaxially oriented PP (BOPP) due to lower variable costs and high output. Also, the technology is more widely available than that for bubble processes. Films ranging from 5μm to 80μm are produced on equipment making widths of 3 m to 10 m at line speeds up to 500 m/min and outputs of 6,000 kg/h.

Two technologies are available for the simultaneous tentering process: the pantograph and the pitch screw technology. However, these processes involve complicated tenter structure and low outputs compared to the sequential process. Recently, Dupont patented a new simultaneous biaxial stretching technology, called LISIM© (linear motor simultaneous) technology, which was further developed by Brückner Maschinenbau GmbH. This technology has been commercialized, and it yields commercial biaxially oriented films and line speeds and outputs comparable to those obtained with sequential production lines.

2.2.3 - Tenter-Frame Stretching Processes

2.2.3.1 - General Principles

The production lines based on sequential and simultaneous biaxial tenter-frame stretching consist of similar components, except for the orientation units. In a typical sequential tenter-frame stretching process, illustrated in Figure 2-5, a sheet is extruded (a), quenched (b), and then reheated to be stretched in the machine direction (MD) (c). The uniaxially stretched sheet is then conveyed at room temperature to the tenter section, where it is reheated (d) and then stretched in the transverse direction (TD) to the desired film width (e). In the heat setting zone (f), the dimensional properties are controlled. Finally, the film is cooled, and the clips are released prior to edge trimming (g), and winding (h).

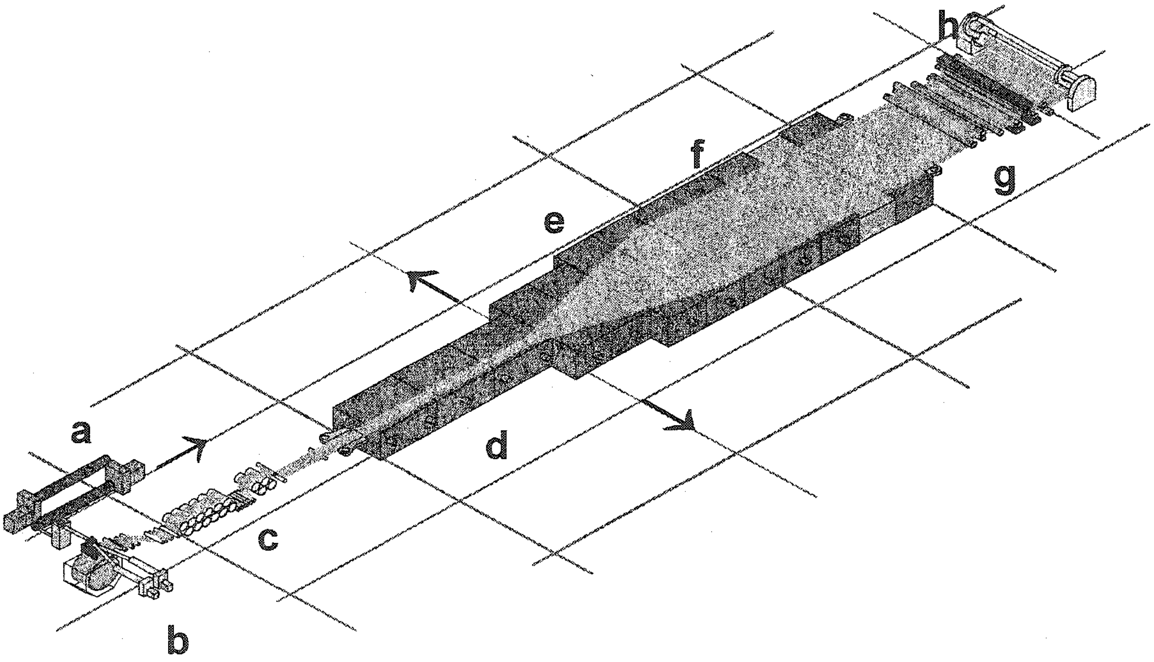

Figure 2-5 *Schematic of a sequential biaxial tenter-frame stretching process; (a) extrusion line, (b) casting unit, (c) MD orientation unit, (d) preheating zone, (e) TD orientation unit, (f) heat setting zone, with cooling zone, (g) pull roll unit, and (h) winding unit*

The simultaneous tentering processes consist of the same sequence as in the sequential process, except that the MD orientation unit is removed and biaxial stretching takes place in one step in hot air. In the simultaneous stretching process a continuous film is gripped along the sides by clips connected by a certain mechanism that increases the inter-clip distance, to produce the MD orientation. Moreover, clips diverge at a predetermined angle, to generate the TD orientation, as illustrated in Figure 2-6(a).

The pantograph and pitch screw simultaneous process technologies involve complex mechanical designs, which causes difficulties in maintenance and in changing the MD stretching ratio. On the other hand, the LISIM© process consists of clips that are individually controlled by linear motors, as illustrated in Figure 2-6(b). The advantages of this technology includes ease of operation, flexibility in varying stretching parameters, good control of shrinkage during heat setting and balanced properties in both directions, and low maintenance (60). LISIM© provides similar line speeds, film width, and line outputs as the sequential process. Another significant advantage of simultaneous biaxial stretching is the lower stresses involved during deformation, especially when compared to those required in transverse orientation in the sequential process. This allows the simultaneous lines to produce specialty films, such as biaxially oriented expanded films with functional layers or synthetic paper (61). The principal stages of the tenter-frame stretching process will be now described in more detail for the special case of BOPP film production. Particular attention is given to cast film preparation and the stretching stage.

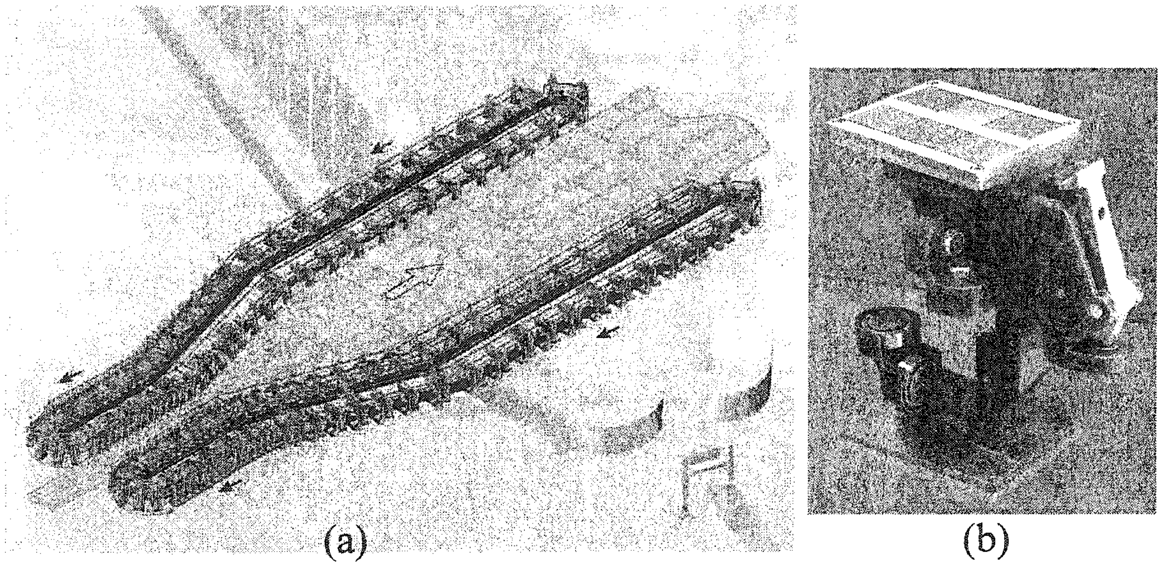
(a) (b)

Figure 2-6 Schematic of the LISIM© technology. (a) clip chains, (b) linear-motor-controlled clip

2.2.3.2 - Cast Film Extrusion

2.2.3.2.1 - Introduction

Cast film extrusion is used to manufacture plastic plates, sheets, and films. It is also used to provide primary sheets with a very uniform thickness for further stretching. In this process, the polymer melt is extruded through a flat die, then slightly stretched in air, and ultimately, rapidly cooled onto a chilled roll to solidify. Depending on the application, a water bath or a water spray system can be added to the chill roll to induce uniform cooling on both sides of the sheet. A very small air gap, distance between the die lips and the chill roll, is desired to minimize the amount of necking and stretching. A schematic of the cast film process without water bath is presented in Figure 2-7. For good cooling efficiency, the polymer melt should be pressed onto the polished surface of the chill roll. This is accomplished by using different methods, such as the air knife, the press roll, and the electrostatic methods. The air knife is generally applied for PP films.

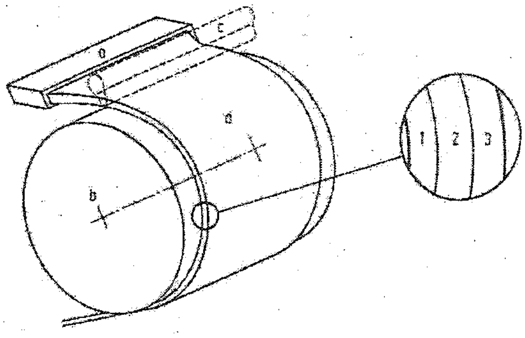

Figure 2-7 Schematic of the cast film process(62)
a: slit die; b: chill roll; c: air knife; d: film; 1: roll zone; 2: median zone; 3: air zone

The main processing parameters in cast film extrusion are the die temperature, extrusion speed, chill roll and water bath temperatures, and air gap. These will affect the stretching and cooling conditions, which in turn will determine the morphology and properties of the resulting cast film.

2.2.3.2.2 - Coextrusion

Another significant technology in cast film extrusion is the possibility of producing multi-layered samples through coextrusion. It provides superior film products by combining unique properties of different resins. For example, the BOPP films used for packaging purposes may be coextruded with a layer of another polyolefin for better heat sealability or with a polyvinyl chloride or acrylic resin for improved barrier and aesthetics.

2.2.3.2.3 - Compounding

The morphology and properties of the cast films or the final stretched films can be generally controlled by compounding with specific additives, depending on the desired application. For example, nucleation agents are employed for improvement of the optical properties, β-nucleating additives for biaxially oriented PP films are used for capacitor applications, and additive packages containing antioxidants, slip and antistatic agents are commonly used to prevent degradation and improve winding and unwinding. Moreover, the stiffness of the final film can be improved by adding some resinous polyterpenes or hydrogenated polycyclopentadienes (63).

2.2.3.3 - Preheating

The PP sheet being conveyed to the stretching oven needs to be preheated before the main or second stretching. Since heating with air provides more precise temperature control than radiation heating, hot air blowing, from above and below nozzles, heats the sheet prior to stretching. The sheet must reach the exact desired temperature, where the clip chains start diverging. In a sequential process, the pre-oriented films will be heated to a slightly higher temperature than in the simultaneous process, since higher stresses are encountered during the TD orientation than for the simultaneous process. The stretching temperature is, however, always below T_m, and is in the range from 150°C to 170°C for the sequential process and from 130°C to 160°C for the simultaneous process.

An important aspect of the preheating zone is the control of the "heat induced crystallization". Indeed, during reheating, important morphological modifications may occur in the sheet. As discussed in section 2.1.3 the smectic and β- phases, eventually present in the sheet, may be transformed upon heating into the more stable α-form of iPP. In addition, preheating at high temperature and/or for a long time promotes self-annealing and/or perfection, which may lead to poor stretchability and poor thickness uniformity of the film (60).

2.2.3.4 - Sequential Tenter-Frame Stretching

After the unoriented sheet is extruded and solidified, it is preheated to between 120°C and 150°C by means of heated rolls and then passed between closely spaced differential speed rolls to achieve MD orientation with restrained width. A small MD stretching gap is used for PP, in order to obtain more stable stretching and better thickness control, because PP has a tendency to necking under deformation. The uniaxially stretched sheet is then cooled and conveyed to the tenter section of the line. After the first MD orientation, the film is deformed in the TD direction by the tenter. The tenter consists of an oven with two rails running along the inside, one on either side. Along these rails, chain loop travels with clips attached to it at equal distances to each other (~75 mm). At the entrance of the oven, clips grasp the MD oriented film, which is led into the tenter oven. After the preheating zone, the film is stretched in the transverse direction by the diverging clip chains. The transverse deformation rate is set by the line speed and the rate of divergence of the rails. The TD draw ratio is set by the final film width.

2.2.3.5 - Simultaneous Tenter-Frame Biaxial Stretching

In the one step, simultaneous biaxial stretching process, the unoriented, cast sheet is first grasped by clips on each side at the entrance of the oven, as illustrated in Figure 2-6. After preheating, the sheet is deformed simultaneously in both the machine and transverse directions. The TD orientation is achieved by the diverging clip moving directions, similar to the sequential process. At the same time, the MD orientation is obtained by individually accelerating the clips along the machine direction. Typically, the clip speed in MD increases linearly in space within the regions where the rails diverge. The deformation rate is thus exponential in time, corresponding to a constant Hencky strain rate. The deformation rate and ratio in MD are controlled by the extrusion speed, the clip acceleration, and the final line speed.

2.2.3.6 - Heat Setting

Stretching is followed by heat setting or annealing. The annealing process is conducted with the aim of relaxing stresses to improve film dimensional stability. In the heat setting section, the tenter chains may converge slightly, and the oven temperature is raised by 5°C to 15°C. In the LISIM© process, MD stress relaxation can be achieved by decelerating the clips during annealing. This provides an additional advantage compared to the sequential process, by controlling shrinkage in both MD and TD directions. Finally, the film is cooled down in the last section of the oven, and the clips are then released prior to edge trimming, optional treatment, and winding.

2.3 - Biaxial Orientation and Texture

Investigation of orientation in polymers has a long history, and several good reviews can be found in the literature (64, 65). A summary of the main concepts of how to achieve, define, and characterize biaxial orientation in polypropylene films is presented here.

2.3.1 - Introduction to Orientation

Polymer orientation refers to alignment of polymer molecules in a particular direction or plane, thus providing greater strength and stiffness in the orientation direction(s). All of the PP fiber applications and 75% of the film applications are oriented (2). Orientation can be achieved by different methods, each imparting characteristic orientation, as discussed below.

2.3.1.1 - Achieving Orientation

Three types of orientation will be considered: uniaxial, constant-width uniaxial, and biaxial, which are illustrated in Figure 2-8. In uniaxial orientation, no constraints are placed in the width or thickness of the item being stretched. Subsequently, reduction in both the width and thickness occurs. For an ideal case, the reduction ratio is the same in both directions and equals the square root of the draw ratio. The direction of the stretching is commonly defined to be the machine direction (MD). The most simple process inducing uniaxial orientation is probably fiber spinning.

As discussed above, film processes such as the tubular and tentering processes, usually involve biaxial orientation. In film orientation, the dimensional change in the transverse direction (TD) (across the machine axis) determines the type of orientation. In some cases, for which the film is stretched over a very short distance compared to the film width (less than 10%), the width is almost unchanged, and the thickness decreases in a ratio equal to the MD draw ratio. This deformation is referred to as constant-width uniaxial. An example is the MD orientation step in a sequential tentering process for making BOPP, as described in section 2.2.

When the film is stretched in the TD direction in a ratio comparable to the MD draw ratio, the film is biaxially oriented, and the thickness decreases by the product of the

MD and TD draw ratios. Equibiaxial orientation corresponds to the stretching in which the MD and TD draw ratios are equivalent.

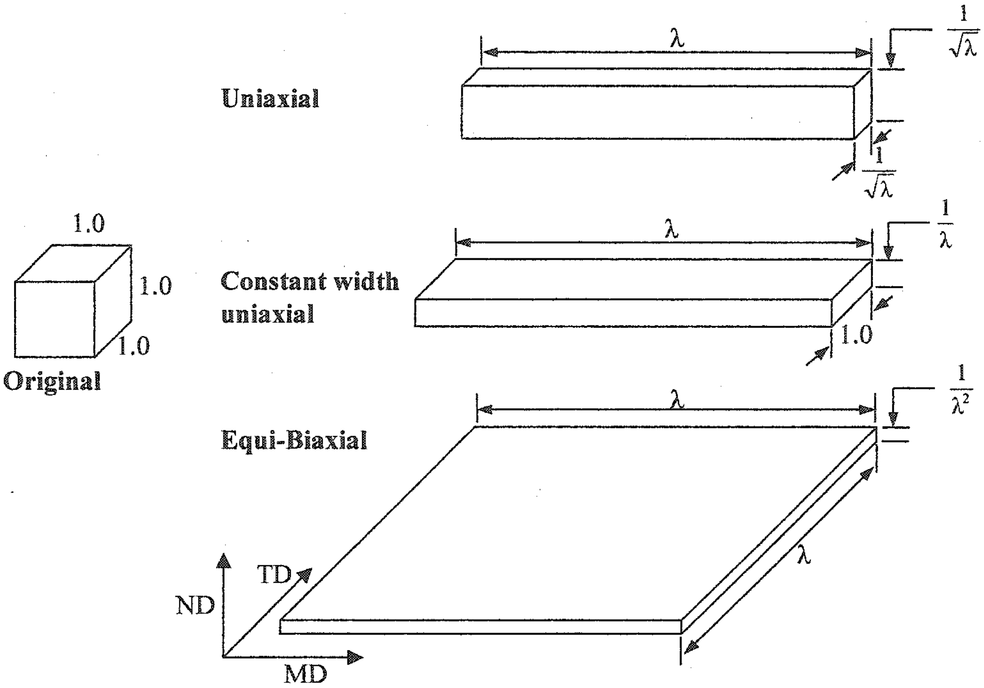

Figure 2-8 Definition of the types of orientation with λ being the stretching ratio

2.3.1.2 - Achieving Biaxial Orientation

Biaxial orientation can be achieved by means of many different processes. The most widely-used processes, for thin sections, such as films, are the tentering, tubular double bubble, and film blowing processes. For thick sections, the available processes for biaxial orientation are continuous forging, tube expansion, and cross-rolling. Forging consist of applying a hydrostatic pressure in compression on thick octagonal sample (41). An example of a tube expansion process consists of a tube filled with water, and then pressurized past the yield stress of the tube, thus providing expansion. Finally, cross-rolling is the operation of shaping and reducing a sheet in thickness by passing it between two sets of heated rolls having a rolling direction at 90° (66).

2.3.2 - Defining Molecular Orientation and Texture

2.3.2.1 - Defining Molecular Orientation

The definition of orientation given here is adapted from a review on characterization of orientation in polymers done by Cole and Ajji (64). Orientation is commonly described on the molecular scale with respect to a macroscopic sample. Therefore, it is necessary to define a coordinate system for the sample and for the structural units of the sample. Most industrial samples possess a certain symmetry which allows us to define a coordinate system in terms of three orthogonal directions. For films, these are described as MD (machine direction), TD (transverse direction), and ND (normal direction), as shown in Figure 2-8. On the molecular scale, the structural units, such as the molecular chain or a crystallographic axis, are usually used to define the second coordinate system, as *a*, *b*, and *c*. For example, in the case of biaxially oriented PP films, the crystalline phase will have the three axes of the monoclinic unit cell.

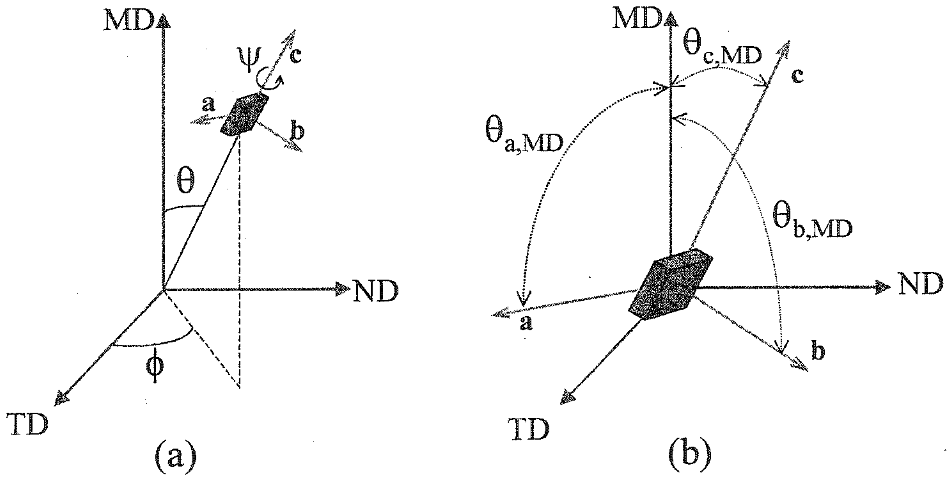

Figure 2-9 Definition of orientation (a) in terms of Eulerian angles and (b) in terms of the angles $\theta_{i,J}$

The orientation of a single structural unit with respect to the sample geometry can be expressed in terms of the three Euler angles θ, ϕ, and ψ, as illustrated for the *c* chain axis in Figure 2-9(a). Angle θ is the polar angle, ϕ is the azimuthal angle; they define the orientation of the c axis with respect to the sample geometry. The third Euler angle ψ represents the rotation of the structural unit about the c axis. The probability of finding a structural unit having the spherical-polar coordinates θ, ϕ. and ψ , is given by the orientation distribution function (ODF) $N(\theta,\phi,\psi)$. This function may be expressed as the sum of a series of generalized spherical harmonics:

$$N(\theta,\phi,\psi)=\sum_{l=0}^{\infty}\sum_{m=-l}^{+l}\sum_{n=-l}^{+l}P_{lmn}Z_{lmn}(\cos\theta)e^{-im\phi}e^{-in\psi} \qquad eq.(2\text{-}1)$$

where the Z_{lmn} are a generalization of the Legendre functions, P_{lmn}. In theory, all the coefficients P_{lmn} must be determined to fully define the orientation distribution. In most of the real cases, the sample and the structural units have at least orthorhombic symmetry, then the P_{lmn} are non-zero only when m and n are even.

The second-order moments of the ODF, where P_{lmn} is with $l = 2$, may be determined by infrared spectroscopy and birefringence. Higher-order moments can be obtained by Raman spectroscopy, nuclear magnetic resonance, and X-ray scattering, but the procedure is rather complex. Therefore, many studies of orientation are limited to the second-order moments, which is in many cases sufficient, except for highly oriented polymer samples. Nevertheless, it is difficult to visualize the physical meaning of the P_{2mn} coefficients.

Another way of describing the orientation is in terms of the angles $\theta_{i,J}$ between each of the axes of the structural units (i = *a*, *b*, or *c*) and each axes of the sample coordinate systems (J = MD, TD, or ND). There are thus nine angles, which are not independent. For a given axis of one coordinate system, the sum of the squared cosines with respect to the three axes of the other system is equal to unity.

The average values of the squared cosines, $<\cos^2\theta_{i,J}>$, are related to the second-order moment, the P_{2mn} coefficients (64). The values of $<\cos^2\theta_{i,J}>$ range from 0 if the axes *i* and *J* are perpendicular, to 1/3 for random orientation, to 1 when the axes *i* and *J* are parallel. For each angle $\theta_{i,J}$, it is also possible to calculate a Hermann's-type orientation function:

$$f_{i,J}=\frac{3<\cos^2\theta_{i,J}>-1}{2} \qquad eq.(2\text{-}2)$$

where the value of *f* will then range from –1/2 if the axes *i* and *J* are perpendicular, to 0 for random orientation, to 1 when the axes *i* and *J* are parallel. The Hermanns orientation functions can be in turn expressed in terms of the P_{2mn} coefficients or vice versa (64).

For the special case of biaxial orientation, White and Spruiell (67) proposed a method of describing biaxial orientation factors, which are related to the $f_{i,J}$ functions previously defined in eq.(2-2) as follows:

$$f_{i,MD}^{B} = \tfrac{2}{3}\left(2f_{i,MD} + f_{i,TD}\right) \qquad eq.(2\text{-}3)$$

$$f_{i,TD}^{B} = \tfrac{2}{3}\left(2f_{i,TD} + f_{i,MD}\right) \qquad eq.(2\text{-}4)$$

where i can be a, b, and c. This approach is relevant when there is preferential orientation around the chain axis, which is usually the case for biaxially oriented films.

If we consider only the chain c-axis, biaxial orientation can be defined in terms of Hermanns-type orientation functions as follows:

$$f_{c,MD} = \frac{3 < \cos^2\theta_{c,MD} > -1}{2} = P_{200} \qquad eq.(2\text{-}5)$$

$$f_{c,TD} = \frac{3 < \cos^2\theta_{c,TD} > -1}{2} = -\tfrac{1}{2}P_{200} + 3P_{220} \qquad eq.(2\text{-}6)$$

$$f_{c,ND} = \frac{3 < \cos^2\theta_{c,ND} > -1}{2} = -\tfrac{1}{2}P_{200} - 3P_{220} \qquad eq.(2\text{-}7)$$

with the sum $f_{c,MD} + f_{c,TD} + f_{c,ND}$ being equal to zero. Therefore, only two quantities are sufficient to define the biaxial orientation. These could be any of the following couples: $f_{c,MD}$ and $f_{c,TD}$, P_{200} and P_{220}, or $f_{c,MD}^{B}$ and $f_{c,TD}^{B}$. In typical biaxially oriented films, as described above, $f_{c,MD}$ and $f_{c,TD}$ are positive and $f_{c,ND}$ is negative. For equibiaxial orientation, $f_{c,MD}$ and $f_{c,TD}$ are equivalent. In the ideal case of uniaxial orientation, $f_{c,MD}$ is positive and the other two are both equal to $-\frac{1}{2} f_{c,MD}$. Hence, only one quantity is needed to define perfect uniaxial orientation.

2.3.2.2 - Defining Texture for Polymers

The term "texture" is used to define a certain state of crystalline orientation. Apart from the general description of orientation, using the orientation distribution functions, it is customary to classify orientation distributions qualitatively. Heffelfinger and Burton(68) developed this approach by denoting frequently occurring preferential orientation of crystalline elements (crystallographic axes or lattice planes) in relation to the sample geometry (MD, TD, ND as defined above) as types of texture. They found six distinct orientation modes or textures: the random, planar, uniplanar, axial, plane/axial, and uniplanar-axial orientation modes, which are defined in *(68)*.

A perfectly uniaxially oriented specimen that has the chain axis (*c*) aligned in the MD direction is classified as having axial texture, whereas a biaxially oriented film may have a planar, uniplanar, or even uniplanar-axial texture depending on the preferred orientation of the *a* or *b* crystal axis. A perfectly equibiaxially oriented film will have either planar texture, if there is no preferential orientation of the *a* or *b* crystal axis, or uniplanar texture if the plane (010) is preferentially oriented in the plane (MD-TD).

2.3.3 - Characterization of Biaxial Orientation

Characterization of orientation usually utilizes parameters obtained from the interaction of electromagnetic radiation with the molecular system. Common techniques are birefringence, X-ray scattering, light scattering, and selective absorption of polarized radiation (linear dichroism). Other methods that do not use electromagnetics are nuclear magnetic resonance (NMR) and the sonic velocity (ultrasonic) method. Numerous reviews for each of the individual techniques as well as reviews comparing these different methods can be found in the literature (65, 69-74). For the characterization of biaxially oriented polypropylene films, the most commonly used methods, alone or combined, are wide-angle X-ray scattering (WAXS), infrared dichroism, and birefringence. In this work, WAXS and infrared dichroism, whose principles are detailed in Chapter 4, were employed to determine orientation functions and texture.

2.4 - Deformation Mechanisms and Morphology of Polypropylene

This section considers the deformation behavior of isotactic polypropylene in the solid state, i.e., below its melting point (T_m) and above the glass transition temperature (T_g). Two approaches are reviewed and discussed here: the macroscopic deformation behavior with its relation to film dimensions and the microstructure development during drawing. Special attention is given to the mechanisms of deformation and structural rearrangements occurring during stretching in the partly molten state. Finally, the effects of initial morphology on deformation and oriented morphology are reviewed.

2.4.1 - Macroscopic Deformation Behavior

Polymers can be oriented in the solid or partly molten state by various processes, such as tensile and die drawing, film stretching, hydrostatic and ram extrusion, rolling, roll-drawing, and hydrostatic compression. In all these solid phase processes, plastic deformation may not take place in a homogeneous manner, but instead, the plastic strain may occur only in certain very localized regions. This phenomenon is commonly referred to as necking, which is generally observed in semicrystalline polymers, when they are cold drawn below T_m and above T_g.

Figure 2-10 illustrates the typical stress-strain curve profile of a cold drawing experiment. The deformation begins with an elastic response (AB) followed by yielding (at B), plastic deformation (BC), and strain hardening (after C). There is a common misconception that the drop in nominal stress must necessarily be due to necking. At high temperature, and sufficiently high strain rates, the strain in PET film drawing was reported to be essentially uniform even though the nominal stress was initially falling after the yield point (75). In fact, any material that strain softens may neck under certain conditions of deformation. Strain softening arises from yielding of the initial structure of the undrawn material. Nevertheless, necking is the manifestation of an instability in the yielding process due to 'defects' on a microscopic or macroscopic level (75).

The complex rearrangements of chains on drawing start in the necking region, either inhomogeneously or homogeneously, depending on deformation conditions (76). The deformation homogeneity is directly related to the local, true draw ratios, which determines the mechanical behavior. Indeed, Ward et al. (77) showed that the elastic modulus of polyethylene fibers depends only the true draw ratio.

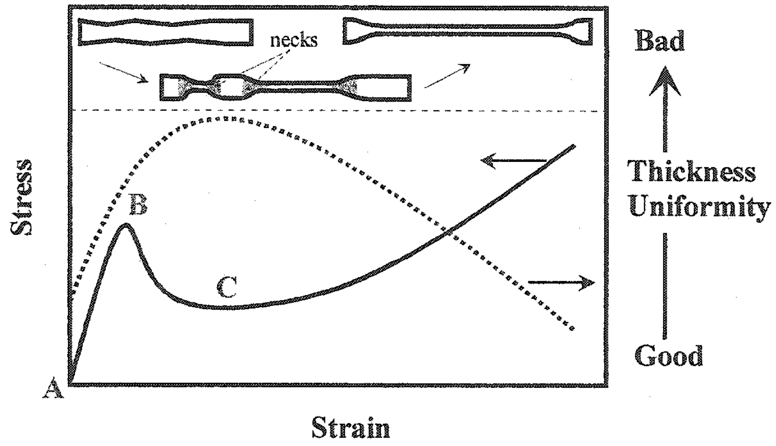

Figure 2-10 Schematic representation of the relation between tensile deformation behavior and thickness uniformity; with elastic deformation along (AB), necking at (B), neck propagation along (BC), and onset of strain hardening at (C)

Necking may cause a non-uniform thickness profile in the specimen. The requirements in terms of thickness uniformity and/or surface roughness are important for biaxially stretched films, depending on the application. For example, smooth surface and good thickness uniformity are needed in order to achieve good film optical properties for packaging applications. On the contrary, films used for adhesion need to have a rough surface. Despite the importance of film dimensions for biaxially stretched films, few reports have dealt with the homogeneity under biaxial deformation and its relation to the uniformity of film dimensions (78, 79). Olley and Bassett (78) investigated the relation between surface morphology and necking for the case of specimens containing both α- and β- spherulites and Sweeney et al. (79) reported some results about the necking behavior of polypropylene, using specially designed specimens.

2.4.2 - Structural Deformation Mechanisms

Several authors have reviewed the main deformation mechanisms involved during cold drawing (80-84). Microstructure development during cold drawing of polymers has been studied mainly at room temperature and in uniaxial extension. Furthermore, the majority of the descriptive deformation models are based on the lamellar level of the microstructure. Spherulite deformation has been also investigated (76, 85-87) but has been only recently observed to have an effect on the final oriented morphology (78, 86).

It was first proposed by Peterlin (80) that the starting folded lamellar structure of polyethylene and polypropylene is transformed into an oriented fibrous structure, followed by the plastic deformation of the fibrous structure. This section reviews in more detail the main structural models and deformation mechanisms involved in this morphological transformation.

2.4.2.1 - Structural Models for Cold Drawing

Several structual models were proposed to explain the possible chain motions during crystal deformation that allow the alignment of the chain axis in the tensile direction. These distinct deformation models can be classified in three groups based on melting and recrystallization (88), dislocation defect propagation, or thermal crystal transition (84). Flory's model (88) has been considered for explaining β-α conversion during deformation of β-iPP (20). Nevertheless, these models do not by themselves explain all the experimental facts.

Most of the models that deal with the lamellar transformation into an oriented structure for polyethylene and polypropylene distinguish three stages (80, 84, 89): (i) lamellae move rigidly apart with the strain accommodated by the interlamellar amorphous regions; (ii) the tie molecules become highly extended and crystal slip starts, inducing the pull out of crystal blocks from the lamellae; (iii) crystal blocks become aligned in the drawing direction, forming the oriented structure, which is being further deformed.

The most widely quoted model for cold drawing is that proposed by Peterlin (80). However, this useful model does not address any crystallinity and crystal size changes on drawing, and microfibrils are not always present in drawn polymers (90).

2.4.2.2 - Deformation Mechanisms of Semicrystalline Polymers

The first stage in deformation of the spherulite lamellar structure is borne principally by the interlamellar amorphous regions that support the applied stress by a combination of three main mechanisms: lamellar separation (b), interlamellar shear (c), and lamellar stack rotation (d), as illustrated in Figure 2-11. These amorphous regions contain the chain folds, chain ends, entanglements, and tie molecules. Drawing will result in more taut and oriented amorphous chains that connect lamellar crystals, which are also oriented by drawing.

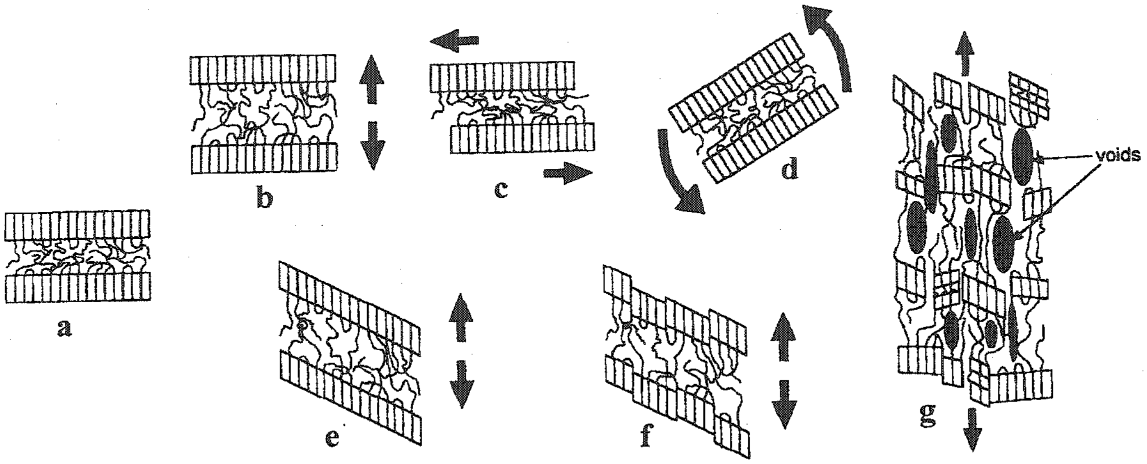

Figure 2-11 Schematic adapted from Zhang et al.(91) showing the different deformation mechanisms operative in semicrystalline polymers; (a) original lamellar structure, (b) lamellar separation, (c) interlamellar shear, (d) lamellar stack rotation, (e) fine chain slip, (f) coarse chain slip or lamellar fragmentation, and (g) lamellar fragmentation coupled with cavitation

The second stage in deformation of semicrystalline polymers is the plastic deformation that starts at yield (92) and has been identified as due to the operation of various mechanisms involving the crystalline lamellae. Commonly identified mechanisms are: chain slip, transverse slip, deformation twinning, and stress-induced phase change (81). Chain slip causes the molecules to slide past each other parallel to the chain direction, while the transverse slip implies that the slip direction is perpendicular to the chain direction. The latter has never been identified as a common operative mechanism for iPP. Two types of chain slip have been identified: fine (e) and coarse (f) chain slip, as illustrated in Figure 2-11. Coarse slip is the mechanism involving the fragmentation of the lamellar structure into small crystalline blocks (crystallites), while the fine slip results from the shearing of lamellar stacks coupled with the rotation of the chains toward the drawing direction (82).

A crystallographic chain slip system is characterized by two vectors, (*hkl*) and [*hkl*], that identify the slip system. The vectors (*hkl*) and [*hkl*] represent the "slip plane" unit normal vector and the "slip direction" in the plane, respectively. When a critical resolved shear stress (CRSS), characteristic of the specific slip system, is reached, the two parts of the crystal separated by the plane undergo a relative translation.

2.4.2.3 - Cavitation during yielding

When the motion of the chains is constrained by entanglements in the amorphous phase and their mobility is reduced in the crystalline lamellae, it has been reported that the lamellar fragmentation may be accompanied by cavitation (also called voiding) (91, 93), as illustrated in Figure 2-11(g). Stress whitening associated with craze-like structure is a direct observation of the occurrence of cavitation (94, 95). Lin and Argon (82) proposed that the voids are formed to overcome the constraints on the chains. In Peterlin's model, large strain local drawing is made possible through the cavitation process. However, this yielding mechanism is thought to be a peculiarity of uniaxial tensile experiments only (82). For example, inhomogeneous deformation without cavitation was observed for polypropylene in shear (85).

2.4.2.4 - Structural Models for the Oriented Fibrous Structure

Several models for the structure of drawn polymers have been proposed (84, 86, 96). Only two models will be considered: the microfiber plus tie molecule model, as proposed by Peterlin (97), and the 'Pisa' structure model recently defined by Bassett et al. (86). Peterlin's model shows that the microfibrils, consisting of alternating crystal blocks (or crystallites) and amorphous regions connected by taut tie molecules, are bundled into fibrils (97). Bassett et al.'s (98) recent microscopic results suggested a model with alternating zones and interspaced regions that are highly fibrillated zones of reduced density (86). The latter model, referred to as Pisa structure, was proposed to explain the

[Refs. on p. 38]

etching resistance of certain morphological regions for the special case of highly uniaxially drawn PE fibers. However, recent experimental observations of biaxially stretched polypropylene films, using atomic force microscopy, revealed that the oriented structure consists of a network of microfibers (99).

2.4.2.5 - Ultradrawability

Ultradrawability refers to the last stage of cold drawing, the plastic deformation of the fibrillar structure at draw ratio greater than 20. Recently, the α-relaxation transition, usually detected by dynamical-mechanical relaxation measurements, has been identified to play a crucial role in polymer ultradrawability (83). Based on NMR evidence, Hu and Schmidt-Rohr (83) proposed that the presence of the crystalline α-relaxation, that provides chain mobility in and through crystallites, explained the ultradrawability characteristics of polymers, such as iPP and PE. The α-relaxation of iPP is associated with helical jumps of the chain helix about itself and was found to occur at approximately 80°C (100). Hu and Schmidt-Rohr (83) identified two requirements for ultradrawability: the α-relaxation chain mobility and a low degree of entanglements.

2.4.2.6 - Peculiarities of the Deformation Mechanisms of iPP

The main deformation mechanisms of isotactic polypropylene have been studied under uniaxial compression (101, 102) and tension (85), simple shear (85, 103), and sequential tentering (104). The principal crystallographic chain slip systems of the crystalline phase are the (010) [001], (100) [001], and (110) [001] as well as the {110} twinning. According to the theoretical predictions (105) and experimental results (101, 104), the (010) [001] slip system is the easiest of the active slip systems for the α-form of iPP and dominates the other mechanisms in biaxially oriented samples (101, 104). A stress-induced phase change may occur when a melt-crystallized iPP sample is deformed between 25°C and 60°C (44, 102). In this case, some of the ordered monoclinic phase will be transformed into the less ordered, smectic phase (42, 44, 102).

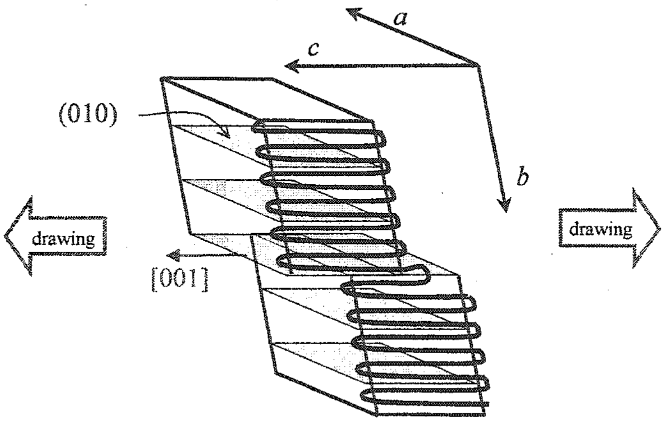

Figure 2-12 Schematic of the (010) [001] crystallographic slip system

Another important aspect of the iPP deformation mechanisms is attributed to the unique lamellar structure of the α-phase, the lamellar branching with radial and tangential lamellae, as discussed in section 2.1.4. The presence of the tangential lamellae creates an interlocked structure that stiffens the spherulite and makes chain slip very difficult (85, 103). Because of this interlocked structure, the α spherulites are less ductile than the β ones (85, 103).

Another peculiarity of the deformation of iPP is the strain-induced phase modification of the β-form iPP into the α-form (18-20, 106). The PP specimens of 100% β-form are known to become opaque when they are stretched below 120-130°C, while the α-form specimens are only partially opaque at lower drawing temperatures. This phenomenon was proved to be induced by microvoid formation, which is caused by a volume contraction during the β-α or β-smectic transformation (21).

2.4.3 - Drawing in the Partly Molten State

Ziegler-Natta-type isotactic polypropylene resins are heated and deformed at temperatures above 130°C and more generally around 150°C, i.e., 10°C to 30°C below their melting points. An optimum temperature has to be reached in order to obtain adequate molecular mobility. It is essential that both the interlamellar shear process (which enables the deformation of the amorphous regions of the initial morphology) and the *c*-axis shear process (which permits slip of the chains through the crystalline regions) are both thermally activated. The draw temperature must therefore be high, close to the melting point, which will induce some partial melting of the crystalline phase. Drawing in the partly molten state will be defined as drawing occurring at temperatures (below T_m), at which other physical processes than drawing, such as self-annealing, partial melting, and thermal-induced phase change, must be taken into account to explain the deformation behavior and the resulting stretched morphology.

Some partial melting and refolding (or self-annealing) were reported to take place during necking from neutron scattering studies on deformation of PE at high drawing temperatures (107). Increase in crystallite size, crystal perfection, and crystallinity are the characteristic features of self-annealing effects (108). As discussed in 2.1.3, thermally-induced phase changes will also take place upon heating and annealing. The smectic and β-phases will be converted into the α-form above 70°C and 150°C, respectively.

Tanaka (109) concluded from nuclear magnetic resonance investigations of relaxation times for iPP that the most notable change introduced at high temperature stretching is the increase in the molecular mobility in the amorphous phase. The effect of the increase in mobility of the amorphous chain with temperature was confirmed experimentally for the drawing of iPP fibers. When stretched at temperatures above about 120°C, fibers with lower stiffness were obtained due to increased relaxation of the molecules in the amorphous phase (110).

2.4.4 - Effect of Initial Morphology on Deformation and Morphology

2.4.4.1 - Effect of Initial Morphology on Deformation

The degree of crystallinity, spherulite size, and crystal phase content are all structural characteristics that were reported to affect the deformation behavior of semicrystalline polymers (44, 111-114). In most of the cases, studies dealt with only uniaxial deformation of PE at room temperature. It was found from these studies that an increase in molecular weight or crystallinity raises the yield stresses. Moreover, it was reported that a slowly crystallized specimen, consequently with high crystallinity, but also low tie molecule and entanglement density, will favor ultradrawability (114). Ward et al. concluded that the three key variables of the initial morphology that control

[Refs. on p. 38]

deformation are (i) the amount of amorphous phase, (ii) the tie molecule fraction, and (iii) the perfection of crystals (59).

The different crystal forms of iPP are also known to play an important role in affecting deformation behavior. The presence of smectic phase was reported to result in a more diffuse and reduced yield (44, 115). Similarly, the β-crystal form is known to have a lower yield stress than the α-crystal form (18). The phase content will affect mainly the necking behavior because, if drawing takes place over 60°C, the above two crystal forms will be transformed into the more stable α-form upon drawing.

There are fewer studies on the effect of the initial morphology on biaxial deformation behavior (116). Tanaka et al. (116) studied the effect of crystallinity on orientation of one-step biaxially stretched PP films and found that below an area stretching ratio of 10, the higher is the crystallization temperature for the initial morphology the lower would be the in-plane birefringence.

2.4.4.2 - Effect of Initial Morphology on Oriented Morphology

Peterlin's work suggested that the initial spherulitic morphology was transformed into a fibrillar structure, whose long period was invariant and depended only upon the drawing temperature (80). Supporting morphological studies were invariably of longitudinal view, i.e., with the draw direction in the plane that was characterized (117). However, more recent studies (86, 118) showed that this real space model was only partly correct and was not considering the transversal view of the morphology. Indeed, the transverse cross-sections of a highly drawn PE at 75°C showed that the morphology in a plane perpendicular to the drawing direction retained a memory of the initial morphology. Amornsakchai et al. (86, 118) suggested that the lateral morphology transforms in a continuous manner, in contrast to the axial morphology, which is transformed out of all recognition by uniaxial drawing.

[Refs. on p. 38]

References

1 - G. Natta, P. Pino, P. Corradini and e. al., "Crystalline high polymers of α–olefins", *J. Am. Chem. Soc.,* 77, 1708-10 (1955).

2 - E. P. J. Moore, ed. *Polypropylene Handbook.* , Hanser Publishers, New York, (1996).

3 - K. Hungenberg, J. Kerth, F. Langhauser, B. Marczinger and R. Schlund, in *Ziegler Catalysts*, G. Fink, R. Mulhaupt and H. H. Brintzinger, Editors. Springer Verlag: Heidelberg. p. 363 (1995).

4 - A. Hanyu and R. Wheat, "Properties and film applications of metallocene-based isotactic polypropylenes", *J. Plast. Film Sheeting,* **15**, 109-119 (1999).

5 - G. Natta and P. Corradini, "Structure and properties of isotactic polypropylene", *Nuovo Cimento Suppl.,* **15**, 40-51 (1960).

6 - R. L. Miller, "On the existence of near-range order in isotactic polypropylenes", *Polymer,* **1**, 135-143 (1960).

7 - A. Turner-Jones, J. M. Aizlewood and D. R. Beckett, "Crystalline forms of isotactic polypropylene", *Makromol. Chem.,* **75**, 134-158 (1964).

8 - S. V. Meille, S. Brückner and W. Porzio, "γ-isotactic polypropylene. A structure with nonparallel chain axes", *Macromolecules,* **23**, 4114-4121 (1990).

9 - V. Petraccone, G. Guerra, C. D. Rosa and A. Tuzi, "Extrapolation to the equilibirum melting temperature for isotactic polypropylene", *Macromolecules,* **18**, 813-14 (1985).

10 - G. Guerra, V. Petraccone, P. Corradini, C. d. Rosa, R. Napolitano and B. Pirozzi, "Crystalline order and melting behavior of isotactic polypropylene (alpha form)", *J. Polym. Sci., Polym. Phys. Ed.,* **22**, 1029-1039 (1984).

11 - B. Schröder, W. Geschwill and J. Breitenbach, eds. *Polymers: New Strategies in polymer science.* , BASF AG, Ludwigshafen, (1995).

12 - M. Fujiyama, Y. Kawamura, T. Wakino and T. Okamoto, "Study on rough surface biaxially oriented polypropylene film. I. Formation of beta.form crystals in sheet cast with T-die extruder", *J. Appl. Polym. Sci.,* **36**, 985-993 (1988).

13 - F. Chu and Y. Kimura, "Structure and gas permeability of microporous films prepared by biaxial drawing of beta from polypropylene", Polymer, **37**, 573-579 (1996).

14 - J. Varga, "*Crystallization, melting and supermolecular structure of isotactic polypropylene*", in *Polypropylene Structures, Blends, and Composites*, J. Karger-Kocsis, Editor. Chapman & Hall: London. p. 56-115 (1995).

15 - J. Varga, "Review

Supermolecular structure of isotactic polypropylene", J. Mat. Sci., **27**, 2557-2579 (1992).

16 - T. Labour, G. Vigier, R. Seguela, C. Gauthier, G. Orange and Y. Bomal, "Influence of the beta-crystalline phase on the mechanical properties of unfilled and CaCO3-filler polypropylene. I. Structural and mechanical characterization", Polymer, **42**, 7127-7135 (2001).

17 - J. X. Li, W. L. Cheung and D. Jia, "A study on the heat of fusion of ß-polypropylene", Polymer, **40**, 1219-1222 (1999).

18 - J. X. Li and W. L. Cheung, "On the deformation mechanisms of ß-polypropylene: 1. Effect of necking on ß-phase PP crystals", Polymer, **39**, 6935-6940 (1998).

19 - J. X. Li, W. L. Cheung and C. M. Chan, "On deformation mechanisms of ß-polypropylene 2. Changes of lamellar structure caused by tensile load", Polymer, **40**, 2089-2102 (1999).

20 - J. X. Li, W. L. Cheung and C. M. Chan, "On deformation mechanisms of ß-polypropylene 3. Lamella structures after necking and cold drawing", Polymer, **40**, 3641-3656 (1999).

21 - F. Chu, T. Yamaoka, H. Ide and Y. Kimura, "Microvoid formation process during the plastic deformation of beta form polypropylene", Polymer, **35**, 3442-3448 (1994).

22 - D. R. Morrow and B. A. Newman, "Crystallization of low-molecular weight polypropylene fractions", J. Appl. Phys., **39**, 4944-50 (1968).

23 - A. Turner-Jones, "Development of the gamma-crystal form in random copolymers of propylene and thei analysis by DSC and x-ray methods", Polymer, **12**, 487-508 (1971).

[Refs. on p. 38]

24 - R. Thomann, C. Wang, J. Kressler and R. Mulhaupt, "On the γ-phase of isotactic polypropylene", *Macromolecules,* **29**, 8425 (1996).

25 - E. C. Bond, J. E. Spruiell and J. S. Lin, "A WAXD/SAXS/DSC study on the melting behavior of Ziegler-Natta and metallocene catalyzed isotactic polypropylene", *J. Polym. Sci.: Polym. Phys. Ed.,* **37**, 3050-3064 (1999).

26 - R. Zannetti, G. Celoti, A. Fichera and R. Francesconi, "The structural effects of annealing time and temperature on the paracrystal-crystal transition in isotactic polypropylene", *Makrom. Chem.,* **128**, 137-142 (1969).

27 - H. W. Wyckoff, "X-ray and related studies of quenched, drawn, and annealed polypropylene", *J. Polym. Sci.,* **62**, 83-114 (1962).

28 - C. C. Hsu, P. H. Geil, H. Miyaji and K. Asai, "Structure and properties of polypropylene crystallized from the glassy state", *J. Polym. Sci.: Part B: Polym. Phys.,* **24**, 2379-2401 (1986).

29 - D. M. Gezovich and P. H. Geil, "Morphology of quenched polypropylene", *Polym. Eng. Sci.,* **8**, 202-209 (1968).

30 - P. Corradini, V. Petraccone, C. D. Rosa and G. Guerra, "On the structure of the quenched mesomorphic phase of isotactic polyprpylene", *Macromolecules,* **19**, 2699-2703 (1986).

31 - V. Caldas, R. S. Nohr, J. G. MacDonald, L. E. Raboin and G. R. Brown, "The structure of the mesomorphic phase of quenched isotactic polypropylene", *Polymer,* **35**, p899-907 (1994).

32 - W. J. O'Kane, R. J. Young, A. J. Ryan, W. Bras, G. E. Derbyshire and G. R. Mant, "Simultaneous SAX/WAX and dsc analysis of the melting and recrytsallization of quenched polypropylene", *Polymer,* **35**, 1352-1358 (1994).

33 - J. A. Gailey and R. H. Ralston, "The quenched state of polypropylene", *SPE Trans.,* **4**, 2933 (1964).

34 - A. Martorana, S. Piccarolo and F. Sciclilone, "The X-ray determination of the amounts of the phase in samples if isotactic poly(propylene) quenched from the melt at different cooling rates", *Macromol. Chem. Phys.,* **198**, 597-604 (1997).

35 - V. Vittoria, "Crystallinity of isotactic polypropylene films annealed from the quenched state", *J. Mat. Sci.,* **27**, 4350-4354 (1992).

[Refs. on p. 38]

36 - V. Vittoria, "Effect of annealing on the structure of quenched isotactic polypropylene", *J. Macromol. Sci.-Phys.,* **B28**, 489-502 (1989).

37 - N. Alberola, M. Fuguier, D. Petit and B. Fillon, "Microstructure of quenched and annealed films of isotactic polypropylene", *J. Mat. Sci.,* **30**, 1187-1195 (1995).

38 - V. Vittoria and A. Perullo, "Effect of quenching temperature on the structure of isotactic polypropylene films", *J. Macromol. Sci.-Phys.,* **B25**, 267-281 (1986).

39 - W. J. O'Kane, R. J. Young and A. J. Ryan, "The effect of annealing on the structure and properties of isotactic polypropylene films", *J. Macromol. Sci.-Phys.,* **B34**, 427-458 (1995).

40 - D. T. Grubb and D. Y. Yoon, "Morphology of quenched and annealed isotactic polypropylene", *Polym. Comm.,* **27**, 84-88 (1986).

41 - S. Osawa and R. S. Porter, "Uniplanar deformation of isotactic polypropylene: 1. Draw characteristics", *Polymer,* **35**, 540 - 544 (1994).

42 - S. Osawa and R. S. Porter, "Uniplanar deformation of isotactic polypropylene: 2. Phase structure", *Polymer,* **35**, 544- 550 (1994).

43 - S. Osawa and R. S. Porter, "Uniplanar oriented isotactic polypropylene: 3. Properties and morphology", *Polymer,* **35**, 551 - 557 (1994).

44 - R. Seguela, E. Staniek, B. Escaig and B. Fillon, "Plastic deformation of polypropylene in relation to crystalline structure", *J. Appl. Polym. Sci.,* **71**, 1873-1885 (1999).

45 - F. J. Padden and H. D. Keith, "Spherulitic crystallization in polypropylene", *J. Appl. Phys.,* **30**, 1479-84 (1959).

46 - D. R. Norton and A. Keller, "The spherulitic and lamellar morphology of melt-crystallized isotactic polypropylene", *Polymer,* **26**, 704-716 (1985).

47 - H. Awaya, "Morphology of different types of isotactic polypropylene spherulites crystallized from melt", *Polymer,* **29**, 591-596 (1988).

48 - D. C. Bassett and R. H. Olley, "On the lamellar morphology of isotactic polypropylene spherulites", *Polymer,* **25**, 935-943 (1984).

49 - B. Lotz and J. C. Wittmann, "The molecular origin of lamellar branching in the alpha (monoclinic) form of isotactic polypropylene", *J. Polym. Sci.,* **24**, 1541-1558 (1986).

[Refs. on p. 38]

50 - K. Yamada, S. Matsumoto, K. Tagashira and M. Hikosaka, "Isotacticity dependence of spherulitic morphology of isotactic polypropylene", *Polymer,* **39**, 5327-5333 (1998).

51 - R. G. Alamo, G. M. Brown, L. Mandelkern, A. Lehtinen and R. Apukkeri, "A morphological study of highly structural regular isotactic polypropylene fraction", *Polymer,* **40**, 3933-3944 (1999).

52 - J. Klein and B. J. Briscoe, "The behavior of long molecules diffusing in solid polyethylene", *Nature,* **266**, 43-44 (1977).

53 - C. J. G. Plummer and H.-H. Kausch, "Deformation and entanglement in semicrystalline polymers", *J. Macromol. Sci. - Phys.,* **B35**, 637-657 (1996).

54 - B. Wunderlich, *Crystal melting*, Academic Press, New York, (1980).

55 - H. Bu, S. Cheng and B. Wunderlich, "Addendum to the thermal properties of polypropylene", *Makromol. Chem. Rapid Comm.,* **9**, 76-78 (1988).

56 - S. Z. D. Cheng, J. J. Janimak, A.-Q. Zhang and E. T. Hsieh, "Isotacticity effect on crystallization and melting in polypropylene fractions: 1. Crystalline structures and thermodynamic property changes", *Polymer,* **32**, 648-655 (1991).

57 - M. Gahleitner, C. Bachner, E. Ratajski, G. Rohaczek and W. Neissl, "Effects of the catalyst system on the crystallization of polypropylene", *J. Appl. Polym. Sci.,* **73**, 2507-2515 (1999).

58 - K. D. Pae and J. A. Sauer, "Effects of thermal history on isotactic polypropylene", *J. Appl. Polym. Sci.,* **12**, 1901-1919 (1968).

59 - I. M. Ward, P. D. Coates and M. M. Dumoulin, *Solid Phase Processing of Polymers*, Hanser, Munich, (2000).

60 - K. Tsunashima, K. Toyoda and T. Yoshii, "*Stretching conditions, orientation, and physical properties of biaxially oriented film*", in *Film Processing*, T. Kanai and G. A. Campbell, Editors. Hanser: Munich. p. 320-352 (1999).

61 - J. Sänze and K. Stopperka, "The biaxial orientation of expanded films", *Kunststoffe,* **91**, (2001).

62 - P. Duffo, B. Monasse and J. M. Haudin, "Influence of Stretching and Cooling Conditions in Cast Film Extrusion of PP Films", *Intern. Polymer Processing,* **5**, 272 - 283 (1990).

[Refs. on p. 38]

63 - E. Martuscelli, M. Canetti and A. Seves, "Phase structure and thermal behaviour of polypropylene / hydrogenated polycyclopentadiene blends", Polymer, **30**, 304-310 (1989).

64 - K. C. Cole and A. Ajji, "*Characterization of orientation*", in *Solid phase processing of polymers*, I. M. Ward, P. D. Coates and M. M. Dumoulin, Editors. Hanser: Munich. p. 33-84 (2000).

65 - J. L. White and M. Cakmak, "*Orientation*", in *Encyclopedia of Polymer Science and Engineering . 2nd Edition*, Mark-Bikales-Overberger-Menges, Editor. Wiley: New York. p. 595-618 (1987).

66 - Z. W. Wilchinsky, "Orientation in cold-rolled polypropylene", J. Appl. Polym. Sci., **7**, 923-933 (1963).

67 - J. L. White and J. E. Spruiell, "Specification of biaxially orientation in amorphous and crystalline polymers", Polym. Sci. Eng., **21**, 859 (1981).

68 - C. J. Heffelfinger and R. L. Burton, "X ray determination of the crystalline orientation distributions of poly(ethylene terephthalate) films", J. Polym. Sci., **47**, 289-306 (1960).

69 - A. Ajji and K. C. Cole, "Characterization of biaxial orientation in polyolefin films", Annu. Tech. Conf. - Soc. Plast. Eng., **58th(vol.2)**, 1610-1614 (2000).

70 - L. E. Alexander, *X-Ray Diffraction Methods in Polymer Science*, Wiley, New York, (1969).

71 - B. Jasse and J. L. Koenig, "Orientational measurements in polymers using vibrational spectroscopy", J. Macromol. Sci. Rev. Macromol. Chem., **C17**, pp 6-135 (1979).

72 - G. L. Wilkes and R. S. Stein, "*Physidochemical approaches to the measurement of molecular anisotropy*", in *Structure and Properties of Oriented Polymers*, I. M. Ward, Editor. Chapman&Hall: London. p. 44-141 (1997).

73 - R. Zbinden, *Infrared Spectroscopy of High Polymers*, Academic Press, New York, (1964).

74 - D. A. Jarvis, I. J. Hutchinson, D. I. Bower and I. M. Ward, "Characterization of biaxial orientation in poly(ethylene terephthalate) by means of refractive index

measurements and Raman and infra-red spectroscopies", Polymer, **21**, pp41-54 (1980).

75 - D. R. Salem, "*Draw-induced structure development in flexible-chain polymers*", in *Structure Formation in Polymeric Fibers*, D. R. Salem, Editor. Hanser: Munich. p. 118-184 (2001).

76 - I. L. Hay and A. Keller, "Polymer deformation in terms of spherulites", *Kolloid-Z. Z. Polym.*, **204**, 43-74 (1965).

77 - J. M. Andrews and I. M. Ward, "The cold-drawing of high density polyethylene", *J. Mat. Sci.*, **5**, 411-417 (1970).

78 - R. H. Olley and D. C. Bassett, "On surface morphology and drawing of polypropylene films", *J. Macromol. Sci. - Phys.*, **B33**, 209-227 (1994).

79 - J. Sweeney and I. M. Ward, "The modeling of multiaxial necking in polypropylene using a sliplink therory", *J. Rheol.*, **39**, 861-872 (1995).

80 - A. Peterlin, "Molecular Model of drawing polyethylene and polypropylene", *J. Mater. Sci.*, **6**, 490-508 (1971).

81 - P. D. Bowden and R. J. Young, "Review Deformation mechanisms in crystalline materials", *J. Mat. Sci.*, **9**, 2034-2051 (1974).

82 - L. Lin and A. S. Argon, "Review: Structure and plastic deformation of polyethylene", *J. Mat. Sci.*, **29**, 294-323 (1994).

83 - W.-G. Hu and K. Schmidt-Rohr, "Polymer ultradrawability: the crucial role of alpha-relaxation chain mobility in the crystallites", *Acta Polymer*, **50**, 271-285 (1999).

84 - R. S. Porter and L. H. Wang, "Uniaxial extension and other development in flexible chain polymers", *J. Macromol. Sci.- Rev. Macromol. Chem. Phys.*, **C35**, 63-115 (1995).

85 - M. Aboulfaraj, C. G. Sell, B. Ulrich and A. Dahoun, "In situ observation of the plastic deformation of polypropylene spherulites under uniaxial tension and simple shear in the scanning electron microscope", *Polymer*, **36**, 731-742 (1995).

86 - T. Amornsakchai, R. H. Olley, D. C. Bassett, M. O. M. Al-Hussein, A. P. Unwin and I. M. Ward, "On the influence of initial morphology on the internal structure of highly drawn polyethylene", *Polymer*, **41**, 8291-8298 (2000).

[Refs. on p. 38]

87 - H. Tanaka, T. Masuko, K. Homma and S. Okajima, "Studies on biaxial stretching of polypropylene film. III. Electron microscopic observation of the one-step biaxial stretching of isotactic polypropylene spherulites", *J. Appl. Polym. Sci.,* **7**, 1997-2006 (1969).

88 - P. J. Flory and D. Y. Yoon, "Molecular morphology in semicrystalline polymers", *Nature,* **272**, 226-229 (1978).

89 - W. W. Adams, D. Yang and E. L. Thomas, "Direct visualization of microstructural deformation processes in polyethylene", *J. Mat. Sci.,* **21**, 2239-2253 (1986).

90 - D. C. Bassett, "*Deformation Mechanisms and Morphology of Crystalline Polymers*", in *Solid Phase Processing of Polymers*, I. M. Ward, P. D. Coates and M. M. Dumoulin, Editors. Hanser: Munich. p. 11-32 (2001).

91 - X. C. Zhang, M. F. Butler and R. E. Cameron, "The ductile-brittle transition of irradiated isotactic polypropylene studied unsing simultaneous SAXS and tensile deformation", *Polymer,* **41**, 3797-3807 (2000).

92 - I. M. Ward and D. W. Hadley, *An Introduction to the Mechanical Properties of Solid Polymers*, John Wiley & Sons, New York, (1993).

93 - M. F. Butler, A. M. Donald and A. J. Ryan, "Time resolved simultaneous small- and wide-angle X-ray scattering during polyethylene deformation - II. Cold drawing of linear polyethylene", *Polymer,* **39**, 39-52 (1998).

94 - K. Friedrich, "Crazes and shear bands in semi-crystalline thermoplastics", *Adv. Polym. Sci.,* **52/53**, 225-274 (1983).

95 - Y. Liu and R. W. Truss, "A study of tensile yielding of isotactic polypropylene", *J. Polym. Sci.: Part B: Polym. Phys.,* **32**, 2037-2047 (1994).

96 - M. I. Abo-El-Maaty, D. C. Bassett and R. H. Olley, "On the internal morphologies of high-modulus polyethylene and polypropylene fibres", *J. Mat. Sci.,* **34**, 1975-1989 (1999).

97 - A. Peterlin, "THe composite structure of fibrous material", *Adv. Chem. Serie,* **142**, 1-13 (1975).

98 - A. G. Gibson, G. R. Davis and I. M. Ward, "Dynamic mechanical behavior and longitudinal crystal thickness measurements on ultra-high modulus linear

polyethylene. A quantitative model for the elastic modulus", *Polymer,* **19**, 683-93 (1978).

99 - H.-Y. Nie, M. J. Walzak and N. S. McIntyre, "Draw-ratio morphology of biaxially oriented poylpropylene films as determined by atomic force microscopy", *Polymer,* **41**, pp2213-2218 (2000).

100 - D. Schaefer, H. W. Spiess, U. V. Suter and W. W. Fleming, "Two-dimensional solid-state NMR studies of ultraslow chain motion: glass transition in atactic polypropylene versus helical jumps in isotactic polypropylene", *Macromolecules,* **23**, 3431-9 (1990).

101 - R. F. Saraf, "Planar and fibre textures induced in isotactic polypropylene on equibiaxial hydrostatic deformation", *Polymer,* **35**, 1359-1368 (1994).

102 - R. F. Saraf and R. S. Porter, "A deformation induced order-disorder transition in isotactic polypropylene", *Polym. Eng. Sci.,* **28**, 842-850 (1988).

103 - G. Coulon, G. Castelein and C. G. Sell, "Scanning force microscopic investigation of plasticity and damage mechanisms in polypropylene spherulites under simple shear", *Po,ymer,* **40**, 95 - 110 (1998).

104 - Z. Bartczack and E. Martuscelli, "Orientation and properties of sequentially drawn films of an isotactic polypropylene/hydrogenated oligocyclopentadiene blend", *Polymer,* **38**, 4139-4149 (1997).

105 - H. P. Klug and L. E. Alexander, *X-Ray Diffraction Procedures*, Wiley, New York, (1954).

106 - F. Chu, T. Yamaoka and Y. Kimura, "Crystal transformation and micropore formation during uniaxial drawing of beta form polypropylene film", *Polymer,* **36**, 2523-2530 (1995).

107 - D. M. Sadler and P. J. Barham, "Structure of drawn fibres: 1. Neutron scattering studies of necking in melt-crystallized polyethylene", *Polymer,* **31**, 36-50 (1990).

108 - B. Wunderlich, *Crystal nucleation, growth, annealing*, Academic Press, New York, (1976).

109 - H. Tanaka, "Proton spin-lattice and spin-spin relaxation time in isotactic polypropylene. II. Effetcs of stretching ratio and temperature", *J. Appl. Polym. Sci.,* **58**, 1707-1715 (1983).

110 - R. G. C. Arridge and P. J. Barham, "A theory for the drawing of oriented crystalline polymers", *J. Polym. Sci. Polym. Phys. Ed.,* **16**, 1297-319 (1978).

111 - V. Vittoria, "*Properties of Isotactic Polypropylene*", in *Encyclopedia of Materials Sciance and Engineering*, M. B. Bever, Editor. Pregamon Press: Oxford. p. 507-555 (1986).

112 - O. Darras and R. Seguela, "Tensile yield of polyethylene in relation to crystal thickness", *J. Polym. Sci. Polym. Phys. Ed.,* **31**, 759-766 (1993).

113 - N. Brown and I. M. Ward, "The influence of morphology and molecular weight on ductile-brittle transitions in linear polyethylene", *J. Mat. Sci.,* **18**, 1405-1420 (1983).

114 - G. Capaccio, I. M. Ward and T. A. Crompton, "The drawing behavior of linear polyethylene I. Rate of drawing as function of polymer molecular wieght and initial treatment", *J. Polym. Sci.: Polym. Phys. Ed.,* **14**, 1641-1658 (1976).

115 - V. Vittoria, F. d. Candia, V. Capodanno and A. Peterlin, "Mechanical and transport properties of highly drawn isotactic polypropylene", *J. Polym. Sci.: Polym. Phys. Ed.,* **24**, 1009 (1986).

116 - H. Tanaka and S. Okajima, "Studies on biaxial stretching of polypropylene film. XII. Effect of crystallinity on the deformation mechanism of the biaxial stretching in one step", *J. Polym. Sci. Polym. Letters,* **15**, 349-362 (1977).

117 - A. Peterlin and A. Sakaoku, *Kolloid Z.,* **212**, 51 (1966).

118 - T. Amornsakchai, R. H. Olley, D. C. Bassett, A. P. Unwin and I. M. Ward, "Remanant morphologies in highly drawn polyethylene after annealing", *Polymer,* **42**, 4117-4126 (2002).

[Refs. on p. 38]

CHAPTER 3

OBJECTIVES

The present work is part of a larger research program involving three partners: an industrial partner, Brückner Maschinenbau GmbH, and two universities, University of Erlangen-Nuremberg and McGill University. The objectives of this program have been to obtain correlations between molecular structure and elongational properties and the determination of material functions for the stretching of isotactic polypropylene. Ultimately, it is desirable to develop a computational model for the sizing of production lines, and the optimization of the simultaneous biaxial film stretching process.

The general objective of this thesis has been to elucidate morphological issues associated with the simultaneous biaxial stretching process, including the evaluation of film morphology before, during, and after stretching.

The specific objectives of the present work are outlined below:

(1) To evaluate the effects of chain tacticity and the casting conditions on the initial morphology, and the effects of the thermal treatment (preheating) on the morphology in order to characterize the morphology of the partly molten state prior to stretching

(2) To evaluate the homogeneity of the simultaneous equibiaxial deformation and to study the effects of stretching conditions, (i.e., stretching ratio, drawing temperature, strain rate, strain profile, and deformation type), initial morphology, and chain tacticity on the deformation behavior and the resulting film dimensions.

(3) To study the effects of stretching conditions, initial morphology, and chain tacticity on the morphology and orientation of the simultaneously biaxially stretched film.

(4) To obtain, wherever possible, structure / property relationships among the end film properties, the stretched film morphology, and the molecular structure of the resin.

CHAPTER 4

EXPERIMENTAL

This chapter is divided into three main parts. Firstly, it describes the molecular characteristics of the four commercial PP grades and the experimental conditions used to prepare the initial films. The second part presents the different experimental techniques employed to characterize the morphology and orientation. Special attention is given to the wide X-ray diffraction technique. The third part of Chapter 4 gives a detailed description of the laboratory film stretcher and its measurement capabilities.

4.1 - Materials and Cast Film Preparation

4.1.1 - Materials

Four commercial grades of isotactic polypropylene obtained by Ziegler-Natta-catalysis were investigated. They were linear homopolymers with different molecular structure, especially having significant differences in isotacticity. The molecular and physical characteristics are given below.

Figure 4-1 illustrates the differences in molecular weight distribution for the first three linear homopolymer resins, as obtained by gel permeation chromatography (GPC). This analysis was carried out on a Waters GPC-150 apparatus, equipped with a light scattering detector and 4 GPC columns (1 Shodex UT807 and 3 Shodex HT806). The GPC experiments were performed at 135°C with 1,2,4,-trichlorobenzene as an eluent. Key molecular parameters for the four polymers are listed in Table 4-1. The first three commercial homopolymers PP1, PP2, and PP3 were chosen because they were all prepared by Ziegler-Natta catalysis and had a similar weight average molecular weight, M_w, but different isotacticity, as measured by xylene solubility (XS) and Fourier transform infrared (FTIR) analysis. The use of the same catalyst system was intended to produce similar distributions of defects along the chains of these resins (1). Therefore, the differences in isotacticity between the resins may be seen as a difference in the quantity of stereo defects (a racemic sequence) (2). PP4 is a grade that was manufactured by peroxide-controlled degradation, also called "controlled rheology". This degradation process aims at narrowing the molecular weight distribution and tailoring the rheology but, at the same time, it affects the crystallization behavior. Indeed, Gahleitner et al.(3) reported that, at comparable molecular weight and isotacticity, reactor-grade PP resins crystallize faster than degraded-grade PP types, which explains the crystallization temperature difference, as shown in Table 4-2. Therefore, PP4 was selected because it is a linear homopolymer with similar molecular structure (M_w and isotacticity) to PP2, but with a different crystallization behavior.

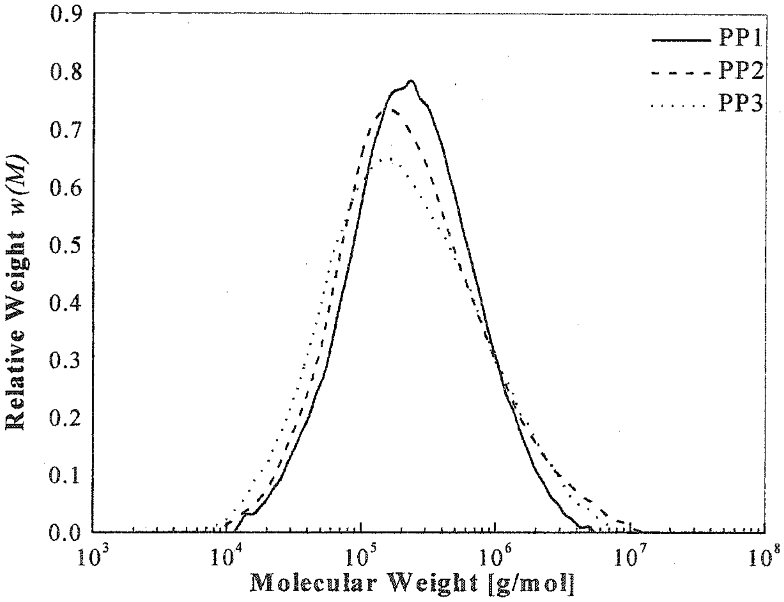

Figure 4-1 Molecular weight distributions of the main three linear homopolymers obtained by gel permeation chromatography (GPC)

The thermal characteristics of the resins, as measured by DSC, are listed in Table 4-2. It can be seen that both the melting point and crystallinity increase with the isotacticity index. The chain irregularities, the stereo defects, are believed to be excluded from the lamellar crystallite (4). Consequently, the maximum crystallite thickness, that can be reached for a particular isotactic polypropylene, depends on the number and the distribution of chain irregularities. The results obtained from the DSC measurements listed in Table 4-2 are in agreement with this concept and the literature (5, 6).

Table 4-1 *Molecular properties of the polypropylene resins; Isotacticity as measured by xylene solubility (XS) and by infrared (IR) measurements*

Polypropylene	Isotacticity		Mn	Mw	Poly-
	XS ± 0.2	IR ± 0.5%	[kg/mol]	[kg/mol]	dispersity
PP1	94.9	0.94	71	463	6.5
PP2	98.6	0.98	119	415	3.5
PP3	99.5	1.03	82	449	5.5
PP4	98.5	0.99	114	411	3.6

Table 4-2 *Morphological characteristics of the raw materials*

Polypropylene	Isotacticity [%]	Melting Temp. [°C]	Cryst. Temp. [°C]	CI_{DSC} [%]
	± 0.2	± 0.2 °C	± 0.2 °C	± 1
PP1	94.9	160.1	112.1	48.5
PP2	98.6	163.8	117.3	49.6
PP3	99.5	168.1	119.8	50.4
PP4	98.6	163.7	112.6	46.3

4.1.2 - Preparation of the Initial Film Morphology

4.1.2.1 - Preparation of the Cast Films

All PP grades were extruded using a single screw extruder equipped with a melt pump. The same screw configurations were used at all times. The polymer melt was extruded through a slit die, 300 mm in width, and then solidified on a chill roll (CR) that was half immersed in a water bath (WB), as schematically shown in Figure 4-2. The exact casting conditions, such as the extrusion temperature and speed, the chill roll and water temperatures, are listed in Table 4-3. The die gap was set between 1.04 and 1.16 mm. The sheet thicknesses varied from 1.05 to 1.20 mm, because of the different melt elasticities of the resins.

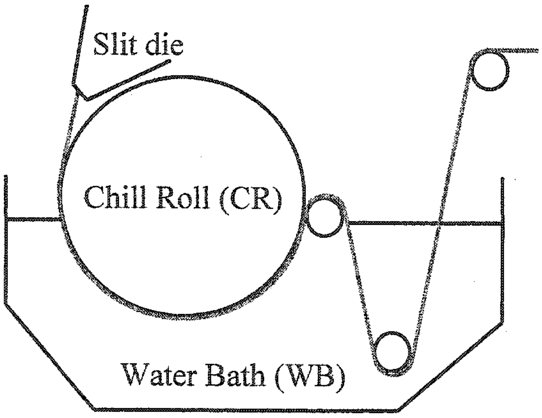

Figure 4-2 Chill roll / water bath unit of the cast film process

The cast film conditions were varied in order to study the effect of the initial morphology on film processing. This was achieved by changing the cooling conditions. The water and chill roll temperatures were set to the following temperatures: 20°C, 55°C and 80°C. A slower cooling condition was also obtained by setting the roll temperature at 85°C and taking away the water bath. A list of the various cast film names and the corresponding casting conditions are shown in Table 4-3.

In order to avoid aging and additional crystallization effects after processing, the films were stored at temperature below 0°C until they were further processed. The cast films had an average thickness of about 1 mm. Square samples of 85 mm x85 mm were cut out from the central part of the cast film to obtain the required specimen for the laboratory film stretcher.

Table 4-3 Casting conditions for the various cast films

		Extrusion Conditions		**Casting Condtions**		**Cast film**
Cast Film	**Resin**	**Die Temp. [°C]**	**Speed [m/min]**	**CR/WB unit Temp. [°C]**	**Die Gap [mm]**	**thickness [μm]**
PP1-CF0	PP1	250	8	20 / 20	1.04	1070
PP2-CF0	PP2	250	8	20 / 20	1.04	1050
PP3-CF0	PP3	250	8	20 / 20	1.04	1135
PP4-CF1	PP4	250	6	20 / 20	1.16	1190
PP4-CF2	PP4	250	6	55 / 55	1.16	1190
PP4-CF3	PP4	250	6	80 / 80	1.16	1195
PP4-CF4	PP4	250	6	85 / -	1.16	1195

4.1.2.2 - Preparation of the Preheated Cast Films

One important aspect of the tenter-frame stretching process is that the solidified initial film needs to be heated to a relatively high temperature before stretching. Since solidified polymers are known to undergo significant morphological modifications upon heating, the effect of the preheating on the initial morphology was studied. Since on-line measurements would be very difficult, it was decided to carry out a comparative study of the cast film morphology before and after preheating. The preheated specimens were prepared using the laboratory film stretcher. This was done by placing the sample in the stretching device and exposing it to the typical thermal history encountered during a stretching experiment, but without stretching. Therefore, at the end of the preheating, the stretching frame carrying the specimen moved back from the stretching oven to the loading zone, where the specimen was allowed to cool to room temperature (about 30°C) for 30 s before being unloaded. Since the preheating temperature varied from 140°C to 168°C, the cooling rates for the preheated samples differed slightly.

4.1.2.3 - Preparation of the Annealed Cast Films

One objective of this work was to study the effect of the morphology of the initial film on film processing and end film properties. The variety of morphologies that can be obtained by varying film casting conditions was rather limited. Therefore, a series of samples with significantly different initial morphologies was prepared by annealing. The annealed cast films were all prepared using the PP2-CF0 cast film. Square samples of PP2-CF0 were annealed in a hot air oven for two hours at the following temperatures: 100°C, 120°C, 143°C, 150°C, 157°C, and 160°C. The specimens were then quenched in air at room temperature (around 20°C).

4.2 - Characterization Techniques

This part describes the experimental techniques used to characterize the raw materials, the morphology and orientation of the starting sheets and the stretched films. Emphasis is placed on the main characterization method used in this work, i.e. wide-angle X-ray diffraction in reflection.

4.2.1 - Wide-Angle X-Ray Diffraction

Wide-angle X-ray diffraction (WAXD) yields information about lattice dimensions, crystal forms, crystallinity, crystallite size, and orientation, while the pole figure technique provides information about texture and orientation distribution.

4.2.1.1 - Principles of X-Ray Diffraction

The prominent crystallographic (*hkl*) planes, i.e., with the most thickly populated lattice points, will diffract X-rays according to Bragg's law:

$$n\lambda = 2d_{hkl} \sin\theta_{hkl} \qquad eq.(4\text{-}1)$$

where λ is the wavelength of the beam, d_{hkl} the interplanar spacing, θ_{hkl} Bragg's angle, n is an integer, and h,k, and l are the Miller indices specifying the diffraction planes. The different positions (2θ angles) of the diffraction peaks are a characteristic of each crystal form for polypropylene (cf. example in Figure A-1 in App. A). Figure 4-3(a) illustrates the position of the main diffraction planes in the monoclinic cell of the α crystal form of iPP. For a certain set of (*hkl*) planes, the diffraction intensity at the corresponding 2θ angle will be anisotropic if the sample has some orientation. The latter principle is exploited in both the pole figure and reflection techniques to measure orientation, as discussed below.

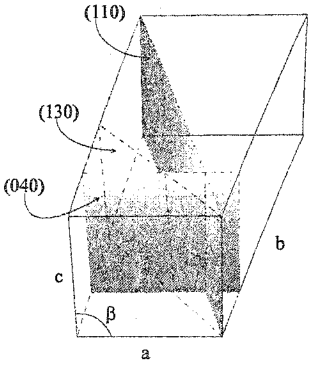

Figure 4-3 *Schematic of the monoclinic space lattice of the α crystal form of iPP showing the three main diffraction planes (110), (040) and (130)*

4.2.1.2 - Wide-Angle X-Ray Diffractometer

4.2.1.2.1 - Apparatus

A Siemens D500 Diffractometer mounted with a θ-2θ goniometer using the CuK_α wavelength was utilized to carry out the diffraction measurements. The voltage and the current of the X-ray source were set to 40kV and 30 mA. The apparatus was equipped with aperture diaphragms of 1° and of 0.05° for the detector diaphragm. A graphite beam monochromator was used to suppress the K_β reflections. Diffracted X-rays were detected by a scintillation counter. WAXD measurements in this work were performed in the symmetrical reflection mode because the (110) and (040) diffraction planes of biaxially oriented polypropylene films are preferentially oriented parallel to the film plane. This is illustrated in a figure discussed later (cf. Figure 7-4), comparing the measurement in reflection and in transmission. A conventional experiment consisted of measuring a 2θ scan from 6° to 32°, with a 0.02° step every 2 seconds.

4.2.1.2.2 - Sample Preparation

The thin film samples were cautiously glued together with a small amount of polyvinylacetate (PVA) glue, so that most of the specimens had a thickness higher than 200 μm. PVA glue was chosen because it is amorphous and thus does not influence the diffraction measurements. A more detailed description of sample preparation is given in Appendix A.

4.2.1.2.3 - X-ray Penetration Depth

X-ray beams have a certain penetration depth that depends on the set-up of the diffractometer, the incidence angle, and the material absorption coefficient. In our case, the X-ray penetration depth was only limited by the experimental set-up and was found equal to about 500μm (cf. App. A). Subsequently, in the case of the cast films, which had an approximate thickness of 1 mm, the samples were characterized on both sides. Average values and curves from measurements on both sides were then computed, when needed

4.2.1.3 - Analysis of X-Ray Diffraction Data

The diffraction data, were not corrected for incoherent scattering and for Lorentz and polarization factors, because such corrections are not important in the evaluation of relative crystallinity (7). Nevertheless, the diffracted intensities were corrected for the loss of scattered intensity for thin samples (cf. App. A).

4.2.1.3.1 - Determination of the X-Ray Crystallinity

The X-ray crystallinity index was first estimated following the method of Weidinger and Hermans (7). However, the much simpler area ratio method was found to give identical results. Therefore, the following definition of the X-ray crystallinity index (CI_{WAXD}) was used:

$$CI_{WAXD} = \frac{A_{total} - A_{am}}{A_{total}} \qquad eq.(4\text{-}2)$$

where A_{total} is the total area under the curve between 10° and 30°, and A_{am} is the area under the amorphous halo. The background curve corresponding to the amorphous halo was constructed, according to a procedure adapted from Weidinger and Hermans (cf. App. A). The same definition was used for samples containing some smectic or β-phase. Hence, the contributions of the other phases were added to the crystallinity index. For oriented samples, X-ray crystallinity index could be computed, but was not discussed. Indeed, X-ray diffraction is known to be very sensitive to orientation. The measurement reproducibility for the X-ray crystallinity index was found equal to 0.5 % in crystallinity (cf. App. A.).

4.2.1.3.2 - Determination of the Apparent Crystallite Sizes

The peak breadth, or the diffraction broadening $\Delta(2\theta)$, in a X-ray diffraction pattern is related to the weight average size of crystallites in the crystalline phase, according to the Scherrer equation (8):

$$D_{hkl} = \frac{K\lambda}{\Delta(2\theta)\cos\theta} \qquad eq.(4\text{-}3)$$

where λ is the X-ray wavelength, θ is the Bragg angle, and K is a constant equal to unity (cf. App. A). $\Delta(2\theta)$ represents the pure diffraction breadth, free of all broadening due to lattice distortion and the experimental method used. The instrumental broadening can be taken into account by using Warren's correction (9):

$$\Delta(2\theta)^2_{pure} = \Delta(2\theta)^2_{obs} - \Delta(2\theta)^2_{inst} \qquad eq.(4\text{-}4)$$

where the subscripts $_{pure}$, $_{obs}$, and $_{inst}$ refer to the pure, the observed, and the instrumental broadening, respectively. Alexander (10) found that the Scherrer equation yields satisfactory values of the relative sizes, even though the rigid assumptions employed in deriving the equation result in considerable uncertainty as to the absolute crystallite sizes. The apparent crystallite size assessed from a (*hkl*) diffraction peak represents the dimension of the lamella in the direction perpendicular to the corresponding (*hkl*) diffraction plane. For instance, the D_{040} crystallite size represents the dimension of lamellar crystals in the direction parallel to the *b* axis, as shown in Figure 4-4.

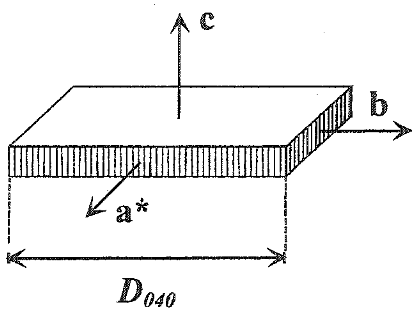

Figure 4-4 Schematic of the (040) apparent crystallite size at the lamellar scale

The observed angular width was obtained from a multi-peak fitting procedure, as shown in Figure 4-5. The remaining crystalline peaks were fitted after subtraction of the amorphous halo. The chosen analytical function was a Pearson-type function, which has been used successfully for polymers by several authors (11-13). The instrumental broadening was estimated by measuring the diffraction peak breadth of a material having crystallites of infinite size (cf. App. A).

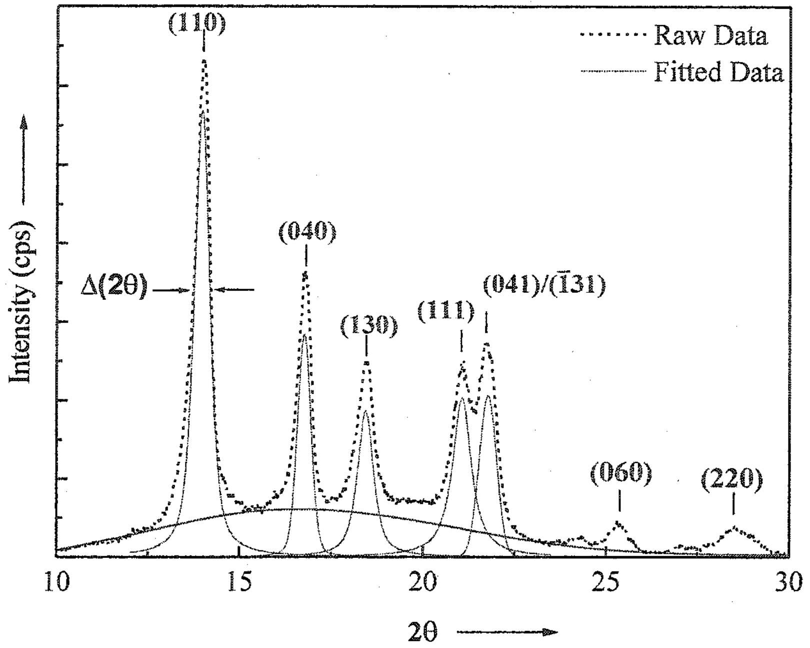

Figure 4-5 *Example of the multi-peak fitting procedure and the constructed amorphous halo for an isotropic iPP sample*

The measurement reproducibility was estimated using the same series of measurements used to evaluate the reproducibility of crystallinity (cf. App. A). It was found that the maximum standard deviation was 3 Å. Since the crystallite size range, measured in this study, was over 100 Å, the percentage error was about 3%. The analytical procedure was slightly different for the oriented specimens (cf. App. A). The maximal standard deviation value for the crystallite size was equal to 3 Å. However, the crystallite size range calculated for oriented samples was around 50 Å, thus giving a percentage error of 6%.

4.2.1.3.3 - *β- and Smectic Crystal form Indices*

Turner Jones et al. (14) first introduced the concept of quantitative analysis of the crystal forms of iPP using WAXD. The authors defined a β-crystal form index as follows (14):

$$k_\beta = \frac{I_{300}^{\beta}}{I_{300}^{\beta} + I_{110}^{\alpha} + I_{040}^{\alpha} + I_{130}^{\alpha}} \qquad eq.(4\text{-}5)$$

where I_{300}^{β} and I_{hk0}^{α} are the intensities of the corresponding diffraction peaks. Measurement reproducibility was evaluated to be about 5%. It is important to note that the β-index value is a relative measure for characterizing the polymorphic composition, but it does not indicate the absolute value of β-form content. However, k_β is 0 for the pure α-form and 1 for the pure β-form of iPP.

A procedure similar to that of Martorana et al. (15) was used for the determination of the smectic index, k_{sm}. It was estimated as follows:

$$k_{sm} = \frac{A_{sm}}{A_{sm} + A_{110} + A_{040} + A_{130}} \qquad eq.(4\text{-}6)$$

where A_{sm} and A_{hk0} are the peak areas of the corresponding diffraction peaks, as shown in Figure A-6 (cf. App. A). Again, the smectic-index is a relative measure of the content of the smectic phase. Because of the complex peak overlapping, measurement reproducibility was lower than for the β-index, i.e., about 10%.

4.2.1.3.4 - *In-Plane Orientation Index*

In this work, an attempt was made to utilize diffraction data from WAXD in reflection to compare quantitatively the texture and orientation of equibiaxially oriented samples. The method described here is limited to the relative comparison of samples having the uniplanar texture, i.e. equibiaxially stretched samples.

In principle, X-rays in the WAXD reflection technique will be only diffracted by the crystallographic planes that are parallel to the sample surface being investigated. The investigated plane is the one that contains the MD and TD directions. The WAXD patterns of simultaneously equibiaxially oriented specimens show only three main diffraction planes oriented parallel to the film surface. These three major peaks correspond to the (110), (040), and (130) crystal planes (cf. results section, Figure 7-4). Consequently, the intensities and areas of these diffraction peaks are proportional to the number of the (110), (040), and (130) crystal planes being oriented in the MD-TD plane. The normal to the (040) crystal plane is the [010] direction, which is by definition parallel to the *b*-axis. Therefore, the area of the (040) diffraction peak, which is related to the (040) crystal plane orientation in the MD-TD plane, will be proportional to the *b*-axis orientation in the ND direction, as shown schematically in Figure 4-6.

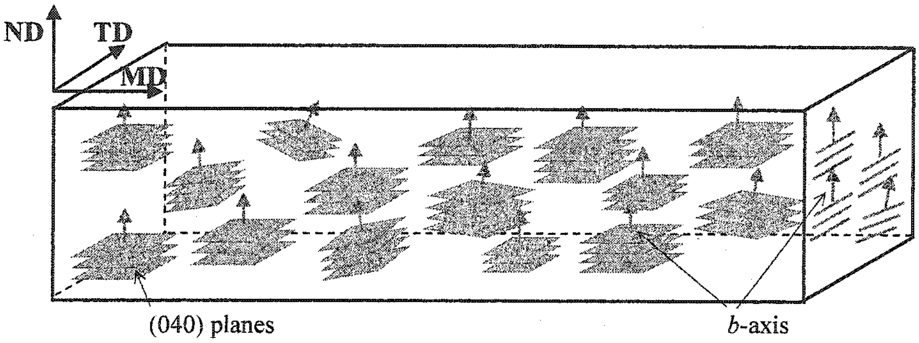

Figure 4-6 Schematic of the in-plane orientation of (040) crystal planes

The area of the (040) diffraction peak was normalized with respect to the sum of the areas of all the major diffraction peaks that appear between 10° and 24°, as shown in Figure 4-5. A (040) in-plane orientation index can be thus defined from the WAXD measurements as follows:

$$I_{(040)}^{in-plane} = \frac{A_{040}}{\sum_{2\theta=10}^{2\theta=24} A_{hkl}} \qquad eq.(4\text{-}7)$$

where A_{hkl} is the area of the corresponding (*hkl*) diffraction peak. The (040) in-plane orientation index can be interpreted as the proportion of (040) crystal planes that are perfectly oriented compared to the other major (*hkl*) crystal planes. Therefore, the (040) in-plane orientation index will be zero when no (040) crystal planes are oriented in the MD-TD plane, and it will be equal to one when only (040) crystal planes are oriented in the MD-TD plane. The same definition can be applied for the (110) peak to calculate the (110) in-plane orientation index. The WAXD patterns and the corresponding values of the (040) in-plane orientation index are shown in Figure A-8 (cf. App. A) for an isotropic specimen and a highly oriented sample. The measurement reproducibility for the (040) and (110) in-plane orientation indices was found to be within 0.005 (0.5%).

The higher is the (040) in-plane orientation index, the higher will be the degree of in-plane orientation of the (040) crystal planes, and thus, the higher is the degree of orientation of the *b* axis in ND (perpendicular to the film plane). This degree of *b* orientation can be also expressed in terms of average squared cosine, $\langle \cos^2\theta_{b,ND} \rangle$, which can be assessed by infrared dichroism or pole figure measurements (cf. 4.2.2 and 4.2.3). The (040) in-plane orientation index from WAXD and $\langle \cos^2\theta_{b,ND} \rangle$ from infrared dichroism were compared for a series of simultaneous equibiaxially oriented films stretched at different ratios. Good qualitative agreement was found (cf. App. A). The *b*-axis orientation in ND yields also information about the *c*-axis orientation in the MD-TD plane. Therefore, the (040) in-plane orientation index can be used to compare the *b*-axis orientation in ND and the *c*-axis orientation in the deformation plane for specimens simultaneously equibiaxially stretched. Nevertheless, it should be noted that the (040) in-plane orientation index obtained from the WAXD measurements in reflection gives an indication only about the (040) crystal planes that are perfectly aligned in the MD-TD plane. It does not provide information about orientation distribution.

4.2.2 - Wide Angle X-Ray Diffraction Pole Figures

WAXD pole figure experiments were also carried out to obtain information about the type of texture obtained under various modes of stretching, such as uniaxial, planar, and biaxial. The orientation distribution functions for the distinctly textured samples were also evaluated.

4.2.2.1 - Principle

The WAXD pole figure technique can be used to characterize the orientation of the various crystallographic axes *a*, *b*, and *c* with respect to the sample axes. For that, the study of the orientation distribution of certain crystallographic (*hkl*) planes with respect to the sample axes must be carried out. Wilchinsky (16-18) first showed that the average *c* axis orientation could be obtained by determination of orientation of two planes, (110) and (040) containing the *c* axis. The same procedure was employed in this work. The diffracted intensity distribution over a whole sphere can be obtained by rotating the sample over two perpendicular axes. Diffraction data may be used to determine the $<\cos^2\theta_{hkl,J}>$ and, thus, the Hermans orientation functions (cf. App. A).

4.2.2.2 - Pole Figure Measurements

X-ray pole figure measurements were carried out with a D500 diffractometer equipped with a pole figure attachment employing CoK_α radiation. The voltage and the current of the X-ray source were set to 35 kV and 14 mA, respectively. The tube length was 100 mm with an aperture of 1°, the secondary aperture diaphragm was 2°-4° and the detector diaphragm was 0.6°. The preparation of the specimens was the same as for the WAXD experiments in reflection (cf. App. A). The intensities were recorded with full circular scans at different tilt angles, from 0 to 90° by 2.5° steps. The circular scans were performed in reflection from 0° to 60° and in transmission from 60° to 90°, with a 5° step. For the circular scan, a speed of $1°.s^{-1}$ was utilized. Only the (110) and (040) pole figures were performed for all the investigated samples.

4.2.2.3 - Pole Figure Data Analysis

The intensity data were corrected for background, defocusing and absorption effects. Background scatter was measured as a function of α and β at $2\theta = 35°$. Defocusing and absorption in the reflection mode were performed using an isotropic iPP sample, obtained by compression molding, of the same thickness as the investigated sample (10). Absorption corrections in transmission were calculated by the Siemens TEX_AT software, according to the procedure developed by Decker et al. (19).

Orientation measurements can always be presented as pole figures. However, an orientation diagram that uses the Hermans-orientation factors may be plotted in the form of equilateral triangle, as shown in Figure A-14 (cf. App. A). The three bisectors can be related to the values of $<\cos^2\theta_{i,J}>$. A given point on such a triangular plot defines the second moment orientation parameters of a given crystal axis or plane with respect to the three sample axes. More explanations about the orientation diagram are given in Appendix A.

4.2.3 - Fourier Transform Infrared (FTIR) – Infrared Dichroism

Infrared measurements were used to characterize orientation of the equibiaxially stretched films. It was also used to determine the infrared isotacticity index of raw materials. The experimental details of this last procedure are given in Appendix A. Several studies investigated the utility of infrared linear dichroism for the determination of orientation in iPP (20-24). Good agreement was found between the crystalline phase orientation functions obtained from infrared dichroism and from X-ray measurements (20, 23). In this work, orientation functions were determined by infrared dichroism using the "tilted film" technique.

4.2.3.1 - Principle

If the infrared radiation is linearly polarized and the polymer chains are preferentially oriented, the absorbance associated with a certain molecular vibration becomes anisotropic. This differential absorption, depending on the polarization direction, is called infrared dichroism. The simplest representation is by the dichroic ratio expressed as

$$D = \frac{A_1}{A_2} \qquad eq.(4\text{-}8)$$

where A_1 and A_2 are the two rates of absorption, when the polarization direction of the incoming light is parallel "1" and perpendicular "2" to the orientation axis, respectively. For the simple case of axial symmetry of the orientation distribution, it has been shown that the orientation function f is given by

$$f_{i,J} = \frac{D-1}{D+2}\frac{D^0+2}{D^0-1} \qquad eq.(4\text{-}9)$$

where D^0 is the dichroic ratio when the chain axes are perfectly aligned with the orientation direction. D^0 is related to the angle between the absorbing unit and the chain axis through $D^0 = 2\cot^2\alpha$ where α represents the angle between the transition moment vector and the electric vector of the incoming polarized light. An alternative representation of the imperfect alignment is to assume that all chains are oriented at a fixed angle θ to the symmetry axis, which yields a Hermans-type relation between the angle θ and $f_{i,J}$. This method is useful for uniaxially oriented sample but may be ineffective for biaxially oriented films.

It is necessary to measure the absorbance in three directions to fully characterize the orientation in a biaxially oriented sample. This is usually easy for the MD and TD directions, but more tedious for the ND direction. For thin films, A_{ND} can be determined by means of the "tilted film" technique (20, 25-27). Spectra S_{MD} and S_{TD} are measured with the polarization in MD and TD with the film being normal to the IR beam. Then, the film is tilted at usually 45° and spectra are measured again with the polarization in the two directions.

The orientation of a given molecular axis with respect to a given sample direction can be obtained from the dichroism of a special peak in the IR spectra by the following equation (28)

$$f_{i,J} = \left(\frac{\phi_J}{\phi_0} - 1 \right) \frac{1}{3\cos^2\alpha_i - 1} \qquad eq.(4\text{-}10)$$

where ϕ_J is the intensity of the peak in the spectrum S_J corresponding to polarization in the J direction, $\phi_0 = \frac{1}{3}(\phi_{MD} + \phi_{TD} + \phi_{ND})$ is the intensity in the structural factor spectrum, and α_i is the angle between the transition moment of the vibration and the molecular axis.

4.2.3.2 - Experimental Details

A Nicolet 750 Fourier Transform infrared spectrometer equipped with a wire-grid polarizer (Spectra Tech Inc.) positioned adjacent to the sample was employed for infrared dichroic measurements. The beam passed first through the polarizer and then through the sample before reaching the detector. Different polarized spectra were obtained by rotating the polarizer, and the sample orientation remained fixed. In all cases, 100 scans at a resolution of 1 cm^{-1} were averaged and transformed with the Happ-Genzel apodization function. Each spectrum was ratioed against a corresponding number of background scans using the same polarizer and instrument settings.

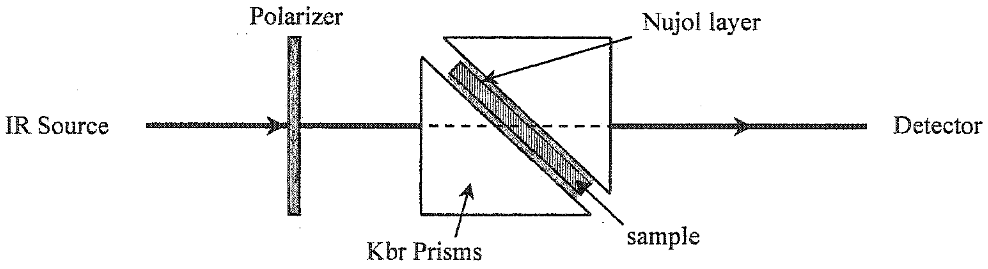

Figure 4-7 Experimental set-up for the tilted infrared dichroism experiments

Two spectra were first measured with the plane of the film perpendicular to the beam. The film was sandwiched between potassium bromide (KBr) plates, to avoid interference. The peak absorbances A_M and A_T for polarization in the machine and transverse directions, respectively, were then obtained for each absorption. The "tilted film" experiments were performed with the plane of the film at 45° with respect to the beam, in order to measure peak absorbances for radiation having a component polarized in the normal direction. This was achieved by positioning the sample between the 45° KBr prims, as illustrated in Figure 4-7. Layers of nujol (liquid paraffin oil) were used to improve optical contact. The nujol spectrum has a region clear of any peak absorption in the region 750 – 1080 cm^{-1}, where the analysis was conducted. The peak absorbances A_{MN} and A_{TN} were obtained for polarization in the normal and transverse directions.

4.2.3.3 - Data Analysis

Only the 770-1080 cm^{-1} "finger print" region was used. This region exhibits at least seven well defined absorption peaks, as shown in Figure 4-8. Among, these peaks, those at 841, 973, and 998 cm^{-1} are strong in intensity and show parallel polarization characteristics, whereas the peaks at 809, 899, and 940 cm^{-1} are medium in intensity and show perpendicular polarization characteristics. Moreover, there is a doublet with peaks at 1036 and 1045 cm-1 which are medium in intensity and show parallel polarization characteristics. Recently, Karacan et al. (20) showed that the 841 cm^{-1} peak could be used to characterize the chain axis orientation for crystalline (or at least highly ordered) material, whereas the peak at 973 cm-1 could be used to determine the average orientation.

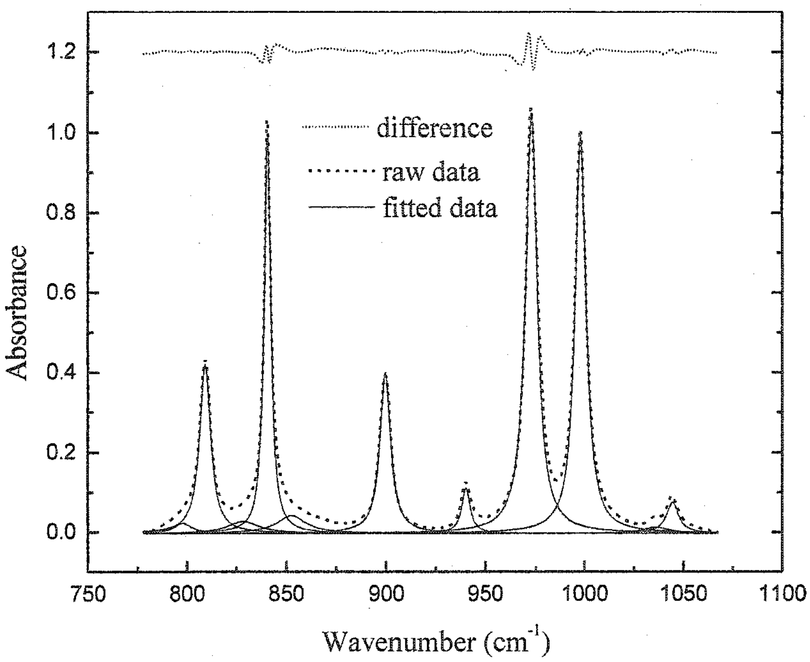

Figure 4-8 *An example of the curve fitting for an equi-biaxially stretched PP film. The polarization is in the machine direction. The upper curve is the difference between the fitted and observed spectrum on the same scale*

All the spectra obtained from the normal and tilted film experiments were fitted with a Lorentzian peak function and a linear background. Firstly, the linear background, built between the contact points at 778 cm^{-1} and 1065 cm^{-1}, was subtracted. In addition to the major peaks, three minor peaks were required at 798, 828, and 858 cm^{-1} to improve the fits in the tails of the major peaks. The same procedure as the one reported by Karacan et al. was used for the curve fitting of the spectra. An example of the curve fitting is shown in Figure 4-8. The A_M, A_T, and A_{MN} were recorded from the curve fitting. Next, the absorbance A_N for the normal direction was calculated as follows:

$$A_N = \frac{\cos 45}{\sin^2 45}\left(A_{MN} - A_M \cos 45\right) \qquad eq.(4\text{-}11)$$

With the assumption that the bands 841, 809, and 973 cm^{-1} are not intense, the peak absorbances A_x can be substituted for ϕ in the equations given by Jarvis et al.(27) to obtain the second-order moments, P_{200}, P_{220}, P_{202}, and P_{222} and thus the orientation functions.

4.2.3.4 - Comparison of the orientation characterization techniques

Quantitative comparison between infrared dichroism, WAXD, and the pole figure technique is illustrated in Figure 4-9. Quantitative agreement in the values of $<\cos^2\theta_{i,J}>$ was poor. Nevertheless, good qualitative agreement for all three methods was obtained.

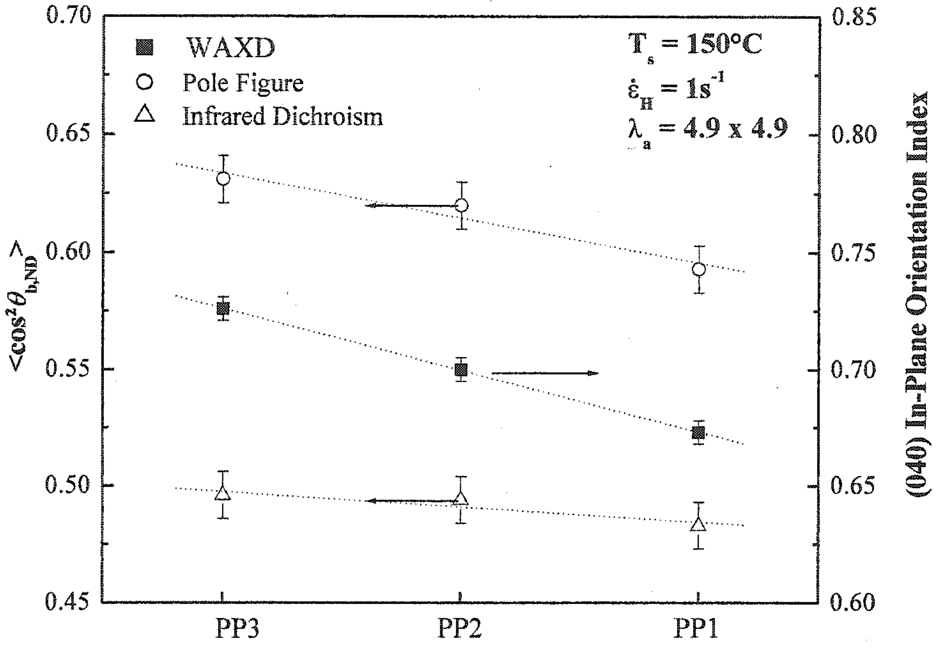

Figure 4-9 *Comparison of the orientation characterization results obtained from the different techniques used in this study for different resins stretched under the same conditions*

4.2.4 - Thermal Analysis (Differential Scanning Calorimeter)

Thermal analysis was performed using differential scanning calorimetry (DSC), with a TA Instruments 2920 DSC apparatus (New Castle, USA). The heating and cooling rate used in this work was 10°K/min, except where otherwise indicated. The DSC apparatus was calibrated against Indium for temperature and heat of fusion at the corresponding heating rate.

4.2.4.1 - Experimental Procedures

The raw materials characteristics, such as the melting point, T_m, the crystallization temperature, T_c, and the heat of fusion, ΔH_f, were all determined under identical thermal history. They were obtained from a sample, which had been heated and maintained for 5 min at 220°C and next cooled at 10°K/min to 0°C. Crystallization temperatures were evaluated from this cooling run, whereas T_m and ΔH_f were obtained from the subsequent reheating run. The thermal properties of the initial and stretched morphologies were obtained from the first melting.

4.2.4.2 - Sample Preparation

For the cast and stretched films, a careful and consistent method for sample preparation was needed to eliminate or reduce the effects of differences in sample preparation. All the investigated samples had a weight ranging from 6 – 10 mg. For the very thin stretched samples, several disks, which were stamped out of the film, were piled into the DSC pan to reach a minimum sample weight of 6 mg.

4.2.4.3 - DSC Curve Analysis

The DSC melting curves were analyzed to obtain the following values: the melting point (T_m), the heat of fusion (ΔH_f), and the onset of melting (T_{om}), as defined in Figure 4-10. The heat of fusion was estimated by drawing a linear baseline between 90°C and the end of melting temperature. The degree of crystallinity was calculated using the value of 209 kg/J for the enthalpy of fusion of a 100% crystalline α-form iPP (29). The determination of the onset of melting by the DSC software can be erroneous for samples not having a clear single peak. For this reason, the more useful definition of the full width at half maximum was chosen to represent the breadth of the DSC melting peak.

Finally, two more quantities were defined to help to characterize the partly molten state: the unmolten crystallinity, UC_{xxx}, and the structured melt, SM_{xxx}, where *xxx* refers to the stretching temperature. They were calculated from the DSC curve as the part of the area, corresponding to the heat of fusion. The unmolten crystallinity corresponded to the area that is superior to a certain chosen temperature, as illustrated in Figure 4-11. The value of UC_{xxx} should ideally be proportional to the crystallinity remaining in a sample, being heated, when it reaches the *xxx* temperature. The amount in structured melt was calculated as follows: $SM_{xxx} = \chi - UC_{xxx}$, where χ is the degree of crystallinity of the initial cast film. The amount of structured melt refers to the quantity of small, defect-full lamellar crystals that have just been melted, due to the thermal energy imported to the system. These "molten" molecules may be considered as having higher structural order than those in the amorphous phase. The concept of "structured melt" has been introduced to explain the high nucleating efficiency and morphology "memory effect" of a polymer melt heated to a temperature just above its melting point (30). Therefore, distinction is made between the molten crystalline phase, referred to as structured melt, and the original amorphous phase.

The measurement reproducibility of the melting temperature was found to be within 0.2°C for the initial cast films and 1.0°C for the stretched films, while that of the degree of crystallinity was found to be within 2% in crystallinity for both the initial cast and stretched films. The same measurement error can be assumed for the amounts of unmolten crystallinity, structured melt, and amorphous phase.

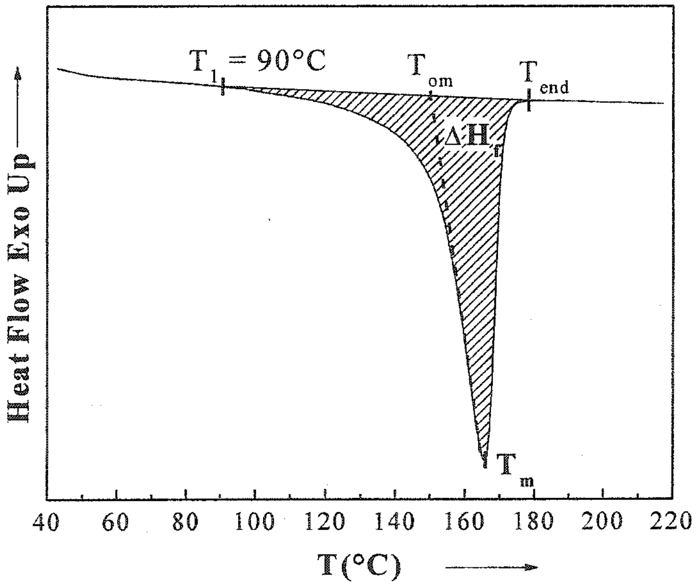

Figure 4-10 *DSC curve analysis illustrating the definitions of the melting temperature (T_m), the melting enthalpy (ΔH_f), and the onset of melting (T_{om})*

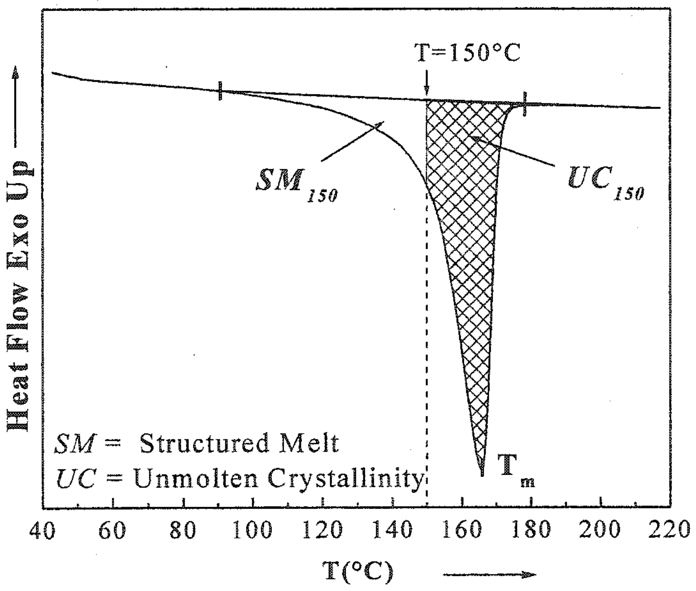

Figure 4-11 *DSC curve analysis illustrating the definitions for the unmolten crystallinity (UC) and the structured melt (SM) quantities*

4.2.5 - Polarized Light Microscopy

Polarized light microscopy (PLM) was employed to characterize the initial morphology of the cast film samples and the preheated cast film specimens. A Leitz ORTHOPLAN polarizing optical microscope with a Leica image processing system (Leica Microsystems AG, Wetzlar, Germany) was used to observe the spherulitic morphology of the undrawn samples. A first order (λ) red plate was used for determination of the sign of birefringence of spherulites (31). Thin sections of 3 – 10 µm were prepared at room temperature by cutting with glass knives in a Reichert-Jung microtome. The determination of the spherulite size was achieved by measuring individually all the visible spherulites along two axes (the shortest and the longest ones) and averaging these data for all spherulites.

4.2.6 - Film End-Use Properties

The mechanical properties, such as tensile strength, elongation at break, and elasticity modulus, the optical properties, such as haze and gloss, and the thermal shrinkage were all determined according the relevant ASTM methods. In all the cases, the property values represent an average value from at least five measurements, but most generally from ten measurements, for each (MD and TD) direction.

The modulus of elasticity, the tensile strength, and the elongation at break were assessed according to the ASTM 882 method, using an Instron Tensile testing machine. The percentage of Haze was determined according to the ASTM 1003 method. The Gloss was measured according to the ASTM 2457 method. The optical properties were characterized using the "Micro-gloss 45" and "Haze-gard plus" devices from BYK Gardner GmbH (Geretsvied, Germany). The thermal shrinkage at 120°C for 5 min was carried out according to the ASTM D 1204 method. All these experiments were carried out at Brückner Maschinenbau GmbH.

Additionally, the film thickness and local draw ratios were assessed. This was done by tracing a central grid of 36 squares of 10 mm x 10 mm on the undrawn cast film specimens. After stretching, the side distances between square corners for the MD and TD directions were measured, with an accuracy of ± 0.5 mm. These values were then averaged for the 36 squares (λ_{36}), for the 16 inner squares (λ_{16}), and for the first four inner squares (λ_4). Film thicknesses were obtained by calculation from the measured local draw ratios for each square, assuming constant volume. A similar notation for the thickness average values as for the draw ratios, i.e., t_{36}, t_{16}, and t_4, was used. The average values were found identical to the average values from the actual measurements in each of the squares, within an accuracy of ±2μm.

4.2.7 - Stress Optical Analysis

To obtain more information regarding the deformation homogeneity, photographs of the fringe patterns of the short drawn samples were obtained using a plane polariscope. The polariscope consisted of a white light source, a polarizer, and an analyzer, in which the film sample is placed between the polarizer and the analyzer. The intensity of the light that has traveled through the polarizer, the sample and the analyzer can be written as:

$$I = K\sin^2(2\alpha)\sin^2\left(\frac{\Delta_2-\Delta_1}{2}\right) \qquad eq.(4\text{-}12)$$

where K is a coefficient depending on the light source, α is the angle that the principal stress direction of the sample makes with the polarizer, and $\Delta_2-\Delta_1$ is the relative retardation defined as:

$$\Delta_2-\Delta_1 = \frac{2\pi t}{\lambda_l}(n_2-n_1) \qquad eq.(4\text{-}13)$$

where t is the thickness, λ_l is the light wavelength, and n_i is the refractive index in the corresponding principal stress direction. This difference is related to the principal stresses, σ_i, by the optical stress law:

$$n_2-n_1 = C(\sigma_1-\sigma_2) \qquad eq.(4\text{-}14)$$

where C is the optical stress coefficient. Extinction will occur if $\alpha = 0$, or if the relative retardation is zero. In the first case, the extinction fringes are the loci of the points where the principal stress directions coincide with the axis of the polarizer or analyzer. In the second case, extinction fringes are the loci of the points where the principal stress difference is zero. Because of the use of white light, fringe patterns appeared as a series of colored bands. Colored fringes that represent the extinction of only a certain wavelength appear when

$$\Delta_2-\Delta_1 = n2\pi \quad \text{or} \quad C(\sigma_1-\sigma_2)\frac{t}{\lambda_l} = n$$

where n is an integer. Therefore, a region with closely spaced color bands will represent an area of high stress gradient and/or of rapidly changing thickness.

4.3 - Biaxial Film Stretcher

This section describes the laboratory biaxial film stretcher, its operating principle, specifications, and precision. Moreover, it provides a detailed description of stretching experiments and their reproducibility.

4.3.1 - General Description

The simultaneous biaxial stretching experiments were carried out with a laboratory scale film stretcher, the KARO IV film stretcher. It was designed by Brückner Maschinenbau GmbH (Siegsdorf, Germany) for the investigation of stretching of polymer films under conditions similar to those encountered in film production lines that use the tenter-frame stretching system. A description of the laboratory film stretcher is given in this section. This description includes some of the modifications applied to the standard machine in order to improve reproducibility and precision of the stretching measurements. A more detailed and thorough description of the film stretcher can be found elsewhere (32).

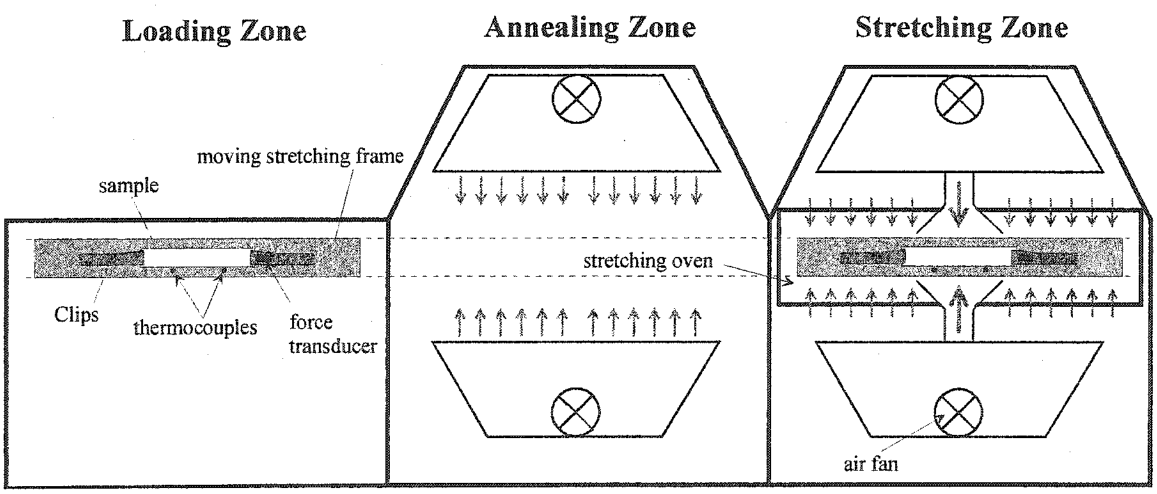

Figure 4-12 Schematic representation of the Brückner laboratory film stretcher

The film stretcher consists of three main zones for loading, annealing, and stretching, as illustrated in Figure 4-12. The stretching takes place discontinuously by moving a horizontal stretching frame. After the specimen is installed on the stretching frame, the latter is moved from the loading zone to the stretching oven. The moving and perpendicular directions are defined as the machine direction (MD) and the transverse direction (TD), respectively. After stretching, the frame is returned to the loading zone, and the film is removed. During such a stretching experiment, the polymer film experiences a thermal history similar to that encountered under commercial processing conditions (cf. section 2.2).

The second oven in the annealing zone may be used for heat treatment and/or further stretching/relaxation of films at a temperature different from that of the stretching oven. This practice is common in film production lines to control dimensional changes, such as shrinkage. In this work the second oven was not used.

The stretching frame allowed biaxial drawing along two perpendicular directions, using a system based on the pantograph principle, as illustrated in Figure 4-13. The stretcher consisted of two servomotors that control the displacement of the two perpendicular pairs of steel base plates, on which the clips were positioned. The specimen was grasped by five clips on each side. The clip gripping jaws were driven by a nitrogen pneumatic system. During stretching, the pantograph-based system ensured the simultaneous movement of each clip and maintained equal distances between the clips. During stretching, two 100 N force transducers, which were mounted on the central clip on each axis, permitted the recording of the machine and transverse direction forces. The two servomotors were under software control, that provided precise and flexible control of displacement on both deformation axes. High strain rates, up to 500 mm/s, as encountered on industrial production lines, could be achieved.

The stretching oven had two symmetrical parts containing heat exchangers and air blowers, which ensured homogeneous heating on the upper and lower faces of the sample, as schematically shown in Figure 4-12. Before stretching and during preheating, two diffusers of 65 mm x 65 mm size, were moved a few millimeters away from the specimen. They blew hot air, to maximize the heat transfer and preheat the sample rapidly to the oven air temperature. A pyrometer, which measured the temperature in the film center, and four thermocouples, positioned in each corner, as shown in Figure 4-13, continuously recorded data throughout the process. A thermocouple was embedded in a dummy specimen to measure sample temperature. At the end of the preheating, the temperature was found to be effectively identical to air temperature. For the temperature range considered in this work (from 140°C to 165°C), a preheating time of 40s was found to be the best compromise between temperature homogeneity and minimum annealing. (32).

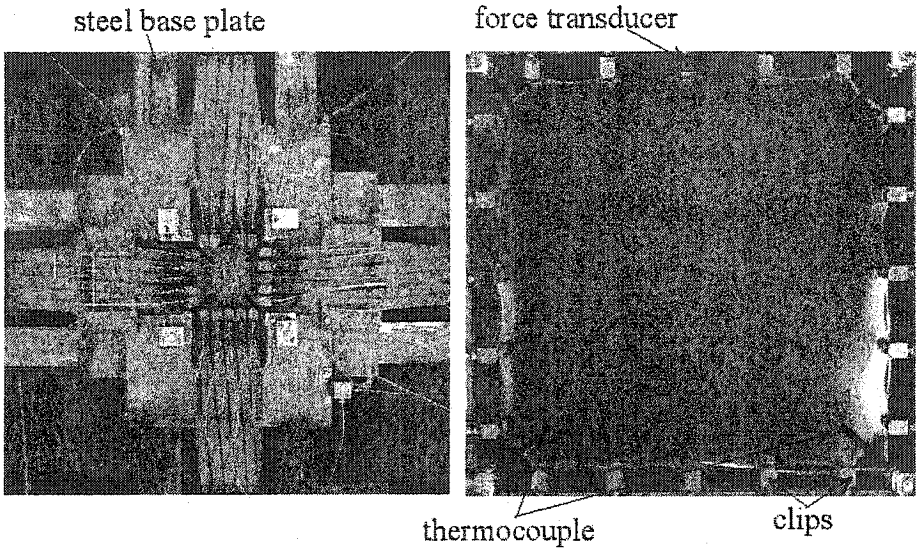

(a) before stretching (b) after stretching

Figure 4-13 Photographs of the stretching frame

A variety of temperature regulators and air blowers were employed in the stretching oven in order to overcome the complex heat losses and temperature variations due to the frame entering and leaving the oven. In spite of these precautions, the temperature distribution in the stretching oven could not be perfectly uniform. For the temperature range under study, the maximum temperature variation, which was always found in the far corners, at a stretching ratio of 8, was 2.8°C at 140°C and 5.1°C at 160°C. This temperature distribution was more or less reproducible, under the operating conditions employed in this study. Built-in thermocouples, on the middle clip of each side, monitored the frame temperature. A stretching experiment was always started with the same frame temperature of 95°C. After preheating, the average clip temperature was found to be around 120°C, for a stretching oven between 145°C and 160°C. Therefore, a temperature gradient in the specimen was inherent in the stretching process, especially near the clip positions. However, similar temperature gradients can also be found in industrial tenter-frame stretching for the production of biaxially oriented polypropylene films.

The nominal strains were obtained by an independent distance measuring system, which employed pulled cables that determined the strain ratios in both directions by assessing axial displacements with an accuracy of ± 1 mm. During an experiment, all temperatures, axial displacements, time and forces were continuously recorded and fed to a user control interface software. The laboratory film stretcher allowed the choice among various modes of stretching, such as sequential (SEQ) and simultaneous biaxial, constant-width uniaxial (or planar), and uniaxial. The other stretching conditions that could be varied were oven temperature, strain ratios and strain rates for each axis, and the strain rate profile (Cauchy or Hencky). Except, where otherwise indicated, in this work, biaxial stretching implies that the drawing process occurred simultaneously in both the MD and TD directions.

4.3.2 - Description of a Stretching Experiment

A stretching experiment or cycle started by loading the specimen in the frame. The specimen orientation, which was defined as MD for the extrusion direction and TD for the transverse direction, matched that of the laboratory stretcher. The clips were attached to the specimen. They were positioned so that the actual specimen size was 70 mm x 70 mm. When the frame temperature reached 95°C, the frame was moved to the stretching oven, at which point the diffusers were positioned to preheat the specimen. An optimized preheating time of 40 s was used. During preheating, the clips were programmed to move sufficiently on each side to compensate for the thermal expansion of the specimen, so that the initial force was zeroed. For the range of stretching temperatures between 140°C and 160°C, the actual initial specimen size was then 74 mm x 74 mm at the end of the preheating. Subsequently, the diffusers were withdrawn, and the stretching was started. Finally, the frame returned to the loading zone, and the film was allowed to cool down under tension to room temperature. Only 20 - 30 seconds were required to cool the sample before removing the stretched sample.

A typical force vs. time curve for the MD and TD directions for a simultaneous equibiaxial stretching at 150°C with a Hencky strain rate of $1s^{-1}$ is shown in Figure 4-14. The force curves in MD and TD were observed to overlap over a large deformation range. However, in the yield region and at the end of stretching, the TD forces were usually slightly lower than the MD forces. This disparity was due to neither a non-isotropic specimen nor a force measurement error. Our results indicate that the difference is due to a limitation of the film stretcher, which made it difficult to produce a true simultaneous biaxial stretching at the very low strain ratios. This slightly imperfect biaxial drawing generated a reproducible, material independent, unsymmetrical stress distribution in the specimen, as it will be discussed later in Chapter 6.

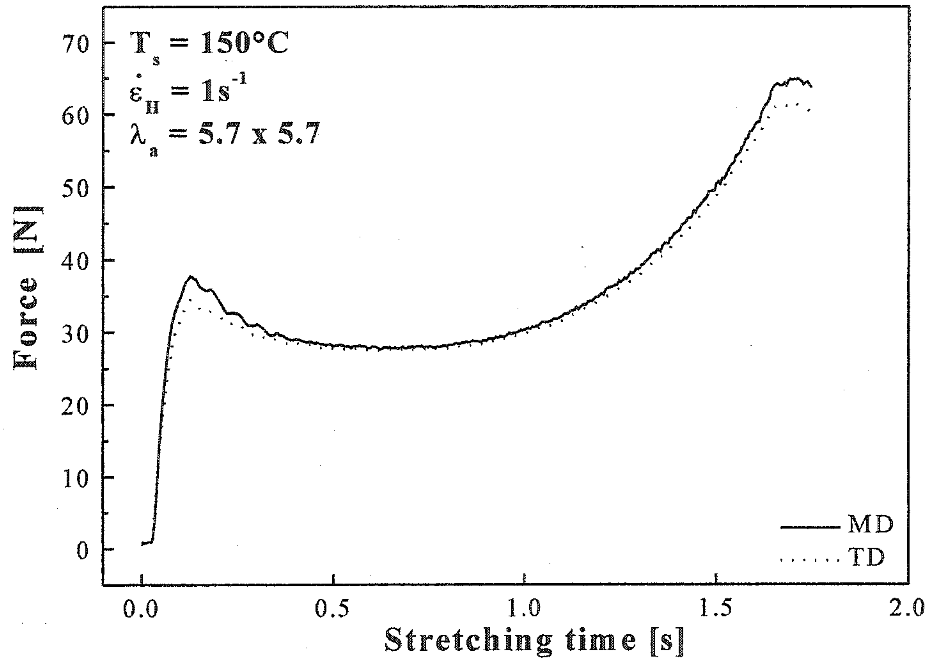

Figure 4-14 Force vs. time for the simultaneous equibiaxial stretching of an iPP cast film.

4.3.3 - Evaluation of Reproducibility

A stretching experiment for a defined set of conditions was always part of a series of five or more repeated stretching cycles with specimens of the same cast film. During a series of repeated experiments, the average oven temperature fluctuated, because thermal conditions varied due to the frame motion. The influence of the small air temperature variation during a series can be evaluated by comparing the force-extension curves for each one of the cycles, as shown in Figure 4-15. These results show that, despite the temperature fluctuations, the reproducibility was good in terms of deformation behavior, as represented by the force-extension curves. In fact, the average standard error for the measured force was found to be below 3%.

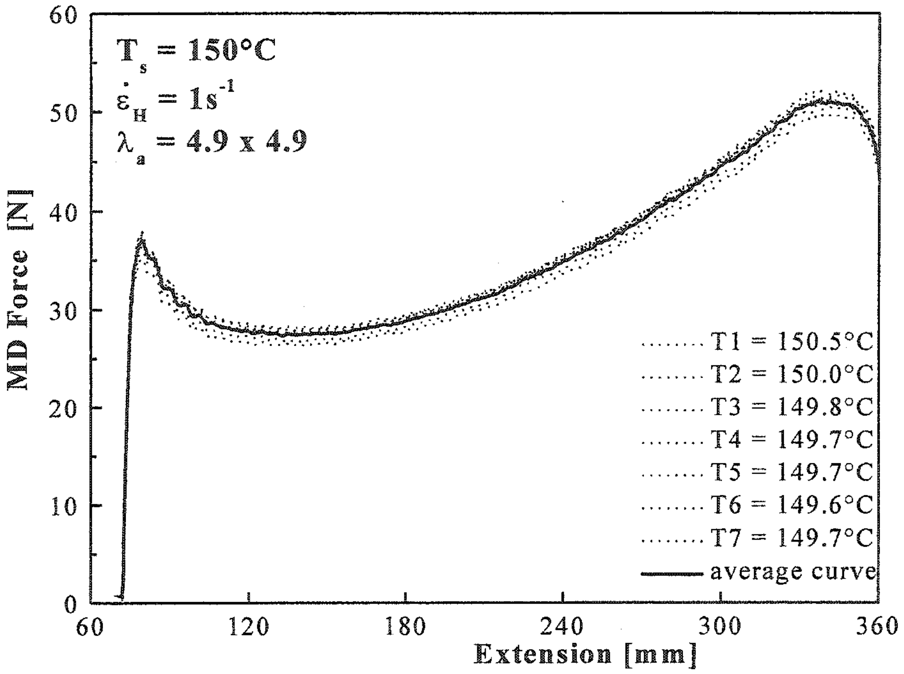

Figure 4-15 Reproducibility of stretching experiments for the same series.

In the rest of this work, all the reported curves will represent the average curve of the corresponding series. The nominal stresses σ_N were defined as the ratio of the draw force to the initial cross section. The nominal strain ε_N is the ratio of the deformed sample length to its initial gauge length. Analyzed values, such as yield stress, were always computed using the average curve. To illustrate the measurement reproducibility for a series of stretching experiments, Figure 4-16 shows and compares various equibiaxial stretching series that differed only in the final strain ratios. The series reproducibility was evaluated to be within 3%.

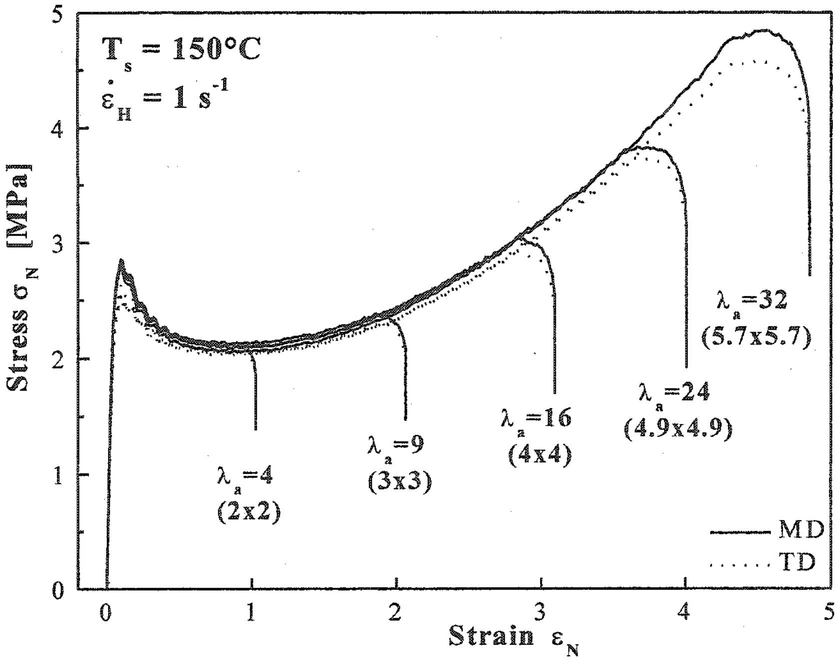

Figure 4-16 Reproducibility of a stretching series for simultaneous equibiaxial drawing experiments.

[Refs. on p. 81]

References

1 - M. Gahleitner, C. Bachner, E. Ratajski, G. Rohaczek and W. Neissl, "Effects of the catalyst system on the crystallization of polypropylene", J. Appl. Polym. Sci., 73, 2507-2515 (1999).

2 - K. Yamada, S. Matsumoto, K. Tagashira and M. Hikosaka, "Isotacticity dependence of spherulitic morphology of isotactic polypropylene", Polymer, 39, 5327-5333 (1998).

3 - M. Gahleitner, K. Bernreitner and W. Neissl, "Influence of molecular structure on crystallization behaviour and mechanical properties of polypropylene", Polymer Testing, 14, 173-187 (1995).

4 - A. Hanyu and R. Wheat, "Properties and film applications of metallocene-based isotactic polypropylenes", J. Plast. Film Sheeting, 15, 109-119 (1999).

5 - B. Wunderlich, Crystal melting, Academic Press, New York, (1980).

6 - J. J. Janimak, S. Z. D. Cheng, P. A. Giusti and E. T. Hsieh, "Isotacticity effect on crystallization and melting in polypropylene fractions. 2. Linear crystal growth rate and morphology study", Macromolecules, 24, p2253-2260 (1991).

7 - A. Weidinger and P. H. Hermans, "On the determination of the crystalline fraction of isotactic polypropylene from X-ray diffraction", Makromol. Chem., 50, p98-115 (1961).

8 - P. Scherrer, "Estimation of the size and internal structure of colloid particles by means of Röntgen rays", Nachr. ges. Wiss. Gottingen, 2, 96-100 (1918).

9 - B. E. Warren, "X-ray diffraction methods", J. Appl. Phys., 12, 375-383 (1941).

10 - L. E. Alexander, X-Ray Diffraction Methods in Polymer Science, Wiley, New York, (1969).

11 - L. Poussin, Y. A. BErtin, J. Parisot and C. Brassy, "Influence of thermal treatment on the structure of an isotactic polypropylene", Polymer, 39, pp4261-4265 (1998).

12 - Y. R. Wang, F. E. Teng, N. Zhang and Y. M. Wang, "X-ray studies on deformed polypropylene films", J. Macromol. Sci.-Phys., B34, 78-93 (1995).

13 - P. Riello, G. Fagherazzi, P. Canton, D. Clemente and M. Signoretto, "Determining the degree of crystallinity in semicrystalline materials by means of the Rietveld analysis", J. Appl. Cryst., 28, 121-126 (1995).

14 - A. Turner-Jones, J. M. Aizlewood and D. R. Beckett, "Crystalline forms of isotactic polypropylene", Makromol. Chem., 75, 134-158 (1964).

15 - A. Martorana, S. Piccarolo and F. Sciclilone, "The X-ray determination of the amounts of the phase in samples if isotactic poly(propylene) quenched from the melt at different cooling rates", Macromol. Chem. Phys., 198, 597-604 (1997).

16 - Z. W. Wilchinsky, "Measurements of orientation in polypropylene film", J. Appl. Phys., 31, 1969-1972 (1960).

17 - Z. W. Wilchinsky, "Recent developments in the measurement of orientation in polymers by X-ray diffraction", Adv. X-ray Anal., 6, 231-241 (1962).

18 - Z. W. Wilchinsky, "Orientation in cold-rolled polypropylene", J. Appl. Polym. Sci., 7, 923-933 (1963).

19 - D. Geiss and D. Hoffman, "Supermolecular Structure of Oriented Semicrystalline Polymers", Prog. Polym. Sci., 15, 1-101 (1990).

20 - I. Karacan, A. K. Taraiya, D. I. Bower and I. M. Ward, "Characterization of orientation of one-way and two-way drawn isotactic polypropylene films", Polymer, 34, 2691-2701 (1993).

21 - J. L. Koenig, S. W. Cornell and D. E. Witenhafer, "Infrared techinque for the measurement of structural changes during the orientation process in polymers", J. Polym. Sci. Part A2, 5, pp 301-313 (1967).

22 - F. M. Mirabella, "Determination of the crystalline and non crystalline molecular orientation in oriented polypropylene by infrared spectroscopy", J. Polym. Sci., Polym. Phys. Ed., 25, 591-602 (1987).

23 - S. Okajima, Y. Kobayashi and A. Narita, "Orientation factor of poylpropylene film by infrared dichroism", J. Appl. Polym. Sci., 11, pp 2515-2523 (1967).

24 - R. J. Samuels, "Infrared dichroism, molecular structure, and deformation mechanisms of isotactic polyproyplene", Makromol. Chem., Suppl., 4, pp241-270 (1981).

25 - J. P. Sibilla, "Orimtation in nylon 6 films as determined by the three-dimensional polarized infrared technique", J. Polym. Sci., 9, pp27-42 (1971).

26 - B. Jasse and J. L. Koenig, "Orientational measurements in polymers using vibrational spectroscopy", J. Macromol. Sci. Rev. Macromol. Chem., C17, pp 6-135 (1979).

27 - D. A. Jarvis, I. J. Hutchinson, D. I. Bower and I. M. Ward, "Characterization of biaxial orientation in poly(ethylene terephthalate) by means of refractive index measurements and Raman and infra-red spectroscopies", Polymer, 21, pp41-54 (1980).

28 - K. C. Cole and A. Ajji, "Characterization of orientation", in Solid phase processing of polymers, I. M. Ward, P. D. Coates and M. M. Dumoulin, Editors. Hanser: Munich. p. 33-84 (2000).

29 - A. Galeski, "Nucleation of polypropylene", in Polypropylene Structure, blends and composites, J. Karger-Kocsis, Editor: Weinheim. p. 133 (1995).

30 - B. Fillon, J. C. Wittmann, B. Lotz and A. Thierry, "Self-nucleation and recrystallization of isotactic polypropylene (apha Phase) investigated by DSC", J. Polym. Sci.: Polym Phys., 31, 1383-1393 (1993).

31 - J. M. Haudin, in Optical Properties of Polymers, G. H. Meeten, Editor. Elsevier Applied Science: New York (1986).

32 - S. Rettenberger, "Uni- und Biaxiales Verstrecken von isotaktischem Polypropylen im teilaufgeschmolzenen Zustand", PhD thesis, University Erlangen-Nuremberg, (2002).

[Refs. on p. 81]

CHAPTER 5

INITIAL FILM MORPHOLOGY

It is important to identify the morphology of the initial cast film and of the partly molten film prior to stretching. This chapter describes the initial morphology of the different cast films samples that were subjected to biaxial stretching. The effects of the chain tacticity of the polypropylene resins, the casting conditions, preheating, and annealing on the morphology of the cast films are presented and discussed.

5.1 - Effect of Chain Tacticity on Initial Film Morphology

The effect of the chain tacticity of the polypropylene resin on initial morphology was evaluated by determination of the morphology of cast films obtained from PP1, PP2, and PP3. These resins have similar molecular characteristics (same M_w) but differ primarily in isotacticity content. They were extruded and cast under identical processing conditions, as shown in Table 4-3.

5.1.1 - Results and Discussion

Figure 5-1 shows the WAXD patterns obtained for both sides of the cast films for the three homopolymer resins. The sides are referred to as "water bath (WB) side" and "chill roll (CR) side", depending on prevailing cooling conditions during solidification. All the WAXD patterns exhibit only the diffraction peaks characteristic of the α-form of iPP.

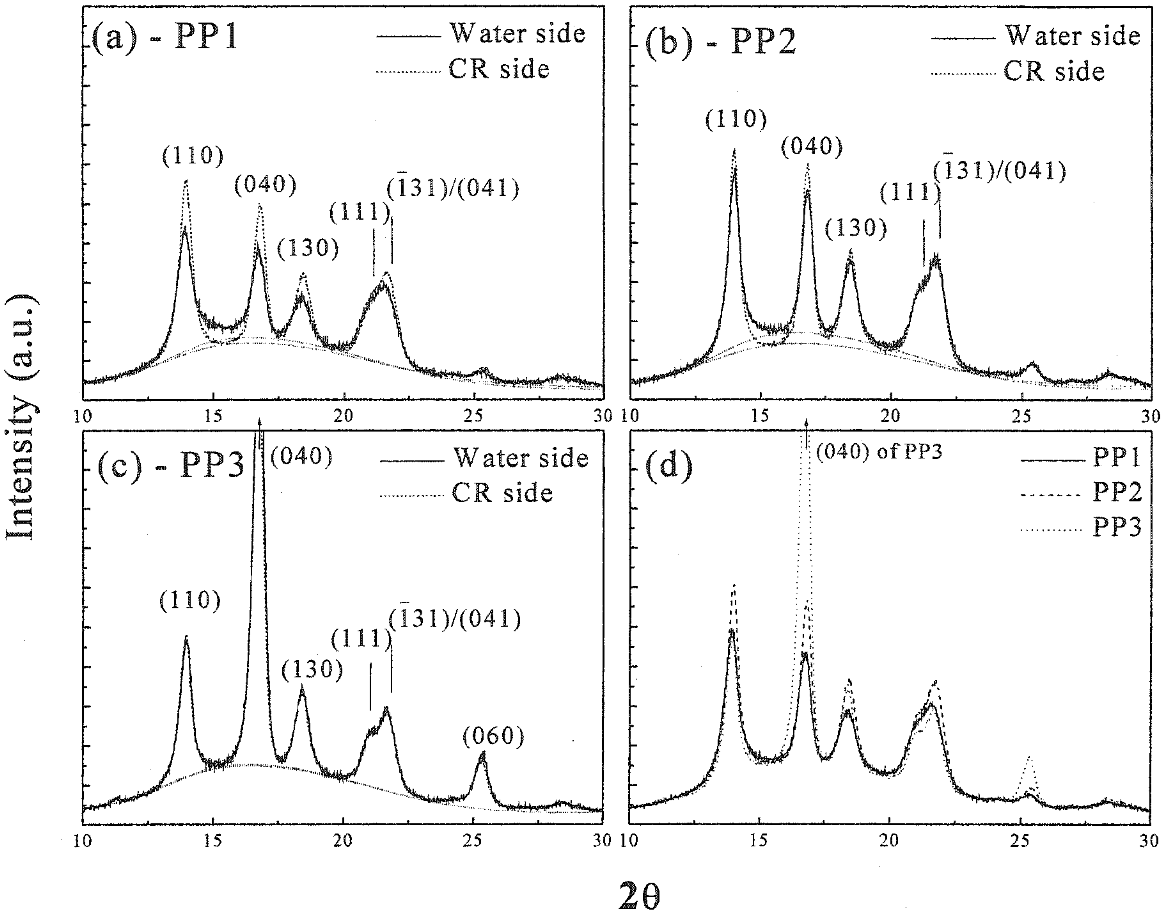

Figure 5-1 WAXD patterns measured on both sides for (a) PP1, (b) PP2, and (c) PP3. (d) Average WAXD patterns of three cast films (all curves plotted on the same intensity scale; the baselines represent the amorphous halos)

The PP1 and PP2 cast films showed a significant difference in the shape of the amorphous halo between both measured sides. In contrast, PP3 showed an almost identical WAXD pattern for both sides. The relatively low intensities of the (110) and (040) peaks in the WAXD pattern measured on the "water side" for the PP1 cast film indicate that this side of the film has a low crystalline content. In fact, both PP1 and PP2 showed better resolved crystalline diffraction peaks for the CR side than for the water side. The average WAXD patterns obtained from both sides are compared for the three cast films in Figure 5-1(d). The major differences between them were in peak intensities, especially for PP3, which exhibited strong (040) and, consequently, (060) diffraction peaks.

The intense (040) diffraction peak observed for the PP3 cast film could be attributed to either anisotropic distribution of the (040) planes or a high density of (040) crystalline planes. The former explanation may be excluded since no preferred orientation was detected by other WAXD measurements. Therefore, the intense peak was attributed to a high density of (040) planes throughout the sample. This can arise when crystallization occurs via epitaxy, or, in other words, favorably upon a certain crystallographic plane, here the (010) plane. An intense (040) peak was also observed for a cast film sample that was nucleated with sodium benzoate. Nucleation agents were reported to promote crystallization via epitaxy (1, 2). This led to the conclusion that the commercial PP3 resin may contain some unknown nucleation agent. However, no indication of a nucleation agent was found by infrared spectroscopy.

The DSC melting curves of the same three cast films are showed in Figure 5-2. A single DSC melting peak was observed for each resin. The melting temperature was seen to change significantly from one resin to another: 160°C for PP1, 165°C for PP2 and 168°C for PP3, and the onset of melting was also found to be shifted to higher temperatures from PP1 to PP3, as listed in Table 5-1. The melting peak width was the narrowest for PP2 cast films and the broadest for PP1.

Crystallization and melting behavior of isotactic polypropylene is known to depend primarily on tacticity (3-7). The effect of molecular weight (M_w) on crystallization behavior was reported to be negligible for high M_w ($M_w > 100$ kg/mol) (3, 8, 9). Moreover, the effect of molecular weight distribution (MWD) on crystallization is of secondary order compared to that of molecular weight and of isotacticity (3). Because the PP1, PP2, and PP3 resins have similar high molecular weight, it can be thus assumed that the differences in initial morphology between these resins are due to tacticity.

DSC and WAXD data summarized in Table 5-1 shows that crystallinity increases with the isotacticity fraction of the resin. Good qualitative agreement was found between the WAXD and DSC crystallinity indices. Increasing isotacticity does not only raise the overall crystallinity, but it also influences the spherulitic and lamellar morphologies. The apparent crystallite size, which represents a dimension at the lamellar scale, can yield information about the lamellar morphology. The D_{110} and D_{040} apparent crystallite sizes increase with increasing isotacticity. In fact, all calculated D_{hkl} were found to follow the same tendency as D_{110} and D_{040}.

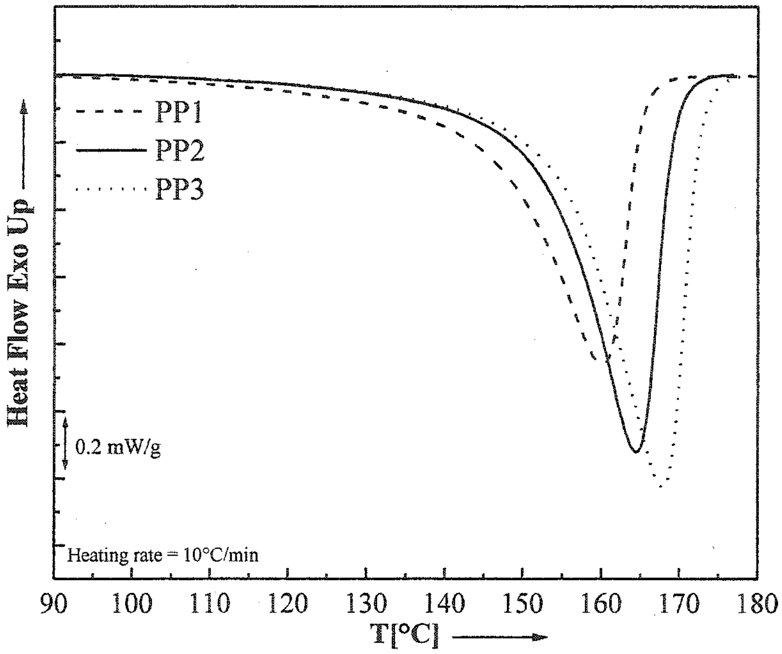

Figure 5-2 *DSC melting curves of the cast films for PP1, PP2, and PP3*

Table 5-1 *Morphological characteristics of the PP1, PP2, and PP3 cast films. WAXD values are averages from both sides. (CI = crystallinity index; D_{hkl} = apparent crystallite size calculated from the (hkl) diffraction peak; FWHM = full width at half maximum of the melting peak; Sph. = spherulite)*

		DSC				WAXD			PLM
Cast Film	**Isotact. [%]**	**CI_{DSC} [%]**	**T_m [°C]**	**T_{om} [°C]**	**FWHM [°C]**	**CI_{WAXS} [%]**	**D_{110} [Å]**	**D_{040} [Å]**	**Sph. size [µm]**
	± 0.2	± 1	± 0.2	± 0.4	± 0.2	± 0.5	± 3	± 3	± 3
PP1	94.9	40.3	159.9	145.8	11.7	45.3	137	165	10
PP2	98.6	43.8	164.6	151.8	10.4	51.1	165	187	5
PP3	99.5	49.6	167.9	153.9	11.0	55.5	174	193	< 5

Polarized light microscopy could not reveal a clear view of the spherulitic morphology. Indeed, the spherulite sizes had no Maltese cross pattern which made it almost impossible to distinguish individual spherulites. An approximate average value of 10 μm and 5 μm could be nevertheless assessed for PP1 and PP2, respectively. For PP3, the average size could not be exactly assessed, but it was certainly below 5μm. The average size of spherulites decreases from PP1 to PP3. The average spherulite size is generally related to the number of effective nuclei formed during solidification. Moreover, the relative nucleating efficiency of a polymer can be, at first, estimated by comparing crystallization temperature under controlled conditions (10). Since the crystallization temperatures of PP1, PP2, and PP3 increase from PP1 to PP3, the decreasing spherulite size can be explained by the corresponding increase of nucleating efficiency from PP1 to PP3. However, the crystallization temperature is a variable that depends not only on the molecular characteristics of the polymer (M_w, tacticity, branching, etc.) but also on the concentration and activity of residual heterogeneous nuclei. Therefore, it is not possible to explain the nucleating efficiency of these samples on the basis of isotacticity content alone.

Information about the lamellar structure can be obtained from the DSC melting point, the melting peak width and from the apparent crystallite size from WAXD. The melting peak temperature is related to the thickness of the most predominant group of crystallites (or lamellar crystals), as formulated by the Gibbs-Thomson equation (11). Thus, the increase of the melting temperature (T_m) with increasing isotacticity may be explained by the increase of crystallite thickness. This increase of T_m and crystallite size with isotacticity is supported by the DSC results of Cheng et al.(4) for isothermally crystallized fractions of iPP with different isotacticity. Their results also indicate that the crystallite dimensions increase both in thickness and also in the lateral directions with increasing isotacticity. This is supported by the fact that increasing the chain stereoregularity augments the linear spherulite growth rate (7). According to Hoffman and Lauritzen model (11), growth of a crystal unit occurs on the lateral surface. Therefore, chains that crystallize faster can be expected to form crystallites with larger lateral dimensions. An increase in the apparent crystallite size can reflect the perfection of the crystallites, and thus, greater thermal stability, as confirmed by the shifting of the DSC melting peak to higher temperatures.

5.1.2 - Conclusions

It can be concluded that the stereoregularity of the chains, i.e., the isotacticity, affects crystallinity and the spherulitic and lamellar structures of the initial cast morphology. The degree of crystallinity, as well as the crystallite dimensions, increased with increasing isotacticity. Spherulites seemed to decrease in size with increasing chain isotacticity. The major effect of chain stereoregularity was on the thermal stability of the crystalline phase. The DSC melting peak of the initial morphology was shifted to higher temperature with increasing isotacticity.

5.2 - Effects of Casting Conditions on Initial Film Morphology

The effects of the casting conditions on initial morphology were investigated by extruding resin PP4 and casting the sheet under four distinct casting conditions (cf. Table 4-3). The cast film samples will be referred to as CF1, CF2, CF3, and CF4 instead of PP4-CF1, etc. Only the cooling severity was varied by changing the temperatures of the chill roll and water bath. The severity of the cooling decreases from casting condition CF1 to CF4. The casting process has inherently asymmetric cooling conditions, as already indicated by the WAXD patterns shown in Figure 5-1. Only the results from the average bulk morphology are discussed here. The results for the "side" morphologies can be found in Appendix B.

5.2.1 - Results and Discussion

Figure 5-3 shows the X-ray diffraction patterns of both sides of each cast film specimen for the four casting conditions. The diffraction patterns differ in shape and number of peaks from one casting condition to another and form one side to the other. The WAXD curves for the most severe casting conditions, CF1, exhibit weak and broad diffraction peaks, characteristic of the α-form. In addition, the high intensity of the minimum between the (110) and (040) peaks, compared to the peak of the amorphous halo, indicates the presence of the smectic form in CF1. The pattern for the chill roll side of CF2 also seems to indicate the presence of some smectic form on that side of the cast film. In contrast, the CF3 and CF4 patterns exhibit an extra peak around 15.8-16.0°, very weak for CF3 and more intense for CF4, corresponding the (300) diffraction plane of the β-form.

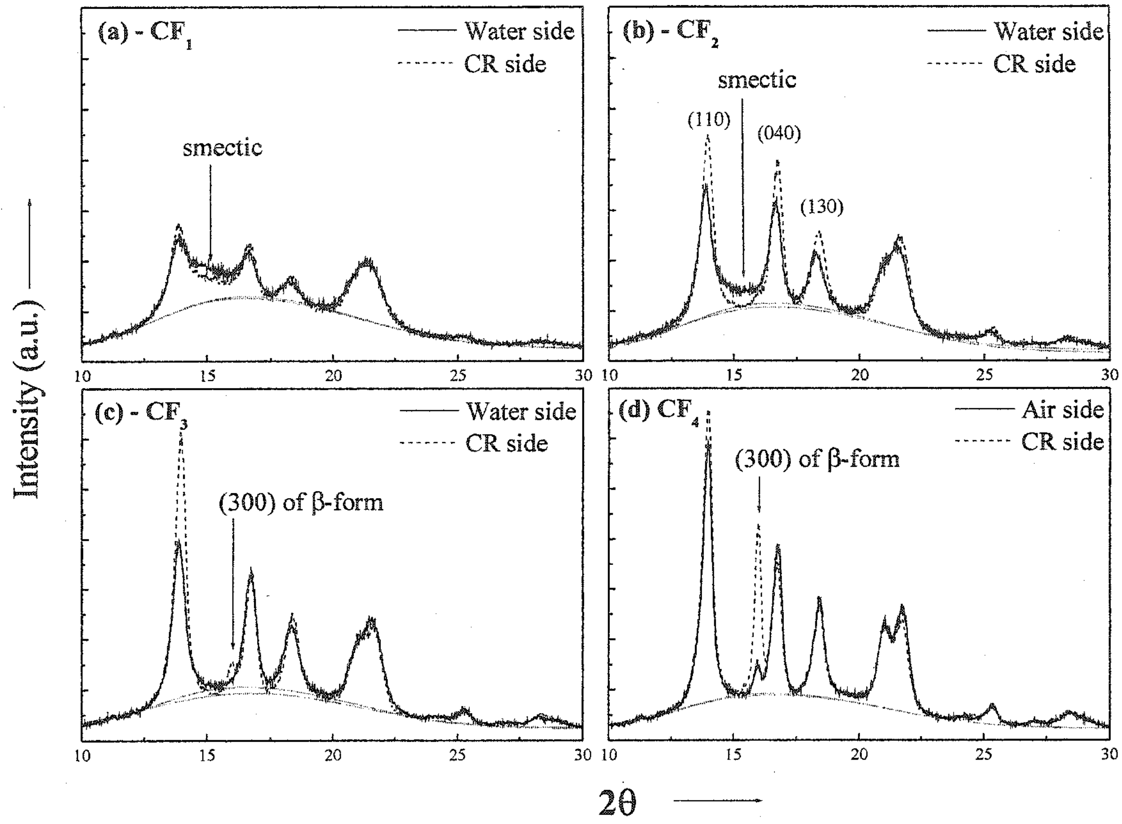

Figure 5-3 *WAXD patterns of the CF1, CF2, CF3, and CF4 cast films (plotted on the same intensity scale; baselines represent the amorphous halos)*

The corresponding average values of the β-form and smectic indices, as defined in section 4.2, are given in Table 5-2. It can be seen that the amount of smectic phase decreases, while the β-phase content increases from CF1 to CF4, i.e., with decreasing cooling severity. The former is explained by the fact that the disordered, smectic phase is favorably formed under severe cooling conditions (12-15). In contrast, the β-phase is known to form in a range of relatively slower cooling rates, as reported by Varga (16) and illustrated in Figure 2-4.

Table 5-2 *Morphological characteristics of the CF1, CF2, CF3, and CF4 cast films. (k_{sm} = smectic phase index; k_β = β-phase index)*

	WAXD						DSC			PLM	
Code	**CI_{WAXD} [%]**	**k_{sm}**	**k_β**	**D_{110} [Å]**	**D_{040} [Å]**	**D_{130} [Å]**	**CI_{DSC} [%]**	**T_m [°C]**	**FWHM [°C]**	**Sph.size [μm]**	**Sph. type**
PP4-CF1	35.7	0.39	0	128	136	122	38.8	163.9	11.6	inhom.	α
PP4-CF2	45.5	0.07	0	157	182	146	42.3	164.4	11.1	17	α,β
PP4-CF3	52.3	0	0.02	166	194	143	42.0	165.5	11.1	41	α,β
PP4-CF4	58.5	0	0.09	202	222	178	44.1	165.4	12.2	59	α,β

The presence of the β-crystal form was confirmed by polarized optical microscopy (PLM), as shown in Figure 5-4. Indeed, CF2, CF3, and CF4 exhibited highly birefringent β-type spherulites dispersed among α-type spherulites. This can be clearly observed in Figure 5-4(b). In contrast, CF1 exhibited no β-type spherulites, but a rather inhomogeneous spherulitic morphology. Indeed, the bulk of CF1 consisted mainly of highly birefringent α spherulites with an average size of 22 μm. Additionally, clusters of small bodies (of about 1 to 5μm) were observed in many regions in the bulk, especially near the surfaces. A cluster can be observed in Figure 5-4(a). This cluster feature was not observed for CF2, CF3 and CF4, which exhibited a more homogeneous size of spherulites. The cluster is thought to consist of poorly formed spherulites. The particularly high birefringence of the spherulites and the formation of the clusters of smaller, not well resolved spherulites observed in CF1 may be attributed to an inhomogeneous nucleation density, inherent to the peroxide-degraded polypropylene grade (8). Unfortunately, further experimental evidence is needed to fully explain the formation of this morphology.

Crystallization conditions are known to affect the level of lamellar branching (the ratio of radial (R) over tangential (T) lamellae), which in turn control the birefringence of the spherulites (16, 17). The dissimilarity in the birefringence of the spherulites for the four cast films suggests that the degree of lamellar branching was also affected by the severity of the cooling. Large β-type spherulites were found dispersed in smaller α-type spherulites. This may be explained by a lower nucleation rate, but a higher growth rate for the β-type than that for the α-type spherulites (17). The average sizes of the α- and β-type spherulites increased from CF2 to CF4, i.e., with decreasing the severity of the cooling.

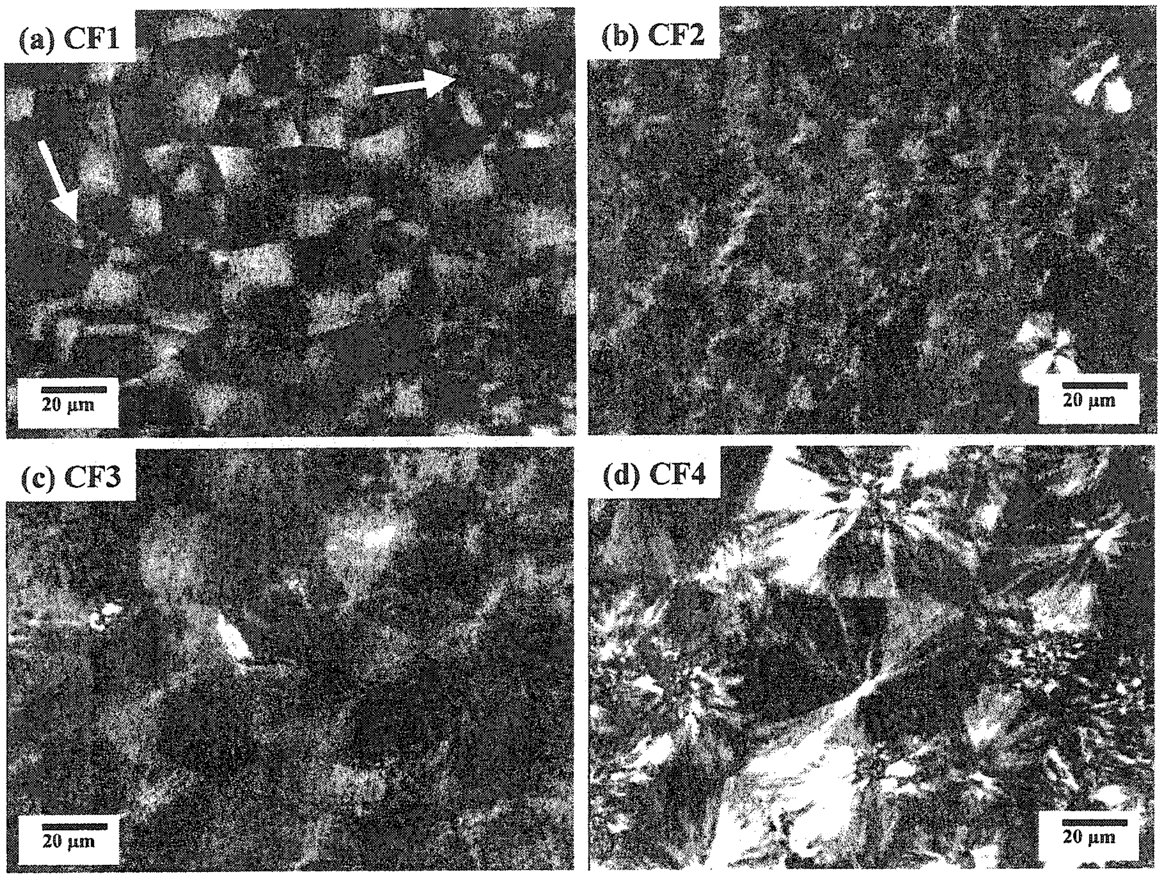

Figure 5-4 *Polarized light microscopy images of the bulk morphology for the CF1, CF2, CF3, and CF4 cast films (the arrow shows clusters of small spherulites)*

Figure 5-5 shows the DSC melting curves for the films prepared under the four casting conditions. The differences between these curves were significant compared to the reproducibility and error limits of DSC measurements. There is no evidence of a low temperature melting peak around 150°C, which would confirm the presence of the β-phase. This led to the conclusion that the amounts in β-phase contained in CF3 and CF4, as detected by X-ray diffraction and PLM, are relatively small compared to the α-phase. The amount of smectic phase seems to be sufficiently significant in CF1 to affect its melting behavior. Indeed, the onset of melting seems to be shifted to higher temperatures. The latter shift is due to the exothermic transformation of the smectic phase into the monoclinic form upon heating (18, 19).

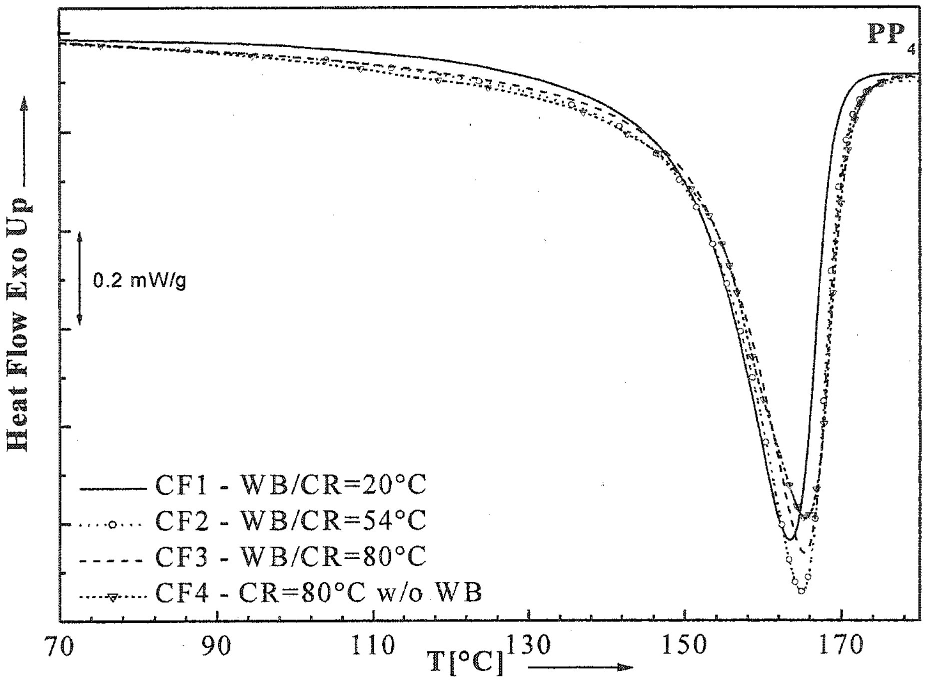

Figure 5-5 *DSC melting curves of the CF1, CF2, CF3, and CF4 cast films*

The DSC melting temperatures increase from CF1 to CF3, and CF4 has a similar melting point as CF3, as shown in Table 5-2. The intensity and sharpness of the WAXD peaks increase from CF1 to CF4, while the amorphous halo reduces in area. This indicates that the amount and the perfection of the crystalline phase increases from CF1 to CF4, as confirmed by the crystallinity index shown in Table 5-2. This increase was confirmed by both characterization techniques. The D_{hk0} apparent crystallite sizes, calculated from the X-ray diffraction peaks, are also presented in Table 5-2. The apparent crystallite size, in all [*hkl*] directions, was found to increase from CF1 to CF4.

If the melting point corresponds to the most probable crystallite thickness (20), then, lamellar thickness increases with decreasing cooling severity. The same dependence is also observed for D_{hk0} crystallite size, i.e., the lateral dimensions of the lamellae. Despite the almost identical melting points of CF3 and CF4, these specimens exhibited rather different apparent crystallite size. This would indicate that the lateral dimensions of the crystallites might be more sensitive than the crystallite thickness to the crystallization conditions. This again suggests that the linear growth rate of polymers is strongly dependent on crystallization conditions (11).

The results for the surface morphologies (cf. App. B) showed that the side of the specimen, cooled briefly in air and then in water, was more rapidly crystallized than the other side in contact with the chill roll. The WAXD measurements in reflection revealed that up to a 10% difference in crystallinity may exist between the two sides of cast sheet of 1 mm in thickness. Moreover, the amounts of smectic or β crystal form also vary significantly from one side to another. In fact, the asymmetric, non-uniform cooling along the thickness produced a spherulitic morphology gradient along the film thickness for the four cast films. Different zones were obtained depending on the crystallization conditions (cf. App. B). Cotto et al. (21) also observed a morphology gradient through the film thickness, consisting of a large middle zone and two thin outer zones. However, almost symmetric morphology was achieved for the casting conditions without the water bath. All these observations are comparable to those reported by Haudin et al. (21, 22).

5.2.2 - Conclusions

The casting process was found to generate a morphology gradient along the cast film thickness. Crystallinity and the apparent crystallite size were greater on the side of the film that was cooled on the chill roll than on the side of the film that was mainly cooled in water. Decreasing the cooling severity of the casting process was found to affect greatly the initial morphology. Crystallinity, spherulite size, and the apparent crystallite size increased with decreasing cooling severity. Moreover, the presence of smectic phase and β-phase appeared to depend on the cooling conditions. Decreasing the cooling severity hindered the formation of the smectic phase and favored the formation of the β-phase.

5.3 - Effect of High Temperature Thermal Treatment on Initial Film Morphology

The effect of high temperature thermal treatment on the morphology of the cast films was studied for two cases. In the first case, the thermal treatment was applied for a long time, 120 min, in a regular hot air oven at high temperature (>100°C) below the melting point of the resin. In the second case, the thermal treatment was applied for a short time, 40 s, using the laboratory film stretcher. The sample preparation followed normal stretching experiments, but without any stretching taking place. The preheated samples were prepared in order to evaluate the part due to the effect of the thermal treatment on the final stretched film and to attempt to indirectly characterize the partly molten state encountered for the temperature range under study.

5.3.1 - Effect of Annealing on Initial Film Morphology

There are two motivations for the study of the effect of annealing on the initial cast film morphology. Firstly, it was important to determine the morphological characteristics of the initial annealed films that were to be stretched. Secondly, it was important to understand the structural arrangements occurring during annealing in the temperature range at which stretching takes place, i.e., at high temperatures below the melting point. PP2 cast film specimens were annealed for 120 min at 100°C, 120°C, 143°C, 150°C, 157°C, and 160°C.

5.3.1.1 - Results

Figure 5-6 shows the WAXD patterns of the unannealed PP2 cast film and the samples annealed for two hours at 100°C, 157C, and 160°C. All annealed specimens exhibited a WAXD pattern corresponding to the α-crystal form. With increasing the annealing temperature, the diffraction peaks became sharper and more intense, the amorphous halos decreased in area, and the difference between both sides almost vanished. The increase in diffraction peak sharpness is quite clear for the peak doublet at 21.5° and 22°. The doublet for the original morphology exhibited only one broad peak, while, for the sample annealed at 160°C, it exhibited two distinct sharp peaks.

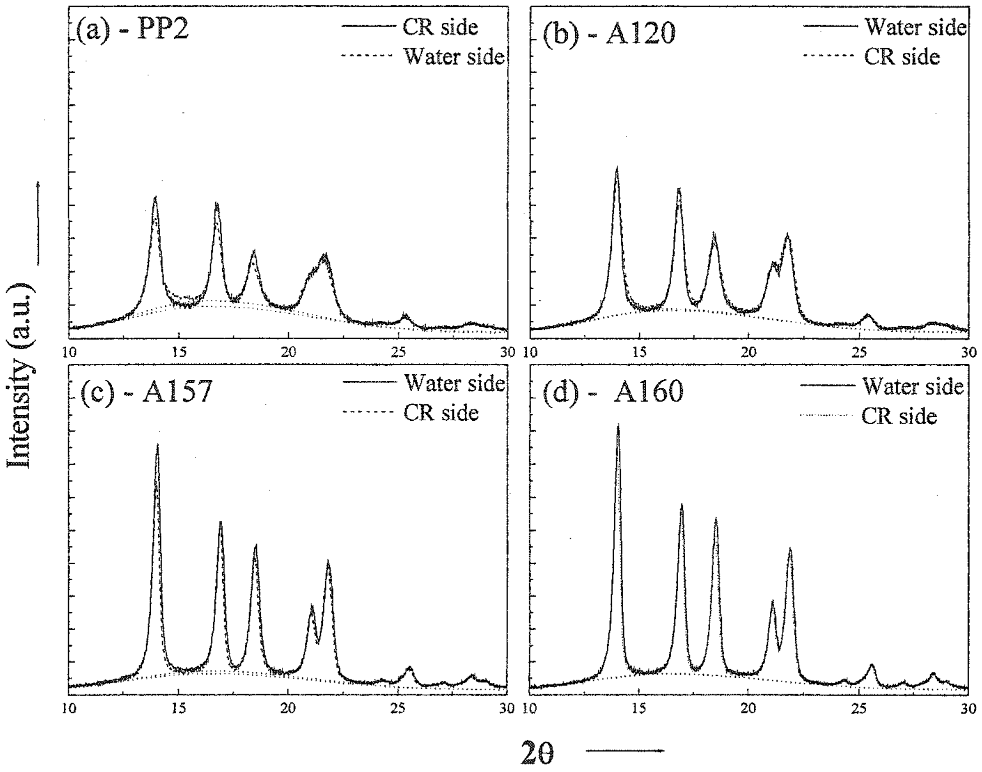

Figure 5-6 *WAXD patterns for both sides of (a) the PP2 cast film and the specimens annealed at (b) 150°C, (c) 157°C, and (d) 160°C (dotted baselines are the amorphous halos)*

The DSC melting curves of the PP2 reference cast film and the annealed specimens are plotted in Figure 5-7. The melting behavior of the annealed specimens was found to be only slightly affected by the thermal treatment for temperatures below 150°C. The melting curve of these annealed specimens overlapped the reference curve of the unannealed sample, except for a low temperature melting peak or shoulder. The A100 curve shows an extra low temperature melting peak at around 110°, and the A143 curve displayed only an extra shoulder at around 150°C. The other curves deviated significantly from the reference curve. These curves have a single melting peak, the position of which is shifted to higher temperature (cf. Table 5-3). The width (FHWM) decreased with increasing annealing temperature. The A150 curve exhibited intermediate characteristics; it has only one single narrow peak and the end of the melting curve matches the reference curve.

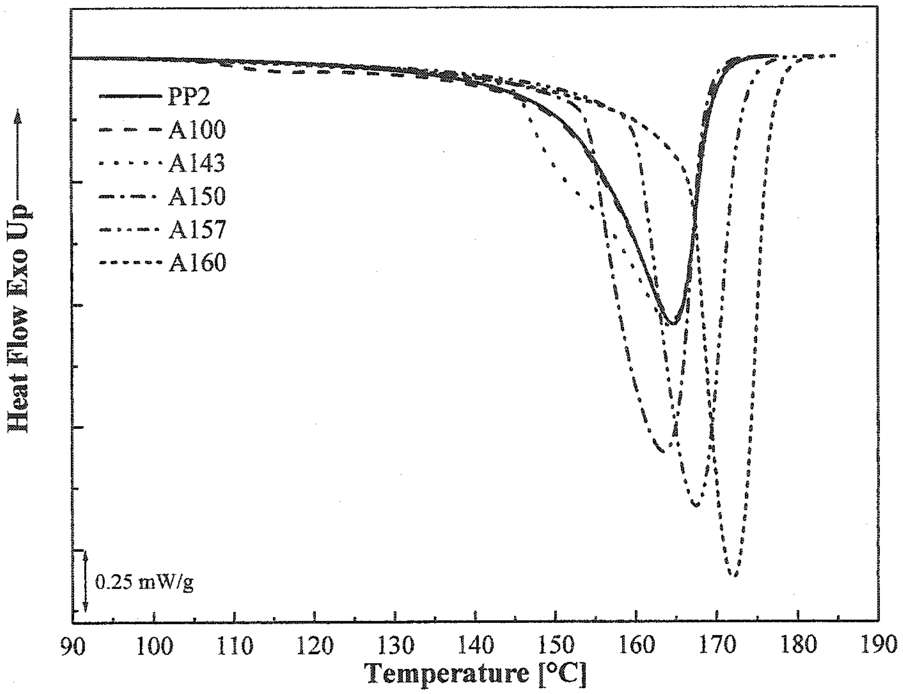

Figure 5-7 DSC melting curves of the PP2 cast film and of the annealed specimens

Polarized light microscopy revealed that, for A100, A120, and A143, the average spherulite size remained identical to that of the PP2 reference film, as shown in Table 5-3. Nevertheless, a change in the optical properties of the spherulites was observed for the A143 sample. The birefringence of the spherulites was reduced. For A157 and A160, the average spherulite size was found to have so decreased that it could not be assessed by PLM.

Table 5-3 Morphological characteristics of the cast film and annealed specimens

	WAXD			**DSC**			**PLM**
Sample	**CI_{WAXS} [%]**	**D_{110} [Å]**	**D_{040} [Å]**	**CI_{DSC} [%]**	**T_m [°C]**	**FWHM [°C]**	**Sph. size [μm]**
PP2	48.6	165	187	44.6	164.6	10.4	5
A100	56.2	174	189	48.1	164.7	11.1	5
A120	59.6	181	190	-	-	-	5
A143	65.0	208	202	52.1	164.5	15.1	5
A150	-	-	-	56.4	163.4	10.2	-
A157	70.0	250	229	56.3	167.5	8.3	<5
A160	73.5	274	246	58.7	172.1	6.6	<5

Crystallinity, as estimated by both techniques, and the apparent crystallite size were found to increase with increasing annealing temperature, as shown in Table 5-3. Furthermore, the melting point decreased slightly with increasing annealing temperature up to 163.4°C for the A150 sample and then significantly increased up to 172°C for A160. Finally, the melting peak breadth increased up to an annealing temperature of 143°C and then decreased.

The increase of the apparent lateral sizes of crystallites with increasing annealing temperature is in agreement with previously published data from Poussin et al. (23). The D_{110} and D_{040} apparent crystallite sizes were plotted versus the X-ray crystallinity for the annealed morphologies, as illustrated in Figure 5-8. There are two domains of linear dependence between the degree of crystallinity and the apparent crystallite sizes. The change in slope occurs for annealing temperature in the range 125-135°C. Above this range, the slope becomes significantly higher. Below 120°C, the crystallite size increased slowly with crystallinity. The increased enlargement of crystallites in the [110] direction above 135°C causes the crystallites to form faster in the a^* direction than in the b direction. The a^* axis is known to be the growth direction of iPP crystallization.

5.3.1.2 - Discussion

The effects of annealing temperature and time on morphology of iPP were investigated extensively by several authors (18, 19, 23-28). The main result is that annealing induces an increase in the size and perfection of the crystalline regions. At long times, the level of crystallinity and crystal perfection reaches a maximum value that depends on the treatment temperature. Several authors reported that there exist a transition temperature, above which the structural rearrangements become faster (28-30). Maiti el al. (30) reported that, for a highly isotactic polypropylene, the lamellar thickening rate was faster above a transition temperature of 157°C. Vittoria (28) concluded that accelerated growth in crystal dimensions and perfection occur for annealing temperatures above 150°C. The values of the transition temperature reported in the literature are in the range between 145°C and 160°C. This differences may be attributed to the differences in the tacticity and molecular structure of the investigated resins.

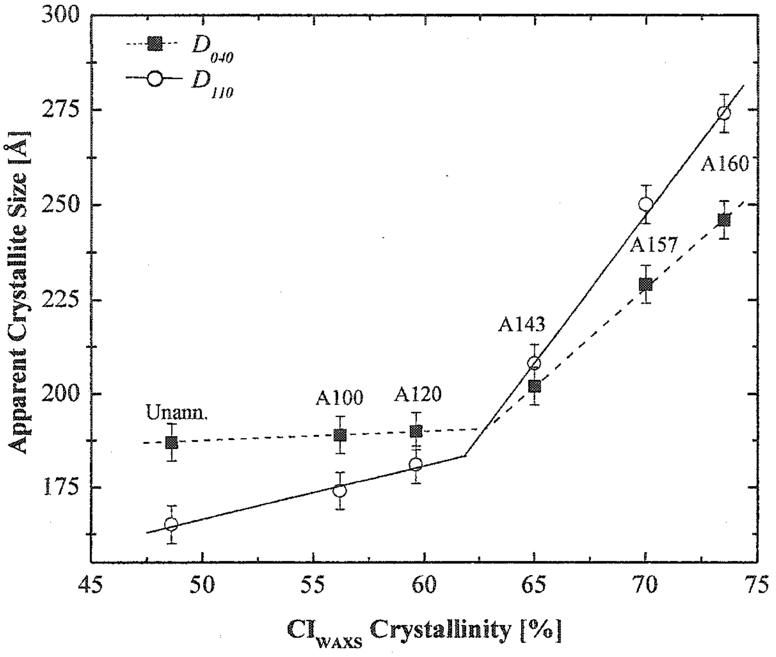

Figure 5-8 *Apparent crystallite sizes as function of X-ray crystallinity for the series of annealed samples*

In the present work, the transition temperature for PP2 occurs in the 130°C - 150°C range. The temperature range is expected to be different for other polypropylene resins, depending on isotacticity content. These regions should be defined with respect to the equilibrium melting point of the raw material. For practical reasons, these regions were defined with respect to the DSC melting point of the resin.

Low Temperature Annealing ($T < T_m - 35$)

The low temperature melting peak observed for morphologies annealed below the transition temperature has been reported in other studies (18, 19, 23). This peak was attributed to either a group of lamellae that was perfected and thickened (26) or to thinner lamellae grown between the primary ones during the thermal treatment (31). The former is associated with annealing below 100°C –120°C, and the latter occurs at higher temperatures (25). It has been also found that the melting peak position depends on the treatment temperature, while the peak area depends on annealing time (18, 19, 23). In this work, the newly-formed structure was observed to melt in a temperature range slightly higher than the treatment temperature (around 12°C higher), except for the A150 sample, in which the melting peak attributed to the annealed morphology merged with the melting peak due to the remaining stable lamellae.

Therefore, in the low annealing temperature region, the arrangement of the initial structure occurs by thickening of the already existing lamellae at the expense of the amorphous phase and/or by formation of thinner lamellae growing between/on the primary ones. This leads to a decrease in entanglement and tie molecule densities (29). Moreover, the number of lamellae being perfected and thickened depends strongly on temperature (and time). However, the average spherulite size remains constant.

High Temperature Annealing ($T > T_m - 15$)

A large change in melting behavior and spherulite size of the annealed morphology was observed for annealing temperature above 150°C. The shift to higher temperature and the reduction in breadth of the melting peak indicate that important structural rearrangements occur during annealing above 150°C. Partial melting, during annealing at high temperature, could contribute to such morphological changes. The disappearance of the original spherulitic morphology supports this concept of partial melting. Fillon et al. (10) reported that annealing very close to the melting point (also referred to as partial melting) had a strong nucleating effect. This is in agreement with the observed sudden decrease in spherulite size through annealing above 150°C.

Therefore, it was concluded that partial melting occurs in the high temperature region. The most stable crystalline entities will be perfected and thickened during annealing and a new lamellar morphology will crystallize upon cooling to room temperature. This phase will be referred to as the unmolten crystalline phase. The high nucleating power of the highly ordered (structured) melt and the high mobility of molecules causes crystallization to occur rapidly and generate smaller spherulites (10). The apparent crystallite size and crystallite thickness are strongly dependent on temperature, in this annealing region. According to our results and literature data, it also seems that the degree of lamellar branching is reduced with increasing annealing temperature, as discussed below.

Annealing in the Transition Region ($T_m - 35 < T < T_m - 15$)

A mix of the above two mechanisms occurs in the transition temperature range, between 130°C and 150°C. However, the most predominant effect in this temperature range will be the increase in perfection of the crystallites (larger crystallites). The faster increase in D_{110} than in D_{040} may be attributed to the preferential recrystallization of the partly molten structure along the radial growth axis (a^* direction). Consequently, the degree of lamellar branching, which occurs by homoepitaxy on the (010) crystal plane, was assumed to be reduced.

5.3.2 - Effect of Preheating on Initial Film Morphology

In a stretching experiment, the initial cast film is heated to the desired drawing temperature before stretching. Structural rearrangements occur during thermal treatment close to the melting point. The cast film specimens were preheated in the laboratory film stretcher, as described in Chapter 4. The effect of preheating time on deformation behavior was investigated to optimize stretching conditions, as reported in Rettenberger's work (32). He found that a preheating time of 40 s was optimal for the sample to reach the desired temperature and to minimize the drawing stresses. Since the preheating time was always kept constant in this work, its effect is not considered any further in the present discussion. The effect of preheating on the initial morphology of the cast films was studied for two cases: the effect of the preheating temperature on the same initial morphology and the effect of the same preheating temperature on different initial morphologies.

The sample notation for preheated samples is as follows: PPX – PY, where X denotes the cast film and Y the temperature of preheating.

5.3.2.1 - Effect of Preheating Temperature on Initial Film Morphology

The effect of preheating temperature on the initial film morphology is presented for the PP2 cast film. The DSC melting curve of the PP2 cast film is presented in Figure 5-9, together with those of the PP2 samples preheated for 40 seconds at 150°C and 160°C. It can be seen that the melting curves of the preheated samples are very similar in shape and position to the corresponding samples annealed at the same temperature. Only the areas of the peaks differ. The similarity between annealed and preheated samples was also found for the WAXD patterns (results not shown). For the latter, only differences in diffraction peak width and intensity were observed. The analysis of the WAXD patterns and DSC curves confirmed this similarity. The degree of crystallinity and the crystallite sizes were observed to increase with increasing preheating temperature, as shown in Table 5-4. As previously seen, there seems to be a transition temperature, above which the melting point rises significantly and the original spherulitic morphology disappears due to preheating.

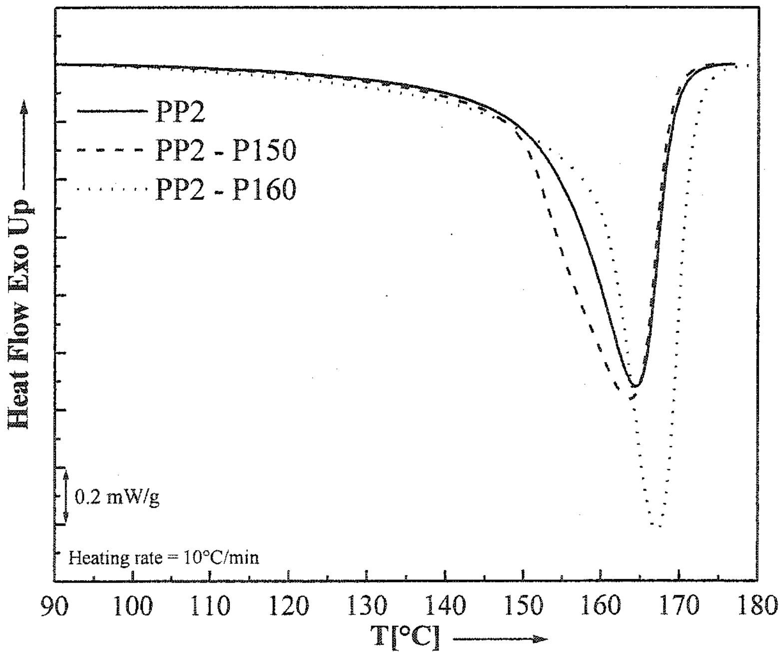

Figure 5-9 *DSC melting curves of the PP2 cast film and the PP2-P150, and PP2-P160 preheated samples*

Table 5-4 Morphological characteristics of the PP2 cast film and preheated samples

	WAXD			**DSC**			**PLM**
Sample	**CI_{WAXS} [%]**	**D_{110} [Å]**	**D_{040} [Å]**	**CI_{DSC} [%]**	**T_m [°C]**	**FWHM [°C]**	**Sph. size [μm]**
PP2	48.6	165	187	44.6	164.6	10.4	5
P145	63.7	201	199	-	-	-	5
P150	64.4	211	204	52.1	163.6	13.6	5
P155	66.6	240	223	55.3	164.1	8.9	<5
P160	65.6	255	233	57.3	167.2	7.7	<5

The results for the melting point and the melting peak width are shown in Table 5-4. They confirm that a partial melting occurs for preheating temperatures above 150°C. As indicated earlier, this temperature depends on the tacticity of the cast film. The amounts of the different phases constituting the partly molten state, i.e., the unmolten crystalline phase (UC), the structured melt (SM) and the amorphous melt (AM), were estimated from the DSC melting curves for the PP1, PP2, and PP3 cast films. These quantities were estimated for preheating at 150°C and at 160°C, as explained in Chapter 4. The partly molten morphology depends on the temperature difference (supercooling) $\Delta T = T_m^0 - T$, where T_m^0 is the equilibrium melting temperature and T is the thermal treatment temperature. T_m^0 is a material property, which depends on molecular structure and particularly on tacticity (3). Since T_m^0 values were not available, the melting temperatures from the DSC analysis of the resins were used as an approximation. The amounts of unmolten crystallinity and structured melt were estimated for the same degree of supercooling at $\Delta T = 10°C$. The values are listed in Table 5-5.

The results show that the initial morphology of the PP2 cast film was significantly molten (> 8%) at 150°C. For the same drawing temperature, the amount of unmolten crystallinity increases, while the amount of structured melt decreases, with increasing chain tacticity. It also indicates that the temperature, at which partial melting becomes important is shifted to higher temperatures with increasing tacticity. This is also suggested by the onset of melting, as indicated by the DSC curves. At the same degree of supercooling, ΔT, the amount of structured melt is identical for all three resins. However, there is still a difference in unmolten crystallinity, due to the difference in initial crystallinity, as shown in Table 5-5. Thus, it appears that the chain tacticity is the dominant parameter controlling the morphology of the partly molten film at the end of the preheating.

Table 5-5 Room temperature crystallinity (CI) and the amounts of unmolten crystallinity (UC) and structured melt (SM) at 150°C, 160°C, and ΔT = 10°C for the PP1, PP2, and PP3 cast films

Cast Film	**Isotact. [%]**	**CI_{DSC} [%]**	**UC_{150} [%]**	**SM_{150} [%]**	**UC_{160} [%]**	**SM_{160} [%]**	**$UC_{(\Delta T=10)}$ [%]**	**$SM_{(\Delta T=10)}$ [%]**
PP1	95.0	40	27	13	9	32	27	13
PP2	98.6	44	36	8	23	21	32	12
PP3	99.6	50	43	7	33	17	37	13

5.3.2.2 - Effect of Preheating on The CF1 – CF4 Cast Films

Figure 5-10 shows the average WAXD patterns of the original cast film samples (CF1 – CF4), which were melt crystallized under different cooling conditions (cf. section 5.2), and of those that were preheated at 150°C for 40 s. The comparison of the diffraction patterns confirms again that the preheated samples exhibit a greater crystallinity and perfection of the crystalline regions than in the initial morphology. Additionally, the smectic and β-phase content decreases considerably after preheating, whereas crystallinity and the apparent crystallite size increase. However, the differences in crystallinity of the various cast films observed before preheating almost vanished after the thermal treatment. A difference in crystallinity of less than 2% was found between the four samples. The same observation may be made regarding the apparent crystallite size.

One important result is the total disappearance of the smectic phase in PP4-CF1 after a short thermal treatment at 150°C. This was expected since the smectic phase is known to transform into the α-phase above 70°C (33).

Table 5-6 shows that the maximum differences in the amounts of unmolten crystallinity and structured melt at 150°C are 2% and 3%, respectively. The PP4-CF1 sample presents the most extreme values at 150°C, while the other cast films exhibit similar values. This indicates that the amount of unmolten crystallinity and structured melt present in the film before the stretching is very similar for the four cast films.

However, there remain differences in the size and perfection of the crystallites, their interconnection, i.e. the tie molecule fraction, and entanglements in the amorphous phase.

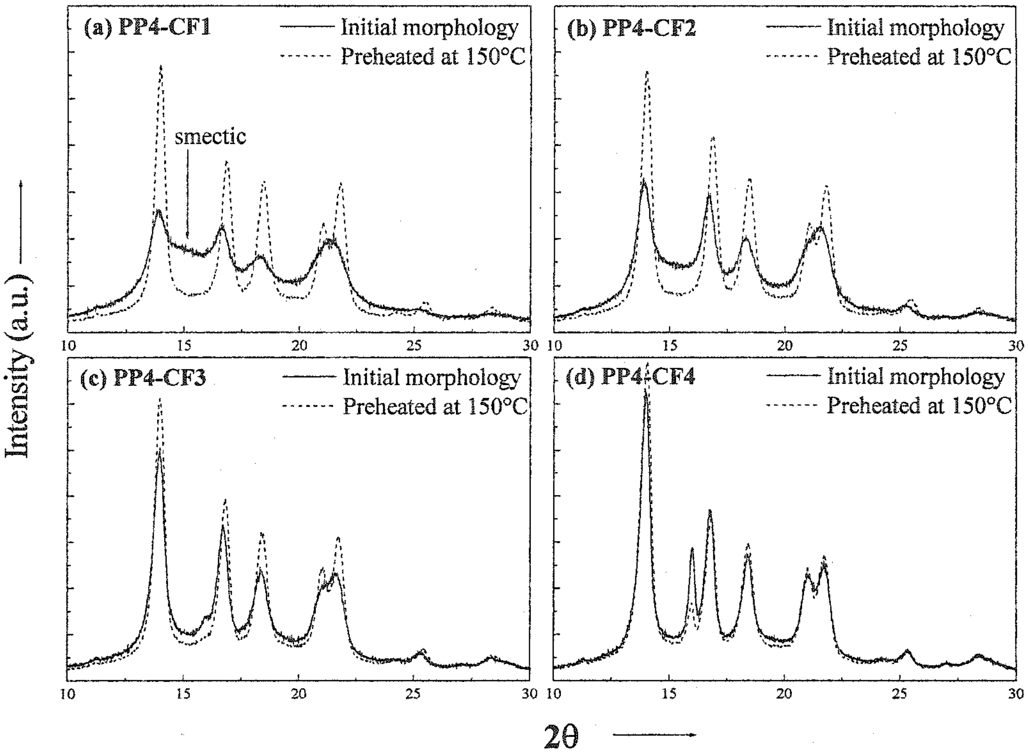

Figure 5-10 *Comparison of the average WAXD patterns between the initial and preheated morphology for the CF1, CF2, CF3, and CF4 cast films*

Table 5-6 *Room temperature crystallinity (CI) and the amounts in unmolten crystalline phase (UC) and structured melt (SM) at 150°C and 160°C for the four CF1-CF4 cast films*

Cast Film	CI_{DSC} [%]	UC_{150} [%]	SM_{150} [%]	UC_{160} [%]	SM_{160} [%]
PP4-CF1	38.8	32	7	19	20
PP4-CF2	42.3	34	8	22	21
PP4-CF3	42.0	34	8	23	19
PP4-CF4	44.1	34	10	22	22

5.4 - Summary

The study of the effects of chain tacticity, casting conditions, preheating, and annealing on the initial morphology led to the following conclusions:

- Chain tacticity affects crystallinity and the spherulitic and lamellar structures of the initial cast film morphology. The degree of crystallinity, as well as the lamellar crystal dimensions, increased with increasing isotacticity. Spherulites seemed to decrease in size with increasing chain isotacticity. The major effect of chain stereoregularity was to shift the thermal stability of the initial film morphology to higher temperature with increasing isotacticity.

- Decreasing the cooling severity of the casting increased the degree of crystallinity, the spherulite size, and the apparent crystallite size of the initial cast film morphology. Moreover, decreasing the cooling severity hindered the formation of the smectic phase and favored the formation of the β-phase.

- There exist two temperature domains in which the dominant structural rearrangements occurring during annealing are dissimilar: below 130°C ($\Delta T > 35°C$), and above 150°C ($\Delta T < 15°C$). Far from the melting point, for $\Delta T > 35°C$, the perfection of the structure occurs by lamellar thickening and/or by formation of additional thinner lamellae. Near the melting point, $\Delta T < 15°C$, partial melting occurs. In the transition region, $15°C < \Delta T < 35°C$, both structural rearrangements compete and the increase in crystallite size and perfection is important due to the increase in molecular mobility of the smallest, unperfected crystallites.

- The effects of preheating on the initial morphology of the cast film were found to be similar in nature to annealing effects, but different in intensity. The most important effect of the preheating is on the state of the morphology at the end of the preheating, and before the stretching, i.e., the partly molten state. It was shown that the initial morphology of the cast films was significantly molten at temperatures close to the melting point (> 12% for $\Delta T = 10°C$). The amounts of unmolten crystallinity, structured melt, and amorphous melt were found to be primarily dependent on the degree of supercooling, ΔT. Thus, isotacticity influences greatly the morphology of the partly molten state, when compared at the same temperature.

[Refs. on p. 107]

References

1 - J. C. Wittmann and B. Lotz, "Epitaxial crystallization of polyethylene on organic substrates: A reppraisal of the mode of action of selected nucleating agents", J. Polym. Sci. Polym. Phys Ed., 19, 1837-1851 (1981).

2 - A. Thierry, C. Straupé, B. Lotz and J. C. Wittmann, "Physical gelation: a path towards ´ideal´ dispersion of additives in polymers", Polymer Communications, 31, 299-301 (1990).

3 - R. Paukkeri and A. Lehtinen, "Thermal behavior of polypropylene fractions: 1. Influence of tacticity and molecular weight on crystallization and melting behavior", Polymer, 34, 4075-4082 (1993).

4 - S. Z. D. Cheng, J. J. Janimak, A.-Q. Zhang and E. T. Hsieh, "Isotacticity effect on crystallization and melting in polypropylene fractions: 1. Crystalline structures and thermodynamic property changes", Polymer, 32, 648-655 (1991).

5 - J. J. Janimak, S. Z. D. Cheng, P. A. Giusti and E. T. Hsieh, "Isotacticity effect on crystallization and melting in polypropylene fractions. 2. Linear crystal growth rate and morphology study", Macromolecules, 24, p2253-2260 (1991).

6 - J. J. Janimak, S. Z. D. Cheng, A. Zhang and E. T. Hsieh, "Isotacticity effect on crystallization and melting in polypropylene fractions: 3. Overall crystallization and melting behavior", Polymer, 33, p728-735 (1992).

7 - K. Yamada, S. Matsumoto, K. Tagashira and M. Hikosaka, "Isotacticity dependence of spherulitic morphology of isotactic polypropylene", Polymer, 39, 5327-5333 (1998).

8 - M. Gahleitner, K. Bernreitner and W. Neissl, "Influence of molecular structure on crystallization behaviour and mechanical properties of polypropylene", Polymer Testing, 14, 173-187 (1995).

9 - C. Duplay, B. Monasse, J.-M. Haudin and J.-L. Costa, "Shear-induced crystallization of polypropylene: influence of molecular structure", J. Mat. Sci., 35, 6093-6103 (2000).

10 - B. Fillon, J. C. Wittmann, B. Lotz and A. Thierry, "Self-nucleation and recrystallization of isotactic polypropylene (apha Phase) investigated by DSC", J. Polym. Sci.: Polym Phys., 31, 1383-1393 (1993).

11 - J. D. Hoffman, G. T. Davis and J. J. Lauritzen, in Treatise on Solid State Chemistry, N. B. Hannay, Editor. Plenum Press: New York (1976).

12 - D. M. Gezovich and P. H. Geil, "Morphology of quenched polypropylene", Polym. Eng. Sci., 8, 202-209 (1968).

13 - J. A. Gailey and R. H. Ralston, "The quenched state of polypropylene", SPE Trans., 4, 2933 (1964).

14 - V. Caldas, R. S. Nohr, J. G. MacDonald, L. E. Raboin and G. R. Brown, "The structure of the mesomorphic phase of quenched isotactic polypropylene", Polymer, 35, p899-907 (1994).

15 - P. Corradini, V. Petraccone, C. D. Rosa and G. Guerra, "On the structure of the quenched mesomorphic phase of isotactic polyprpylene", Macromolecules, 19, 2699-2703 (1986).

16 - J. Varga, "Review: Supermolecular structure of isotactic polypropylene", J. Mat. Sci., 27, 2557-2579 (1992).

17 - D. R. Norton and A. Keller, "The spherulitic and lamellar morphology of melt-crystallized isotactic polypropylene", Polymer, 26, 704-716 (1985).

18 - N. Alberola, M. Fuguier, D. Petit and B. Fillon, "Microstructure of quenched and annealed films of isotactic polypropylene", J. Mat. Sci., 30, 1187-1195 (1995).

19 - W. J. O'Kane, R. J. Young and A. J. Ryan, "The effect of annealing on the structure and properties of isotactic polypropylene films", J. Macromol. Sci.-Phys., B34, 427-458 (1995).

20 - R. Hingmann, J. Rieger and M. Kersting, "Rheological Properties of a Partially Molten Polypropylene Random Copolymer during Annealing", Macromolecules, 28, 3801 - 3806 (1995).

21 - D. Cotto, P. Duffo and J. M. Haudin, "Cast Film Extrusion of Polypropylene Films", Intern Polymer Processing, 4, 103 - 113 (1989).

[Refs. on p. 107]

22 - P. Duffo, B. Monasse and J. M. Haudin, "Influence of Stretching and Cooling Conditions in Cast Film Extrusion of PP Films", Intern. Polymer Processing, 5, 272 - 283 (1990).

23 - L. Poussin, Y. A. BErtin, J. Parisot and C. Brassy, "Influence of thermal treatment on the structure of an isotactic polypropylene", Polymer, 39, pp4261-4265 (1998).

24 - D. T. Grubb and D. Y. Yoon, "Morphology of quenched and annealed isotactic polypropylene", Polym. Comm., 27, 84-88 (1986).

25 - A. Martorana, S. Piccarolo and D. Sapoundjieva, "SAXS/WAXS study of the annealing process in quenched samples of istactic poly(propylene)", Macromol. Chem. Phys., 200, 531-540 (1999).

26 - K. D. Pae and J. A. Sauer, "Effects of thermal history on isotactic polypropylene", J. Appl. Polym. Sci., 12, 1901-1919 (1968).

27 - V. Vittoria, "Effect of annealing on the structure of quenched isotactic polypropylene", J. Macromol. Sci.-Phys., B28, 489-502 (1989).

28 - V. Vittoria, "Crystallinity of isotactic polypropylene films annealed from the quenched state", J. Mat. Sci., 27, 4350-4354 (1992).

29 - K. Yamada, M. Kamezawa and M. Takayanagi, "Relationship between orientation of amorphous chains and modulus in highly oriented polypropylene", J. Appl. Polym. Sci., 26, 49-60 (1981).

30 - P. Maiti, M. Hikosaka, K. Yamada, A. Toda and F. Gu, "Lamellar thicknening in isotactic polypropylene with high tacticity crystallized at high temperature", Macromolecules, 22, 9069-9075 (2000).

31 - B. Wunderlich, Crystal nucleation, growth, annealing, Academic Press, New York, (1976).

32 - S. Rettenberger, "Uni- und Biaxiales Verstrecken von isotaktischem Polypropylen im teilaufgeschmolzenen Zustand", PhD thesis, University Erlangen-Nuremberg, (2002).

33 - R. Zannetti, G. Celoti, A. Fichera and R. Francesconi, "The structural effects of annealing time and temperature on the paracrystal-crystal transition in isotactic polypropylene", Makrom. Chem., 128, 137-142 (1969).

[Refs. on p. 107]

CHAPTER 6

SIMULTANEOUS BIAXIAL DEFORMATION BEHAVIOR OF POLYPROPYLENE FILMS

This chapter presents and discusses the simultaneous equibiaxial deformation behavior of polypropylene films at a macroscopic level in terms of necking, film thickness profile, and stress-strain curves. The effects of stretching temperature, strain rate, and of the initial morphology on biaxial deformation behavior are discussed. An effort is made to find correlations between deformation behavior, on one hand, and the morphological characteristics of the initial film and the stereoregularity of the resin, on the other hand.

6.1 - Homogeneity of the Simultaneous Biaxial Deformation

6.1.1 - General Definition of Homogeneous Deformation

An important and common property of semicrystalline polymers is the occurrence of necking during cold drawing. Necking, the reduction in the cross section of the specimen caused by uniaxial deformation, is usually associated with the presence of a drop in nominal stress in the stress-strain curves. However, there is a common misconception that the drop in nominal stress must necessarily be due to necking (cf. 2.4.1). At high temperatures, and sufficiently high strain rates, the strain in PET film drawing was reported to be essentially uniform, even though the nominal stress was initially falling after the yield point (1).

6.1.2 - Homogeneity of the Equibiaxial Deformation

In order to determine whether the simultaneous equibiaxial deformation proceeds homogeneously or not, photographs of samples stretched after yield were taken under unpolarized and cross polarized white light, as illustrated in Figure 6-1. Under unpolarized white light, photographs gave information about the localization of the highly stretched regions. The gray level is proportional to the degree of stretching; the brighter the region is, the less stretched it is. Under cross polarized light, photographs gave complementary information about the stress distribution in the form of a fringe pattern, as explained in Chapter 4. The comparison of both types of photographs allowed the evaluation of the homogeneity of the equibiaxial deformation.

The deformation behavior for the equibiaxial stretching was compared for two extreme cases: (i) low and (ii) high drawing temperatures and rates, as shown in Figure 6-1. The PP2 cast film was stretched up to the same draw ratio of 2.0 x 2.0 under the (i) and (ii) stretching conditions. Figure 6-1(a) and (b) illustrate the photographs taken under unpolarized white light, identifying the stretched regions. Figure 6-1(c) and (d) show the photographs taken under cross polarized light, giving information about the principal stress distribution and its symmetry in the stretched regions.

Figure 6-1(a) shows the photograph of a poor biaxially stretched sample. Various regions can be identified: whole unstretched regions (the bright regions), numerous local necks (the sharp transition from the bright to dark regions) and stretched regions (the dark regions). Figure 6-1(c) shows the fringe pattern of the same sample as in (a). It shows that, in the stretched regions, the fringes are closely spaced and exhibit complex patterns. The black areas with a white arrow, in Figure 6-1(c) indicate regions where the principal stresses are parallel to one polarization axis (arrow direction). Comparison of both photographs shows that the necking regions correspond to regions in the fringe patterns where the fringes are closely spaced. In the central area of the film, the necking regions have no symmetry. This sample, therefore, undergoes an inhomogeneous, simultaneous, equibiaxial deformation.

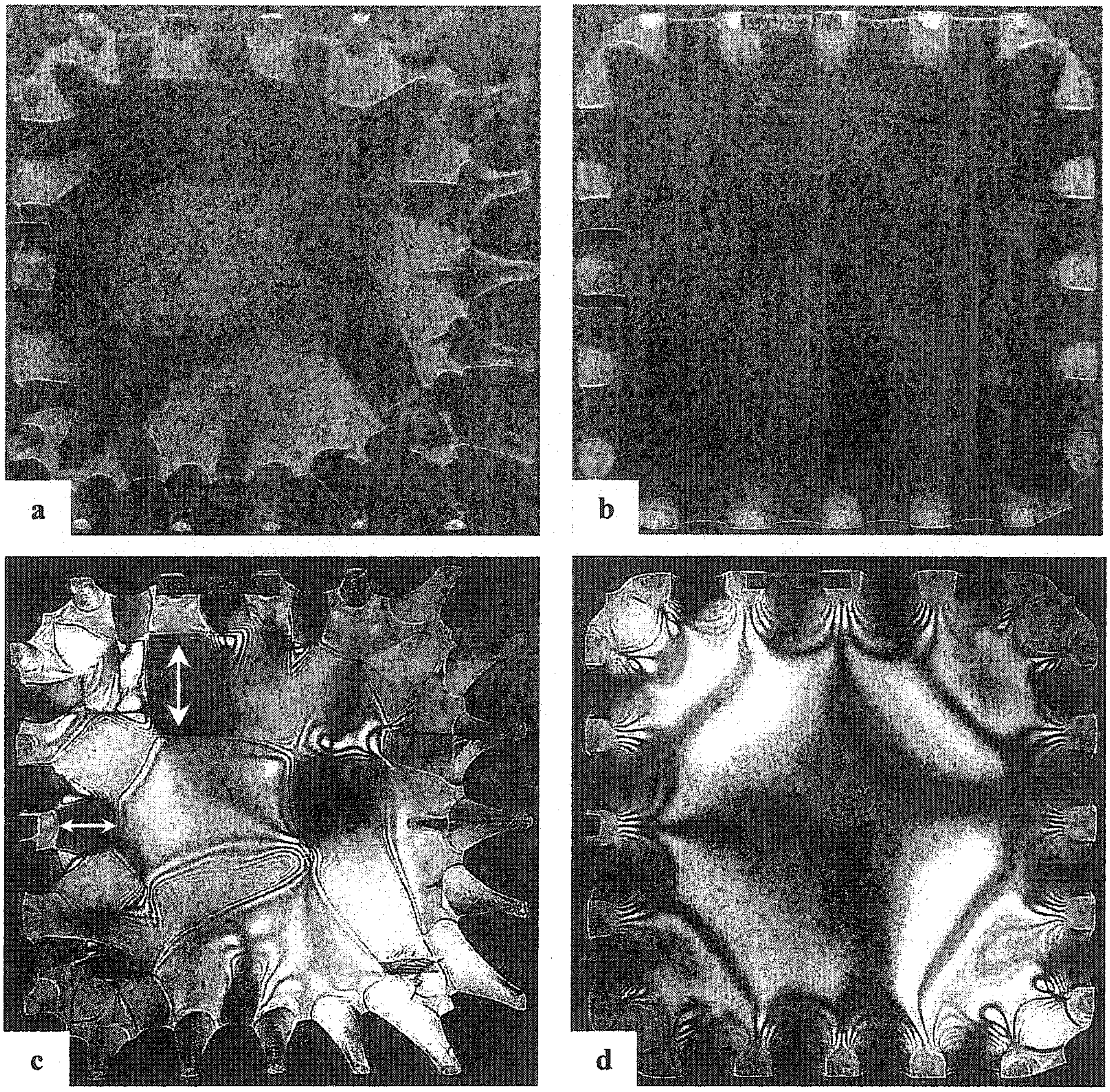

Figure 6-1 *Photographs of samples (a)&(b) and of the corresponding fringe patterns (c)&(d) of films simultaneously equibiaxially stretched up to a 2.0 x 2.0 ratio. (a)&(c)* T_s= *150°C and* $\dot{\varepsilon}_H = 0.01\ s^{-1}$; *(b)&(d)* T_s= *155°C and* $\dot{\varepsilon}_H = 1\ s^{-1}$. *(arrows in (c) indicate the local principal stress direction. Upper-left and lower-right corner high brightness is due to the light source)*

In contrast, Figure 6-1(b) shows a sample where appropriate stretching conditions were employed. The unstretched regions were only found uniformly positioned around the clips and in the corners. Moreover, the fringe pattern exhibits an almost perfect fourfold symmetry, as shown in Figure 6-1(d). The symmetrical dark region in form of a cross in the central part of the drawn film refers to a region in which the principal stress difference was zero. This is supported by the observation of a similar black cross pattern when the sample was rotated by 45°. The regions of closely spaced fringes, correlated with necking regions, could be observed only between the clips and in the corners. Figure 6-1(b) and (d) illustrate the case for which the film sample undergoes a uniform simultaneous equibiaxial deformation. The stress-strain curves of this stretching experiment still exhibited a weak yield stress, as will be shown later (in Figure 6-5; T = 155°C). This supports the observation that homogeneous deformation can occur along with a drop in nominal stress after yield (1).

Throughout this work, the homogeneity of the equibiaxial deformation will be confirmed by the character of the yield region in the stress-strain curve and the symmetry of the fringe pattern.

6.1.3 - Evolution of the Macroscopic Biaxial Deformation

Drawing experiments were carried out at 155°C and with Hencky rates of 0.01 s^{-1} and 1 s^{-1}. They were stopped at various draw ratios between the yield point and the onset of stress hardening. The fringe patterns of the stretched films are presented in Figure 6-2 andFigure 6-3. The effect of strain rate on biaxial deformation is considered later (cf. in 6.2.2). The extension rates were chosen because they represented two extreme deformation conditions.

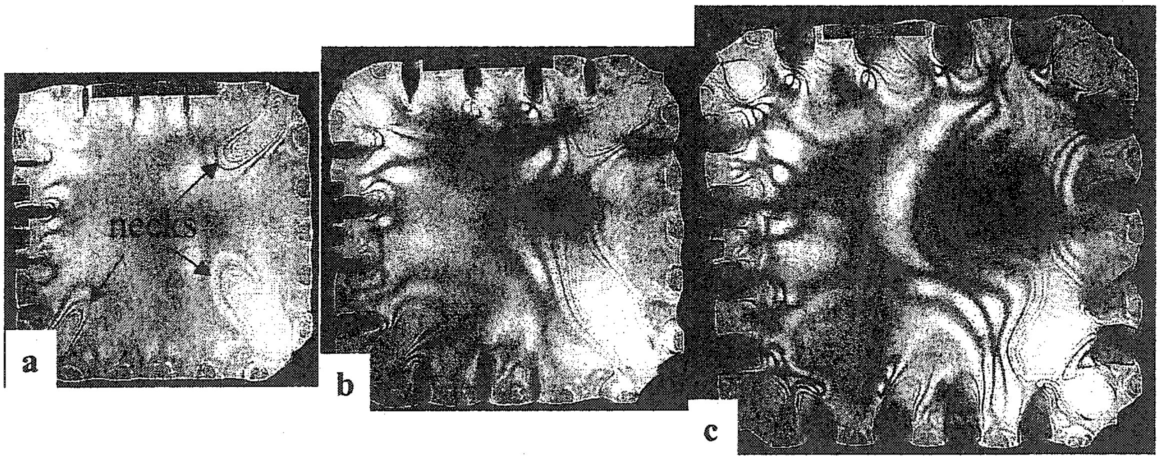

Figure 6-2 *Fringe patterns of PP2 samples equibiaxially stretched at 155°C with a* $\dot{\varepsilon}_H$ *of 0.01* s^{-1} *(a) 1.3 x 1.3; (b) 1.5 x 1.5; and (c) 2.0 x 2.0.*

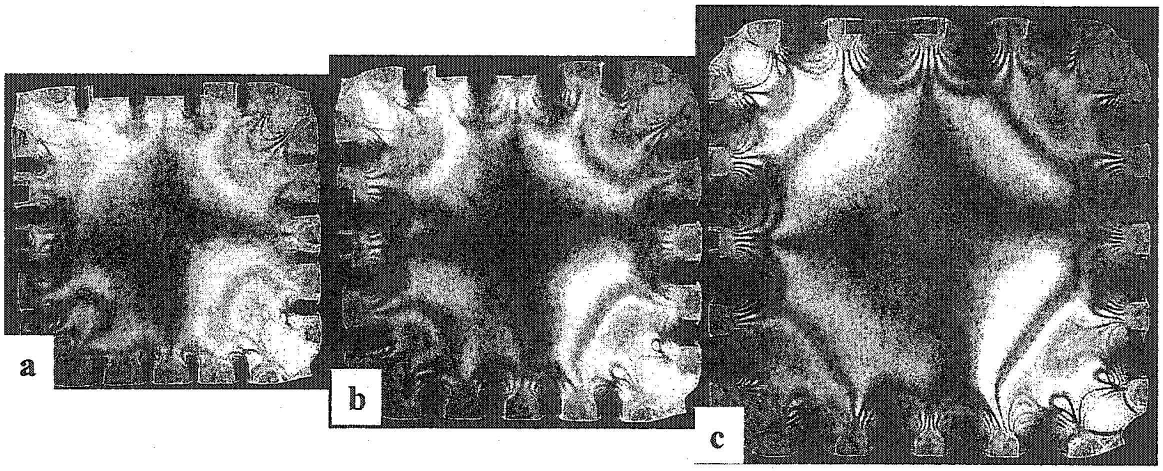

Figure 6-3 *Fringe patterns of PP2 samples equibiaxially stretched at 155°C with a $\dot{\varepsilon}_H$ of $1s^{-1}$ (a) 1.3 x 1.3; (b) 1.5 x 1.5; and (c) 2.0 x 2.0.*

Figure 6-2 illustrates the equibiaxial deformation behavior for the case of a poorly biaxial stretching experiment, whereas Figure 6-3 illustrates the case for which deformation was homogeneous. In Figure 6-2 (a), it can be seen that there are three localized regions, in which fringes are closely spaced, indicating that necking took place predominantly in the corners. The necking regions expanded and even merged on further stretching, resulting in the unsymmetrical fringe pattern observed in Figure 6-2 (c).

In contrast, Figure 6-3 illustrates that, at a draw ratio of 1.3 x 1.3, the closely spaced fringes, thus the main necking regions, were located in the outer parts: in the corners and around the clips. Nevertheless, a symmetrical extinction region and distantly spaced fringes were observed in the main, central part of the specimen. With further drawing, the fringe pattern preserved its form with localized necking in the outer parts and an enlarged, symmetrical extinction area in the middle. The fringe pattern resulting from the macroscopic biaxial deformation just after yield was preserved, at least up to a stretching ratio of 2.0 x 2.0.

To complete the information on the homogeneity of the biaxial deformation at 155°C, the evolution of the true, local draw ratios and the film thickness with increasing nominal draw ratio were evaluated for ratios above 2.0 x 2.0 (cf. Table 6-1). The MD and TD mean average true draw ratios, λ_{MD36} and λ_{TD36} , were found identical and only slightly greater than the nominal draw ratios. The local values corresponding only to the central part of the film, λ_{MD4} and λ_{TD4} , were found greater than the nominal ratios. Increasing the draw ratio reduced the film thickness standard deviation, which was more obvious for t_{36}. Furthermore, the difference between t_4 and t_{36}. decreased and almost vanished with raising the draw ratio.

λ_{MD} x λ_{TD}	λ_{MD36}	λ_{MD4}	λ_{TD36}	λ_{TD4}	t_{36} [μm]	t_{16} [μm]	t_4 [μm]
2.0 x 2.0	**2.1 ± 0.2**	**2.3 ± 0.1**	**2.1 ± 0.2**	**2.2 ± 0.1**	**238 ± 31**	**207 ± 4**	**204 ± 4**
3.0 x 3.0	**3.2 ± 0.2**	**3.5 ± 0.1**	**3.2 ± 0.2**	**3.3 ± 0.1**	**101 ± 11**	**90 ± 2**	**90 ± 2**
4.0 x 4.0	**4.3 ± 0.2**	**4.5 ± 0.1**	**4.2 ± 0.2**	**4.3 ± 0.1**	**58 ± 4**	**55 ± 1**	**54 ± 1**
4.9 x 4.9	**5.1 ± 0.2**	**5.2 ± 0.1**	**5.1 ± 0.2**	**5.2 ± 0.1**	**41 ± 2**	**39 ± 1**	**39 ± 1**
6.0 x 6.0	**6.1 ± 0.1**	**6.2 ± 0.1**	**6.1 ± 0.1**	**6.3 ± 0.1**	**28 ± 1**	**27 ± 1**	**27 ± 1**

Table 6-1 *Effect of the nominal draw ratio on the local true draw ratio and film thickness for PP2 samples simultaneously equibiaxially stretched at 155°C with a Hencky strain rate of 1* s^{-1}

6.1.4 - Discussion

In a poorly stretched specimen, as shown in Figure 6-1 (a), biaxial drawing proceeded mainly by localized necking. It is believed that, in the necking zones, deformation is mainly uniaxial, as confirmed by the stress orientation in zone (C) in Figure 6-1 (a). This observation is in agreement with the conclusion of Olley and Bassett (2). For other stretching conditions, as illustrated in Figure 6-3, it is believed that, while localized uniaxial deformation still occurred around the clips, the main deformation in the central part of the film was homogeneous and biaxial. This conclusion is supported by the measured local true draw ratios that revealed effectively identical MD and TD local draw ratios, with higher drawing near the center of the film.

6.2 - Effect of Stretching Conditions on Biaxial Deformation Behavior

In this section, the effects of stretching temperature and deformation rate, on the macroscopic biaxial deformation and the resulting film profile are discussed for standard stretching conditions. The effects of the other processing variables, such as strain rate profile, deformation type, and preheating time, on the biaxial deformation behavior of isotactic polypropylene can be found in the thesis of Rettenberger (3).

6.2.1 - Effect of Drawing Temperature on Biaxial Deformation Behavior

Figure 6-4 shows four fringe patterns of samples that were stretched up to 1.5 x 1.5 under the same conditions, but at different temperatures.

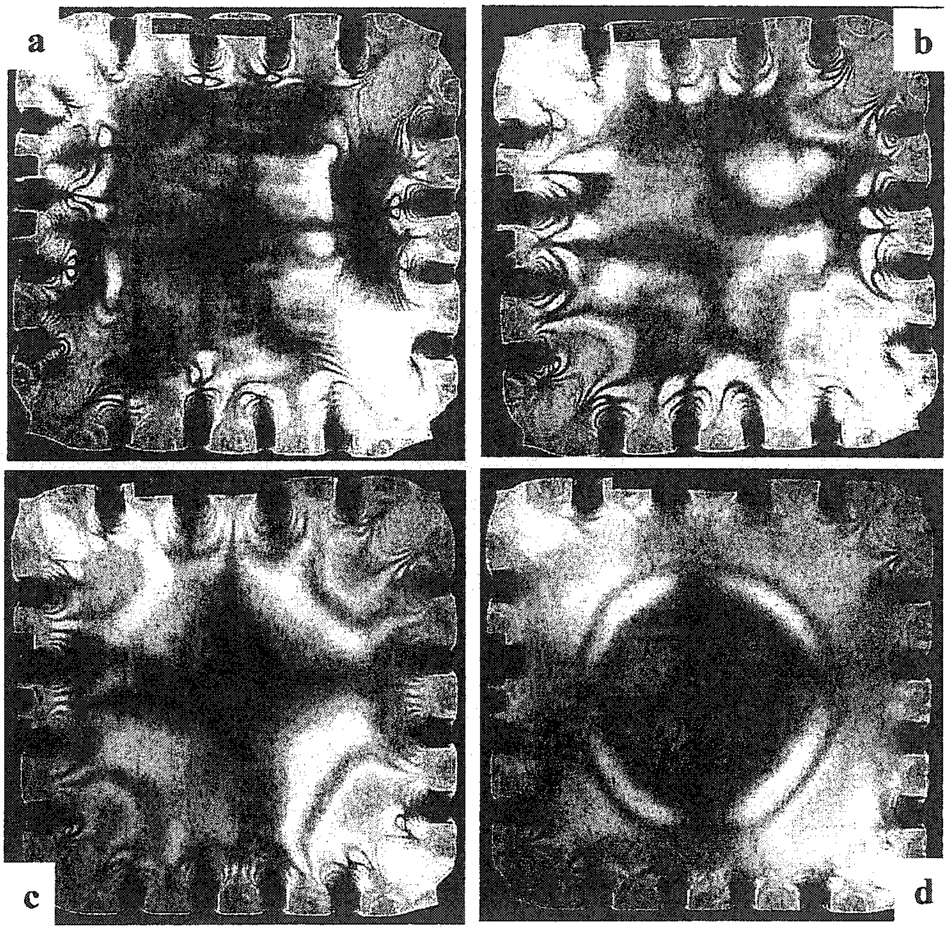

Figure 6-4 *Fringe patterns of films equibiaxially stretched up to a 1.5 x 1.5 ratio with a Hencky strain rate of 1* s^{-1} *at various temperatures (a) 140°C; (b) 150°C; (c) 155°C; (d) 160°C.*

The sample stretched at 140°C exhibited large areas of closely spaced fringes without any symmetrical extinction pattern around the clips. In contrast, the sample stretched a 160°C showed a large, almost circular extinction pattern without areas of closely spaced fringes. Overall, increasing the drawing temperature from 140°C to 160°C caused the extinction regions of zero principal stress difference to expand and their symmetry to improve, while the regions of closely spaced fringes became smaller.

The results from the fringe patterns were then compared with the corresponding nominal stress-strain curves shown in Figure 6-5. The stress-strain curves in both directions for the 140-155°C temperature range followed the typical ductile deformation behavior (a yield region followed by strain hardening), for semicrystalline polymers in tensile experiments. For the highest drawing temperature (160°C), 5°C below the melting point, rubber–like deformation (no yield) was observed. The magnitude of the yield stress, the yield region sharpness, the overall stress level, and the extent of strain hardening were all observed to decrease with increasing stretching temperature. The dependence of the biaxial yield stresses on drawing temperature, for the range under study, from 140°C to 160°C, was found to be linear (3). These results are similar to previous results from uniaxial deformation (4) and to results from biaxial deformation obtained on a similar device (5). In fact, the temperature dependences of uniaxial and biaxial yield stresses were found to be identical in slope (3).

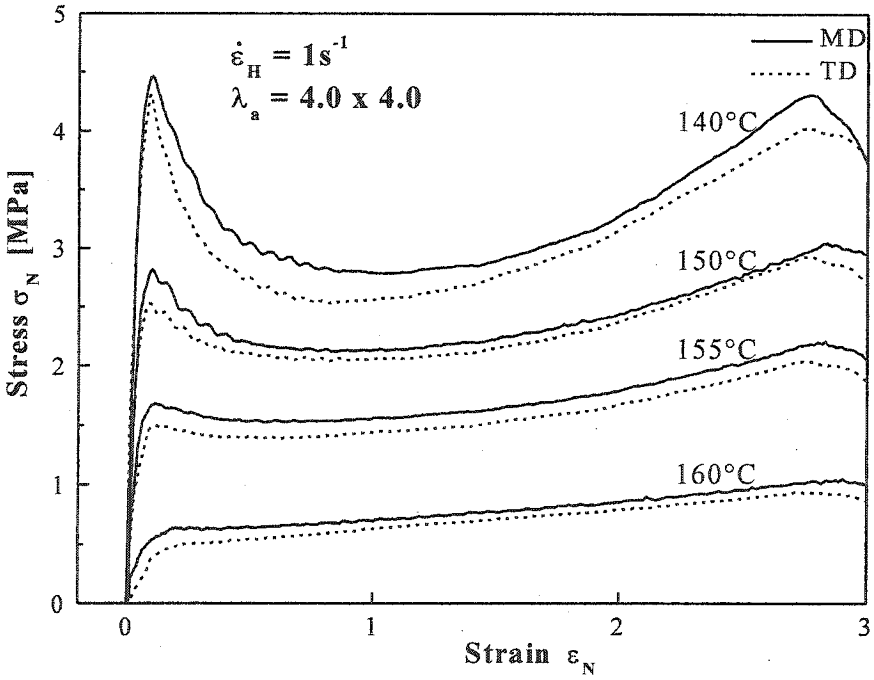

Figure 6-5 *Effect of stretching temperature on the stress-strain curves for the equibiaxial deformation of the PP2 cast film*

The average film thicknesses and the true draw ratios were measured for samples stretched under the same conditions as above, but to a 4.9 x 4.9 area stretching ratio. The data are listed in Table 6-2. The measured true draw ratios for the maximal area λ_{36} differ from the nominal strains because the strain measurements were carried out on a grid of 60 mm x 60 mm for an actual sample size of 70 mm x 70 mm. These measurements revealed that, with increasing stretching temperature, the overall average film thickness, t_{36}, decreased and, thus, the true draw ratios, λ_{MD36} and λ_{TD36}, increased. Moreover, the average film thicknesses from the film central area, t_4, were found smaller than those calculated for the whole grid, t_{36}. As expected, the opposite tendency was observed for the corresponding true draw ratios, λ_4 and λ_{36}. The true draw ratios for the 150-160°C temperature range decreased from the film center to the outer regions. Also, the difference between λ_4 and λ_{36} increased significantly with increasing temperature.

Table 6-2 *Effect of drawing temperature on true draw ratios and film thickness for samples equibiaxially stretched up to 4.9 x 4.9 with a Hencky strain rate of 1* s^{-1} *and where* $\Delta t = (t_{36} - t_4)/t_{36}$

T[°C]	λ_{MD36}	λ_{MD4}	λ_{TD36}	λ_{TD4}	t_{36} [μm]	t_4 [μm]	Δt [%]
145	4.78 ± 0.14	4.82 ± 0.07	4.92 ± 0.11	4.98 ± 0.04	44 ± 2	44 ± 1	1.9
150	5.07 ± 0.25	5.13 ± 0.04	4.88 ± 0.20	5.03 ± 0.05	43 ± 3	40 ± 2	3.1
155	5.13 ± 0.17	5.23 ± 0.05	5.06 ± 0.15	5.18 ± 0.04	41 ± 2	39 ± 1	4.8
160	5.29 ± 0.42	5.78 ± 0.07	5.26 ± 0.47	5.90 ± 0.08	39 ± 11	24 ± 1	23.1

An attempt was made to quantify the homogeneity of the thickness profile as follows:

$$\Delta t = (t_{36} - t_4) / t_{36}.$$

where t_4 and t_{36} are the average film thicknesses over the 4 inner squares and the total 36 squares of the grid, respectively. Δt will be close to zero for a homogeneous thickness profile, positive for an inhomogeneous film more stretched in the central area, and negative for a film more stretched in the outer parts. The relative thickness difference is plotted in Figure 6-6 for film samples stretched at various temperatures and area stretching ratios. Figure 6-6 shows that Δt is negative for 140°C and becomes positive above 145°C. For all temperatures, |Δt| decreased with area stretching ratio. Up to a temperature of 155°C, |Δt| was reduced to below 5% after a stretching ratio of 4.9 x 4.9.

For 160°C, the thickness ratio varied greatly, from 36% to 7%, with stretching. In fact, up to a 5.7 x 5.7 stretching ratio, the thickness ratio was as high as 14%. This suggests that, close to T_m, the film thickness profile was strongly inhomogeneous, because the stretching took place predominantly in the center, especially below a 4 x 4 stretching ratio.

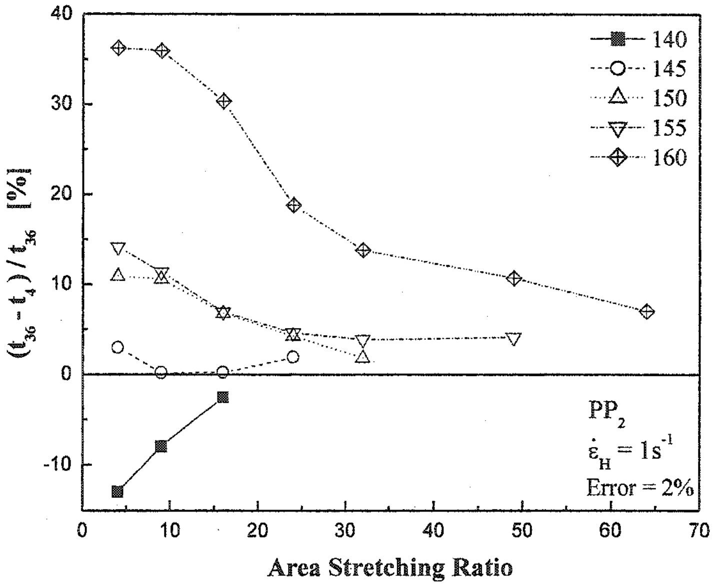

Figure 6-6 *Effect of stretching temperature and stretching ratio on the film thickness profile, expressed as the normalized difference between the average thickness of the central area and that of the total area.*

Raising the drawing temperature led to larger biaxial deformation of the central part of the specimen. Furthermore, less pronounced tensile necking was observed around the clips. In fact, there is a temperature gradient in the specimen inherent in the stretching device. This gradient is temperature dependent. At high stretching temperatures, drawing took place in an area of high deformability rather than high stresses. This explains the poor thickness profile obtained at $T < T_m - 5$°C.

The nominal stress-strain curves showed that the drop in nominal stress after yield was not necessarily associated with inhomogeneous equibiaxial stretching. Homogeneous equibiaxial deformation was obtained for the following temperature range, $T_m - 20 < T < T_m - 10$°C, even though a yield stress was observed.

6.2.2 - Effect of Strain Rate on Biaxial Deformation Behavior

Figure 6-1 - 6-3 illustrate the effect of strain rate on the deformation homogeneity. These figures show clearly that the homogeneity of the equibiaxial deformation is greatly affected by the strain rate. With regard to the stress-strain curves, it should be mentioned that the study of the effect of the strain rate was limited due to apparatus limitations, i.e., the frame acceleration and deceleration at high strain rates (3).

It is assumed in this work that the adiabatic heating effect is negligible, because the stretching takes place at temperature much higher than the glass transition (T_g) temperature, and the strain rate range is limited to one decade. Recent work indicated that for PET films, the increase in temperature during drawing above T_g does not exceed 2 or 3°C at strain rates as high as 15 s^{-1} (1).

Inhomogeneous deformation was always observed for deformation rates at $0.01s^{-1}$ and lower, as indicated by the series of fringe patterns in Figure 6-2. At very low strain rate, deformation started with localized necking regions (i.e., in corners), then, depending on drawing temperature, other necks would appear, and eventually necking regions would merge. Even at a temperature close to the melting point, T_m −10°C, inhomogeneous deformation was observed. However, for deformation rates equal to and above $0.1s^{-1}$, the stretching homogeneity was significantly improved for the temperature range under study.

The results obtained in the reliable range of strain rates showed that increasing the strain rate will raise the yield stress and the global level of stress needed to deform the specimen, as shown in Figure 6-7. Comparison of the stress-strain curves for rates between $0.1s^{-1}$ and $1.5s^{-1}$ shows that the sharpness of the yield stress and the magnitude of strain hardening were very similar, except for the slowest rate, as shown in Figure 6-7. In fact, for the slowest deformation rate (0.1 s^{-1}), the stress curve exhibited larger strain hardening than for the other strain rates. It should be noted that slower deformation rates involve the longer stretching times. It was observed that more pronounced strain hardening occurred when the stretching time was in the range of ten seconds. This represents a seldom-discussed, important phenomenon that occurs during stretching at high temperature below the melting point. This phenomenon was attributed to thermal or annealing effects, such as lamellar thickening, inter-lamellar reorganization, and crystal perfection. These effects reduce molecular mobility and contribute to raising deformation energy requirements. Nevertheless, the difference in strain hardening behavior might also be partly attributed to the adiabatic heating occurring due to faster deformation. This would have an influence on both the morphology and on the strain hardening behavior. However, in this work, the strain hardening was found to be not affected by the strain rate, for stretching times below 5 s.

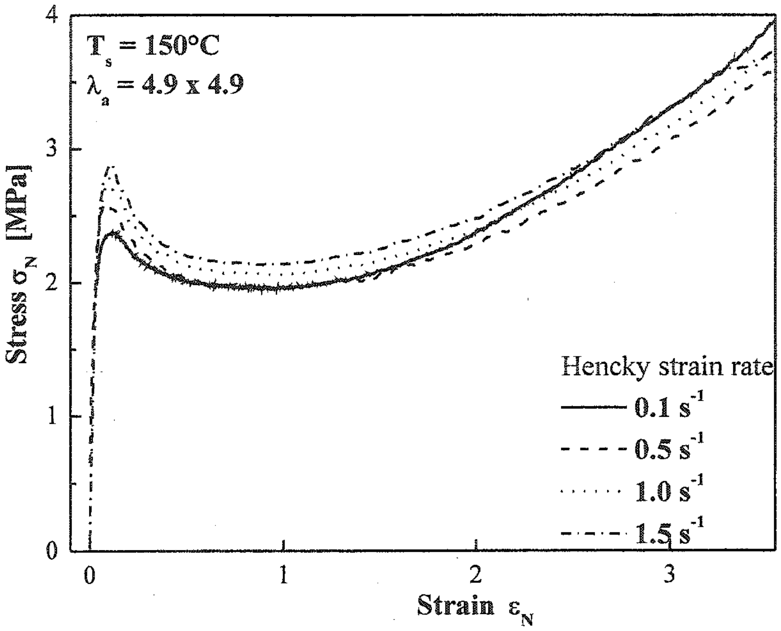

Figure 6-7 *Effect of the strain rate on the nominal strain-stress curves. Only MD stresses are represented for specimens equibiaxially stretched at various strain rates*

6.2.3 - Conclusions

Below a certain strain rate, $\dot{\varepsilon}_H$ = 0.01 s^{-1}, the equibiaxial deformation proceeds mainly inhomogeneously, i.e. at several localized necking zones. Above 0.1 s^{-1}, the equibiaxial deformation takes place uniformly, through simultaneous stretching of the entire central part of the specimen. The presence of the yield stress in the stress-strain curves could not be directly associated with the occurrence of local necking.

The study of the effect of drawing temperature showed the importance of the temperature difference below the melting point of the resin (degree of supercooling), at which stretching took place. This was found to greatly influence the deformation behavior and the resulting thickness profile. For temperatures below or equal to T_m – 10°C, the equibiaxial deformation was found to be ductile. Above or at T_m – 5°C, the deformation was rubber-like. At temperatures very close to T_m, the temperature gradient present in the specimen just before stretching produces a film specimen with poor thickness distribution, due to a higher stretching rate in the central area.

6.3 - Effect of Initial Film Morphology on Biaxial Deformation Behavior

Two sets of distinct cast films were investigated under simultaneous equibiaxial deformation in order to assess the effect of the initial film morphology on deformation behavior and the resulting film thickness profile. The morphological characteristics of these two sets were described in Chapter 5. The first set was the series of cast films crystallized from the melt, the PP4 – CFx samples. These films were extruded and cast on a chill roll half immersed into a water bath. This processing history corresponds to the standard cooling conditions encountered on a production line. The second set consisted of the series of annealed morphologies, the PP2 – A1xx samples. It should be noted that the thermal treatment applied to the latter set of films does not correspond to any step of an industrial stretching process. These films were investigated for the sake of understanding the more general effect of initial film morphology on deformation behavior.

6.3.1 - Effect of Melt-Crystallized Film Morphology on Deformation Behavior

Each of the CF1-CF4 cast films investigated here had a distinct initial morphologies, as described in Chapter 5 (Table 5-2). The cooling severity of the casting conditions was reduced from CF1 to CF4. These four cast films were stretched simultaneously equibiaxially at 150°C and 160°C with a Hencky strain rate of $1s^{-1}$. Figure 6-8 shows the nominal stress-strain curves of the stretching experiments at 150°C and 160°C. Only the MD stresses are shown for clarity purposes.

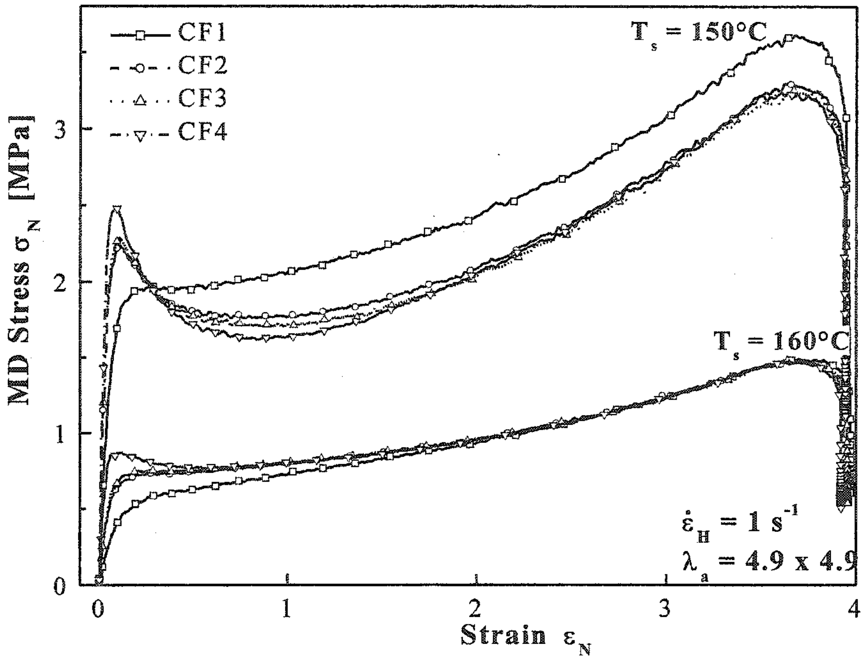

Figure 6-8 *Effect of the initial morphology on the nominal stress-strain curves for the equibiaxial stretching at 150°C and 160°C of the melt-crystallized samples (only MD stresses are shown)*

The major difference in deformation behavior among the four cast films is in the yield region for both drawing temperatures. They exhibit similar strain hardening behavior. The yield stresses and the yield region sharpness increase from CF1 to CF4. CF1 films exhibit diffuse yield and the shape of the stress-strain curve differs significantly from those of the other cast films, upon stretching at 150°C. The higher level of nominal stresses for CF1 is an indirect manifestation of the effect of the initial morphology on deformation behavior. In fact, the homogeneous deformation of CF1 led to a more uniform and thicker thickness profile than that for the other cast films, as shown in Table 6-3. The differences between nominal stresses will be significantly reduced if the true stress-true strain are plotted.

Table 6-3 shows the influence of the initial film morphology on the film dimensions for films equibiaxially stretched up to 4.9 x 4.9 stretching ratio at 150°C. The local true draw ratios, the local film thicknesses, and the thickness profiles are almost identical for the CF2, CF3, and CF4 samples. Only the CF1 exhibits smaller true draw ratios and a thicker, more uniform thickness profile than the other morphologies. There seems to be a relationship between the deformation behavior in the yield region of the stress-strain curves and the film thickness profile.

Table 6-3 Local true draw ratios, thicknesses, and thickness profile coefficient of the films stretched at 150°C up to 4.9 x 4.9 with a Hencky strain rate of a s^{-1} for the four PP4 melt-crystallized cast films ($\Delta t = (t_{36} - t_4)/t_{36}$)

Cast Film	λ_{MD36}	λ_{MD4}	λ_{TD36}	λ_{TD4}	t_{36} [μm]	t_4 [μm]	Δt [%]
CF1	**4.90 ± 0.14**	**5.00 ± 0.06**	**4.88 ± 0.17**	**4.98 ± 0.09**	**50 ± 2**	**48 ± 1**	**3.6**
CF2	**5.00 ± 0.16**	**5.13 ± 0.05**	**4.96 ± 0.18**	**5.12 ± 0.07**	**48 ± 3**	**45 ± 1**	**5.4**
CF3	**5.02 ± 0.15**	**5.17 ± 0.05**	**4..99 ± 0.19**	**5.13 ± 0.07**	**47 ± 3**	**45 ± 1**	**5.3**
CF4	**5.04 ± 0.17**	**5.18 ± 0.04**	**4.97 ± 0.21**	**5.13 ± 0.05**	**48 ± 3**	**45 ± 1**	**5.8**

6.3.2 - Effect of Annealed Film Morphology on Deformation Behavior

The deformation behavior of the series of annealed films morphologies was investigated in order to better understand which morphological characteristics control the biaxial deformation behavior. The series of annealed film morphologies presented also the advantage of containing only the stable, monoclinic α-form. The annealed films were simultaneously equibiaxially stretched at 150°C with a constant rate of 0.68 s^{-1}. The nominal stress-strain curves are shown in Figure 6-9. Only the MD stresses are shown for clarity purposes.

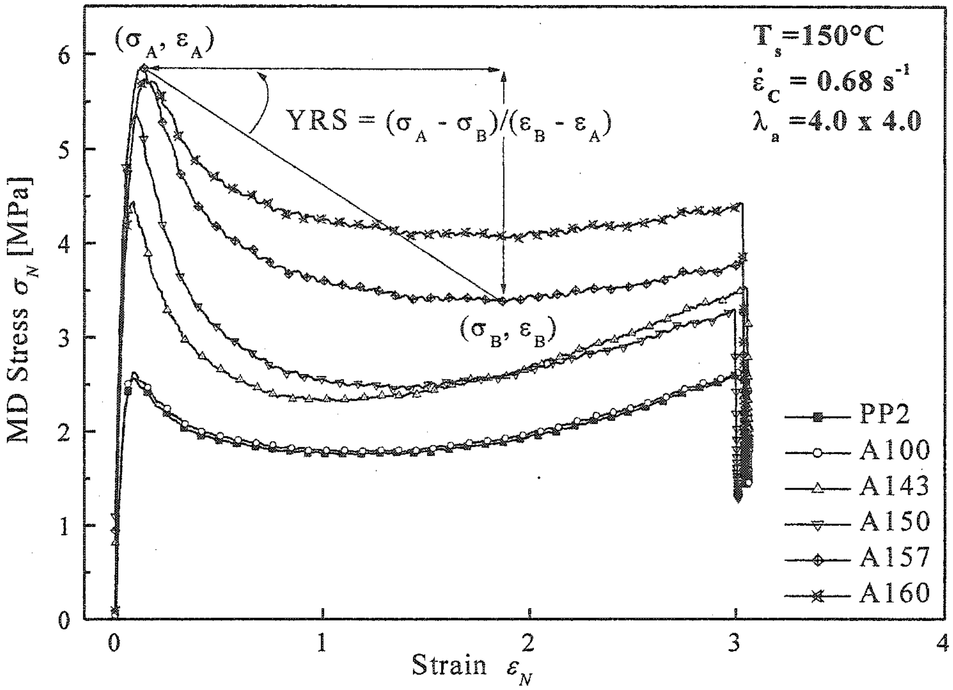

Figure 6-9 *Effect of the initial morphology on the nominal stress strain curves for the equibiaxial stretching of the annealed samples (YRS = Yield Region Sharpness)*

The differences in stress-strain profiles and stress levels are much more pronounced for the annealed films than for the series of melt-crystallized films. The nominal yield stress and the overall stress level were observed to increase with the temperature at which the cast film was annealed. The sharpness of the yield region was affected by the annealing temperature. For instance, the sample annealed at 100°C, A100, exhibited the identical deformation behavior as the original PP2 cast film, whereas the sample annealed at 143°C, A143, showed a sharp yield region and a high yield stress.

An attempt was made to quantify the yield region sharpness (YRS) as the positive slope between the yield point and the curve minimum after yield, as shown in Figure 6-9. The value of YRS would be nonzero if yielding occurs, and zero if no yield is observed.

Table 6-4 *True draw ratios, film thicknesses, and YRS of the films stretched at 150°C up to 4.0 x 4.0 with a strain rate of 0.68 s^{-1} for the PP2 and annealed cast films*

Cast Film	YRS_{MD}	λ_{MD36}	λ_{MD4}	YRS_{TD}	λ_{TD36}	λ_{TD4}	t_{36} [μm]	t_4 [μm]	Δt [%]
PP2	0.8	4.4 ± 0.3	4.6 ± 0.1	0.6	4.3 ± 0.4	4.5 ± 0.1	56 ± 5	51 ± 1	9.1
A100	0.8	4.4 ± 0.3	4.7 ± 0.1	0.6	4.2± 0.4	4.4 ± 0.1	56 ± 6	50 ± 1	9.8
A143	2.5	4.5 ± 1.0	5.4 ± 0.1	2.2	4.3 ± 1.0	5.0 ± 0.1	60 ± 24	39 ± 1	34.9
A150	2.3	4.5 ± 0.7	5.0 ± 0.1	2.0	4.1 ± 0.8	4.4 ± 0.1	59 ± 19	47 ± 1	20.8
A157	1.4	4.3 ± 0.3	4.5 ± 0.1	1.3	4.1 ± 0.1	4.3 ± 0.1	60 ± 6	55 ± 1	8.0
A160	1.0	4.1 ± 0.2	4.3 ± 0.1	0.8	3.9 ± 0.1	4.2 ± 0.1	65 ± 7	59 ± 1	9.6

Table 6-4 lists the YRS values, the local, true draw ratios and thicknesses and the film thickness profile coefficient, Δt, of the annealed samples stretched up to a 4 x 4 stretching ratio. It can be seen that the yield region sharpness can be correlated with the true draw ratios and the film thickness profile. The sharper is the yield region, the larger is the true draw ratios and the less uniform is the thickness profile.

The yield region sharpness and the film thickness profile agreed well with the fringe patterns of the 1.3 x 1.3 stretched samples, as shown in Figure 6-10. Figure 6-10(b) shows that the A143 sample exhibited the least homogeneous deformation. In each corner, large necking regions were observed. In contrast, Figure 6-10(a) shows that PP2 had a more symmetrical fringe pattern and smaller necking regions. For the A160 sample, the drawn portion of the equibiaxially stretched sample was completely white, as shown in Figure 6-10(c). The dark regions correspond to the white of the specimen, due to the formation of voids and/or intrinsic crazing (6). Therefore, the A160 fringe pattern could not be observed, because of the light scattering due to the formation of voids during deformation.

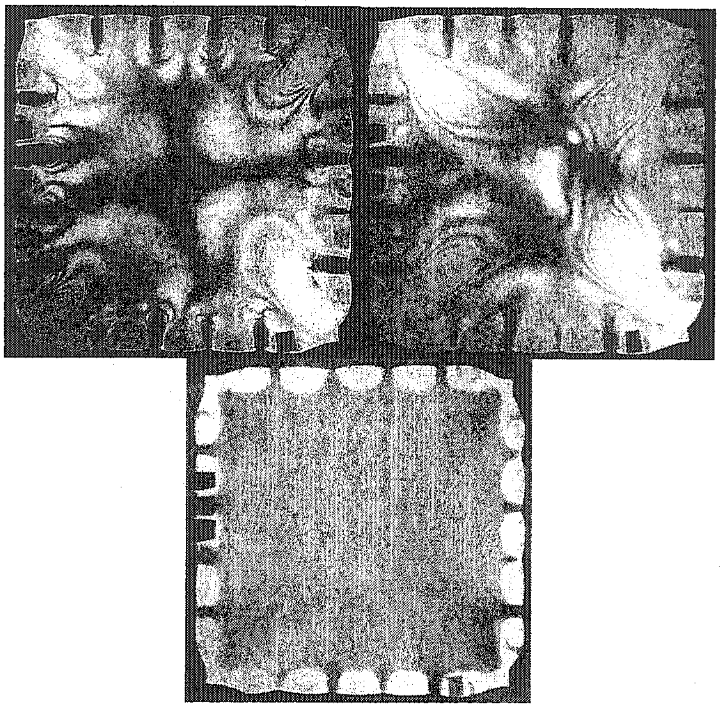

Figure 6-10 Fringe patterns of samples equibiaxially stretched up to a 1.3 x 1.3 ratio with $\dot{\varepsilon}_H = 1\ s^{-1}$ *at 150°C. (a) PP2 cast film; (b) A140, and (c) A160*

6.3.3 - Discussion

Part of the crystalline structure melts, when the initial film is heated at temperatures close to the melting point, as discussed in Chapter 5. The nature of the deformation at high temperature would then be expected to depend on the structural characteristics of the partly molten state. At the stretching temperature, the morphology can be considered as a rubbery phase, composed of a mix of amorphous melt and structured melt, filled with crystallites. The viscosity and amounts of the amorphous and molten phases, the size and perfection of the crystalline entities, and the fraction of tie molecules influence deformation behavior. In a series of papers on the uniaxial deformation of iPP at room temperature, Nitta and Takayanagi (7, 8) concluded that the interlamellar amorphous regions, the tie molecule fraction, and the lamellar crystal stiffness were the structural factors that control yielding.

In the following, we shall discuss the effects of initial film morphology on biaxial deformation behavior in terms of the amount of unmolten crystallinity, the crystallite size (lamellar stiffness), and the tie molecule fraction.

6.3.3.1 - Relations between the structural factors of initial film morphology and the level of yield stress

Rettenberger (3) showed that the magnitude of the uniaxial yield stress increased with increasing the degree of crystallinity for the melt-crystallized cast films. Other researchers showed that the magnitude of the yield stress may be correlated with the degree of crystallinity (9), the lamellar thickness (10), and the spherulite size (11), for uniaxial deformation of iPP and PE at room temperature. In our work, all these parameters increased with reducing the severity of cooling, as reported for the series of melt-crystallized cast films (cf. Table 5-2). However, some of the above relationships were not preserved after the annealing of the samples (cf. Chapter 5). Therefore, the investigation of the deformation behavior of the annealed samples should provide valuable information about the order of importance of the main structural factors affecting the magnitude of yield stress.

Firstly, the stress-strain curves for the annealed samples showed that there is no correlation between the average spherulite size and deformation behavior, in agreement with the literature (9, 12). Secondly, an in-depth study of the uniaxial deformation of similar samples by Rettenberger showed that the linear dependence of the yield stress on crystallinity does not apply for the annealed films (3). In fact, his results showed that there is a good correlation between the D_{040} crystallite size and the level of yield stress. Moreover, it has been reported that if the crystals are thin, then they have a low stiffness and the yield stress is low, according to the dislocation model (14). Alternatively, thin crystals are less stable and more easily melted, according to the melting-crystallization model (15, 16). This reasoning regarding the crystal thickness can be extended to the lateral dimensions of the crystallites, the D_{040} crystallite size. Accordingly, large and perfected crystallites, which have high stiffness, would contribute to high yield stress.

6.3.3.2 - Relation between the structural factors of the initial film morphology and deformation homogeneity

The above results for the melt-crystallized cast films and the annealed films indicate that the initial film morphology affects the homogeneity of deformation and the resulting film thickness profile. In the following, we attempt to identify the structural factors in the initial film morphology that determine the homogeneity of deformation, and especially the yield region sharpness.

The homogenous deformation of CF1 is associated with certain characteristics of its initial morphology. The CF1 cast film was crystallized under the most severe cooling conditions. This resulted in a large amount of smectic phase, a low degree of crystallinity, a low apparent crystallite size (cf. Chapter 5), and a high density of tie molecules and entanglements (17). The smectic phase is transformed into the monoclinic form upon heating above 70°C(19). Thus, the homogeneous deformation behavior of the CF1 cast film cannot be directly associated with the presence of smectic phase. The low degree of crystallinity cannot explain it either because of the homogeneous deformation also observed for the CF1 sample annealed at 100°C, which exhibits higher crystallinity. Consequently, the yield region sharpness for the melt-crystallized films may be related to the remaining structural factors: the lamellar stiffness (size and perfection of the crystallites) and the tie molecule and entanglement densities. The results on the melt-crystallized films suggest that the deformation will be homogeneous if the tie molecule and entanglement fractions are high and the stiffness of the crystallites is low. It should be noted that the small amount of β-phase present in CF3 and CF4 may affect the deformation behavior.

The results for the annealed films showed that the yield region sharpness is correlated with neither the amount of crystallinity nor the crystallite size of the annealed film morphology (cf. Tables 5-3 and 6-4). Thus, the remaining relevant structural features that might explain the yield region sharpness are the tie molecule and entanglement. In fact, in a study on the effect of taut tie molecules on the modulus of oriented iPP, Yamada et al. (21) reported that the taut tie molecules are loosened by annealing below 147°C, but would be incorporated into folded lamellar crystals above the annealing temperature of 147°C. Annealing through lamellar folding leads also to a loss of entanglements. This indicates that the number of tie molecules and entanglements depends on the annealing temperature and that the A143 morphology should contain the smallest fraction of tie molecules and entanglements. The yield region was the sharpest for the A143 morphology, while the samples annealed above 150°C exhibited a more diffuse yield stress. This supports the idea that the tie molecule fraction and entanglements might be the primary structural features controlling the yield region sharpness and, therefore, the necking behavior and the film thickness profile. The concept developed by Takayanagi et al. (22) is in agreement with this view. They assumed that post-yielding deformation of crystalline polymers is governed primarily by tie molecules (22).

6.3.4 - Conclusions

For films with melt-crystallized morphologies, for a given resin, the magnitude of the yield stress is dependent on the initial crystallinity. This dependence is due to the direct correlation between crystallite dimensions and crystallinity, which is only valid for melt-crystallized samples. The yield stress was found to be dependent on the D_{040} crystallite size. The crystallite size can be also associated with crystal stiffness. Therefore, the magnitude of the yield stress is primarily governed by crystallite stiffness and the amount of crystalline phase. The yield region sharpness was found to be correlated with the resulting film thickness profile, for a given temperature below T_m. The more diffuse is the yield region, the more uniform is the film thickness. The yield region sharpness appears to be primarily related to the fraction of tie molecules and entanglement density in the initial film morphology. A more diffuse yield stress is obtained for a higher density in tie molecules and entanglements.

6.4 - Effect of Chain Tacticity on Biaxial Deformation Behavior

For the investigation of the effect of chain tacticity on the simultaneous equibiaxial deformation behavior, the PP1, PP2, and PP3 cast films were all stretched under the same conditions and the stress-strain curves, fringe patterns, and true draw ratios were then compared. The isotacticity contents of PP1, PP2, and PP3 are 94.9%, 98.6%, and 99.5%, respectively.

6.4.1 - Results

Figure 6-11 shows the nominal stress-strain curves of the PP1, PP2, and PP3 cast films simultaneously equibiaxially stretched under the same conditions. Differences were observed in the global stress level and the yield region for the three cast films. The PP1 cast film exhibited a diffuse yield region, whereas PP3 showed a high, sharp yield region. PP2 exhibited intermediate behavior between the other two samples. The yield stress increased with increasing isotacticity. The same classification order in deformation behavior was observed, when the films were stretched at 155°C and 160°C (results not shown).

It is assumed in this discussion that, for constant stretching conditions, the major difference in stress level encountered during deformation is primarily due to the differing isotacticity content of the resins. The increase of the yield stress with increasing isotacticity is in agreement with the results of Bullock and Cox (5) for similar biaxial deformation experiments. However, the reasons for the increase of yield stress or the change in yield sharpness have not been considered heretofore.

The fringe patterns of the 2 x 2 stretched samples show that the stress level and sharpness of the yield region are associated with the size of the regions of closely spaced fringes, as shown in Figure 6-12. Furthermore, although PP3 exhibited a relatively high and sharp yield point, the fringe patterns still showed a uniform fourfold symmetry. In Figure 6-12(c), the central dark extinction area was reduced to a very thin cross, which corresponds to the regions where the stresses were parallel to the polarization axes. On the other hand, for PP1, in Figure 6-12(a), the extinction area was rather large, indicating more uniform stretching of the central area than for PP3.

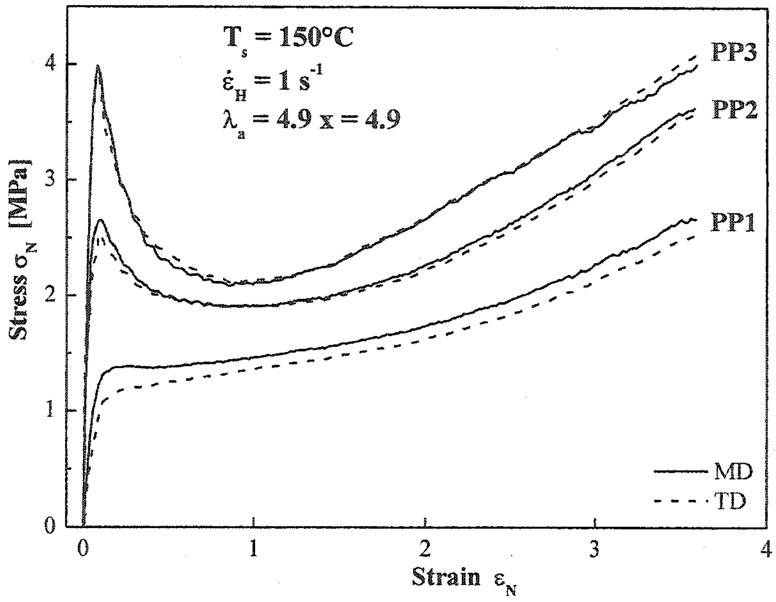

Figure 6-11 *Nominal stress-strain curves of the simultaneous equibiaxial stretching experiments at 150°C with a strain rate of 1 s^{-1} for PP1, PP2 and PP3*

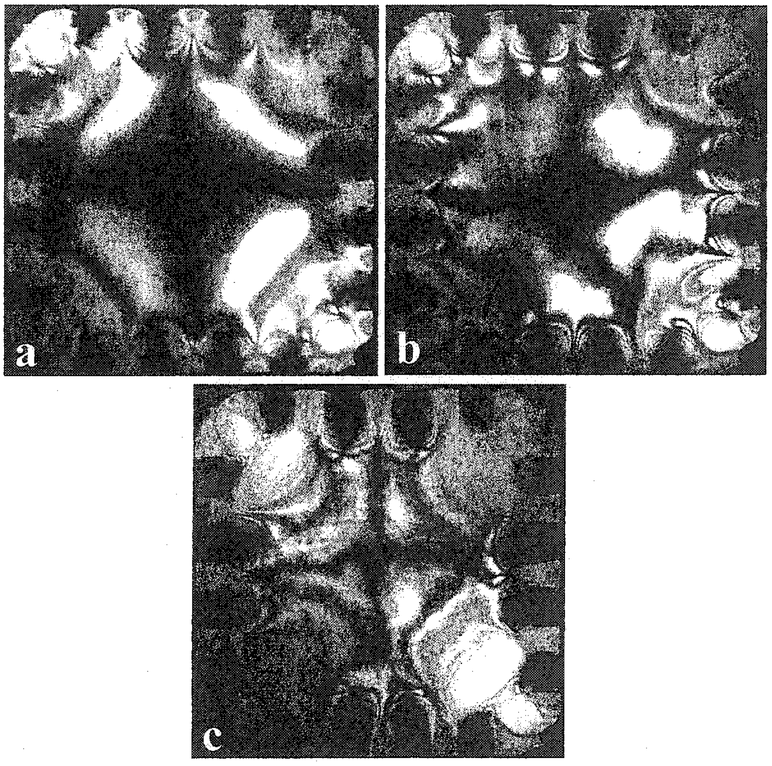

Figure 6-12 *Fringe patterns of films simultaneously equibiaxially stretched at 150°C up to a 2 x 2 area ratio for (a) PP1, (b) PP2, and (c) PP3*

The results for the true draw ratios, film thicknesses, and the film thickness profiles of the same samples stretched up to a 4.0 x 4.0 area ratio supported the previous results of section 8.2, as shown in Table 6-5. For all three film samples, the equibiaxial stretching took place predominantly in the center, as indicated by the positive, relatively high value of Δt. The lowest Δt value was observed for PP2, while that for PP1 was only slightly higher and that of PP3 and more than double that of PP2.

Table 6-5 True draw ratios, film thicknesses, and YRS of the films stretched at 150°C up to 4.0 x 4.0 for the PP1, PP2, and PP3 cast films

Cast Film	YRS_{MD}	λ_{MD36}	λ_{MD4}	YRS_{TD}	λ_{TD36}	λ_{TD4}	t_{36} [μm]	t_4 [μm]	Δt [%]
PP1	**0.1**	**4.19 ± 0.17**	**4.33 ± 0.02**	**0.0**	**4.16 ± 0.24**	**4.38 ± 0.12**	**62 ± 5**	**57 ± 2**	**8.1**
PP2	**1.0**	**4.27 ± 0.15**	**4.43 ± 0.04**	**0.9**	**4.13± 0.23**	**4.32 ± 0.07**	**59 ± 4**	**55 ± 1**	**7.0**
PP3	**2.5**	**4.35 ± 0.40**	**4.72 ± 0.07**	**2.5**	**4.22 ± 0.49**	**4.58 ± 0.09**	**61 ± 9**	**52 ± 1**	**14.8**

The results from the characterization of the initial morphology of the samples showed that the thermal stability of the crystallites was strongly affected by the chain isotacticity (cf. Chapter 5). With increasing tacticity, the DSC melting peak was shifted to higher temperature and the degree of crystallinity and the apparent crystallite size were increased. Therefore, the differences in deformation behavior with tacticity can be first explained by differences in thermal stability, size and amount of the crystalline phase. For a given thermal history and stretching temperature, the amount of unmolten crystallinity and the size and perfection of the crystallites are increased as isotacticity increases (cf. Table 5-5). Therefore, the increases in yield and overall stress with isotacticity were attributed to the reduced amounts of amorphous an structured melt and the increased crystallite stiffness.

The results from Chapter 5 showed that the thermal stability and the partly molten state are strongly dependent on the temperature difference $\Delta T = T_m - T$. Therefore, the three cast films were then stretched at the same temperature difference below their respective melting points (supercooling). This was performed for three temperature differences: T_m – 15°C, T_m – 10°C, and T_m – 5°C. Figure 6-13 illustrates the nominal stress-strain curves for the stretching experiments at T_m - 10°C. Except for the yield region, the nominal stress curves were almost identical for the three cast films, especially when compared to Figure 6-11. In the yield region, the yield stress and sharpness were still observed to increase from PP1 to PP3. Similar results were obtained for all three temperature differences.

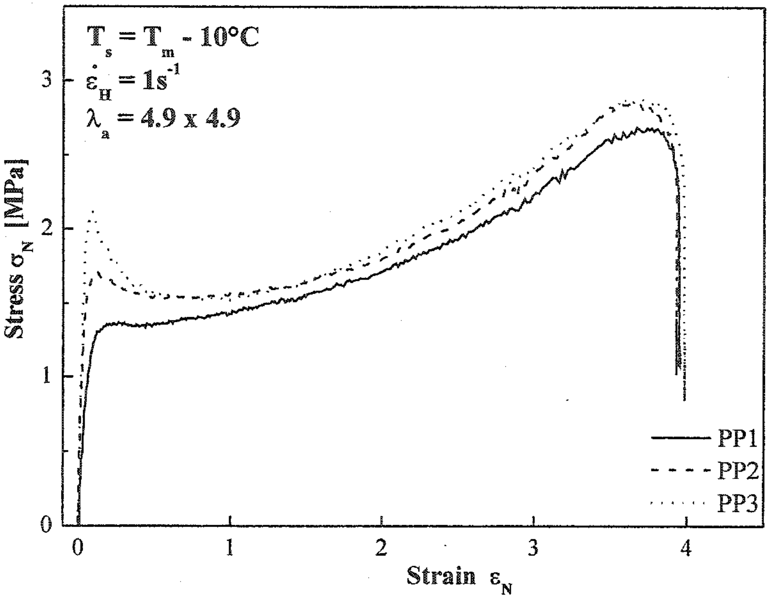

Figure 6-13 *Nominal stress-strain curves for samples stretched simultaneously equibiaxially at T_m – 10°C. PP1 at 150°C, PP2 at 155°C, and PP3 at 158°C.*

The important result from these experiments is that the deformation behavior seems to be strongly dependent on the temperature difference $\Delta T = T_m - T_S$ and thus on the characteristics of the partly molten state. The similar nominal stress-strain curves for the three resins observed in Figure 6-13 indicate that the temperature difference below T_m (degree of supercooling) seems to determine the nominal drawing stress. Rettenberger showed that there is a linear correlation between the true drawing stresses and the umolten crystallinity, which is independent of the isotacticity of the raw material (3).

The increase in the yield stress and yield region sharpness with increasing isotacticity observed at ΔT = 10°C can be related to the structural characteristics of the partly molten film. The unmolten crystallinity and the size of the crystallites increase with isotacticity at constant ΔT. Furthermore, the work of Ishikawa et al.(26) on crazing of iPP suggests that the volume fraction of tie molecules decreased with increasing tacticity. Therefore, at a given ΔT, the increase in yield stress may be attributed to the increase in the size of the crystallites. Also, the rise in yield sharpness may be due to the decreased density of tie molecules with increasing tacticity.

6.5 - Summary

It was found that the equibiaxial deformation behavior depended on three key variables: the drawing temperature, the strain rate, and the initial film morphology. The following conclusions could be made about the effect of stretching conditions on biaxial deformation behavior:

- The degree of supercooling, at which stretching took place, was found to greatly influence the deformation behavior and the resulting thickness profile. For temperatures below or equal to T_m – 10°C, the equibiaxial deformation was found to be ductile. Above or at T_m – 5°C, the deformation was rubber-like. At temperatures very close to T_m, a film specimen with poor thickness distribution was obtained, due to a higher stretching rate in the central area.
- Below a certain strain rate, $\dot{\varepsilon}_H = 0.01\ s^{-1}$, the equibiaxial deformation proceeds mainly inhomogeneously, i.e. at several localized necking zones. Above 0.1 s^{-1}, the equibiaxial deformation takes place uniformly, through simultaneous biaxial stretching of the entire central part of the specimen.

The following conclusions could be made about the effect of the initial film morphology on biaxial deformation behavior:

- The yield stress is primarily governed by crystallite stiffness. In fact, the magnitude of the yield stress is dependent on the D_{040} crystallite size of the initial film morphology, and the crystallite stiffness can be associated with crystallite size.

[Refs. on p. 137]

- The yield region sharpness in the stress-strain curves is correlated with the resulting film thickness profile, for a given temperature below T_m. The more diffuse is the yield region, the more uniform is the film thickness. The yield region sharpness appears to be primarily related with the fraction of tie molecules and entanglement density of the initial morphology.
- For conventional molecular weight characteristics and constant stretching conditions, increasing tacticity leads to the increase of the overall stress required for deformation. In fact, the tacticity of the resin is the most significant factor affecting the thermal stability of the initial morphology, which, in turn, is the primary morphological property that controls the level of drawing stress.

[Refs. on p. 137]

References

1 - D. R. Salem, "*Draw-induced structure development in flexible-chain polymers*", in *Structure Formation in Polymeric Fibers*, D. R. Salem, Editor. Hanser: Munich. p. 118-184 (2001).

2 - R. H. Olley and D. C. Bassett, "On surface morphology and drawing of polypropylene films", J. Macromol. Sci. - Phys., **B33**, 209-227 (1994).

3 - S. Rettenberger, "Uni- und Biaxiales Verstrecken von isotaktischem Polypropylen im teilaufgeschmolzenen Zustand", PhD thesis, University Erlangen-Nuremberg, (2002).

4 - S. Rettenberger, L. Capt, H. Münstedt, J. Sänze and K. Stopperka. in *17th PPS annual meeting*, "Deformation behavior of different polypropylene cast films at elevated temperatures", (2001).

5 - W. W. Cox and E. K. Bullock. in *Polyolefins X: International Conference*, "Draw stress characterization of polypropylene for improved biaxial film processability", 397-415 (1997).

6 - K. Friedrich, "Crazes and shear bands in semi-crystalline thermoplastics", Adv. Polym. Sci., **52/53**, 225-274 (1983).

7 - K.-H. Nitta and M.-H. Takayanagi, "Role of tie molecules in the yielding deformation of isotactic polypropylene", J. Polym. Sci. ParB: Polym. Phys., **37**, pp357-368 (1999).

8 - K.-H. Nitta and M. Takayanagi, "Tensile yield of isotactic polypropylene in terms of a lamellar-cluster model", Journal of Polymer Science, **38**, 1037-1044 (2000).

9 - R. Popli and L. Mandelkern, "Influence of structural and morphological factors on the mechanical properties of the polyethylenes", J. Polym. Sci. Polym. Phys. Ed., **25**, 441-483 (1987).

10 - O. Darras and R. Seguela, "Tensile yield of polyethylene in relation to crystal thickness", J. Polym. Sci. Polym. Phys. Ed., **31**, 759-766 (1993).

11 - A. O. Ibhadon, "Fracture mechanics of polypropylene: Effect of molecular characteristics, crystallization conditions, and annealing on morphology and impact performance", J. Appl. Polym. Sci., **69**, 2657-2661 (1998).

12 - M. A. Kennedy, A. J. Peacock and L. Mandelkern, "Tensile properties of crystalline polymers: linear polyeythelene", Macromolecules, **27**, 5297-5310 (1994).

13 - R. Seguela, E. Staniek, B. Escaig and B. Fillon, "Plastic deformation of polypropylene in relation to crystalline structure", J. Appl. Polym. Sci., **71**, 1873-1885 (1999).

14 - W. J. O'Kane, R. J. Young and A. J. Ryan, "The effect of annealing on the structure and properties of isotactic polypropylene films", J. Macromol. Sci.-Phys., **B34**, 427-458 (1995).

15 - T. Juska and I. R. Harrison, "A criterion for craze formation", Polym. Eng. Sci., **22**, 766-776 (1982).

16 - G. Meinel and A. Peterlin, "Small-angle X-ray diffraction studies of plastically deformed polyethylene III. Small draw ratios", Makromol. Chem., **142**, 227-240 (1971).

17 - N. Brown and I. M. Ward, "The influence of morphology and molecular weight on ductile-brittle transitions in linear polyethylene", J. Mat. Sci., **18**, 1405-1420 (1983).

18 - V. Vittoria, "*Properties of Isotactic Polypropylene*", in *Encyclopedia of Materials Sciance and Engineering*, M. B. Bever, Editor. Pregamon Press: Oxford. p. 507-555 (1986).

19 - R. Zannetti, G. Celoti, A. Fichera and R. Francesconi, "The structural effects of annealing time and temperature on the paracrystal-crystal transition in isotactic polypropylene", Makrom. Chem., **128**, 137-142 (1969).

20 - T. Labour, G. Vigier, R. Seguela, C. Gauthier, G. Orange and Y. Bomal, "Influence of the beta-crystalline phase on the mechanical properties of unfilled and CaCO3-filler polypropylene. I. Structural and mechanical characterization", Polymer, **42**, 7127-7135 (2001).

21 - K. Yamada, M. Kamezawa and M. Takayanagi, "Relationship between orientation of amorphous chains and modulus in highly oriented polypropylene", J. Appl. Polym. Sci., **26**, 49-60 (1981).

22 - M. Takayanagi and K. H. Nitta, "Application of a tie molecule model to the postyielding deformation of crystalline polymers", Macromol. Theory Simul., **6**, 181-195 (1997).

23 - P. D. Bowden and R. J. Young, "Review Deformation mechanisms in crystalline materials", *J. Mat. Sci.,* **9**, 2034-2051 (1974).

24 - D. C. Bassett and R. H. Olley, "On the lamellar morphology of isotactic polypropylene spherulites", *Polymer,* **25**, 935-943 (1984).

25 - K. Yamada, S. Matsumoto, K. Tagashira and M. Hikosaka, "Isotacticity dependence of spherulitic morphology of isotactic polypropylene", *Polymer,* **39**, 5327-5333 (1998).

26 - M. Ishikawa, K. Ushui, Y. Kondo, K. Hatada and S. Gima, "Effect of tie molecules on the craze strength of polypropylene", *Polymer,* **37**, 5375-5379 (1996).

[Refs. on p. 137]

CHAPTER 7

MORPHOLOGY DEVELOPMENT DURING SIMULTANEOUS BIAXIAL STRETCHING

This chapter presents the evolution of the morphology of isotactic polypropylene films during simultaneous biaxial stretching. It presents the effects of drawing temperature, stretching ratio, strain rate and deformation type on the equibiaxially stretched film morphology. Then, it discusses the effects of the initial morphology and chain tacticity on the stretched film morphology.

7.1 - Effects of Stretching Conditions on the Equibiaxially Stretched Film Morphology

The effects of stretching conditions on the final morphology were investigated for the PP2 resin. The effects of drawing temperature, stretching ratio, strain rate, and deformation type on the stretched film morphology were studied.

7.1.1 - Effects of Drawing Temperature and Stretching Ratio on the Equibiaxially Stretched Film Morphology

7.1.1.1 - Results and Discussion

The PP2 cast film was simultaneously equibiaxially stretched with a Hencky strain rate of 1 s^{-1} up to various increasing stretching ratios, in the 140°C - 160°C range. The melting curves of the films stretched at 150°C were chosen to illustrate the melting behavior of the films stretched in this temperature range. Figure 7-1 shows that all the curves exhibit one single melting peak. The melting peak is shifted to slightly higher temperature with increasing area stretching ratio, while the peak width is reduced. The relatively broad peak of the 2 x 2 stretched sample was found to be similar in shape to that of the preheated sample (P150). The comparison of the melting curves of samples stretched up to 4.9 x 4.9, at different temperatures, showed that the melting peak is shifted to higher temperatures with increasing drawing temperature (cf. Table C-1 in App. C).

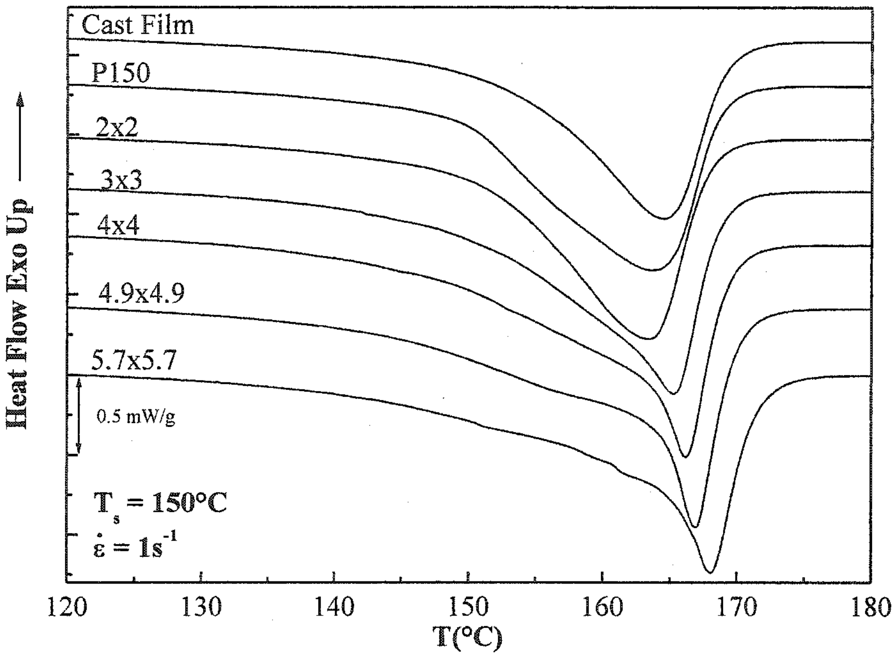

Figure 7-1 *Effect of area stretching ratio on the DSC melting behavior for the PP2 films equibiaxially stretched at 150°C*

The DSC results showed that there was only one melting peak for the variously stretched morphologies. The melting point increased with area stretching ratio, in agreement with the DSC results for the other resins and from the literature (1, 2). Tanaka et al. (3) explained that the thermal stability of the oriented structure is improved because of the healing of the defects during stretching.

On drawing, the structural transformation from lamellar to the oriented structure proceeds from the weakest (thermally stable) lamellae to the strongest ones. This explains the reduction of the melting peak width from the low temperature side on increasing drawing. In addition, the similarity in melting behavior of the weakly stretched and preheated films indicates that the stretching temperature influences greatly the thermal stability of the stretched films. The higher is the drawing temperature, the more thermally stable is the resulting stretched film morphology.

Figure 7-2 shows the evolution of the degree of crystallinity of the stretched films with increasing drawing temperature and stretching ratio. A scatter of the data was observed. Nevertheless, the degree of crystallinity tends to increase slightly with the stretching ratio, up to a stretching ratio of 7x7, in agreement with the literature (4). In fact, this increase is approximately linear. The slope is effectively identical in the 150°C – 160°C range. When compared at constant stretching ratio, the degree of crystallinity increases with increasing drawing temperature.

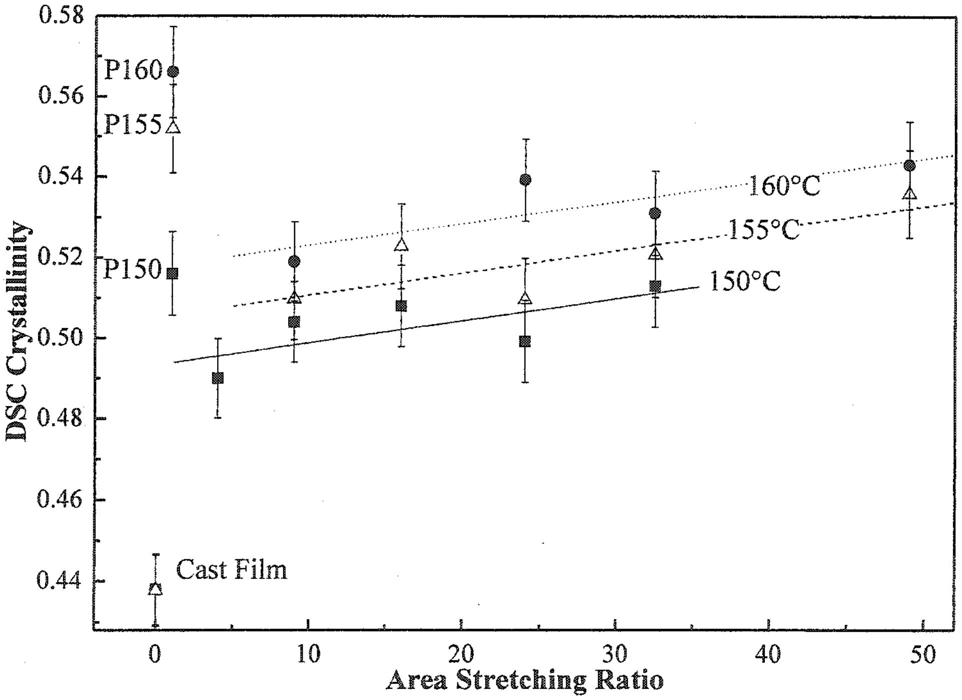

Figure 7-2 *Effects of the area stretching ratio and drawing temperature on the DSC crystallinity for equibiaxially stretched PP2 films*

The degree of crystallinity of the stretched films is higher than that of the original cast film. Moreover, the degree of crystallinity of the preheated films is even higher than that of the stretched films. This indicates that stretching has two competing effects on the degree of crystallinity. Firstly, stretching hinders the structural rearrangements, such as lamellar thickening, partial melting, and recrystallization, that occur in a pure preheating experiment. Secondly, the increase of crystallinity with further stretching suggests that stretching also participates in increasing the crystalline order (i.e., increase in orientation). These results suggest that, for high temperature stretching, the increase in crystallinity on stretching is controlled, in order of importance, by (a) the stretching temperature and (b) the orientation state of the morphology. The higher is the stretching temperature, the greater is the degree of crystallinity, in agreement with the DSC results from a similar study by Tanaka et al. (2).

Figure 7-3 shows the wide-angle X-ray diffraction (WAXD) patterns of the PP2 films that were equibiaxially stretched at 150°C between 2 x 2 and 5.7 x 5.7. The patterns for the original cast film and the preheated sample are also included. All the WAXD patterns exhibit only the characteristic peaks of the α–form of iPP. With increasing area stretching ratio, there is an increase in peak intensity for the (040), (110), and (060) diffraction peaks and a reduction for the (111)/(041)$(\bar{1}31)$ peak doublet. The peak doublet disappeared completely above a 4 x 4 area stretching ratio, for drawing at 150°C. The amorphous halo was also assessed from these measurements. The area and width of the halo decreased with increasing stretching.

The X-ray measurements in reflection were compared to the WAXD patterns measured in transmission for the simultaneously equibiaxially stretched films, in order to explain the increase in intensity of the (040) peak and the disappearance of the peak doublet. It is important to note that the (*hkl*) peak intensities refer only to the (*hkl*) crystal planes perfectly oriented in the sample plane used for measurements. Therefore, the measurements in reflection will describe the (*hkl*) crystal planes oriented in the MD-TD plane, while the measurements in transmission describe the planes aligned in the TD-ND or MD-ND sample plane.

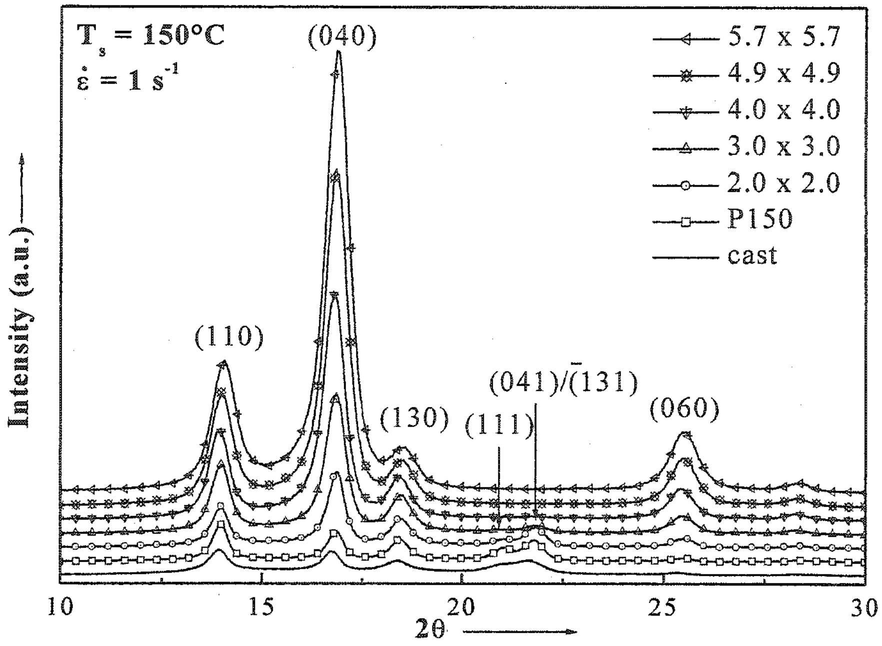

Figure 7-3 *Effect of area stretching ratio on the WAXD pattern for the PP2 films equibiaxially stretched at 150°C*

Figure 7-4 displays these measurements for a film stretched up to a 4.9 x 4.9 area stretching ratio. It can be seen that, for simultaneously equibiaxially stretched samples, the (040) crystal planes are oriented in the MD-TD sample plane, while the $(111)/(041)(\bar{1}31)$ crystal planes are in the TD-ND plane. On the other hand, the (110) planes are oriented in both planes, with a slight preference for the TD-ND plane. Finally, the (130) crystal planes are shifted from the MD-TD and TD-ND planes to be aligned at some angles from those planes. The above specific crystal plane orientations indicate that a strain-induced crystalline texture change occurs during drawing. This is also observed for deformation of iPP at room temperature (5).

The pole figure measurements (cf. 7.1.3) revealed that the crystalline texture of the equibiaxially stretched films was uniplanar, according to the classification of Heffelfinger and Burton(6). In fact, two major uniplanar textures coexist, the (010) [001] and the (110) [001] textures, as discussed in 7.1.3. The (010) [001] texture may be interpreted as the preferential orientation of the *b* crystallographic axis perpendicular to the MD-TD plane, with the *c* axis oriented uniformly in the plane of the film, as schematically represented in Figure 4-5. This type of preferential orientation of the *b* axis for biaxially oriented iPP films has been reported by several authors using pole figure measurements (7-9). Another study reported that the predominance of the (010) [001] texture in biaxially oriented iPP films was attributed to the fact that deformation of iPP is dominated by the (010) [001] chain slip mechanism (10). The (010) [001] chain slip system consists of the *c*-axis shearing of the lamellae along the (010) plane, as illustrated in Figure 2-12. The equibiaxial deformation is thus dominated by this chain slip system, for the 140°C – 160°C temperature range.

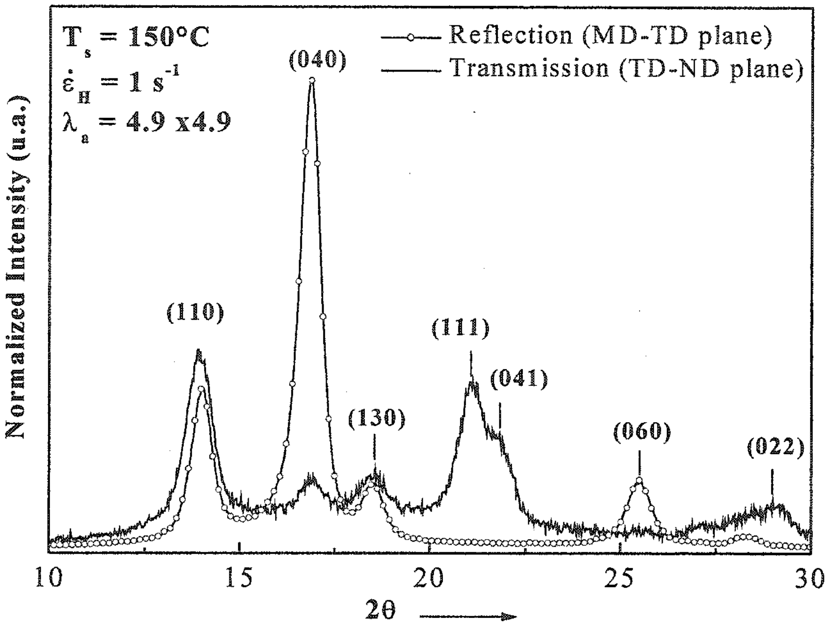

Figure 7-4 *Comparison between the WAXD patterns measured in reflection (MD-TD plane) and transmission (TD-ND plane) for a simultaneously equibiaxially stretched film*

All the WAXD patterns of the films simultaneously equibiaxially stretched in the 140°C – 160°C temperature range showed the same tendency with increasing stretching ratio, as illustrated in Figure 7-3. Only the peak intensities and widths varied with drawing temperature, as discussed below. The measurements in reflection were chosen for investigating the evolution of the morphology during stretching, because they provide information about the orientation of the main crystal planes in the stretching plane. The WAXD patterns measured in reflection showed that the main remaining peaks for highly stretched samples were the (110) and (040) diffraction peaks. Thus, the widths of these peaks were used to estimate the D_{110} and D_{040} apparent crystallite sizes, using Scherrer equation (cf. Chapter 4).

Figure 7-5 displays the evolution of the D_{110} and D_{040} apparent crystallite sizes with increasing stretching ratio for the PP2 samples stretched at 140°C, 150°C, and 160°C. The apparent crystallite sizes D_{110} and D_{040} decrease with increasing stretching at constant temperature, and increase with raising drawing temperature at constant stretching ratio. The apparent crystallite sizes of the 2 x 2 stretched film are similar to the values for the preheated sample. A change in slope occurs in the apparent crystallite size vs. stretching ratio at around the 3 x 3 stretching ratio. The D_{110} and D_{040} apparent crystallite sizes behave similarly in most cases, and the (040) diffraction peak tends to be stronger in intensity. Therefore, only the D_{040} apparent crystallite size was used to characterize stretched film morphology.

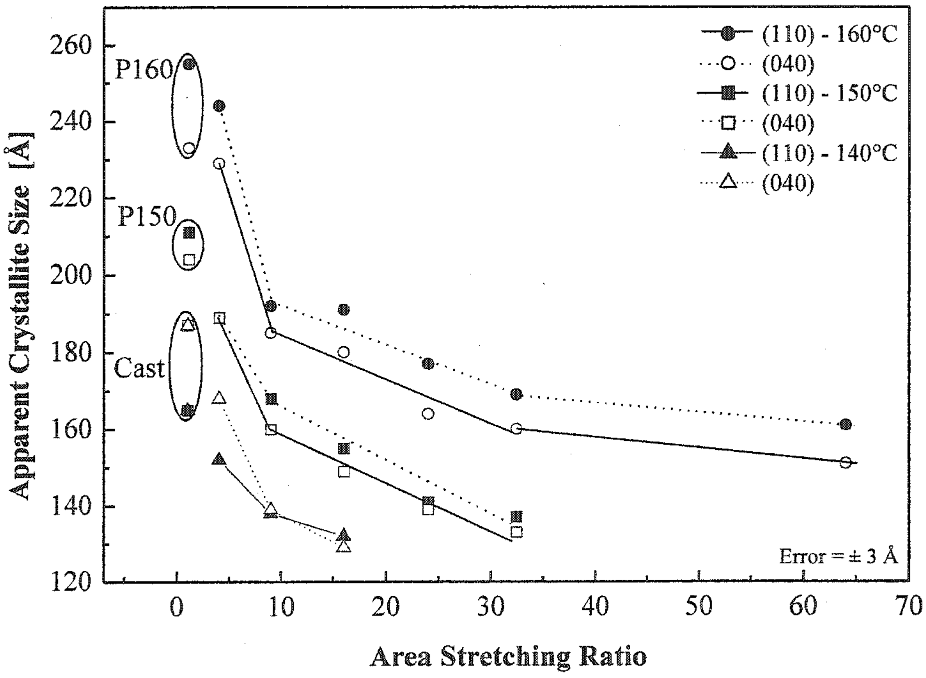

Figure 7-5 *Effects of the area stretching ratio and drawing temperature on the D_{110} and D_{040} apparent crystallite sizes for equibiaxially stretched PP2 films*

The D_{110} and D_{040} distances represent a weight average of the crystallite size in the directions perpendicular to the (040) and (110) crystal planes. For an ideal lamellar crystal, the value of D_{040} can be simply related to the lamellae size in the *b*-axis direction. Because the X-ray measurements were carried out in the MD-TD sample plane, D_{110} and D_{040} represent a dimension normal to the MD-TD plane, i.e. in the ND sample direction. Therefore, the decrease in D_{110} and D_{040} can be seen as a the reduction in size of the unit structure of the oriented morphology in the direction perpendicular to the stretching plane. Sakai et al. (11) reported similar results for polyethylene gels that were biaxially stretched. Most importantly, the decrease in D_{040} and D_{110} is in agreement with the dominant crystallographic chain slip mechanisms known for the α-form of iPP, the (010) [001] and (110) [001] slip systems (10, 12-14).

The D_{110} and D_{040} crystallite sizes increase with increasing temperature, at constant stretching ratio. Similarly to the DSC results, the stretching temperature influences greatly the dimensions of the crystal blocks forming the oriented fibrous structure. Raising temperature contributes to an increase in partial melting (cf. Chapter 5) and to a rise in chain mobility, which loosens some tie molecules and entangled chains. This contributes to increased deformation through the fine chain slip mechanism and, thus, to reduced lamellar fragmentation. Fine chain slip consists of the tilting of the *c*-axis chains in lamellae and rotation of the lamellar crystals in the drawing direction without lamellar break-up (cf. Figure 2-11). The high chain mobility contributes also to high chain rearrangement during stretching and subsequent cooling, which leads to more perfected and larger crystallites.

Figure 7-6 shows the evolution of the (040) in-plane orientation index with drawing temperature and stretching ratio. The in-plane orientation increased with area stretching ratio, at all temperatures, following the pseudo-affine deformation pattern (15). It shows a rapid initial increase, followed by a gradual approach towards a plateau. It is interesting to note that all the curves intersect at $\lambda_a \sim 10$ (3.3 x 3.3). An area stretching ratio of 10 represents a critical value, since below that value, the in-plane orientation index increases with drawing temperature, while it decreases with increasing drawing temperature above that stretching ratio.

The evolution of the *b*-axis orientation in ND was shown to be proportional to the (040) in-plane orientation index, which is defined in eq.(4-7) (cf. Chapter 4). An increase in the (040) in-plane orientation index indicates that the *b*-axis orientation in ND and the c-axis orientation in the MD-TD plane increase.

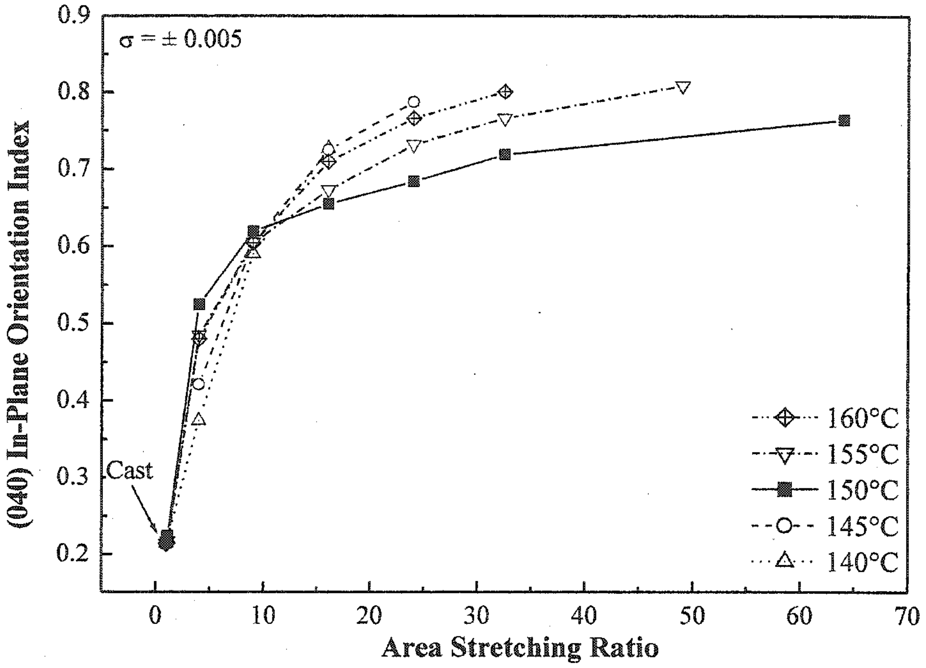

Figure 7-6 *Effects of the area stretching ratio and drawing temperature on the (040) in-plane orientation index for equibiaxially stretched PP2 films*

The area stretching ratio of 10 (3.3 x 3.3) represents an orientation state in which the proportion of (040) crystal planes oriented in the MD-TD plane is independent of stretching temperature, for the 140°C – 160°C range. The 3.3 x 3.3 stretching ratio seems to be the ratio at which the major part of the original film morphology has been transformed into an oriented structure. Indeed, a similar study on biaxially stretched iPP by Tanaka et al. (16) indicated that the area stretching ratio of 10 represented an important transition in deformation mechanisms. The authors suggested that the unfolding of lamellae becomes dominant above this area stretching ratio. Furthermore, the value of 10 was also reported to be the initial draw ratio measured in the necked regions for uniaxially deformed samples (17). It was deduced that, above an area stretching ratio of 10, the crystalline deformation is dominated by the *c*-axis shearing of the oriented structure through the (010) chain slip mechanism.

7.1.1.2 - Conclusions

The deformation at room temperature of the original spherulitic-lamellar model of iPP can be summarized as follows. Initially, the deformation is borne by the relatively mobile amorphous regions (17). Subsequently, for $\lambda_a < 10$, lamellar stacks are rotated to the draw axis and lamellae break into many small folded chain blocks (18). These blocks become highly extended on drawing and form the structural units of the oriented fibrous structure (18). Finally, for $\lambda_a > 10$, shear deformation of the oriented structure occur, (18). Deformation of iPP at room temperature can be seen as a strain-induced crystalline texture change (5).

The study of the effects of drawing temperature and stretching ratio on film morphology showed that the biaxial stretching in the partly molten state involves more than just a strain-induced crystalline texture change. Lamellar thickening, melting, and recrystallization are among the mechanisms that must be considered in addition to the deformation mechanisms to understand the development of the morphology.

The equibiaxial stretching in the 140°C-163°C temperature range was found to induce the coexistence of two uniplanar textures, the (010) [001] and (110) [001] textures, with a predominance of the former one. The (010) [001] texture corresponds to the preferential orientation of the (040) crystal planes in the deformation plane and to the *b*-axis orientation in the ND sample direction. The *c*-axis is randomly oriented in the deformation plane. Wide angle X-ray diffraction measurements in reflection were used to estimate the (040) in-plane orientation index.

The degree of crystallinity, the thermal stability (T_m), and the crystallite size all increase with an increase in the drawing temperature. Only the in-plane orientation was found to decrease with increasing temperature, for the films stretched above the critical area stretching ratio of 10. At that stretching ratio, most of the initial morphology is transformed into the oriented fibrous structure. Crystallinity and the melting point increase slightly with increasing area stretching ratio, while the crystallite size decreases considerably. The (040) in-plane orientation increases with stretching. The decrease in

D_{110} and D_{040} crystallite size and the increase in (040) in-plane orientation with increasing stretching ratio were explained by the dominant chain slip mechanisms. Above an area stretching ratio of 10, the crystalline deformation is dominated by the *c*-axis shearing of the oriented structure through the (010) chain slip mechanism.

7.1.2 - Effect of Strain rate on the Biaxially Stretched Film Morphology

A series of PP2 cast film samples were stretched up to the same area stretching ratio (4.9 x 4.9) with different strain rates and strain rate profile to study the effect of the latter on the stretched film morphology. Both Cauchy ($\dot{\varepsilon}_C$) and Hencky ($\dot{\varepsilon}_H$) strain rate profiles were employed. Cauchy strain rates correspond to a constant extension speed, while Hencky strain rates to a constant strain rate. The range of strain rates investigated here was restricted to one decade, due to apparatus limitations, as discussed in Chapter 6.

7.1.2.1 - Results

All the stretched films showed the same melting behavior for the same area stretching ratio, i.e., a single melting peak, similar to that shown in Figure 7-1. The degree of crystallinity of the different films was found to be constant within measurement error (cf. Figure C-1 in App. C). Figure 7-7 shows the dependence of the melting point on strain rate and strain rate profile for the equibiaxially stretched PP2 films. All the measured temperatures were within 1°C. Nevertheless, a very slight decrease of the melting point with increasing strain rate was observed for both Cauchy and Hencky strain rates. The melting points for the Hencky strain rate profile were overall slightly lower (0.4°C) than those for the Cauchy profile.

The X-ray measurements yielded similar WAXD patterns for all stretched films. Nevertheless, the peak intensities and widths differed slightly. Figure 7-8 illustrates the influence of the strain rate on the apparent crystallite size. For the range of strain rates under consideration, the apparent crystallite size was found to increase with increasing strain rate.

Figure 7-9 displays the (040) in-plane orientation index as a function of the strain rate for the same series of films. The (040) in-plane orientation decreases with increasing strain rate. The average squared cosine of the *b*-axis orientation in ND obtained from the pole figure measurements confirmed the decrease of the amount of (040) crystal planes that are oriented in-plane (cf. Figure 7-9). A small influence of the strain rate profile can be distinguished. The Hencky strain rate profile produced specimens with lower (040) in-plane orientation.

7.1.2.2 - Discussion and Conclusions

The results showed that the total amount of crystalline entities and the melting behavior were not significantly affected by the strain rate or strain rate profile. Nevertheless, the apparent crystallite size was found to increase with strain rate. This increase can be explained by the effect of the strain rate on the macroscopic deformation behavior of the specimen, as discussed in Chapter 6. The unexpected decrease of orientation was also attributed to the deformation behavior of the stretched films. The film thickness profile was influenced by the strain rate; the lower is the strain rate, the thinner is the end film. Decreasing the strain rate led to a film thickness decrease (5%) that was found quantitatively comparable to the increase in the true draw ratio (5%) of the final film, and to the increase in orientation (6%) and the decrease in crystallite size (6%) in the final film morphology.

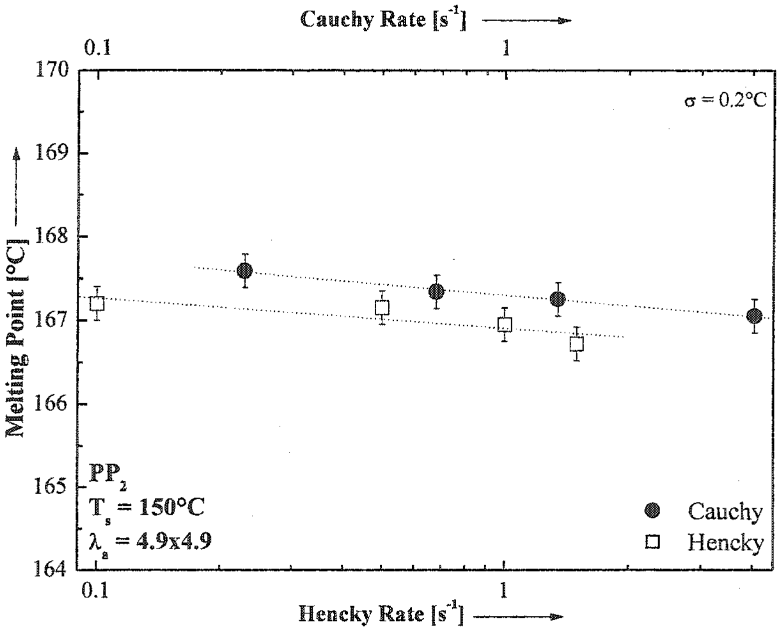

Figure 7-7 *Effect of strain rate on the melting point for PP2 films equibiaxially stretched at 150°C up to a 4.9x4.9 area stretching ratio*

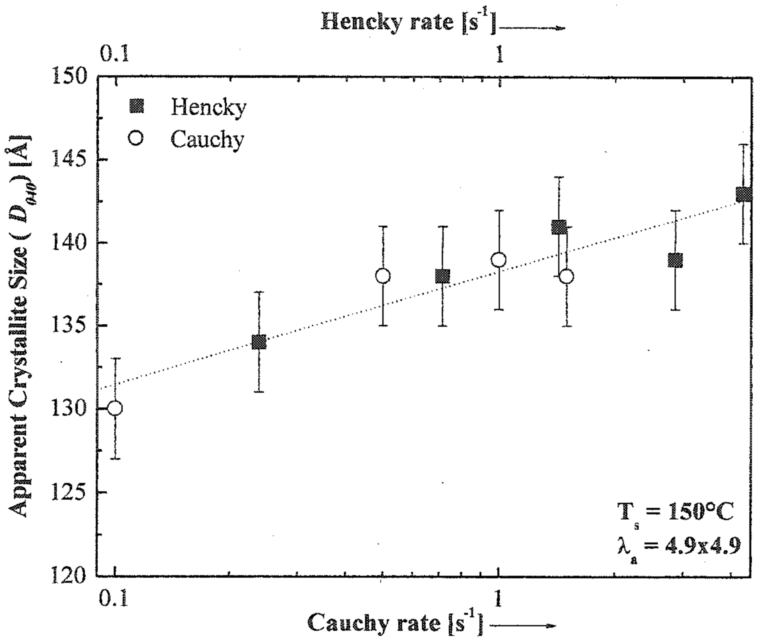

Figure 7-8 *Effect of strain rate on the apparent crystallite size for PP2 films equibiaxially stretched at 150°C up to a 4.9x4.9 area stretching ratio*

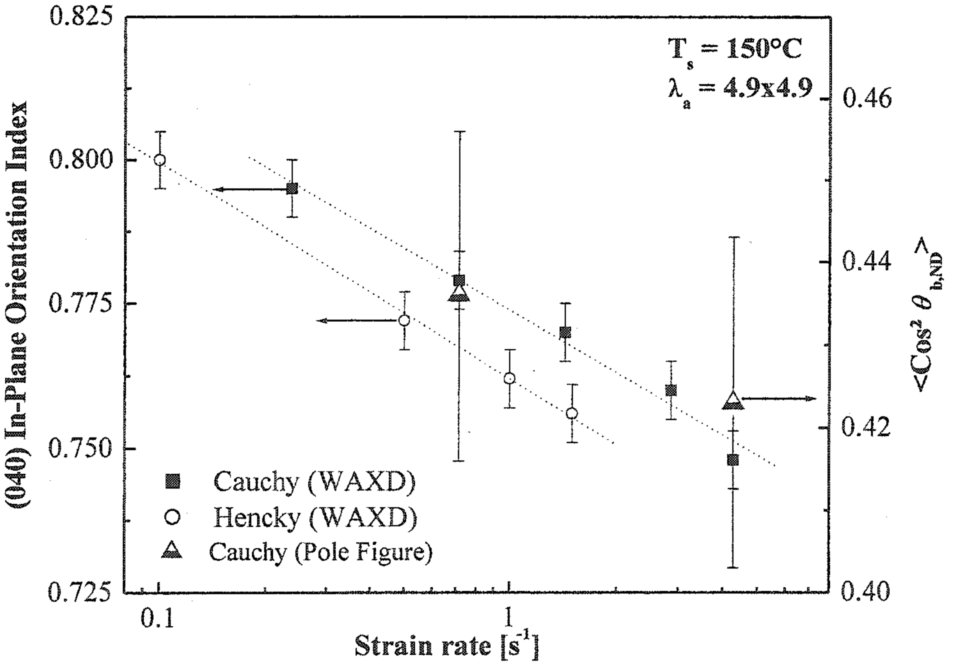

Figure 7-9 Effect of strain rate on the (040) in-plane orientation for PP2 films equibiaxially stretched at 150°c up to a 4.9x4.9 area stretching ratio

7.1.3 - Effect of Deformation Type on the Equibiaxially Stretched Film Morphology

The effect of the type of deformation on stretched film morphology was investigated by drawing samples under uniaxial, planar, non-equibiaxial, and equibiaxial deformation. Non-equibiaxial stretching corresponds to deformation in which a specimen was simultaneously biaxially stretched up to different stretching ratios in the MD and TD directions. The results are presented and discussed in Appendix C.

The following conclusions were made about the effect of deformation type on the resulting crystalline texture. The pole figure measurements confirmed the previous conclusion that simultaneous equibiaxial deformation generates a crystalline texture with two components: the (010) [001] and (110) [001] uniplanar textures (10). It was also confirmed that the (010) [001] texture dominates the (110) [001] texture in the equibiaxially stretched samples. The deformation type influences the crystalline texture and orientation distribution along the sample directions. Equibiaxial stretching produces a uniform morphology and orientation in the deformation plane. Decreasing the biaxiality led to a preferential orientation of the chain axis in the direction of the main stretching direction, while keeping the *b*-axis preferentially oriented in ND and in the minor stretching direction. Uniaxial and planar deformation were found to have similar crystalline textures.

The study of the effect of deformation type on film morphology showed that the other major effect of deformation type is on the lamellar morphology. At a given area stretching ratio, equibiaxial stretching led to a much larger decrease in crystallite size in the major deformation direction and lower melting point than uniaxial or planar deformation. This may be attributed to (1) increased lamellar fragmentation due to the reduced mobility of the lamellar crystals, when subjected to plane deformation compared to axial deformation and (2) to the differences in the actual area stretching ratio.

7.2 - Effect of Initial Film Morphology on the Equibiaxially Stretched Film Morphology

Two sets of distinct film morphologies prepared with the PP2 and PP4 resins were investigated under simultaneous equibiaxial deformation, in order to assess the effect of the initial film morphology on the final biaxially stretched film morphology. The structural characteristics of the two sets of initial films and their deformation behavior can be found in Chapters 5 and 6, respectively. Initially, the results for the standard, melt-crystallized cast films are discussed. Subsequently, we discuss the results for the annealed cast films.

7.2.1 - Melt-Crystallized Cast Films

The PP4-CFx and PP2 cast films were produced under similar conditions, by casting the extruded melt onto a chill roll half immersed in a water bath. The cooling temperatures were different for the PP4-CFx cast film, increasing from 20°C (CF1) to 85°C (CF4), and PP2 was also produced with a cooling temperature of 20°C (cf. Table 4-3). PP2 was included in this comparison, since it has similar molecular characteristics to resin PP4, but differs in crystallization behavior (cf. Table 4-1). The cast films were equibiaxially stretched under the same stretching conditions at 150°C and 160°C.

The DSC melting curves for the stretched films exhibited one single narrow melting peak, comparable to the curves shown in Figure 7-1. The WAXD patterns showed also the same three characteristic diffraction peaks observed for equibiaxially stretched films, as shown in Figure 7-3. The final degree of crystallinity for the various stretched samples increased slightly (about 2%), as the initial crystallinity increased from 38% to 44% for both stretching temperatures (cf. Figure C-2 in App. C). The crystallinities of the PP2 stretched films were similar to the corresponding PP4 stretched films. Figure 7-10 illustrates the effect of the various initial melt-crystallized film crystallinities on the high temperature melting point of the equibiaxially stretched films up to a 4.9 x 4.9 stretching ratio at 150°C and 160°C. The melting point of the stretched specimen increases with increasing drawing temperature, as already reported in 7.1. In addition, a small increase is observed in the melting point of the stretched films (less than one degree Celsius), as the cast film crystallinity increases by about 6%. This was observed for both stretching temperatures. The effect of stretching on T_m was found to follow the same trend for both temperatures and for the PP2 cast film.

It can be concluded that the final degree of crystallinity and the thermal stability (T_m) are only slightly influenced by the initial morphology. Both characteristics increase slightly for a large increase in initial crystallinity. The differences in crystal form contents, spherulite size and type, lamellar morphology, and tie molecule fraction for the CFx cast samples make it difficult to make additional conclusions.

Figure 7-11 shows the apparent crystallite size as a function of the initial degree of crystallinity for the various cast films, stretched at both temperatures. The apparent crystallite size increases slightly with increasing initial crystallinity, for both resins and both temperatures.

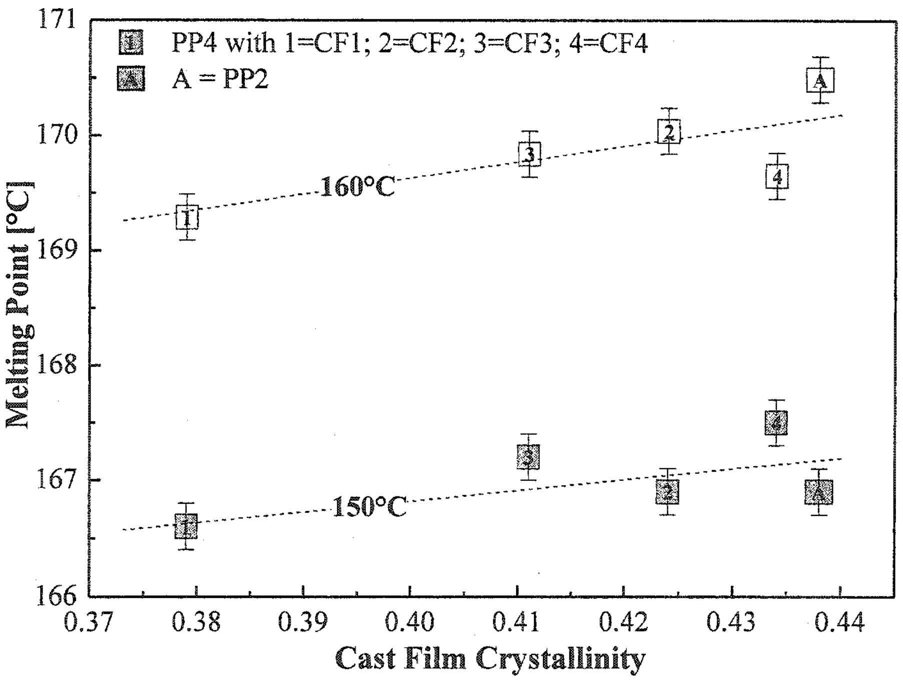

Figure 7-10 *Effect of the initial cast film crystallinity on the melting point of equibiaxially stretched films at 150°C and 160°C C (Cast film crystallinity obtained from DSC measurements)*

Figure 7-12 shows the influence of the initial cast film crystallinity on the (040) in-plane orientation index. The latter decreases with increasing initial crystallinity for stretching at 150°C, while it seems to be independent of the initial crystallinity for stretching at 160°C. The PP2 cast film seems to exhibit similar behavior.

The results for the melt-crystallized films suggested that the apparent crystallite size increases and the (040) in-plane orientation decreases slightly with increasing the initial crystallinity, when stretched at 150°C. The reduced in-plane orientation was significant only for the CF4 morphology. The decrease in (040) in-plane orientation indicates reduced lamellar fragmentation through the (010) [001] chain slip mechanism. This reduction in orientation is probably related to the presence of the β-phase. The combined thermal and mechanical transformation of the β-phase into the monoclinic phase may hinder deformation and reduce orientation. The role of the β-phase is supported by the fact that at 160°C, when the β-phase is completely melted, the orientation for the CF4 is similar to that for the other samples.

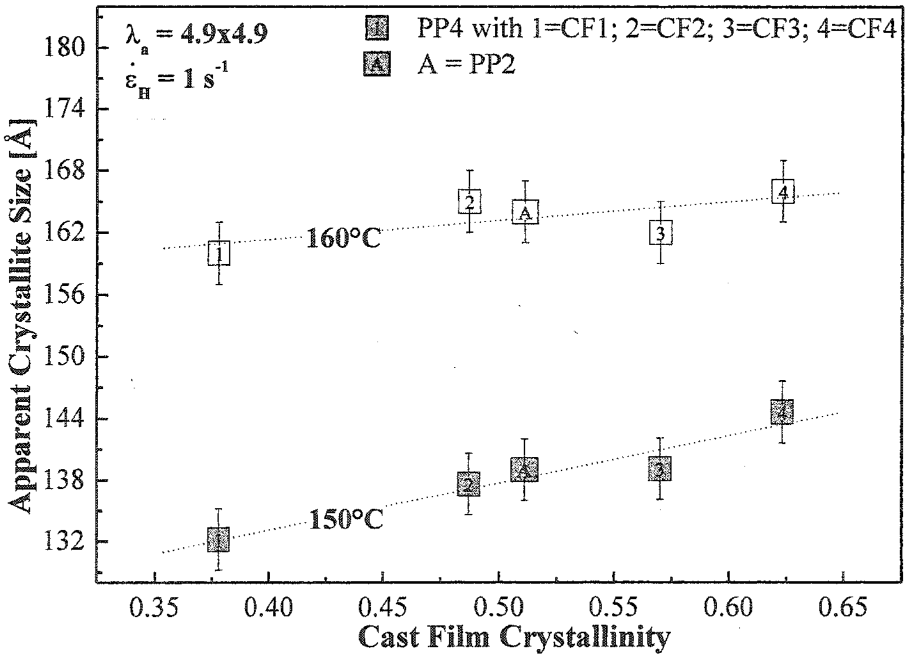

Figure 7-11 *Effect of the initial cast film crystallinity on the D_{040} apparent crystallite size of equibiaxially stretched films at 150°C and 160°C (Cast film crystallinity obtained from WAXD measurements)*

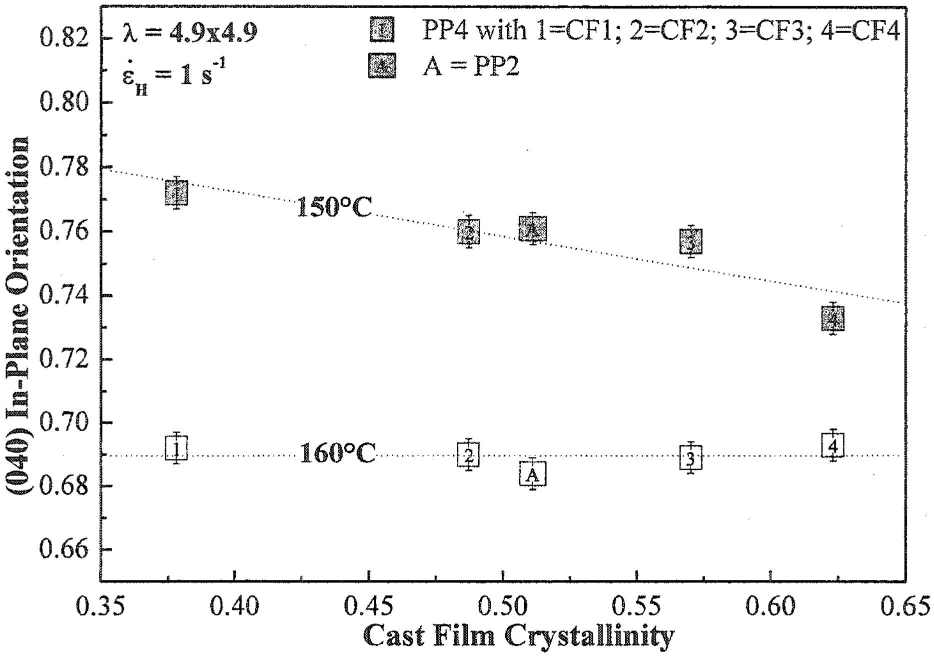

Figure 7-12 *Effect of the initial cast film crystallinity on the (040) in-plane orientation of equibiaxially stretched films at 150°C and 160°C (Cast film crystallinity obtained from WAXD measurements)*

7.2.2 - Annealed Cast Films

The PP2 melt-crystallized cast film was annealed at different temperatures to provide a set of annealed cast films having different morphology from that for the standard, melt-crystallized cast films. The annealed cast films were simultaneously equibiaxially stretched at 150°C with a constant strain rate of 0.68 s^{-1}. The films were then characterized by DSC and WAXD. The DSC crystallinity of the stretched film was found to increase only slightly with increasing initial crystallinity. The final crystallinity increased by 3% for an increase in initial crystallinity from 44% to 59% (cf. Figure C-3 in App. C and in Table 7-1). These results confirmed the results for the melt-crystallized samples, i.e., the weak increase in final crystallinity with increasing the initial crystallinity. The increase was approximately linear as a function of the unmolten crystallinity. Therefore, for constant stretching conditions, the amount of crystalline phase present in the partly molten morphology appears to influence, to some extent, the final crystallinity.

Table 7-1 Morphological characteristics of the PP2 annealed films equibiaxially stretched up to a 4 x 4 stretching ratio at 150°C

Cast Film	**CI_{DSC}** [-]	**Tm** [°C]	**D_{110}** [Å]	**D_{040}** [Å]	**IPO_{040}** [-]	**IPO_{110}** [-]
PP2	0.5194	167.3	157	150	0.729	0.185
PP2-A100	0.5091	167.4	158	150	0.741	0.180
PP2-A143	0.5163	166.7	132	126	0.789	0.170
PP2-A150	0.5139	167.0	131	127	0.766	0.186
PP2-A157	0.5289	167.0	-	-	-	-
PP2-A160	0.5340	169.7	126	122	0.688	0.200

The melting points of the stretched films were found to range within 1°C around 167°C, except for the film stretched from the sample annealed at 160°C, which had a melting point of about 169°C, as shown in Table 7-1. This can be explained by the interlamellar cavitation associated with the appearance of stress whitening (19, 20). Zhang et al. (20) reported that void formation is a necessary precursor to interlamellar shear, when the chains in the amorphous phase are constrained or crystal shear is difficult because of large crystal thickness. Moreover, cavitation is usually coupled with the generation of fibrils perpendicular to the stress directions (19). Generally, deformation is assumed to occur at constant volume. However, the appearance of the mircro-voids implies a volume increase in the case of the stretching of A160. This means that the local true stretching ratio is higher than the measured value, which could partly explain the higher melting point.

The crystallite size and in-plane orientation appeared to have no specific dependence on variations in the initial crystallinities. Since it was shown previously (cf. Chapter 6) that the annealed cast films exhibited differences in deformation behavior (i.e., yield region sharpness) that caused differences in stretched film thickness profiles, correlations were sought between film thickness and apparent crystallite size. Figure 7-13 shows the change in crystallite sizes for the PP2-A1xx stretched films, as plotted versus the corresponding film thickness. The crystallite sizes for the sample annealed at 100°C are almost identical to those of the original PP2 cast film. However, the crystallite sizes are reduced considerably for the other annealed films, even for comparable film thickness. In fact, the crystallite sizes for the three other samples are almost identical, despite the large differences in their thicknesses.

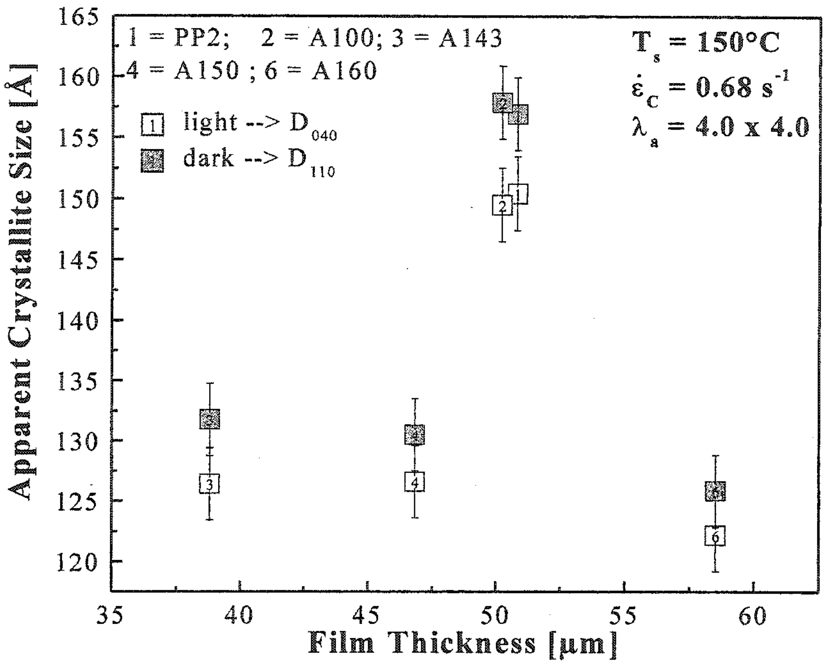

Figure 7-13 Relation between the film thicknesses and the apparent crystallite sizes for the annealed cast films equibiaxially stretched at 150°C

Figure 7-14 shows the variation of the (040) in-plane orientation index and the average squared cosine of the *b*-axis orientation in ND (from infrared dichroism), as functions of the film thickness. The (040) in-plane orientation obtained from X-ray experiments and $\langle\cos^2\theta_{b,ND}\rangle$ from infrared dichroism measurements are in reasonably good agreement. The (040) in-plane orientation increases with decreasing film thickness, for films stretched up to the same area stretching ratio. These results point out the importance of the effect of the initial film morphology on the film thickness profile, as will be discussed below.

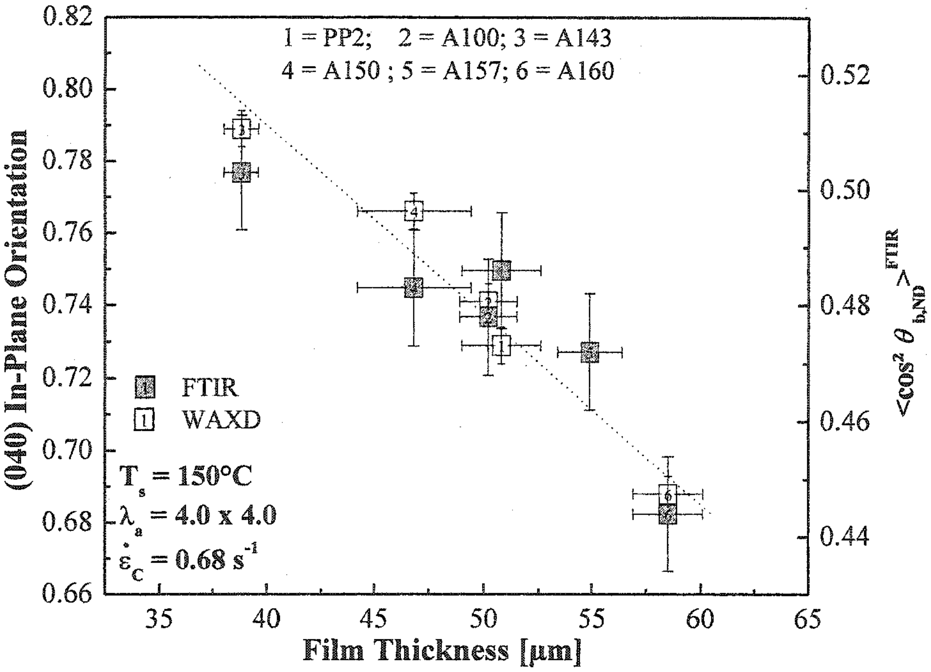

Figure 7-14 *(040) in-plane orientation from WAXD and <$\cos^2\theta_{b,ND}$> from infrared dichroism measurements for the annealed cast films equibiaxially stretched at 150°C, plotted versus film thickness*

The annealed films showed a different dependence on initial morphology compared to the melt-crystallized samples. The in-plane orientation index is mainly correlated with the true area stretching ratio or the film thickness. This result is a direct consequence of the macroscopic deformation behavior. In Chapter 6, it was shown that the film thickness profile was correlated with the yield region sharpness, which is associated mainly with the fraction of tie molecules in the initial film morphology.

The large decrease in crystallite size of ~ 19% observed for the A143 film matches the increase in true draw ratio of ~ 17%. However, the even lower values (max. of ~4%) for the A150 and A160 stretched samples could not be explained by the true draw ratio, which decreased by ~ 20%. If the crystallite size in the final stretched film morphology is an indicator of the severity of the lamellar break-up and shear deformation of the oriented structure that occurs during stretching, then the A150 and A160 initial film morphologies were subjected to an important lamellar fragmentation. The following possible structural features could explain the situation: (i) the tie molecule fraction and (ii) the unmolten crystallinity. In fact, these two annealed cast film morphologies were shown to have a higher density of tie molecules and larger unmolten crystallinity (cf. Chapter 5 & 6). The tie molecules hinder interlamellar rearrangements and fine chain slip deformation. They contribute to more important lamellar fragmentation via other chain slip mechanisms, as confirmed by the increased (110) in-plane orientation, as shown in Table 7-1. Furthermore, the large amount of unmolten crystalline phase present during stretching would also impede the lamellar mobility contributing to the enhanced break-up of the crystallites, rather than fine chain slippage.

7.2.3 - Conclusions

The study of the effect of the initial film morphology on the equibiaxially stretched film morphology showed that the initial crystallinity has a small effect on the final degree of crystallinity and the melting point. The final crystallinity was correlated with the amount of unmolten crystalline phase present in the partly molten morphology. The in-plane orientation was significantly influenced by the initial annealed film morphology. The in-plane orientation was correlated with the local true draw ratio of the film, which is determined by the deformation behavior of the initial film. The crystallite size was strongly influenced by the level of unmolten crystallinity and the tie molecule fraction. Both contributed to an enhanced fragmentation of the lamellar structure.

7.3 - Effect of Chain Tacticity on the Equibiaxially Stretched Film Morphology

The effect of chain tacticity on the stretched film morphology was investigated for the PP1, PP2, and PP3 homopolymer resins. They had isotacticity indices of 94.8 %, 98.6 %, and 99.5 %, respectively. The three corresponding cast films were simultaneously equibiaxially stretched under various, but similar conditions. In the present work, it has been assumed that, in the range of molecular weights and molecular weight distributions considered, these two properties do not have a significant influence on film morphology in comparison with the effect of chain tacticity. Therefore, only the effect of isotacticity content is considered in this analysis.

7.3.1 - Results

The DSC melting behavior is compared in Figure 7-15 for the PP1, PP2, and PP3 films equibiaxially stretched under identical conditions. The characteristics of the melting curves for the three films are similar: a broad low-temperature tail followed by a narrow melting peak. However, a large difference in the position of the melting peak can be observed. The melting peak is seen to be shifted from 162°C to 168°C with increasing chain tacticity from 94.8 % to 99.5 %, as listed in Table 7-2.

Table 7-2 lists the DSC crystallinity, melting point, crystallite size, and (040) in-plane orientation indices of the PP1, PP2, and PP3 films that were stretched at various temperatures. It can be seen that the degree of crystallinity increases with the drawing temperature for all three resins (cf. Figure C-4 in App. C). Furthermore, the degree of crystallinity increases with chain tacticity, for constant stretching conditions. The crystallinity for the PP3 films is particularly larger than for the PP1 and PP2 films.

Table 7-2 shows also that the melting point increases with increased stretching temperature for the three resins. Moreover, the melting point increases with increasing chain tacticity, for constant stretching conditions (cf. Figure C-5 in App. C). The differences in crystallinity and melting point due to tacticity are large, compared to those attributed to the effects of the strain rate or the initial morphology.

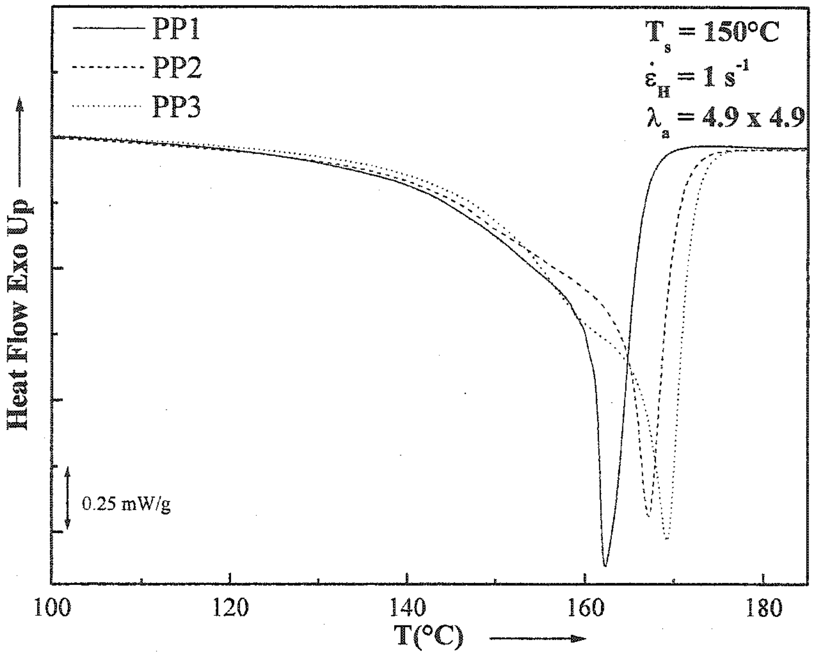

Figure 7-15 *DSC melting curves of the three homopolymer resins stretched equibiaxially at 150°C up to a 4.9 x 4.9 stretching ratio*

Crystallinity (DSC) [-]

Cast Film (I.I.)	**145**	**150**	**153**	**155**	**158**	**160**	**163**
PP1 (94.8)	0.4652	0.4887	-	0.4928	-		-
PP2 (98.6)	0.4835	0.4952	-	0.5096	-	0.5392	-
PP3 (99.5)	-	0.5636	0.5617	0.5641	0.5718	-	0.6134

Melting Point [°C]

Cast Film (I.I.)	**145**	**150**	**153**	**155**	**158**	**160**	**163**
PP1 (94.8)	162.5	163.4	-	164.1	-	-	-
PP2 (98.6)	166.4	167.2	-	168.7	-	170.2	-
PP3 (99.5)	-	169.6	170.3	170.4	171.0	-	172.0

D040 Apparent Crystallite Size [Å]

Cast Film (I.I.)	**145**	**150**	**153**	**155**	**158**	**160**	**163**
PP1 (94.8)	137	150	-	166	-	-	-
PP2 (98.6)	128	140	-	150	-	164	-
PP3 (99.5)	-	139	144	-	158	-	181

(040) In-Plane Orientation Index [-]

Cast Film (I.I.)	**145**	**150**	**153**	**155**	**158**	**160**	**163**
PP1 (94.8)	0.759	0.730	-	0.703	-	-	-
PP2 (98.6)	0.787	0.761	-	0.732	-	0.684	-
PP3 (99.5)	-	0.778	0.767	-	0.744	-	0.712

Table 7-2 *DSC crystallinity index, melting point, crystallite size, and (040) in-plane orientation of the PP1,PP2, and PP3 film samples that were stretched at different temperatures up to a 4.9 x 4.9 stretching ratio*

All the WAXD patterns obtained for the different stretched films followed the same pattern, exhibiting strong (110) and (040) peaks, as already discussed in 7.1. Table 7-2 shows that the apparent crystallite size exhibits the same trend for all three resins. The crystallite size increases with stretching temperature. Additionally, the PP2 and PP3 resins exhibit similar values of the apparent crystallite size at the different drawing temperatures, whereas PP1 shows the highest values for all temperatures investigated.

The (040) in-plane orientation decreases with increasing drawing temperature for all three resins, as shown in Table 7-2. For constant stretching conditions, the (040) crystal plane orientation increases with increasing tacticity.

To our knowledge, no studies have been reported about the effect of the isotacticity content of polypropylene resins on the morphology of biaxially stretched films. The present DSC and X-ray results show that the equibiaxially stretched morphology is strongly influenced by chain tacticity. The degree of crystallinity, the melting point, and the (040) in-plane orientation increase considerably with increasing chain tacticity. A similar increase in orientation with tacticity was recently reported for iPP fibers by Choi et al. (21). The apparent crystallite size was found to be less dependent on chain tacticity.

7.3.2 - Discussion and Conclusions

An attempt was made to correlate the chain tacticity, the structural features of the partly molten morphology, and the final stretched morphology. It was shown in Chapters 5 & 6 that the thermal stability of the initial lamellar morphology increased with chain tacticity. The thermal stability, in turn, determines the structural characteristics of the partly molten state: the amount of melt phase that results from the melting of crystallites, i.e., the structured melt. The concept of "structured melt" has been introduced to explain the high nucleating efficiency of a polymer melt heated to a temperature just above its melting point (22). These "molten" molecules may be considered as having higher structural order, and thus, less entangled than those in the amorphous phase. Therefore, the dependence of the morphological characteristics of the equibiaxially stretched films was investigated with respect to the amount of structured melt.

The degrees of crystallinity and the melting points of the stretched films for three resins exhibited similar dependence on temperature. However, the overall level of both properties was increased notably with increasing tacticity, as seen in Table 7-2. The increase in crystallinity, $\Delta\chi = \chi^{Film} - \chi^{Cast}$, and the increase in melting point, $\Delta T_m = T_m^{Film} - T_m^{Cast}$ were plotted versus the molten crystallinity. Figure 7-16 shows that the increase in crystallinity during stretching exhibits linear dependence on the amount of structured melt present in the film, and is independent of the isotacticity content. A similar dependence on the structured melt was observed for the melting point, as shown in Figure 7-17. X-ray measurements revealed similar results for the (040) in-plane orientation, as shown in Figure 7-18. There seems to be again a linear relationship between the (040) in-plane orientation and the amount of structured melt for all three resins.

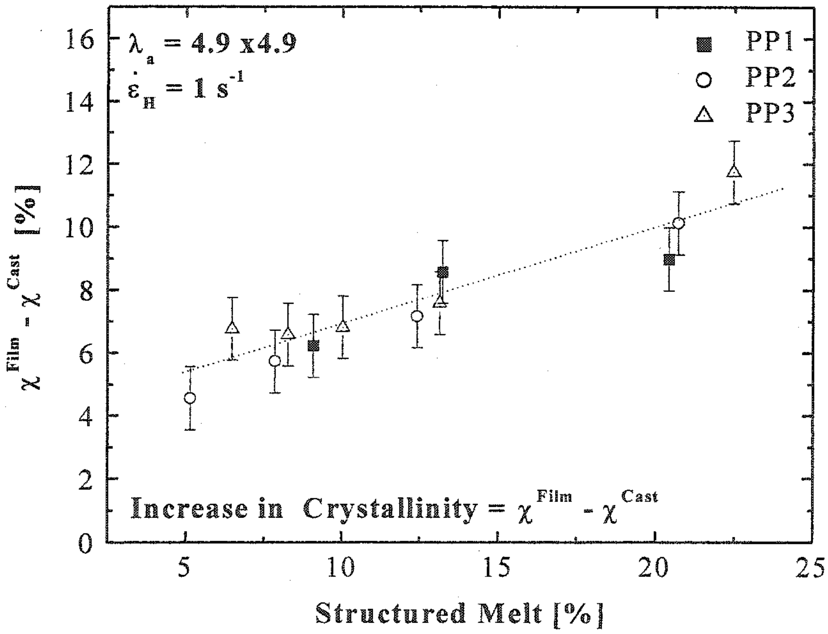

Figure 7-16 Increase in crystallinity due to stretching versus the structured melt for the three homopolymer resins

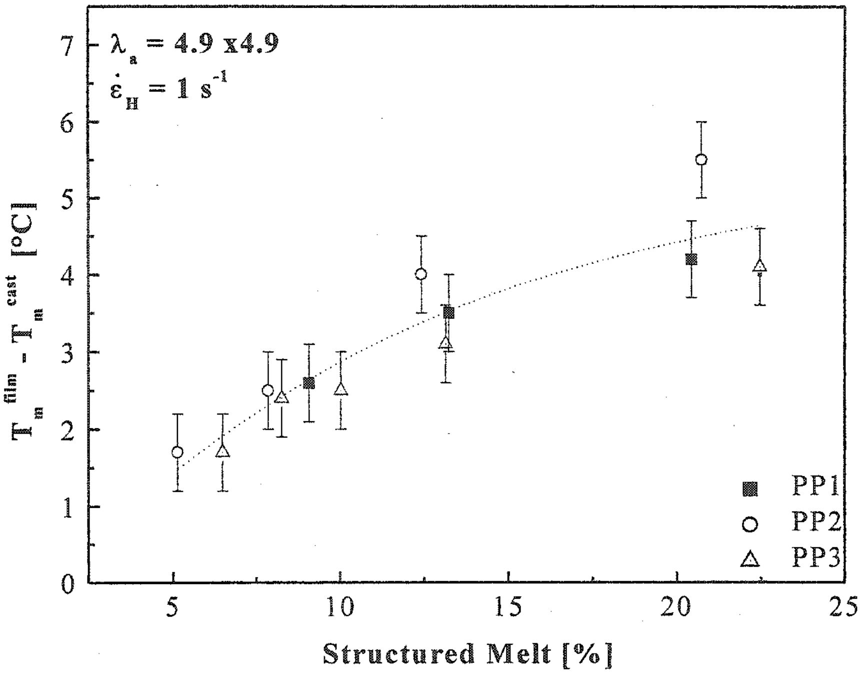

Figure 7-17 *Increase in melting temperature due to stretching versus the molten crystallinity for the three homopolymer resins*

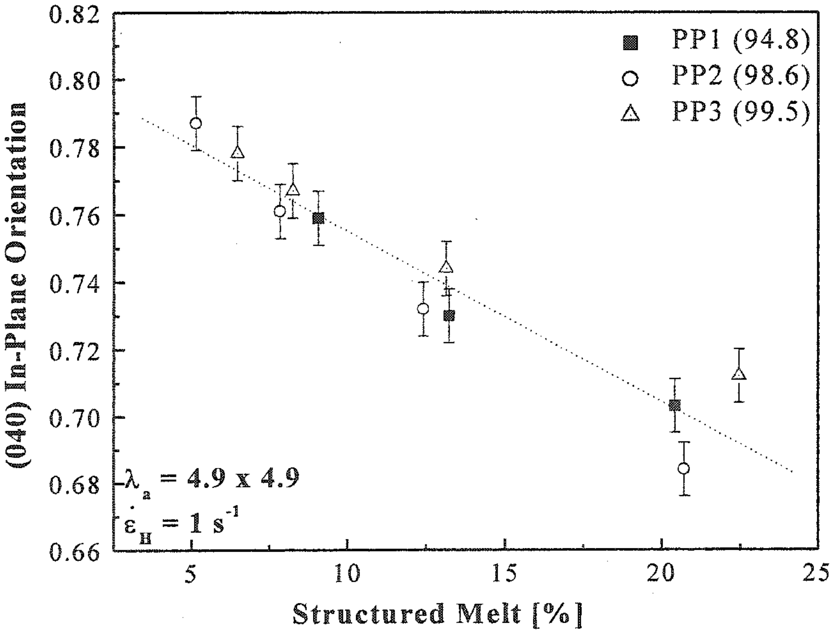

Figure 7-18 *(040) in-plane orientation versus $T_m - T_s$ for the three homopolymer resins*

The change in crystallite size due to stretching is also dependent on the amount of structured melt. However, this dependence was not independent of the resin. The change in crystallite size was identical for both PP2 and PP3 and lower for PP1, when compared for the same amount of structured melt. In the end, the final crystallite sizes were found within a small range of about 10 Å for all three resins, when compared at the same amount of structured melt.

It was found that there is linear correlation between the in-plane orientation and the amount of structured melt present in the film at the stretching temperature. It is proposed that the molecular chains in the structured melt will bear the deformation, after the short-range rearrangements in the amorphous phase have occurred in the first step of stretching. The weakly structured molten phase is more orientable than the amorphous phase because the "molten" chains are less entangled than the chains in the amorphous phase. Thus, it is assumed that large deformation will be first borne by the structured melt phase, where the molecular mobility is high, compared to the other two phases. This contributes to large molecular extension and rearrangements before the unmolten crystallites start to deform. Deformation of the crystalline phase will occur through the mechanisms reported for deformation of semi-crystalline polymers at room temperature (cf. section 2.4). Lamellar fragmentation of the crystallites through the predominant chain slip mechanisms explain the decrease in the lateral dimension of the crystallites sizes (decrease in D_{110} and D_{040}) and the increase in the number of (040) planes being oriented in the deformation plane (increase in (040) in-plane orientation). Finally, a large amount of structured melt also implies that a large proportion of molecules possess high mobility, and thus will easily relax at the end of stretching, and eventually recrystallize with a random orientation, which will thus reduce in-plane orientation.

7.4 - Summary

The effects of stretching conditions, initial morphology, and chain isotacticity on the evolution of the morphology were studied for the simultaneous biaxial stretching of isotactic polypropylene films. It was shown that the biaxial stretching in the partly molten state involves more than just a strain-induced crystalline texture change. Lamellar thickening, melting, and recrystallization are among the mechanisms that must be considered in addition to the deformation mechanisms to understand the development of the morphology.

Effect of Stretching Conditions on Final Film Morphology

Equibiaxial stretching in the 140°C-163°C temperature range was found to induce the coexistence of two uniplanar textures, with a predominance of the (010) [001] texture. This corresponds to the preferential orientation of the (040) crystal planes in the deformation plane and to the *b*-axis orientation in the ND sample direction. The *c*-axis is randomly oriented in the deformation plane.

The degree of crystallinity, the thermal stability (T_m), and the crystallite size increase with an increase in the drawing temperature. Only the in-plane orientation was found to decrease with increasing temperature, for the films stretched above the critical area stretching ratio of 10. At that stretching ratio, most of the initial morphology is transformed into the oriented fibrous structure. Crystallinity and T_m increase slightly with increasing area stretching ratio, while the crystallite size decreases considerably. The (040) in-plane orientation increases with stretching. The decrease in D_{110} and D_{040} crystallite size and the increase in (040) in-plane orientation with increasing stretching ratio were explained by the dominant chain slip systems.

The deformation type influences the crystalline texture and orientation distribution along the sample directions. Equibiaxial stretching produces a uniform morphology and orientation in the deformation plane. Decreasing the biaxiality led to a preferential orientation of the chain axis in the direction of the main stretching direction, while keeping the *b*-axis preferentially oriented in ND and in the minor stretching direction. Uniaxial and planar deformation were found to have similar crystalline textures.

[Refs. on p. 170]

Over the 0.1 to 1.5 s^{-1} range of Hencky strain rate, the *c*-axis in-plane orientation decreased with increasing strain rate. The unexpected decrease of orientation was explained by the effect of strain rate on the macroscopic deformation behavior. A different film thickness profile was obtained; the lower is the strain rate, the thinner is the end film, thus, the higher is the actual draw ratio.

Effect of Initial Film Morphology on Final Film Morphology

It was concluded that the initial crystallinity has a small effect on the final degree of crystallinity and the melting point. The final crystallinity was correlated with the amount of unmolten crystalline phase present in the partly molten morphology. The initial morphology influenced significantly deformation behavior and, thus, the final thickness profile and local true draw ratios. This was finally correlated with the in-plane orientation. The crystallite size was strongly influenced by the level of unmolten crystallinity and the tie molecule fraction. Both contributed to an enhanced fragmentation of the lamellar structure.

Effect of Chain tacticity on Final Film Morphology

The final stretched film morphology depends strongly on the isotacticity content of the resin. The final degree of crystallinity, the thermal stability, and the in-plane orientation were considerably increased by increasing the isotacticity content.

It was also concluded that the effect of stretching on the final film morphology and orientation depends strongly on the morphology of the partly molten film. In fact, the amount of molten crystalline phase (structured melt) present in the morphology before stretching was correlated with the in-plane orientation, and the increase in crystallinity and thermal stability (T_m), independently of the isotacticity of the resin. The molten phase may be treated as consisting of molecules in a structured melt state that exhibits higher deformability than the amorphous phase, because of a lower density of entanglements.

[Refs. on p. 170]

References

1 - R. J. Yan and B. Jiang, "Melting behavior of drawn polypropylene", J. Polym. Sci. Polym. Phys. Ed., 31, 1089-1094 (1993).

2 - H. Tanaka, T. Masuko and S. Okajima, "Studies on biaxial stretching of polypropylene film. IX. Melting behavior of biaxially stretched film in one step", J. Appl. Polym. Sci., 17, 1715-1725 (1973).

3 - H. Tanaka, N. Tagaki and S. Okajima, "Melting behavior of highly stretched isotactic polypropylene film", J. Polym. Sci. Polym. Chem. Ed., 12, 2721-2728 (1974).

4 - J. H. Magill, M. J. Shankernarayanan, D. C. Sun and M. Kojima, "Rolltrusion: Doubly-orientation processing and morphology-properties relationships for commercial plastics", Int. Polym. Process., , 66-76 (1987).

5 - R. Seguela. in Polymer Films and Fibers, "On the strain-induced crystalline phase changes in semicrystalline polymers: a critical review of the mechanisms and resulting properties", (2002).

6 - C. J. Heffelfinger and R. L. Burton, "X-ray determination of the crystalline orientation distributions of poly(ethylene terephthalate) films", J. Polym. Sci., 47, 289-306 (1960).

7 - H. Sobue and Y. Tabata, "Measurements of X-ray diffraction of biaxially oriented specimens of isotactic polypropylene", J. Appl. Polym. Sci., 2, pp62-65 (1959).

8 - Z. W. Wilchinsky, "Orientation in cold-rolled polypropylene", J. Appl. Polym. Sci., 7, 923-933 (1963).

9 - H. Uejo and S. Hoshino, "Structure of biaxially oriented polypropylene film", J. Appl. Polym. Sci., 14, 317-328 (1970).

10 - Z. Bartczack and E. Martuscelli, "Orientation and properties of sequentially drawn films of an isotactic polypropylene/hydrogenated oligocyclopentadiene blend", Polymer, 38, 4139-4149 (1997).

11 - Y. Sakai and K. Miyasaka, "Development of fibrillar texture during simultaneous biaxially drawing of ultra-high molecular weight polyethylene dried gels", Polymer, 31, 51-57 (1990).

12 - G. Coulon, G. Castelein and C. G. Sell, "Scanning force microscopic investigation of plasticity and damage mechanisms in polypropylene spherulites under simple shear", Po,ymer, 40, 95 - 110 (1998).

13 - M. Aboulfaraj, C. G. Sell, B. Ulrich and A. Dahoun, "In situ observation of the plastic deformation of polypropylene spherulites under uniaxial tension and simple shear in the scanning electron microscope", Polymer, 36, 731-742 (1995).

14 - R. F. Saraf, "Planar and fibre textures induced in isotactic polypropylene on equibiaxial hydrostatic deformation", Polymer, 35, 1359-1368 (1994).

15 - I. M. Ward, ed. Structure and Properties of Oriented Polymers. 2nd ed. , Chapman&Hall, London, (1997).

16 - H. Tanaka and S. Okajima, "Studies on biaxial stretching of polypropylene film. XII. Effect of crystallinity on the deformation mechanism of the biaxial stretching in one step", J. Polym. Sci. Polym. Letters, 15, 349-362 (1977).

17 - R. S. Porter and L. H. Wang, "Uniaxial extension and other development in flexible chain polymers", J. Macromol. Sci.- Rev. Macromol. Chem. Phys., C35, 63-115 (1995).

18 - A. Peterlin, "Molecular Model of drawing polyethylene and polypropylene", J. Mater. Sci., 6, 490-508 (1971).

19 - K. Friedrich, "Crazes and shear bands in semi-crystalline thermoplastics", Adv. Polym. Sci., 52/53, 225-274 (1983).

20 - X. C. Zhang, M. F. Butler and R. E. Cameron, "The ductile-brittle transition of irradiated isotactic polypropylene studied unsing simultaneous SAXS and tensile deformation", Polymer, 41, 3797-3807 (2000).

21 - D. Choi and J. L. White. in Polymer Films and Fibers 2002, "Crystallization and orientation development in film and fibers processing of polypropylenes of varying stereo form and tacticity", (2002).

22 - B. Fillon, J. C. Wittmann, B. Lotz and A. Thierry, "Self-nucleation and recrystallization of isotactic polypropylene (apha Phase) investigated by DSC", J. Polym. Sci.: Polym Phys., 31, 1383-1393 (1993).

[Refs. on p. 170]

CHAPTER 8

END-FILM PROPERTIES AND STRUCTURE-PROPERTY RELATIONSHIPS

This chapter presents the mechanical, optical, and shrinkage properties of the biaxially stretched films obtained with the laboratory film stretcher. The mechanical properties include the elastic modulus, the tensile strength (stress at break), and the elongation at break. The optical properties include gloss and haze. The effects of stretching ratio, drawing temperature, and strain rate are first presented. Then, the effects of the initial film morphology and chain tacticity are discussed. Finally, correlations between the end-film properties and the structural characteristics of the stretched film morphology are discussed.

8.1 - Effects of Stretching Conditions on End-Film Properties

The effects of the stretching conditions on the mechanical and optical properties were investigated for the PP1, PP2, and PP3 homopolymer resins. However, we shall present only the results for the PP2 resin, since the study of the effects of stretching conditions on the stretched morphology was mainly carried out for the PP2 resin. The effects of stretching ratio, drawing temperature, and strain rate on the mechanical and optical properties and shrinkage are discussed. The mechanical properties, including the elastic modulus, the elongation at break, and the tensile strength, and the optical properties, including gloss and haze, were all measured according to ASTM standards, as explained in Chapter 4. The thermal shrinkage was measured after heating for 5 min treatment at 120°C, according to a standard method developed by Brückner Maschinenbau GmbH.

8.1.1 - Effect of Area Stretching Ratio on End-Film Properties

Figure 8-1 presents data on the elastic modulus (E-modulus) and the elongation at break, measured in both MD and TD, for PP2 films equibiaxially stretched at 155°C with a Hencky strain rate of 1 s^{-1}. For both mechanical properties, the MD and TD values are almost identical, within measurement error. However, the MD values are slightly higher than the TD values. This small difference is in harmony with the deformation behavior observed from the stretching stress-strain curves. The MD stresses during stretching were always slightly higher than in TD. Nevertheless, the quasi-equivalence of the MD and TD mechanical properties indicates that it is possible to obtain a balanced film with equivalent properties and morphology in MD and TD, using the laboratory film stretcher. Figure 8-1 shows also that the E-modulus increases linearly with increasing area stretching ratio, while the elongation at break decreases linearly. Figure 8-2 illustrates the effect of stretching ratio on the tensile strength and shrinkage for the same PP2 films equibiaxially stretched at 155°C. The average values calculated from the values in MD and TD were plotted for clarity purposes. Both the tensile strength and the shrinkage increase with increasing area stretching ratio. These results show that biaxial stretching leads to increased tensile modulus and strength, lower tensile elongation, and higher thermal shrinkage in the drawing directions.

Figure 8-3 shows the influence of the area stretching ratio on the optical properties for the same PP2 films stretched at 155°C. Gloss and haze are both improved by stretching, i.e. increase in gloss and decrease in haze. However, with increasing stretching ratio, gloss and haze seem to start to level off above an area stretching ratio of 50.

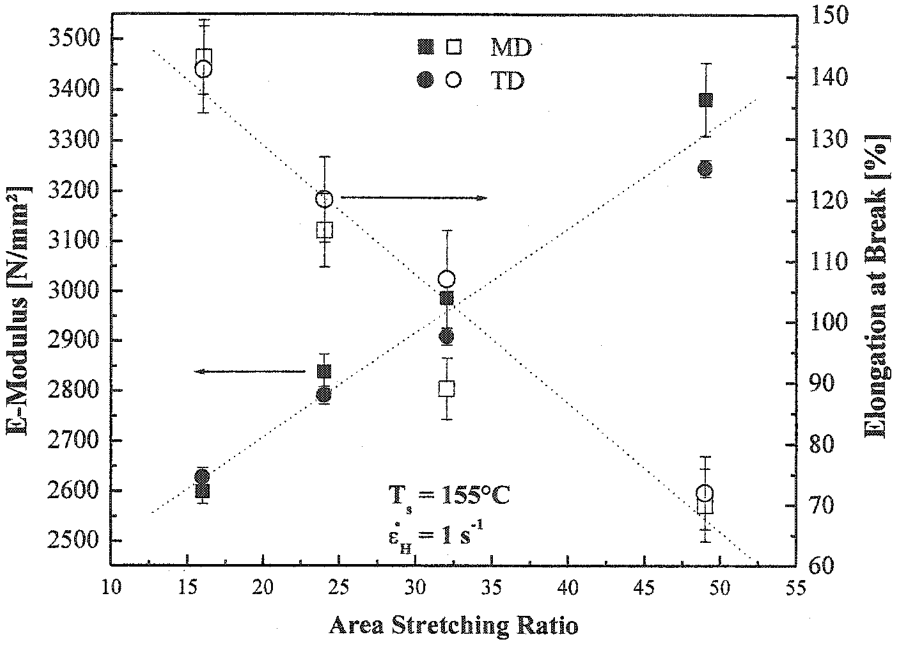

Figure 8-1 *Effect of area stretching ratio on the E-modulus and the elongation at break for the PP2 films simultaneously equibiaxially stretched at 155°C*

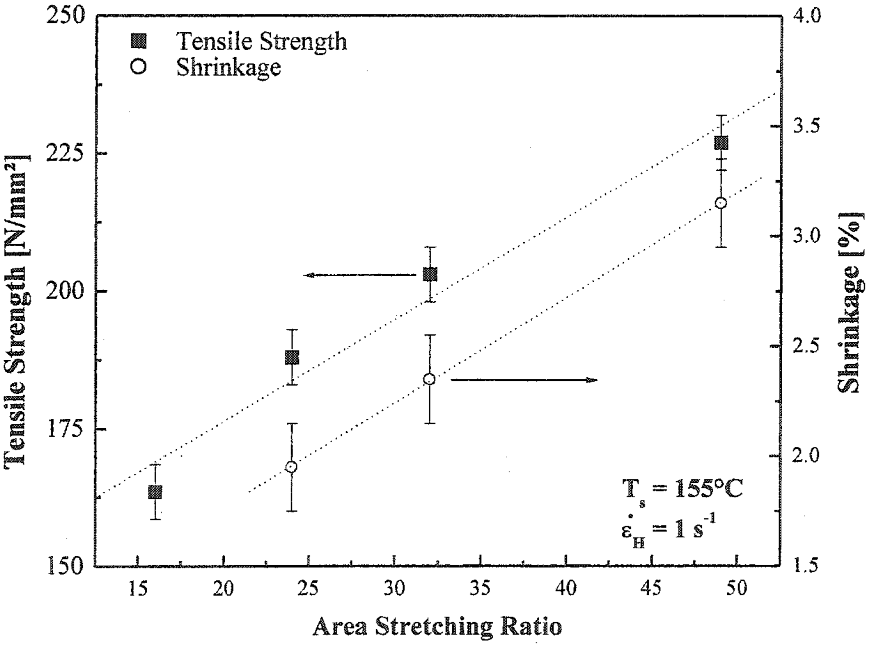

Figure 8-2 *Effect of area stretching ratio on the tensile strength and the shrinkage for the PP2 films simultaneously equibiaxially stretched at 155°C (average values from the MD and TD results are plotted)*

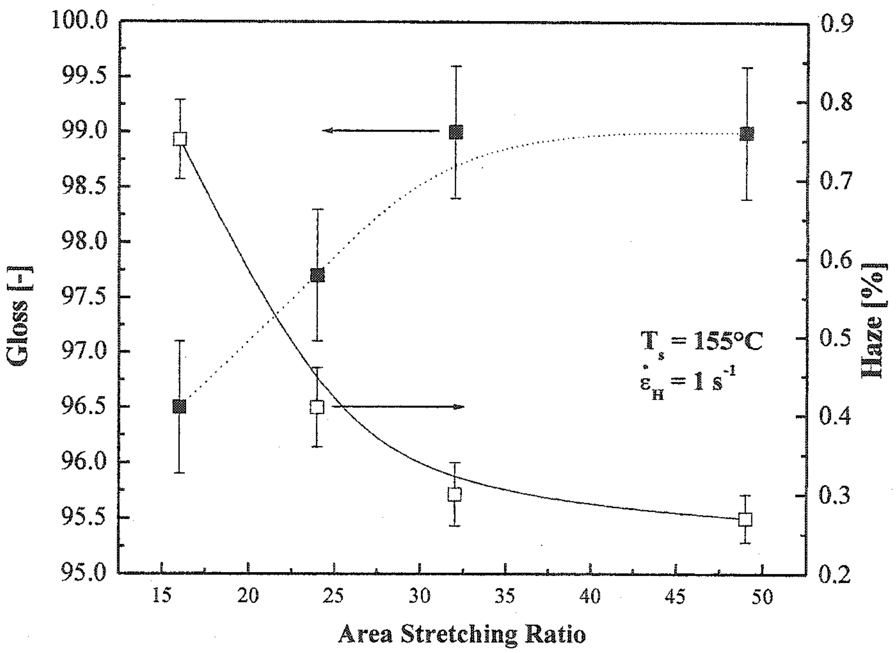

Figure 8-3 *Effect of area stretching ratio on Gloss and Haze for the PP2 films simultaneously equibiaxially stretched at 155°C*

8.1.2 - Effect of Drawing Temperature on End-Film Properties

Figure 8-4 and Figure 8-5 display the effect of the drawing temperature on the mechanical properties of PP2 films, simultaneously equibiaxially stretched up to a 4.9 x 4.9 area stretching ratio with a Hencky strain rate of 1 s^{-1}. The E-modulus and the elongation at break appear to increase linearly with increasing drawing temperature from 145°C to 160°C. The tensile strength and the shrinkage were found to decrease with raising the drawing temperature. The tensile strength decreases more rapidly above 150°C, while the shrinkage tends to decrease more slowly.

Figure 8-6 illustrates the effect of drawing temperature on the optical properties. Gloss remains almost constant over the 145°C - 155°C temperature range and then decreases abruptly. Haze shows a similar behavior; there is a slight increase over the 145°C - 155°C temperature range, followed by a large increase when stretched at 160°C. The optical properties deteriorate strongly when films are stretched at 160°C.

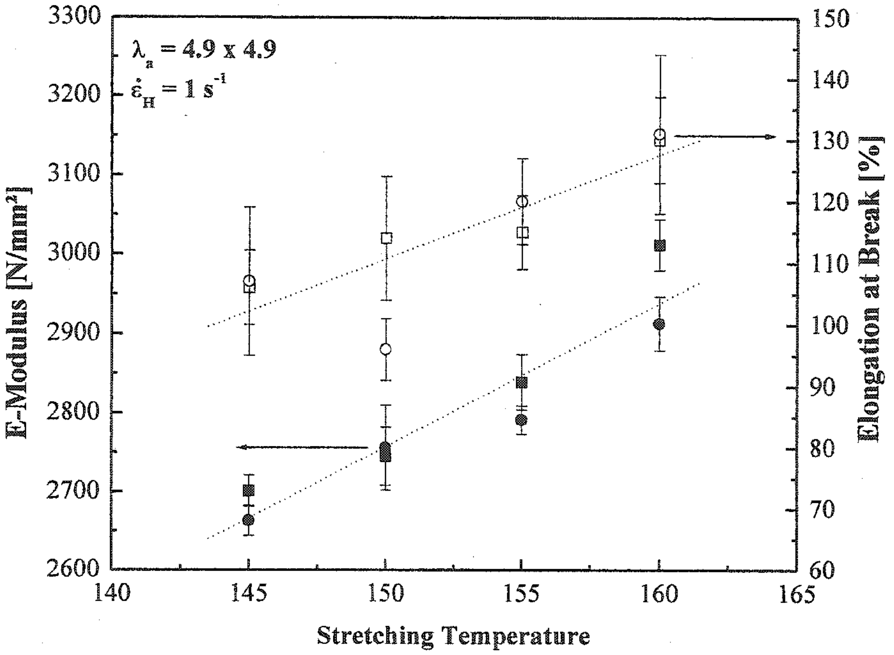

Figure 8-4 *Effect of stretching temperature on the E-modulus and the elongation at break for the PP2 films simultaneously equibiaxially stretched up to a 4.9 x 4.9 area stretching ratio*

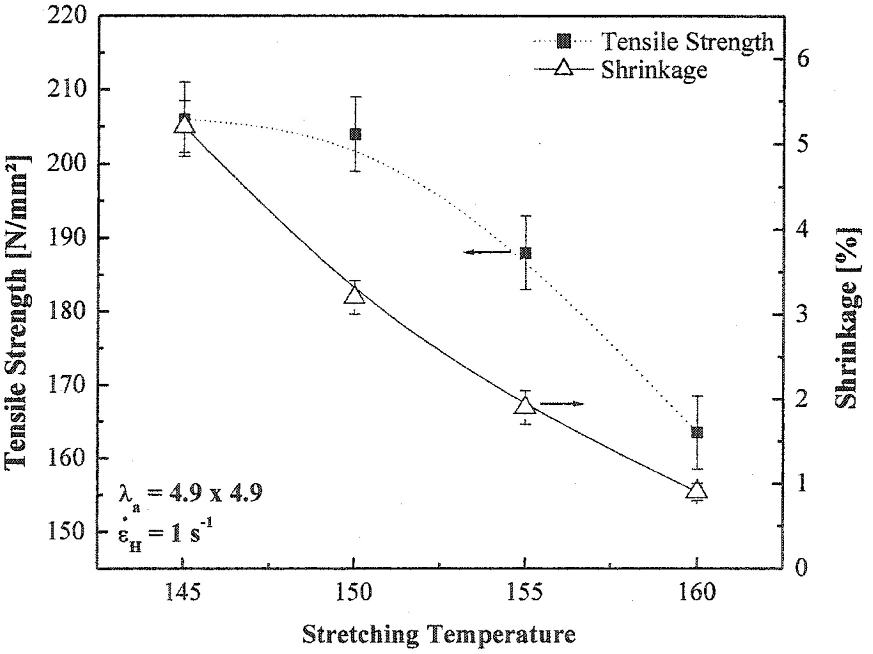

Figure 8-5 *Effect of stretching temperature on tensile strength and shrinkage for the PP2 films simultaneously equibiaxially stretched up to a 4.9 x 4.9 area stretching ratio*

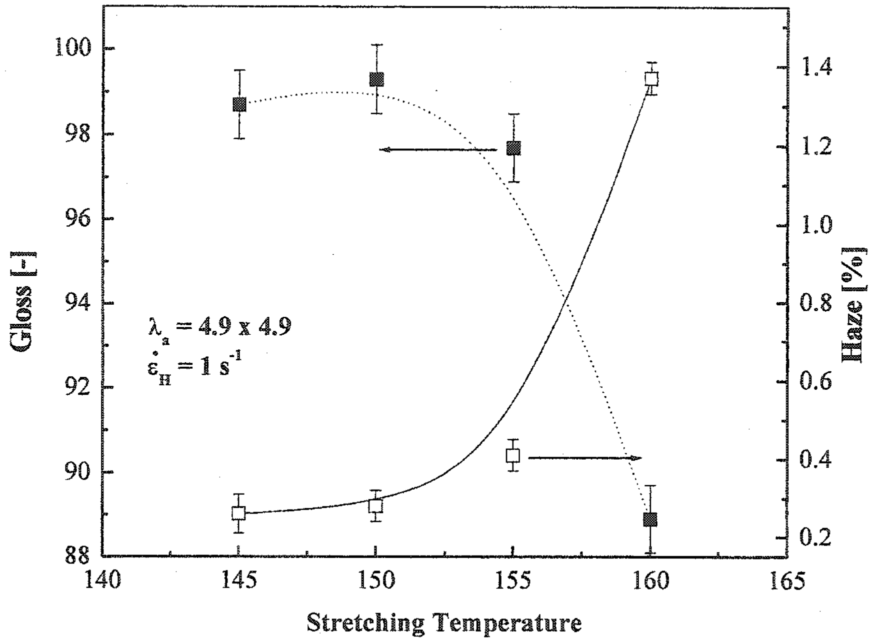

Figure 8-6 Effect of stretching temperature on Gloss and Haze for the PP2 films simultaneously equibiaxially stretched up to a 4.9 x 4.9 area stretching ratio

8.1.3 - Effect of Strain Rate on Film Properties

The study of the effect of strain rate on the film properties was carried out over a limited range of Hencky strain rate. Figure 8-7 and Figure 8-8 show the effect of strain rate on the mechanical properties of PP2 films, simultaneously equibiaxially stretched at 150°C up to a 4.9 x 4.9 stretching ratio. The E-modulus, the tensile strength, and the shrinkage decrease, while the elongation at break increases with increasing strain rate. The increase in E-modulus and tensile strength and the decrease in elongation at break represent a change of around 12% over the 0.1 - 1.5 s^{-1} range. The optical properties are marginally influenced by the strain rate. Only a slight improvement in haze was observed for the lowest strain rate.

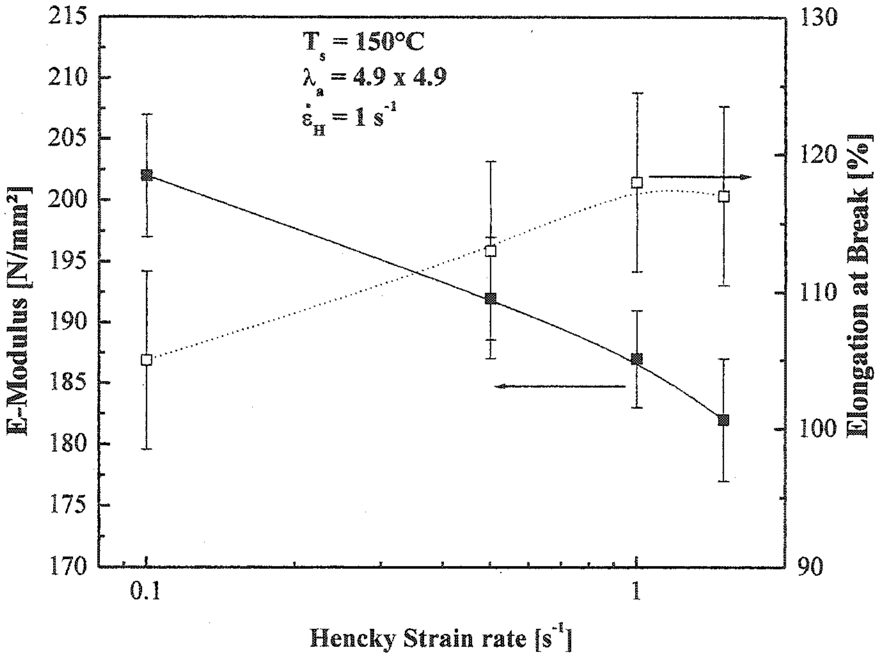

Figure 8-7 Effect of strain rate on the E-modulus and the elongation at break for the PP2 films simultaneously equibiaxially stretched at 150°C up to a 4.9 x 4.9 area stretching ratio

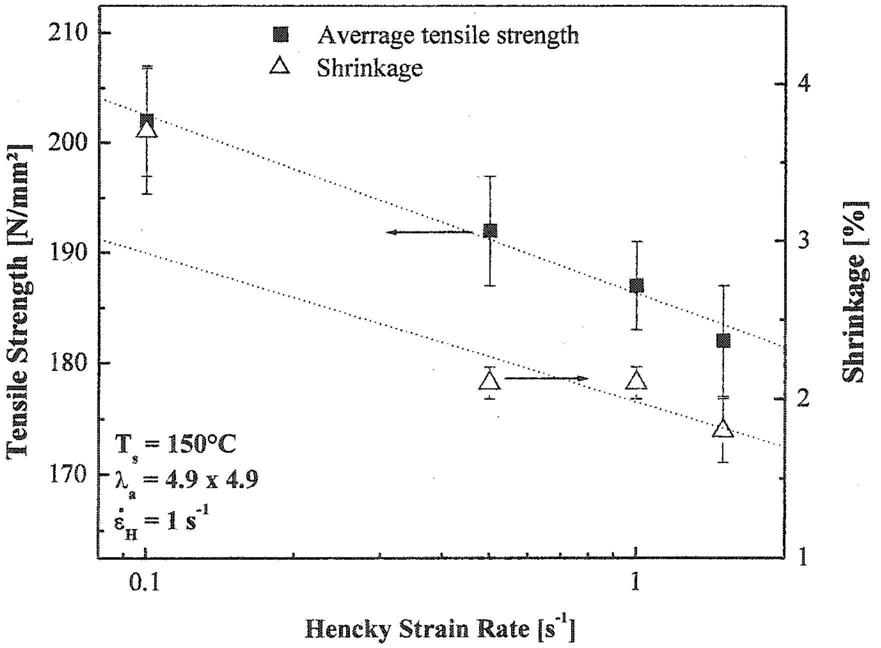

Figure 8-8 Effect of strain rate on the tensile strength and shrinkage for the PP2 films simultaneously equibiaxially stretched at 150°C up to a 4.9 x 4.9 area stretching ratio

The unexpected lowering of the mechanical properties with increasing strain rate was found to be correlated with the effect of strain rate on the macroscopic deformation behavior. Indeed, the film thickness profile was affected by the strain rate; the lower is the strain rate, the thinner is the end film. The film thickness is directly proportional to the true draw ratio of the final film, and the mechanical properties are dependent on the true draw ratio (1). It was concluded that the differences in mechanical properties were attributed to the differences in film thickness among the various samples.

8.2 - Effect of Initial Film Morphology on End-Film Properties

The effect of the initial film morphology on the mechanical properties of the end-film properties was investigated for the series of melt-crystallized morphologies, the PP4-CFx cast films. The latter were obtained by varying the cooling conditions of the casting process (cf. Chapter 4 & 5). Figure 8-9 shows the variation of the average values of the E-modulus and the tensile strength of films simultaneously equibiaxially stretched at 150°C up to a 4.9 x 4.9 stretching ratio. The mechanical properties are plotted versus the initial crystallinity of the cast films. The changes in mechanical properties observed for the series of melt-crystallized morphologies were very small compared to those changes due to the stretching conditions. The tensile strength is seen to decrease slightly (6%) from CF1 to CF4, while the E-modulus increases to some extent (2%).

The small differences in film thickness, and thus in true draw ratio, were not sufficient to explain the change in mechanical properties for the films stretched from the melt-crystallized samples. The property changes were correlated with the structural characteristics of the film, as explained in section 8.4. The (040) in-plane orientation was found to decrease slightly (5%) from CF1 and CF4, which is similar to the 6% decrease in tensile strength. The minor increase in E-modulus (2%) was correlated with the small rise in crystallinity (3%) from CF1 to CF4.

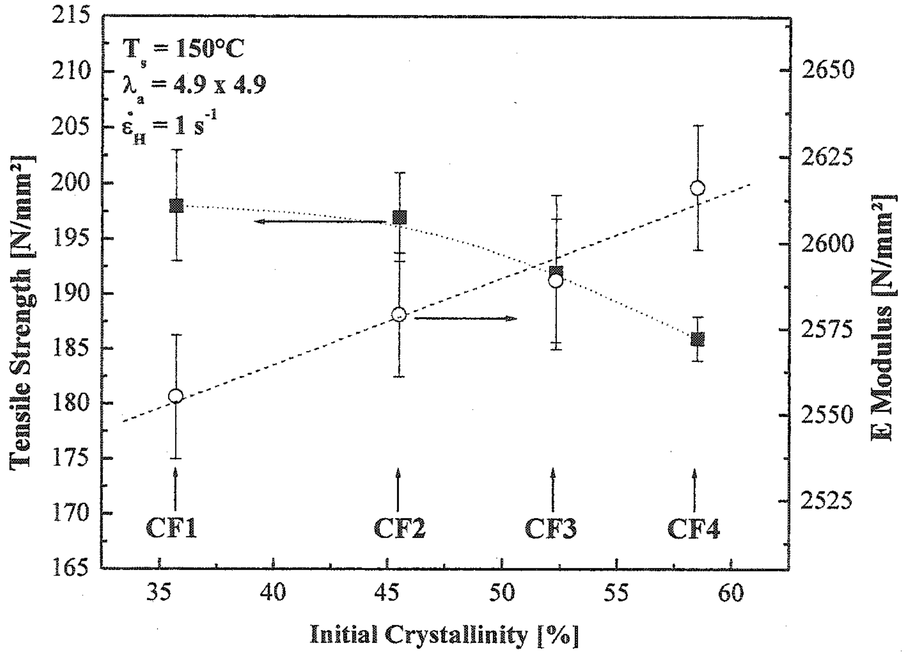

Figure 8-9 *Effect of initial film morphology the tensile strength and the E-modulus for the PP4-CFx films simultaneously equibiaxially stretched at 150°C up to a 4.9 x 4.9 area stretching ratio*

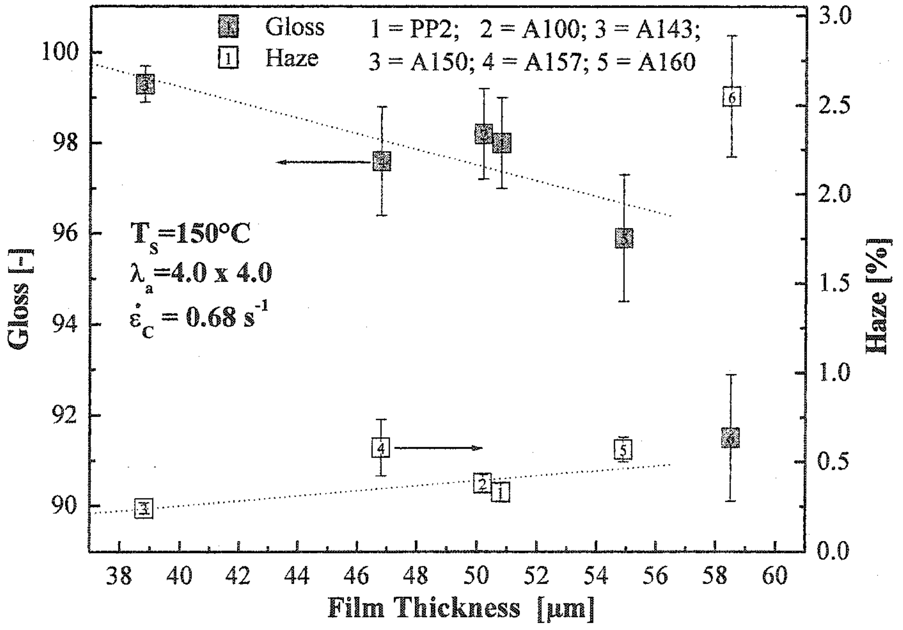

Figure 8-10 *Effect of initial film morphology on Gloss and Haze for the PP2 annealed films simultaneously equibiaxially stretched at 150°C up to a 4.0 x 4.0 area stretching ratio*

The optical properties of the series of melt-crystallized films are almost constant. Only the PP4-CF4 film has a slightly lower gloss and higher haze. The PP4-CF4 cast film was processed without a water bath in the casting unit, which produced a rough surface, observable with the unaided eye. The deterioration of the optical properties for the PP4-CF4 films was attributed to the initial film surface roughness.

The effects of the initial film morphology on the optical properties were also studied for the series of annealed morphologies, the PP2-A1xx cast films. These were simultaneously equibiaxially stretched at 150°C up to a 4.0 x 4.0 area stretching ratio with a Cauchy strain rate of 0.68 s^{-1}. Haze and gloss showed a maximum or minimum for the stretched PP2-A143, and generally showing the worst properties for the PP2-A160 sample, as shown in Figure 8-10. Although all the films were stretched to the same nominal draw ratio, there was strong variation in film thickness, as mentioned in Chapter 6. There appears to be a correlation between the optical properties and the film thickness, except for the PP2-A160 morphology. This was expected, since the A160 film exhibited strong stress whitening, as discussed in Chapter 6. The whitening effect is attributed to interlamellar cavitation occurring during equibiaxial deformation. The voids contributes to light scattering, and thus affect the optical properties of the stretched film.

With the exception of the special morphology that exhibited interlamellar cavitation, haze and gloss were found to be related to the film thickness and thus to the local true draw ratio. The more highly stretched is the film, the smaller are the crystallites, and thus the better are the optical properties.

8.3 - Effect of Chain Tacticity on End-Film Properties

The effect of chain tacticity on the mechanical properties was investigated for the three commercial PP1, PP2, and PP3 resins, which had an isotacticity content of 94.8%, 98.6%, and 99.5%, respectively. The initial cast films of the three resins were then stretched under various conditions. The mechanical and optical properties of the films simultaneously equibiaxially stretched up to a 4.9 x 4.9 area stretching ratio at different temperatures are listed in Table 8-1 for the three resins. The average values of the mechanical properties, which were calculated from the results in MD and TD, are reported in this table. Figure 8-11 shows the effect of stretching temperature on the E-modulus for all three resins. The elastic modulus increases considerably with chain tacticity, for constant stretching conditions. The small increase in elastic modulus with increasing drawing temperature, which was observed for PP2 in 8.1.2, was confirmed for the other two resins. The tensile strength and the elongation at break showed a temperature dependence that was qualitatively similar for all three resins. The tensile strength and the E-modulus increase, while the elongation at break decreases with increasing tacticity, for films stretched at the same temperature. The changes in the mechanical properties are directly related to the increase in orientation (cf. section 8.4), in agreement with a recent study on orientation development in iPP fibers (2). Figure 8-12 shows the temperature dependence of the shrinkage of the equibiaxially stretched film for the three resins. Shrinkage depends mainly on drawing temperature, and it appears to be independent of the tacticity level of the resin.

Table 8-1 *Mechanical and optical properties of films equibiaxially stretched at different temperatures for the PP1, PP2, and PP3 resins*

		Thickness	**Elasticity Modulus**		**Tensile Strength**		**Elongation at Break**		**Shrinkage**		**Gloss**		**Haze**	
		[µm]	[N/mm²]	±	[N/mm²]	±	[%]	±	[%]	±	[-]	±	[%]	±
PP1	140	43	2145	20	195	9	112	12	7.4	0.3	96.0	1.0	0.49	0.03
	145	41	2289	16	198	5	117	7	5.4	0.4	97.1	0.4	0.55	0.03
	150	38	2357	30	185	4	119	6	3.8	0.1	93.1	1.0	0.86	0.04
	155	29	2369	67	161	5	135	13	2.0	0.1	84.8	1.6	2.14	0.04
PP2	145	43	2682	19	206	8	106	9	5.3	0.3	98.7	0.8	0.26	0.03
	150	38	2750	45	204	6	105	7	3.2	0.2	99.3	0.8	0.28	0.04
	155	36	2815	26	188	3	118	6	1.9	0.2	97.7	0.8	0.41	0.04
	160	30	2963	33	164	4	130	10	1.0	0.1	88.9	1.0	1.37	0.04
PP3	150	39	3450	52	219	6	100	7	2.9	0.2	96.3	0.0	0.73	0.03
	155	37	3368	24	203	8	102	12	1.9	0.2	97.8	0.0	0.57	0.03
	160	33	3488	48	174	6	113	13	1.0	0.2	95.8	0.0	0.83	0.04

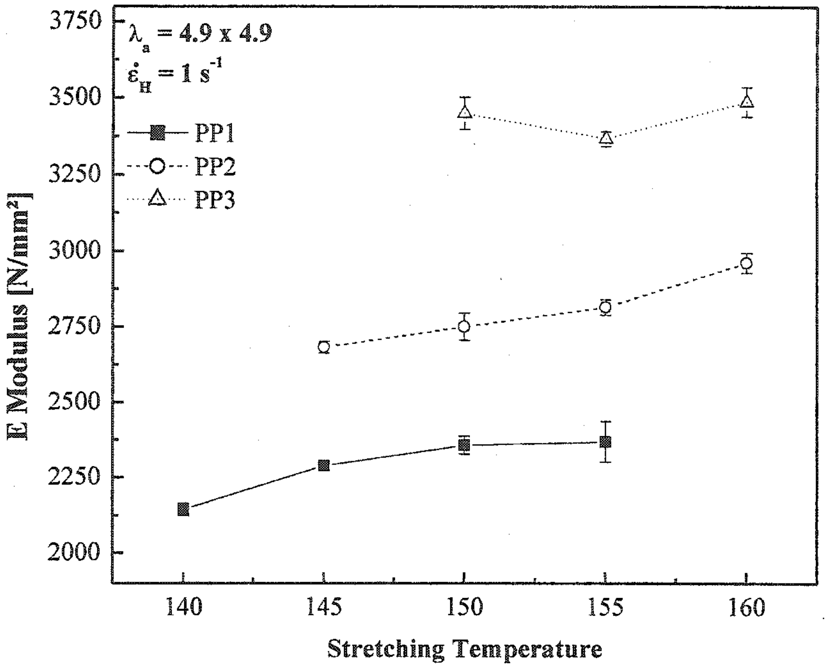

Figure 8-11 *Effect of stretching temperature on the E-modulus for the PP1, PP2, and PP3 films simultaneously equibiaxially stretched up to a 4.9 x 4.9 area stretching ratio*

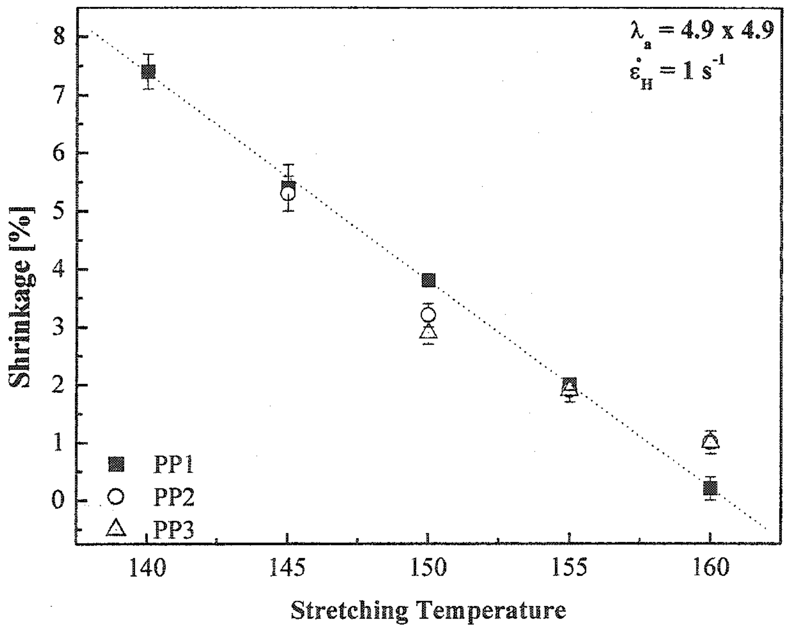

Figure 8-12 *Effect of stretching temperature on the shrinkage for the PP1, PP2, and PP3 films simultaneously equibiaxially stretched up to a 4.9 x 4.9 area stretching ratio*

The analysis of the optical properties showed that gloss and haze behave similarly for all three resins with respect to the stretching temperature, as shown in Table 8-1. It shows also that gloss and haze do not show any specific dependence on chain tacticity when compared at the same drawing temperature. Haze increases with increasing drawing temperature, while gloss exhibits a slightly more complex temperature dependence. Gloss shows maxima at around 145°C, 150°C, and 155°C for PP1, PP2, and PP3, respectively. These maxima occur at supercooling degrees, $\Delta T = T_m - T_s$, between 13°C and 15°C, where T_m is the resin melting point and T_s the stretching temperature. This suggests that, for higher temperatures, the greater amount of molten crystallinity influences the optical properties as a result of lamellar thickening and recrystallization on subsequent cooling after stretching.

The concept of structured melt and unmolten crystallinity was introduced in 5.4.2 to characterize the partly molten state of the film morphology at the end of preheating and before stretching. The previous results on deformation behavior and stretched morphology suggested that the structural characteristics of the partly molten film morphology control the stretching process. It was found that there is a tacticity independent linear relationship between the tensile strength and the amount of structured melt, as shown in Figure 8-13. The tensile strength decreases with increasing the amount of structured melt. Similarly, the elongation at break for the same series of stretched films showed a linear dependence on the unmolten crystallinity that is also independent of tacticity, as shown in Figure 8-14. The elongation at break decreases with increasing unmolten crystallinity. No tacticity-independent relation was found for the E-modulus.

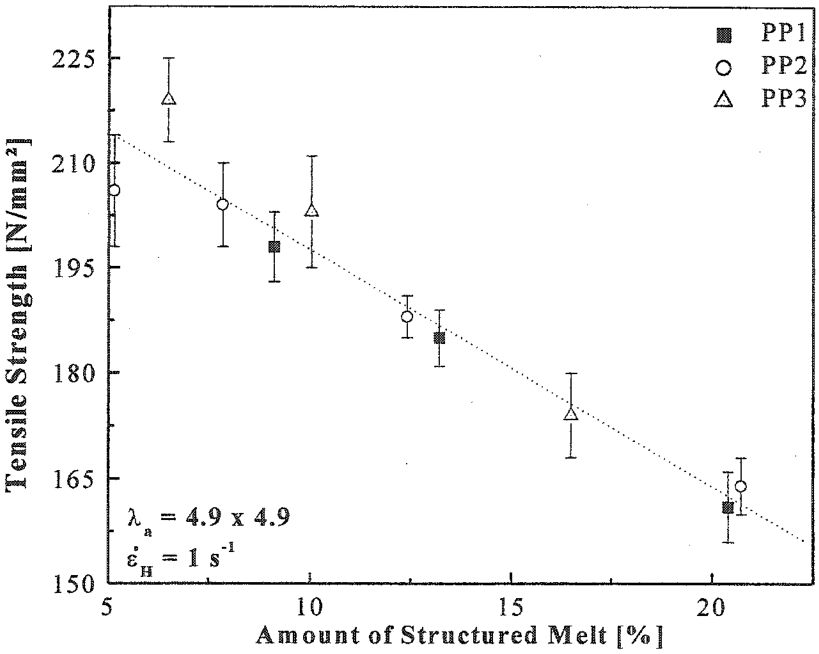

Figure 8-13 *Tensile strength versus the amount of structured melt for the PP1, PP2, and PP3 films simultaneously equibiaxially stretched up to a 4.9 x 4.9 area stretching ratio*

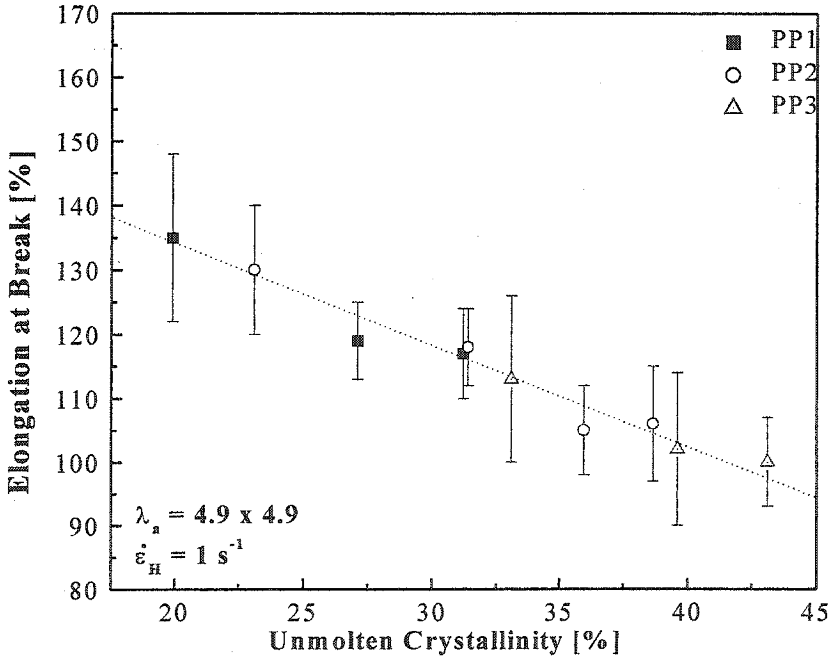

Figure 8-14 *Elongation at break versus the unmolten crystallinity for the PP1, PP2, and PP3 films simultaneously equibiaxially stretched up to a 4.9 x 4.9 area stretching ratio at different temperatures*

[Refs. on p. 190]

These results indicate that the higher is the amount of unmolten crystalline phase during stretching, the lower will be the elongation at break and thus the higher will be the orientation (3). Moreover, a large amount of structured melt will lead to a decrease in tensile strength, because the structured melt tends to reduce the efficiency of the orientation process, as explained in Chapter 7.

8.4 - Correlations between Film Morphology and End-Film Properties

An effort was made to find correlations between the end-film properties and the structural features of the final film morphology, characterized by differential scanning calorimetry and wide-angle X-ray diffraction.

8.4.1 - Mechanical properties

Simultaneous equibiaxial stretching led to higher tensile modulus and strength and increased thermal shrinkage in the drawing directions. This is in agreement with other studies on biaxially stretched iPP films (4-7). Increasing drawing temperature was found to increase the elastic modulus and the elongation at break, but to lower the tensile strength and the shrinkage. The shrinkage of stretched iPP films is known to be related to the level of amorphous orientation (5). Also, for a given strain rate and draw ratio, the amorphous orientation decreases with increasing drawing temperature, because the relaxation rate of the molecular chains in the amorphous phase increases with increasing temperature (8). The decrease of the tensile strength and the elongation at break for higher drawing temperature have been related to the decrease of average orientation with increasing temperature (6, 7, 9).

The tensile strength and the elongation at break were plotted versus the (040) in-plane orientation for a series of films stretched up to the same draw ratio, but at different temperatures, for the three commercial resins, as shown Figure 8-15 and Figure 8-16. Some of the points showed in these figures for PP3 were extrapolated from data obtained at smaller and larger area stretching ratios. It can be seen that the tensile strength and elongation at break are correlated to the (040) in-plane orientation, independently of the

[Refs. on p. 190]

isotacticity of the resins. The tensile strength increases quasi-linearly with increasing the in-plane orientation, while the elongation at break seems to decrease in an exponential-decay manner.

Figure 8-17 shows the dependence of the elastic modulus on the DSC crystallinity for the same series of films. It shows that the elastic modulus depends on crystallinity similarly for all three resins. The E-modulus increases with the overall crystallinity of the stretched film morphology. However, there is no tacticity-independent correlation. The actual level of the E-modulus increases with increasing chain tacticity.

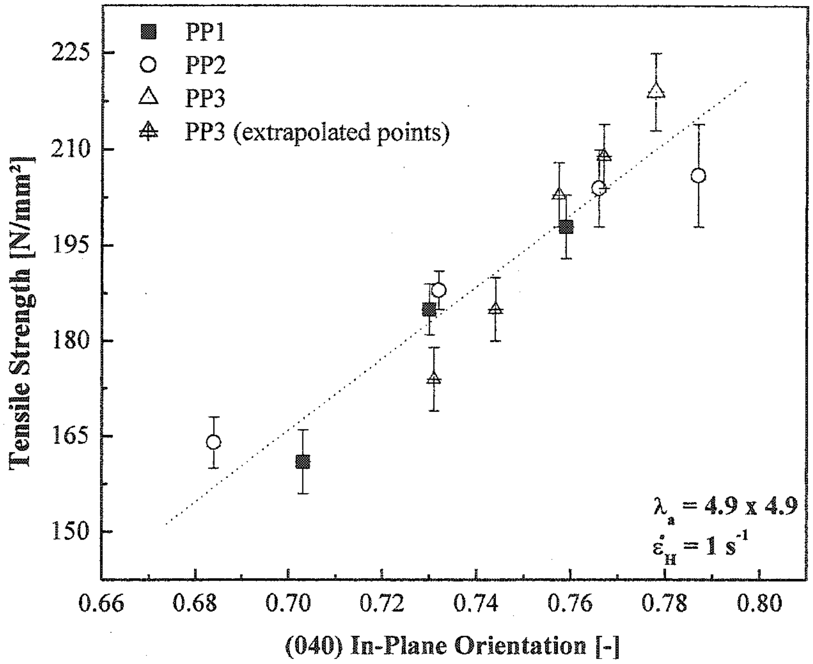

Figure 8-15 Tensile strength versus the (040) in plane orientation index for a series of equibiaxially stretched films at different temperatures for the three homopolymer resins

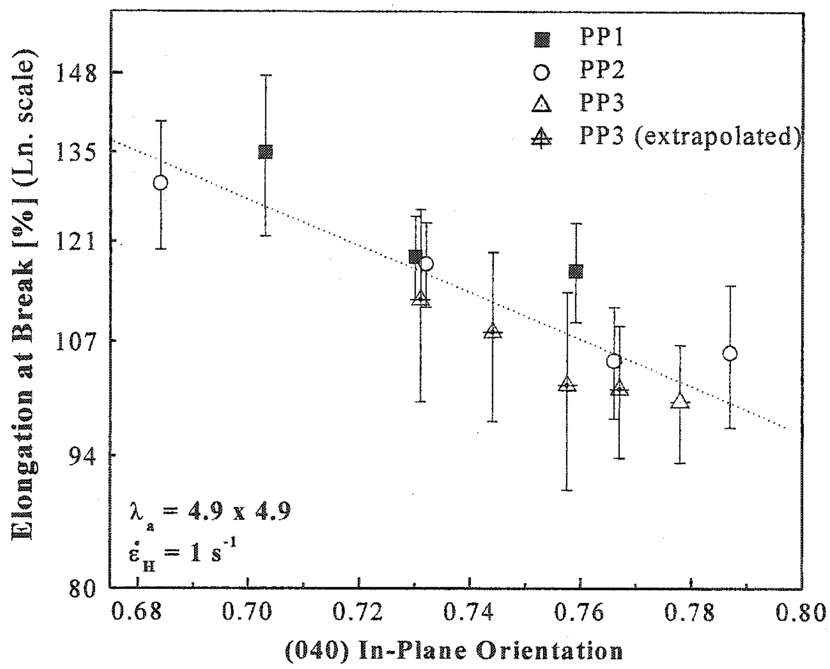

Figure 8-16 *Elongation at break versus the (040) in-plane orientation index for a series of equibiaxially stretched films at different temperatures for the three homopolymer resins*

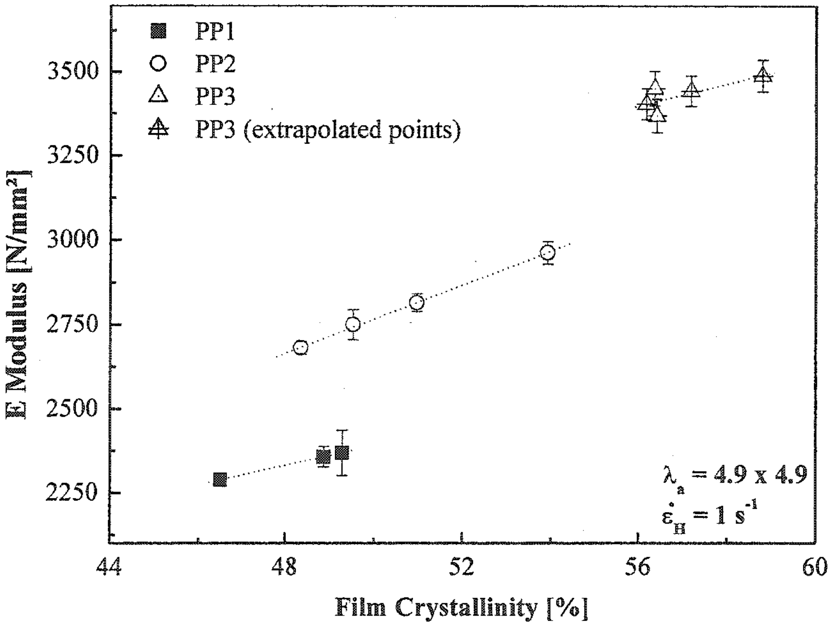

Figure 8-17 *E-modulus versus the film crystallinity for a series of equibiaxially stretched films at different temperatures for the three homopolymer resins*

Because the E-modulus is measured by tensile drawing of a film specimen up to very low strain ratio (<0.5%) , it involves mainly the deformation of the amorphous regions. Thus, the stresses are mostly supported by the interlamellar regions. The differences in E-modulus values arise from the properties of the amorphous regions between lamellae. Therefore, the increase in E-modulus may be attributed to an increased tie molecules content with increasing chain tacticity. Ishikawa et al. (10) studied the effect of tie molecules on the craze of PP and found that the tie molecule fraction in oriented samples was higher for high tacticity PP, compared to low tacticity "conventional" PP. This could partly explain the increase in E-modulus with increasing tacticity.

8.4.2 - Optical properties

The results illustrated the improvements of the optical properties on biaxial stretching. For constant drawing temperature, increasing the stretching ratio enhance gloss and clarity. Haze and gloss, are known to be associated with the light scattering from the bulk and the surface of the film. The enhancement in optical properties on stretching may be attributed to the break-up of the supermolecular and lamellar structure into the smaller fibrillar structure (11). The observed decrease in crystallite size on stretching is in agreement with this concept. Increasing stretching temperature has the reverse effect. The increased mobility of the macromolecules promotes lamellar thickening, crystal perfection and recrystallization processes which contribute to larger crystallites. Thus, the larger scattering centers cause deterioration of the optical properties (decrease in gloss and increase in haze). It was found that the crystallite size exhibit some correlation with haze. However, the crystallite size represents the average lateral dimension of the crystallites, that are oriented in the plane of the films, while light is scattered by all crystalline entities. Furthermore, the other dimensions (e.g., thickness) of the lamellae could also affect light scattering. This is why no direct relationships could be found between the crystallite size and optical properties.

[Refs. on p. 190]

References

1 - I. M. Ward, P. D. Coates and M. M. Dumoulin, Solid Phase Processing of Polymers, Hanser, Munich, (2000).

2 - D. Choi and J. L. White. in Polymer Films and Fibers 2002, "Crystallization and orientation development in film and fibers processing of polypropylenes of varying stereo form and tacticity", (2002).

3 - I. M. Ward and D. W. Hadley, An Introduction to the Mechanical Properties of Solid Polymers, John Wiley & Sons, New York, (1993).

4 - A. J. d. Vries, "Structure and properties of uni- and biaxially oriented polypropylene films: Part 2 - Mechanical and other end use properties", Pure & Appl. Chem., 54, 647-670 (1982).

5 - A. J. d. Vries, "Structure-properties relationships in biaxially oriented polypropylene films", Polym. Eng. Sci., 23, 241-246 (1983).

6 - J. Nordmeier and G. Menges, "The influence of processing conditions on the optical and properties of extruded and biaxially stretched PP films", Adv. Polym. Techn., 6, 59-64 (1986).

7 - S. A. Jabarin, "Orientation and properties of polypropylene", J. reinforced Plast. Comp., 12, 480-488 (1993).

8 - D. R. Salem, "Draw-induced structure development in flexible-chain polymers", in Structure Formation in Polymeric Fibers, D. R. Salem, Editor. Hanser: Munich. p. 118-184 (2001).

9 - H. P. Nadella, J. E. Spruiell and J. L. White, "Drawing and annealing of polypropylene fibers: structural changes and mechanical properties", J. Appl. Polym. Sci., 22, 3121-33 (1978).

10 - M. Ishikawa, K. Ushui, Y. Kondo, K. Hatada and S. Gima, "Effect of tie molecules on the craze strength of polypropylene", Polymer, 37, 5375-5379 (1996).

11 - I. M. Ward, ed. Structure and Properties of Oriented Polymers. 2nd ed. , Chapman&Hall, London, (1997).

CHAPTER 9

SUMMARY

The present work involved a comprehensive study of the simultaneous biaxial stretching of isotactic polypropylene films in the partly molten state. Four commercial grades (PP1 – PP4) of isotactic PP were investigated. The first three resins differed principally in isotacticity levels, which were 94.8%, 98.6%, and 99.5%, and the fourth resin was a peroxide degraded resin ("controlled rheology" grade), that had similar molecular weight and isotacticity level to the PP2 resin. PP4 differed in crystallization behavior from PP2. The four iPP resins were then extruded and cast under constant conditions. The severity of the cooling was varied for PP4, in order to study the effect of different initial morphologies on the process and product. The cast films were stretched on the laboratory film stretcher that simulates closely the stretching conditions encountered in the industrial tenter-frame stretching process. The cast films were simultaneously equibiaxially stretched in the 140°C – 163°C temperature range, for Hencky strain rates varying from 0.01 s^{-1} to 1.5 s^{-1}. The morphology of the cast films and the final stretched film morphology were characterized by differential scanning calorimetry and wide-angle X-ray diffraction. The reflection technique and occasionally the transmission and pole figure techniques were used for the X-ray measurements. Finally, the mechanical and optical properties of the films were determined, and the results were correlated with the film morphology and orientation.

The production of biaxially stretched films of isotactic polypropylene using the simultaneous tenter-frame process involves a series of thermal treatments and deformations applied to the polymer. The tenter-frame stretching process can be seen at the morphological level as follows. The polymer molecules are first melted, extruded, and then crystallized under asymmetric, rapid cooling conditions, which generates a morphology gradient along the cast film thickness. The molecular characteristics of the resin, especially the isotacticity content, control the degree of crystallinity, the content in crystal forms, and the spherulitic and lamellar morphologies. Next, the initial morphology of the cast film undergoes partial melting at the end of preheating prior to stretching. At this point, the film morphology consists of an unmolten crystalline phase, an amorphous melt, and a third phase, referred to as the "structured melt". The structured melt is the phase issued from the least thermally stable lamellae that has a higher deformability than the amorphous phase, due to a higher organization of these "molten" molecules (reduced entanglement density). The three-phase system is next simultaneously equibiaxially stretched. At first, the amorphous and structured melt phases bear most of the deformation. Next, the unmolten crystalline phase undergoes deformation. Crystallites are fragmented and oriented in the drawing plane. At the end of stretching, the molecules of the structured melt undergo molecular relaxation and rapidly recrystallize during cooling after stretching, thus reducing orientation.

The effects of drawing temperature, stretching ratio, strain rate, initial morphology, and chain tacticity on deformation behavior, stretched film morphology, and end-film properties were studied, and correlations were sought.

Initial Morphology of the Cast Films

For a given resin, crystallinity, spherulite size, and the apparent crystallite size increased with decreasing cooling severity. Moreover, the presence and amount of smectic phase and β-phase appeared to depend on the cooling conditions. Decreasing the cooling severity hindered the formation of the smectic phase and favored the formation of the β-phase.

Furthermore, increasing isotacticity led to an increase in the degree of crystallinity and the crystallite dimensions. Spherulites seemed to decrease in size with increasing chain isotacticity. However, the major effect of chain stereoregularity was on the thermal stability of the crystalline phase. The thermal stability (i.e., peak DSC melting temperature) of the initial cast film morphology was shifted to higher temperature with increasing isotacticity.

Morphology of the Partly Molten State

The morphology of the partly molten state in the films was defined and characterized, based on the DSC melting curves of the initial cast films. In addition to the unmolten crystalline phase and the amorphous melt phases, a third phase, referred to as "structured melt" was defined. The amount of structured melt represents the fraction of crystallites or lamellae that just melted among the least thermally stable lamellar crystals. The amount of structured melt was found to be primarily dependent on the temperature difference (supercooling), $\Delta T = T_m - T_s$, where T_s is the stretching temperature and T_m is the melting peak in the DSC trace.

For a given temperature, the amounts of unmolten crystallinity and structured melt were greatly affected by the isotacticity content of the PP resin. The higher is the isotacticity, the smaller is the amount of structured melt present in the partly molten film.

Homogeneity of the Equibiaxial Deformation Behavior

It was found that, for a given resin, the equibiaxial deformation behavior depended on three key variables: the drawing temperature, the strain rate, and the initial morphology. For the 140°C-160°C temperature range and below a strain rate of $\dot{\varepsilon}_H$ = 0.01 s^{-1}, the equibiaxial deformation proceeds, to a great extent, inhomogeneously, i.e. at several localized necking positions. Above 0.1 s^{-1}, the equibiaxial deformation takes place uniformly, by simultaneous stretching of the entire central part of the specimen. The homogeneous equibiaxial deformation exhibited a yield stress and stress drop after yield for the temperature range: $T_m - 25°C < T < T_m - 5°C$. At higher temperatures, the deformation becomes rubber-like and no stress drop after yield was observed.

The investigation of the different initial cast film morphologies revealed that the yield stress was primarily dependent on the crystallite size. The stiffness of the films is correlated with the dimensions of the lamellae. Thus, it was concluded that the lamellar stiffness together with the amount of crystallinity seems to be the primary morphological properties controlling the magnitude of the yield stress. Furthermore, the yield region sharpness was found to be correlated with the resulting film thickness profile, for a given temperature below T_m. The more diffuse was the yield region, the more uniform was the film thickness. It is suggested that the yield region sharpness is primarily related to the fraction of taut tie molecules in the initial cast film morphology.

For the same casting and stretching conditions, increasing the chain tacticity caused an increase in the overall stress required for deformation and the sharpness of the yield region. For given casting conditions, the isotacticity content of the resin increases significantly the thermal stability (melting temperature) of the initial morphology and, thus, affects the phase content of the partly molten state. In general, it is concluded that the thermal stability of the crystalline structure is the primary morphological property that determined the overall level of drawing stress.

Development of Crystalline Textures under Simultaneous Biaxial Stretching

The simultaneous equibiaxial stretching of iPP films in the 140°C-163°C temperature range was found to lead to the coexistence of two uniplanar textures, the (010) [001] and (110) [001] textures, with a predominance of the former. The (010) [001] texture corresponds to the preferential orientation of the (040) crystal planes in the deformation plane and to the *b*-axis orientation in the ND sample direction, while the *c*-axis is randomly oriented in the deformation plane. Wide angle X-ray diffraction measurements in reflection gave an estimate of the amount of (040) crystal planes that are preferentially oriented in the deformation plane. Good agreement was found between the (040) in-plane orientation index from WAXD and the average squared cosines of the *b*-axis orientation in ND, obtained by infrared dichroism.

The deformation type was found to affect mainly the crystalline texture and orientation distribution along the sample directions. Equibiaxial stretching produced uniform morphology and orientation in the deformation plane. Decreasing the biaxiality led to a preferential orientation of the chain axis in the direction of the main stretching direction, while keeping the *b*-axis preferentially oriented in ND and in the minor stretching direction. Uniaxial and planar deformation were found to have similar crystalline textures.

Effect of Stretching Conditions on Biaxially Stretched Film Morphology and End-Film Properties

The degree of crystallinity and the thermal stability of the biaxially stretched iPP films were found to increase slightly with increasing area stretching ratio, while the crystallite size decreased considerably. The (040) in-plane orientation increased with stretching. Thus, the observed increase in *c*-axis orientation in the stretching plane could explain the increase in tensile strength and shrinkage and the decrease in elongation at break. The increase in crystallinity could also be correlated with the rise of the E-modulus with stretching. The increase in (040) in-plane orientation and the decrease in D_{040} crystallite size with increasing stretching ratio were explained by the predominant deformation mechanism of isotactic polypropylene, i.e., the (010) [001] chain slip mechanism. The decrease in crystallite size could partly explain the improvements of the optical properties upon stretching.

The drawing temperature was found to greatly influence the stretched film morphology. The degree of crystallinity, the thermal stability (T_m), and the crystallite size all increase with raising the drawing temperature, for a given draw ratio. This resulted in an increase in the elasticity modulus, but a deterioration of the optical properties. The in-plane orientation was found to decrease with increasing temperature, for the films stretched above the critical area stretching ratio of 10. This value of 10 represented the area stretching ratio, above which the major part of the initial morphology was transformed into oriented fibrous structure. Above an area stretching ratio of 10, the crystalline deformation appears to be dominated by the *c*-axis shearing of the fibrils through the (010) chain slip mechanism.

Finally, the following correlations were found between the stretched morphology and the end-use properties. A quasi linear relationship was found between the (040) in-plane orientation and the tensile strength. A correlation was also found between the in-plane orientation and the elongation at break. Finally, the degree of crystallinity was the dominant property that determines the elasticity modulus for a given resin. However, the chain tacticity is important in this respect.

Effect of Chain Tacticity on Deformation Behavior, Stretched Morphology, and End-Film Properties

It was found that the dimensions and perfection of the crystallites are mainly determined by the regularity of tacticity of the chains, which in turn determines the thermal stability and the stiffness of these crystallites. A low isotacticity content leads to reduced thermal stability of the crystallites, which in turn affects the partly molten morphology, for a given temperature. The reduced lamellar stiffness and the structural features of the partly molten morphology then govern the deformation behavior, the film morphology, and the mechanical end-use properties.

The mechanical properties of the stretched films were observed to depend strongly on the isotacticity content. Increasing the isotacticity content raised significantly the tensile strength and the elasticity modulus and decreased the elongation at break, for constant stretching conditions. Shrinkage appeared to be independent of the isotacticity of the PP resins. Similarly, the optical properties were not found to be directly dependent on tacticity. The results only showed that an optimal gloss for a given stretching ratio would be obtained, if the cast film was stretched about 15°C below its melting point, which is tacticity dependent.

On one hand, the final degree of crystallinity, the thermal stability, the in-plane orientation of the biaxially stretched films were all found to be considerably increased with the isotacticity content, which explained the change in the mechanical properties. On the other hand, the effect of biaxial stretching on the final morphology and orientation was found to depend strongly on the structural features of the partly molten morphology. In fact, the amount of structured melt was found to be linearly correlated with the in-plane orientation, and the increase in crystallinity and thermal stability (T_m), independently of the isotacticity of the resin. In addition, a tacticity independent linear relationship was found between the tensile strength and the amount of structured melt and between the elongation at break and the unmolten crystallinity, but not for the E-modulus. The level of E-modulus showed primarily a dependence on the isotacticity content of the initial cast film.

CHAPTER 10

CONCLUSIONS & ORIGINAL CONTRIBUTIONS

10.1 - Conclusions

The following conclusions could be made:

1) The simultaneous biaxial stretching for the laboratory film stretcher is homogeneous for Hencky strain rates above 0.1 s^{-1} and for a temperature range : $T_m - 25°C < T < T_m - 5°C$. Under these stretching conditions, a uniform thickness profile could be obtained at any stretching ratio.

2) The level of stress during deformation, for constant stretching conditions, is influenced by isotacticity and the crystallite size. The yield region is influenced by the tie molecule fraction and entanglement density.

3) The crystallite size of the simultaneously biaxially stretched films is influenced by stretching ratio and temperature.

4) The degree of crystallinity of the simultaneously biaxially stretched films is influenced by stretching temperature and isotacticity.

5) The in-plane orientation of the simultaneously biaxially stretched films is significantly influenced by stretching ratio, temperature, and isotacticity.

6) The most important factors influencing end film properties are shown below:

- Isotacticity and film crystallinity for the elastic modulus
- In-Plane orientation for the elongation and tensile strength at break
- Crystallite size for haze

7) The study explains the important role of isotacticity with regard to the biaxial stretching process and the end film properties

10.2 - Recommendations for Future Work

It would be of interest to extend the present work by investigating the simultaneous biaxial stretching of other series of polypropylene resins in order to study the effect of different types of tacticity defects, and tacticity defect distribution. Furthermore, an investigation of the effect of molecular structure on biaxial stretching of iPP films could be carried out by carefully selecting resins with similar isotacticity but different in molecular weights and molecular weight distributions. Furthermore, a series of linear and long-chain branched polypropylene resins could be selected to study the effect of long-chain branching on biaxial stretching in the partly molten state. Finally, a series of samples from the same resin with known fractions of tie molecules could be prepared to confirm the influence of tie molecules on the yield region.

Industrial production lines usually include a post-annealing section after stretching. A study of the effects of annealing temperature, time, and conditions (constrained in MD and/or TD) on the final properties of biaxially oriented PP (BOPP) films would be valuable for understanding the shrinkage and dimensional stability of the end films.

Commercial BOPP films are usually co-extruded with a pure iPP resin as the core layer and some blends in the outer layers. Therefore, it will be helpful to investigate the deformation behavior of such multi-layer systems under simultaneous biaxial stretching.

10.3 - Claims to Original Contribution to Knowledge

The claims to original contribution to knowledge are the followings:

1) The present work is the first comprehensive study of simultaneous biaxial stretching of isotactic polypropylene films, using a new laboratory film stretcher that simulates closely the stretching conditions encountered in industrial simultaneous biaxial stretching film lines.

2) This work is the first investigation of the evolution of the morphology at the various stages of the simultaneous biaxial stretching process.

3) The end film properties and the morphology at the various stages of the process were related to processing conditions and resin isotacticity.

4) It is proposed that the stretching behavior of films may be explained by the balance between and characteristics of the following three phases: unmolten crystalline phase, amorphous melt, and structured melt. This balance, in the partly molten cast film, is determined by isotacticity and temperature.

APPENDICES

TABLE OF CONTENTS

APPENDIX A COMPLEMENT OF CHAPTER 4 A1
A.1 - Wide-Angle X-Ray Diffraction A-3
  A.1.1 - Principles A-3
  A.1.2 - Measurement Techniques A-6
  A.1.3 - Wide-Angle X-Ray Diffractometer A-7
  A.1.4 - Analysis of X-Ray Diffraction Data A-8
  A.1.5 - Measurement Reproducibility A-18
A.2 - Wide Angle X-Ray Diffraction Pole Figures A-20
  A.2.1 - Principle A-20
  A.2.2 - Pole Figure Measurements A-21
  A.2.3 - Pole Figure Data Analysis A-23
A.3 - Measurement of the Isotacticity Index A-26
  A.3.1 - Principle A-26
  A.3.2 - Experimental Procedure A-26

APPENDIX B COMPLEMENT OF CHAPTER 5 B-1
  Surface Morphology of the Cast Films B-1

APPENDIX C COMPLEMENT OF CHAPTER 7 C-1
C.1 - Effect of Stretching Conditions on Biaxially Stretched Morphology C-1
  C.1.1 - Effect of Stretching Temperature and Strain Ratio on Stretched Morphology C-1
  C.1.2 - Effect of Stain Rate on Equibiaxially Stretched Morphology C-2
C.2 - Effect of Initial Morphology on Biaxially Stretched Morphology C-3

C.3 - Effect of Chain Tacticity on Equibiaxially Stretched Morphology C-5
C.4 - Effect of Deformation Type on the Equibiaxially Stretched Film Morphology C-7
    C.4.1 - Effect on Crystalline Texture - Results and Discussion C-7
    C.4.2 - Effect on Film Morphology - Results and Discussion C-11
    C.4.3 - Conclusions C-16

APPENDIX D COMPLEMENT OF CHAPTER 8 D-1
D.1 - Effect of Stretching Ratio on the End-Film Properties for the PP2 Cast Film D-1
D.2 - Effect of Drawing Temperature on the End-Film Properties for the PP1 Cast Film D-2
D.3 - Effect of Drawing Temperature on the End-Film Properties for the PP2 Cast Film D-3
D.4 - Effect of Drawing Temperature on the End-Film Properties for the PP3 Cast Film D-4
D.5 - Effect of Strain Rate on the End-Film Properties for the PP2 Cast Film D-5
D.6 - Effect of Initial Morphology on the End-Film Properties for the PP2 Cast Film D-6

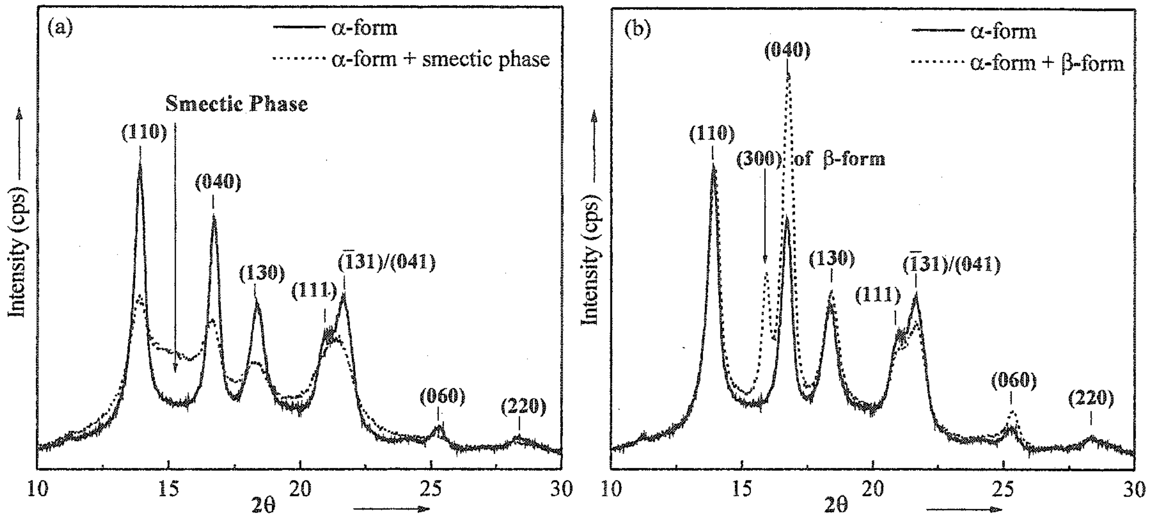

Figure A-1 *Wide-angle X-ray diffraction patterns for isotropic iPP specimens that contain some α -crystal form and some (a) smectic phase and (b) β-crystal phase*

A.1.1.2 - Determination of X-Ray Crystallinity

Several approaches have been reported for the determination of the X-ray relative crystallinity, or crystallinity index (CI) (1-5). The most rigorous approaches are those based on the method of Ruland (2), usually applied in the computerized version of Vonk (1), or according to the procedure proposed by Gehrke and Zachmann (6), involving the fitting to the diffraction data of a measured amorphous contribution plus analytical peak functions for the crystalline part. The main drawbacks of the Ruland-based procedures are the huge amount of experimental data needed and the need for the separation of the scattering of the amorphous from the crystalline phase. In practice, the separation of the amorphous from the crystalline component of the WAXD pattern is easily performed only for the most crystalline, isotropic samples. For the less crystalline samples, the problem of the separation of the two phases may have different solutions, especially in the presence of a third phase, the smectic phase. Moreover, the shape of the amorphous halo may change for different samples, especially for oriented samples, as shown in Figure A-8, which will be discussed later. Consequently, a procedure was developed in this work to determine the contribution of the amorphous phase from the X-ray patterns for both the isotropic and the oriented samples.

APPENDIX A

COMPLEMENT OF CHAPTER 4

A.1 - Wide-Angle X-Ray Diffraction

Wide-angle X-ray diffraction (WAXD) was used to obtain information about lattice dimensions, crystals forms, crystallinity, crystallite size, and orientation, while the pole figure technique provided information about texture and orientation distribution.

A.1.1 - Principles

A.1.1.1 - Principles of X-Ray Diffraction

X-ray diffraction is the constructive combination of X-ray waves scattered from an ordered region of high electron density. These ordered regions can be represented by a crystallographic symmetry having a certain space lattice and crystallographic planes, as discussed for polypropylene in section 2.1.3. The prominent crystallographic (*hkl*) planes, i.e., with the most thickly populated lattice points, will diffract X-rays according to Bragg's law. For a certain set of (*hkl*) planes, the diffraction intensity at the corresponding 2θ angle will be anisotropic if the sample has some orientation. The latter principle is exploited in both the pole figure and reflection techniques, as discussed below. For an isotropic iPP specimen, the main crystallographic planes of each crystal form will give diffraction peaks at certain 2θ angles. The different positions (2θ angles) of the diffraction peaks are a characteristic of each material. The diffraction peaks that are the characteristics of the crystal forms for polypropylene are shown in Figure A-1.

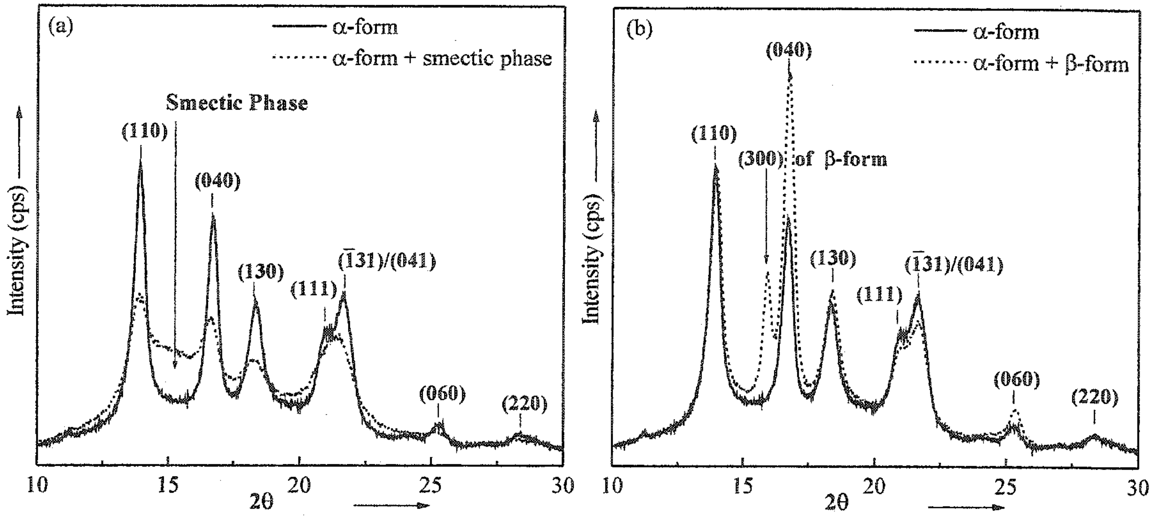

Figure A-1 *Wide-angle X-ray diffraction patterns for isotropic iPP specimens that contain some α-crystal form and some (a) smectic phase and (b) β-crystal phase*

A.1.1.2 - Determination of X-Ray Crystallinity

Several approaches have been reported for the determination of the X-ray relative crystallinity, or crystallinity index (CI) (1-5). The most rigorous approaches are those based on the method of Ruland (2), usually applied in the computerized version of Vonk (1), or according to the procedure proposed by Gehrke and Zachmann (6), involving the fitting to the diffraction data of a measured amorphous contribution plus analytical peak functions for the crystalline part. The main drawbacks of the Ruland-based procedures are the huge amount of experimental data needed and the need for the separation of the scattering of the amorphous from the crystalline phase. In practice, the separation of the amorphous from the crystalline component of the WAXD pattern is easily performed only for the most crystalline, isotropic samples. For the less crystalline samples, the problem of the separation of the two phases may have different solutions, especially in the presence of a third phase, the smectic phase. Moreover, the shape of the amorphous halo may change for different samples, especially for oriented samples, as shown in Figure A-8, which will be discussed later. Consequently, a procedure was developed in this work to determine the contribution of the amorphous phase from the X-ray patterns for both the isotropic and the oriented samples.

lateral dimensions of the crystallites. Moreover, the D_{040} crystallite size gives a good estimation of the perfection of the crystalline structure on the lamellar scale.

A.1.2 - Measurement Techniques

Wide-angle X-ray diffraction (WAXD) experiments can be carried out in reflection or transmission. For a simple 2θ scan, polymer characterization is generally carried out in transmission, because of the very small absorption coefficient of polymers and the possibility of obtaining an average measurement over the sample thickness. Nevertheless, the transmission mode provides a limited amount of structural information compared to the reflection mode, for certain types of samples, such as those with the main diffraction planes oriented perpendicular to the measurement direction. This is the case of biaxially oriented polypropylene films. WAXD measurements in this work were performed in the symmetrical reflection mode. Measurements in reflection and transmission are illustrated in Figure A-2.

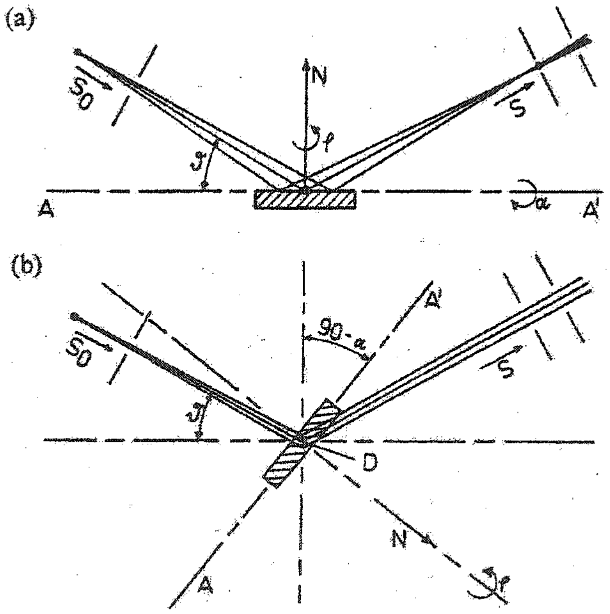

Figure A-2 *Schematic of the X-ray measurement in the (a) reflection and (b) transmission modes*

A.1.3 - Wide-Angle X-Ray Diffractometer

A.1.3.1 - Apparatus

A Siemens D500 Diffractometer mounted with a θ-2θ goniometer using the CuK_α wavelength was utilized to carry out the diffraction measurements in symmetrical reflection. The voltage and the current of the X-ray source was set to 40kV and 30 mA. The apparatus was equipped with aperture diaphragms of 1° (for I,II, and III) and of 0.05° for the detector diaphragm. A graphite beam monochromator was used to suppress the K_β reflections. Diffracted X-rays were detected by a scintillation counter. A conventional reflection experiment consisted of measuring a 2θ scan from 6° to 32° with a 0.02° step every 2 seconds.

A.1.3.2 - Sample Preparation for the reflection technique

A poly(methyl methacrylate) sample holder, having a square plate shape which had its central part hollowed, was designed to eliminate the scattering background due to the sample holder. This allowed the use of thin films. However, the intensity of the diffracted peaks is strongly dependent on film thickness. Consequently, thin film samples were cautiously cut into square form (45 mm x 45 mm) and glued together with a small amount of polyvinylacetate (PVA) glue, in order to increase diffracted intensity and improve the accuracy of the measurement. The minimum sample thickness to give sufficient accuracy was 200 µm. Most of the specimens had a thickness higher than 200 µm and up to 1.2 mm for the cast films. PVA glue was chosen because it is amorphous and thus does not influence the diffraction measurements. The specimen orientation was carefully noted and aligned with the sample holder. For most of the specimens, after measuring in one direction, the sample holder was rotated by 90° and a second recording was then carried out.

A.1.3.3 - X-ray Penetration Depth

For the experimental evaluation of the X-ray penetration depth of the diffractometer used in this work, a series of samples of various thicknesses with an aluminum oxide (Al2O3) support were characterized. The diffracted intensity of the crystalline peak at $2\theta = 24.3°$, which is only a characteristic of Al2O3 and does not overlap with other iPP crystalline peaks, was measured for the different film thickness. This intensity was normalized to one for the intensity without any iPP specimen. The results plotted in Figure A-3 show that for an iPP sample of about 630 μm the intensity of the Al2O3 reaches zero. Therefore, it can be assumed that the X-ray penetration depth was at least 500 μm.

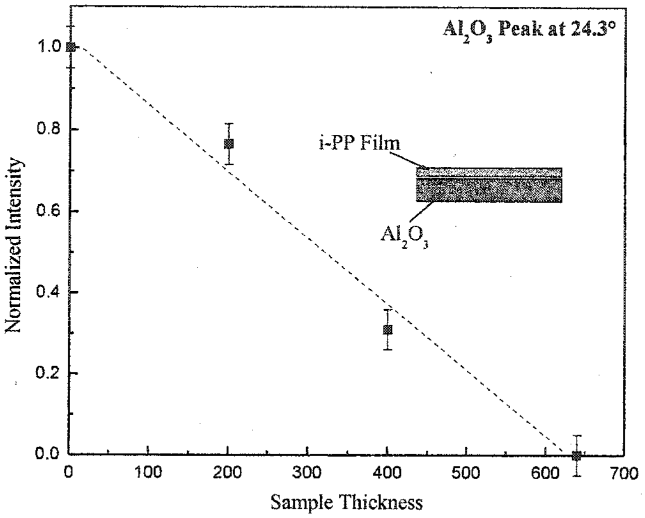

Figure A-3 *Normalized intensity of the characteristic Al2O3 crystalline peak at* $2\theta=24.3°$ *as function of the iPP film thickness*

Subsequently, in the case of the cast films, which had an approximate thickness of 1 mm, the samples were characterized on both sides. The reflection technique has thus the advantage of yielding structural information about each side of the cast films, which are known to have asymmetric morphology. Average values and curves from measurements on both sides were then computed, when needed. A small difference may be obtained between the values between calculated from the bulk and the ones averaged from the surfaces, as already reported by Nishino et al. (10).

A.1.4 - Analysis of X-Ray Diffraction Data

X-ray diffracted intensities provide information about the degree of crystallinity, the crystal forms, the size of the crystallites, and the average orientation of crystallites. The diffraction data, were not corrected for incoherent scattering and for Lorentz and polarization factors, because such corrections are not important in the evaluation of relative crystallinity (5). Nevertheless, the diffracted intensities were corrected for the loss of scattered intensity for thin samples, as follows (11):

$$I_{corr} = I_{\exp} / (1 - \exp(-2\mu t / \sin\theta)) \qquad eq.(A\text{-}3)$$

where μ is the linear absorption coefficient, t the sample thickness, and θ the diffraction angle. The reproducibility of the WAXD measurements is shown for three specimens of the same isotropic sample in Figure A-10). It shows that the WAXD patterns are identical at this level of data representation.

A.1.4.1 - Determination of the X-Ray Crystallinity

A.1.4.1.1 - Determination of the Amorphous Contribution

A background curve corresponding to the amorphous halo was constructed, according to a procedure adapted from Weidinger and Hermans (5). The method assumes that the maximum height of the background corresponds to that of the minimum between the two (110) and (040) peaks. Furthermore, the maximum of the background lies at the same diffraction angle ($2\theta = 16.3°$) as that in the diffraction curve of an entirely amorphous polypropylene sample. A background curve is then constructed congruent with the diffraction curve of an amorphous sample, as explained below.

As a guidance, the following steps are taken:

1) A baseline is drawn between $2\theta = 7°$ and $2\theta = 31°$ and is then subtracted
2) A point at $2\theta = 16.3°$ is set at a height a, corresponding to the scattering intensity minimum between the (110) and (040)
3) Another point of the background at $2\theta = 14{,}8°$ is then found at the vertical distance of 0,9 a.
4) The background curve is finally drawn as a cubic spline curve, starting at 10°, passing through the two above constructed points and tangential to the diffraction curve at the angles of about 12° and 23.5°, and ending at 30°.

This method was slightly modified for the determination of the background for the samples containing some smectic phase. For the former case, the smectic phase is known to have two broad diffraction peaks at about 15.3° and 21.4°(12). Therefore, the first smectic diffraction peak overlaps with the (110) and (040) peaks. For this reason, the construction modification consist of shifting the two points at 14.8° and 16.3° to lower intensity so that the background curve becomes nearly tangent to the diffraction curve at the diffraction curve minimum between the (130) and (111) peaks, as illustrated in Figure 5-6.

For the oriented samples, the shape of the amorphous halo is affected by the type and amount of orientation, as shown in Figure A-4. Therefore, the construction of the background curve was modified. The procedure was the same as for an isotropic sample up to step 3). In addition, the tangent point at 23.5° was shifted to about 22° and two other contact points were added at approximately 19.5° and 27.5°. Finally, a cubic spline curve was drawn between the points at 10° and 22° and a cubic B-spline curve was drawn between the points 22° and 30°. Finally, the amorphous halo was the composition of these two curves.

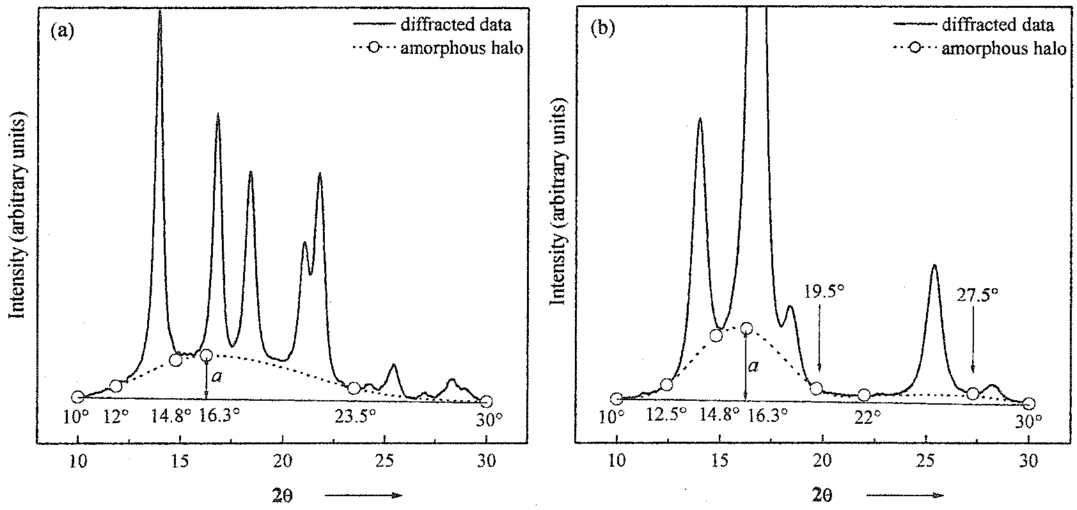

Figure A-4 *Construction of the amorphous halo for (a) an isotropic cast film and (b)n for an biaxially oriented samples*

A.1.4.1.2 - Calculation of the X-Ray Crystallinity

The X-ray crystallinity index was first estimated following the method of Weidinger and Hermans (5). However, the much simpler area ratio method was found to give identical results. Therefore, the following definition of the X-ray crystallinity index (CI_{WAXD}) was used:

$$CI_{WAXD} = \frac{A_{total} - A_{am}}{A_{total}} \qquad eq.(A\text{-}4)$$

where A_{total} is the total area under the curve between 10° and 30° and A_{am} the area under the amorphous halo. The same definition was used for samples containing some smectic or β-phase. Hence, the contributions of the other phases were added to the crystallinity index. For oriented samples, X-ray crystallinity index could be computed, but was not discussed. Indeed, X-ray diffraction is known to be very sensitive to orientation.

A.1.4.1.3 - Measurement Reproducibility

In order to account for all the possible sources of error, three different specimens from the same isotropic, compression molded sample were investigated by WAXD under identical experimental conditions at different times. The standard deviation of the CI from these three measurements was found to be equal to 0.5 % crystallinity. The curves and the detailed results of the reproducibility experiments are presented in Appendix A.

A.1.4.2 - Curve fitting procedure

The remaining crystalline peaks were fitted using a multi-peak fitting procedure, after subtraction of the amorphous halo. The chosen analytical function was a Pearson-type function, which has been used successfully for polymers by several authors (4, 13, 14) and is the reference shape function for other materials in the Rietveld method (15). The Pseudo-Voigt peak function was used with the following parameters: the baseline height, the angular position, the area, the peak width, and the shape parameter, which is a coefficient between 0 and 1. The fitting procedure was performed by the Microcal Origin© software, which used a non-linear least-squares method. The fitting was considered satisfactory when the χ^2 was minimum and, in most cases, the R^2 coefficient was equal to at least 0.99.

A typical result of the curve fitting procedure for an isotropic cast film is presented in Figure A-5. The multi-curve fitting yielded the full angular width at half maximum (FWHM), the intensity, angular position, and area of the main diffraction peaks. The apparent crystallite size, the phase content index, and the in-plane orientation could be then computed using the fitted peak information.

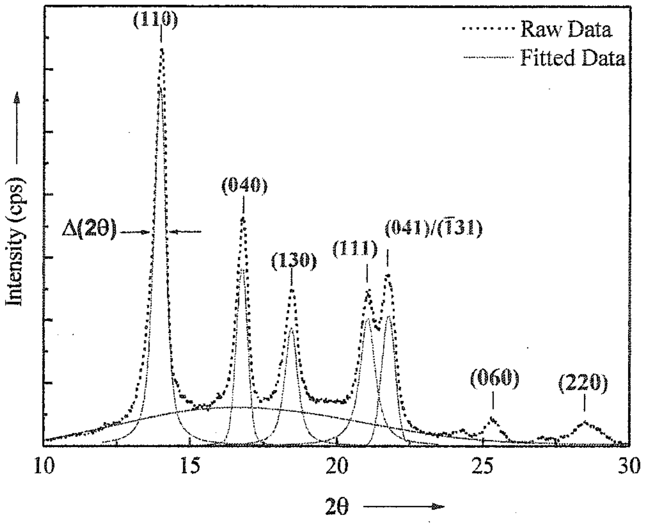

Figure A-5 *Example of the multi-peak fitting procedure and the constructed amorphous halo for an isotropic iPP sample*

A.1.4.3 - Determination of the Apparent Crystallite size

The average size of the crystallite can be calculated using Scherrer's equation. The observed angular width, as obtained from the fitting procedure, was corrected for the instrumental broadening. The instrumental broadening was estimated by measuring the diffraction peak breadth of a material having crystallites of infinite size. Aluminum oxide, which is the most widely used reference material for such measurement, was chosen to estimate the machine broadening. This was found to be equal to 0.175° and was utilized as $\Delta(2\theta)_{\text{inst}}$ for Warren's correction.

The measurement reproducibility was estimated using the same series of measurements used to evaluate the reproducibility of crystallinity. It was found that the maximum standard deviation was 3 Å. Since the crystallite size range, measured in this study, was over 100 Å the percentage error was about 3% (cf. section A.1.5).

The analytical procedure was slightly different for the oriented specimens. The measurement direction may affect the results. Therefore, two identical oriented samples were prepared and measured in both MD and TD. In addition, one sample was rerun (cf. section A.1.5). The maximal standard deviation value for the crystallite size was equal to 3 Å. However, the crystallite size range calculated for oriented samples was around 50 Å, giving thus a percentage error of 6%.

A.1.4.4 - Crystal form Indices

A.1.4.4.1 - β-Crystal Form Index

Turner Jones et al. (16) first introduced the concept of quantitative analysis of the crystal forms of iPP using WAXD. The authors defined a β-crystal form index as follows (16):

$$k_\beta = \frac{I_{300}^{\beta}}{I_{300}^{\beta} + I_{110}^{\alpha} + I_{040}^{\alpha} + I_{130}^{\alpha}} \qquad eq.(A\text{-}5)$$

where I_{300}^{β} and I_{hk0}^{α} are the intensities of the corresponding diffraction peaks, as seen in Figure A-1(b). Measurement reproducibility was evaluated to be about 5%. It is important to notice that the β-index value is a relative measure for characterizing the polymorphic composition, but it does not indicate the absolute value of β-form content. However, k_β is 0 for the pure α-form and 1 for the pure β-form of iPP.

A.1.4.4.2 - Smectic Phase Index

Zannetti et al. (17) first proposed a simplified method using WAXD to follow the disappearance of the smectic phase in favor to the α-form. They used the reciprocal of the half-height broadening of the (110) diffraction peak. Recently, Martorana et al. (18) developed a more accurate procedure for the determination of the smectic phase together with the α-form and the amorphous phase for quenched iPP samples. The method involves multiple peak fitting of WAXD patterns for various specimens quenched at different cooling rates. The fractional amount of the phases were determined as the ratio of the relevant calculated peak area to the total one.

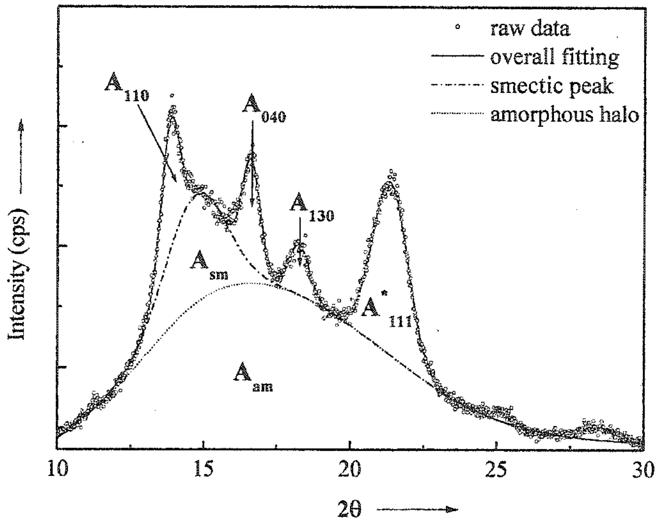

Figure A-6 *Example of the multi peak fitting applied to a specimen containing some smectic phase (A_{sm} and A_{hk0} are the peak areas of the corresponding diffraction peaks, except A_{111} which includes the (111) & (131)/(041) peak doublet of the α-form and the second peak of the smectic phase)*

A similar approach as Martorana et al. was followed here. However, the WAXD patterns were analyzed individually, because of the few investigated samples containing some smectic phase. The smectic phase index, k_{sm}, was estimated as follows:

$$k_{sm} = \frac{A_{sm}}{A_{sm} + A_{110} + A_{040} + A_{130}} \qquad eq.(A\text{-}6)$$

where A_{sm} and A_{hk0} are the peak areas of the corresponding diffraction peaks, as shown in Figure A-6. Again, the smectic-index is a relative measure of the content of the smectic phase. Because of the complex peak overlapping, measurement reproducibility was lower than for the β-index, i.e., about 10%.

A.1.4.5 - In-Plane Orientation Index

The most common method to determine the state of orientation of an anisotropic sample is by X-ray diffraction pole figure measurements (see section A.2). Even though this technique provides a complete characterization of orientation and texture, it is time consuming and requires rather complex data analysis. In this work, an attempt was made to utilize diffraction data from WAXD in reflection to compare quantitatively the texture and orientation of equibiaxially oriented samples. The method described here is limited to the relative comparison of samples having the uniplanar texture, i.e. equibiaxially stretched samples.

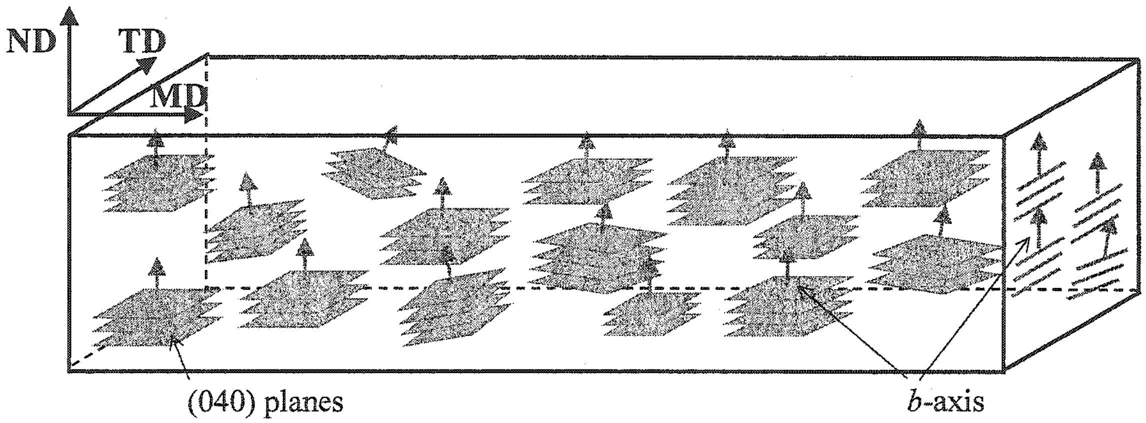

Figure A-7 Schematic of the in-plane orientation of (040) crystal planes

In principle, X-rays in the WAXD reflection technique will be only diffracted by the crystallographic planes that are parallel to the sample surface being investigated. The investigated plane is the one that contains the MD and TD directions. The WAXD patterns of simultaneously equibiaxially oriented (SEBO) specimens show only three main diffraction planes oriented parallel to the film surface. These three major peaks corresponds to the (110), (040), and (130) crystal planes (cf. results section, Figure 9-4). Consequently, the intensities and areas of these diffraction peaks are proportional to the amount of the (110), (040), and (130) crystal planes being oriented in the MD-TD plane. The normal to the (040) crystal plane is the [010] direction, which is by definition parallel to the *b*-axis. Therefore, the area of the (040) diffraction peak, which is related to the (040) crystal plane orientation in the MD-TD plane, will be proportional to the *b*-axis orientation in the ND direction, as schematically shown in Figure A-7. The area of the (040) diffraction peak was normalized with respect to the sum of the areas of all the major diffraction peaks that appear between 10° and 24°, as shown in Figure A-5. A (040) in-plane orientation index can be thus defined from the WAXD measurements as follows:

$$I_{(040)}^{in-plane} = \frac{A_{040}}{\sum_{2\theta=10}^{2\theta=24} A_{hkl}} \qquad eq.(A\text{-}7)$$

where A_{hkl} is the area of the corresponding (*hkl*) diffraction peak. The (040) in-plane orientation index can be interpreted as the proportion of (040) crystal planes that are perfectly oriented compared to the other major (*hkl*) crystal planes. Therefore, the (040) in-plane orientation index will be zero when no (040) crystal planes are oriented in the MD-TD plane, and it will be equal to one when only (040) crystal planes are oriented in the MD-TD plane. The same definition can be applied for the (110) peak to calculate the (110) in-plane orientation index. The WAXD patterns and the corresponding values of the (040) in-plane orientation index are shown in Figure A-8 for an isotropic specimen and a highly oriented sample. The measurement reproducibility for the (040) and (110) in-plane orientation indices was found to be within 0.005.

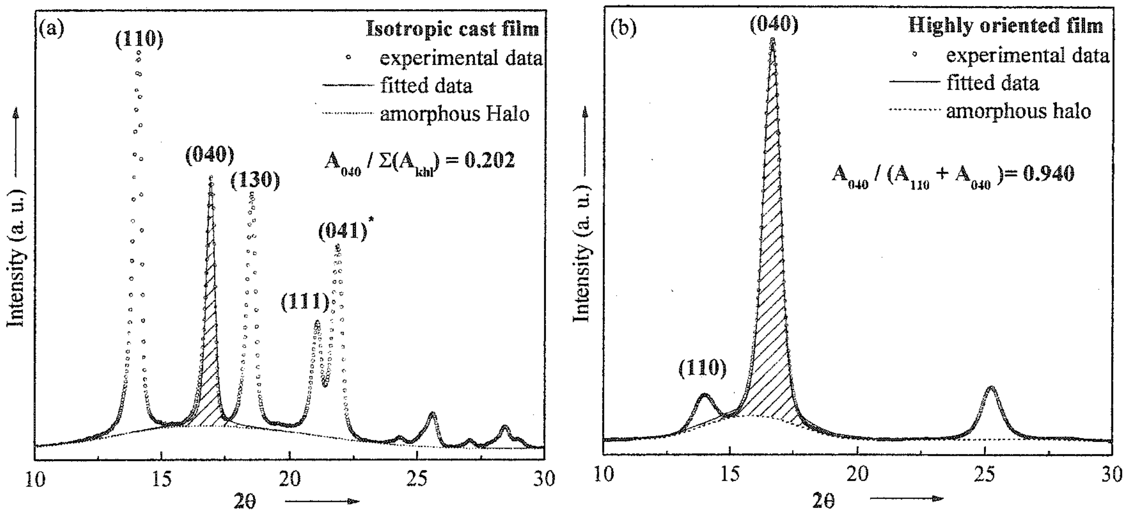

Figure A-8 *WAXD patterns illustrating the (040) in-plane orientation index, TI, for (a) an isotropic sample and (b) a highly oriented film.*

The higher is the (040) in-plane orientation index, the higher will be the degree of in-plane orientation of the (040) crystal planes, and thus, the higher is the degree of orientation of the *b* axis in ND (perpendicular to the film plane). This degree of *b* orientation can be expressed in terms of average squared cosine, $<\cos^2\theta_{b,ND}>$, which can be assessed by infrared dichroism or pole figure measurements (cf. Chapter 4). The (040) in-plane orientation index from WAXD and $<\cos^2\theta_{b,ND}>$ from infrared dichroism are compared for a series of simultaneous equibiaxially oriented films stretched at different ratios, as illustrated in Figure A-9.

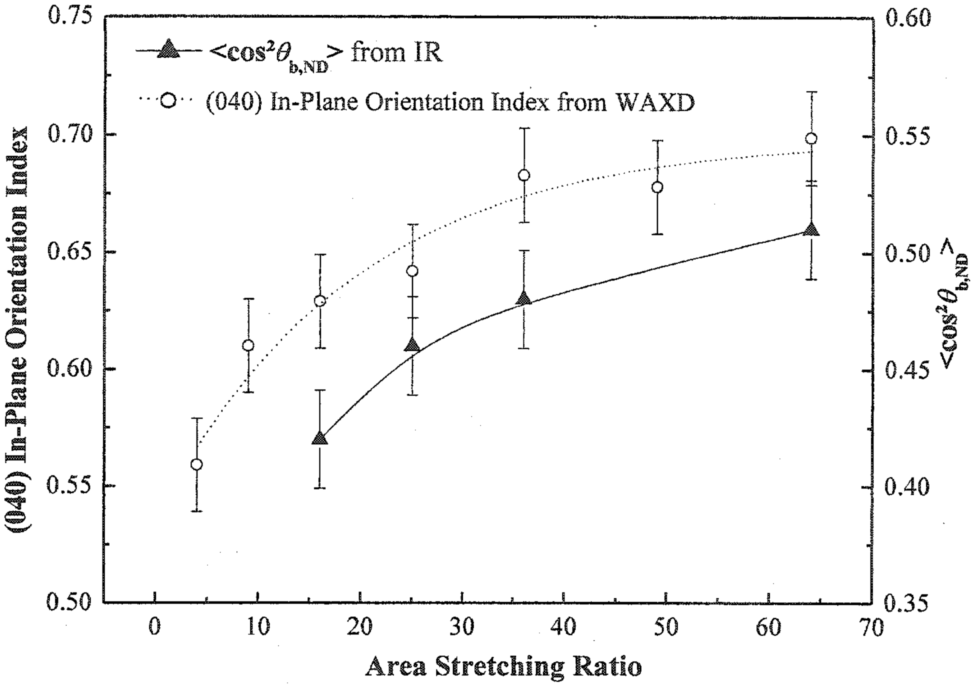

Figure A-9 *Comparison of the (040) in-plane orientation index from WAXD measurements with the $<\cos^2\theta_{b,ND}>$ from infrared dichroism for a series of simultaneous equibiaxially oriented films*

Figure A-9 shows that there is very good qualitative agreement between the (040) in-plane orientation index and the average cosine of the *b*-axis orientation in ND obtained by infrared dichroism. The *b*-axis orientation in ND yields also information about the *c*-axis orientation in the MD-TD plane. Indeed, when the *b*-axis is oriented in ND, the *c*-axis must be in the MD-TD plane by crystallographic symmetry. In fact, simultaneous equibiaxial stretching was reported to yield random *c*-axis orientation in the MD-TD plane around ND (19). Therefore, the (040) in-plane orientation index can be used to compare the *b*-axis orientation in ND and the *c*-axis orientation in the deformation plane for specimens simultaneously equibiaxially stretched. Nevertheless, it should be noted that the (040) in-plane orientation index gives only an indication about the (040) crystal planes that are perfectly aligned in the MD-TD plane. It does not provide information about orientation distribution.

[Refs. on p. A27]

A.1.5 - Measurement Reproducibility

A.1.5.1 - Isotropic, Thick Films

The reproducibility for isotropic cast films was assessed by measuring three different samples cut out from a same compression molded specimen and measured at different times. The experimental curves are shown in Figure A-10. A good reproducibility of the WAXD patterns can be observed in this figure. The subsequent curve fitting and data analysis led to the following reproducibility errors of 2 Å, 0.002 Å, and 0.5% for the D_{hkl} apparent crystallite sizes, the d_{hkl} interplanar spacing, and the X-ray crystallinity, respectively.

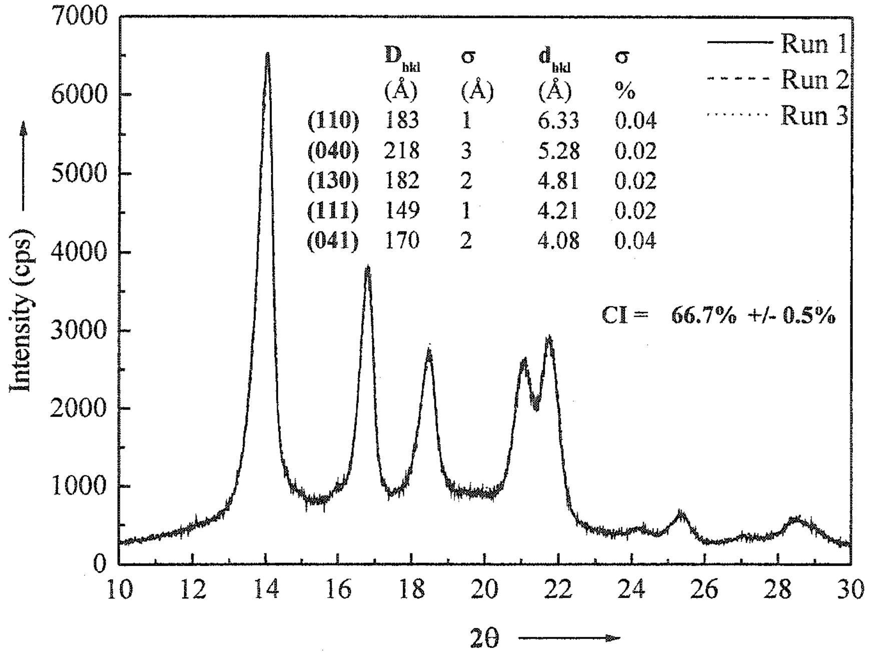

	D_{hkl} (Å)	σ (Å)	d_{hkl} (Å)	σ %
(110)	183	1	6.33	0.04
(040)	218	3	5.28	0.02
(130)	182	2	4.81	0.02
(111)	149	1	4.21	0.02
(041)	170	2	4.08	0.04

CI = 66.7% +/- 0.5%

Figure A-10 *Reproducibility of WAXD measurements showing the average results and the standard deviations from three measurement(σ) of the different crystallite sizes (Dhkl), the interplanar spacing (dhkl), and the crystallinity index (CI)*

A.1.5.2 - Stretched, Thin Films

The reproducibility of the WAXD measurements and the subsequent analysis for two film samples equibiaxially stretched at 150°C up to a 5.7x5.7 area stretching ratio is illustrated in Figure A-11 and in Table A-1. It can be seen that the standard deviation of seven measurements carried out in different directions and for the two different samples is 2 Å, 0.01 Å, and 0.002 for the D_{hkl} apparent crystallite sizes, the d_{hkl} interplanar spacing, and the in-plane orientation, respectively.

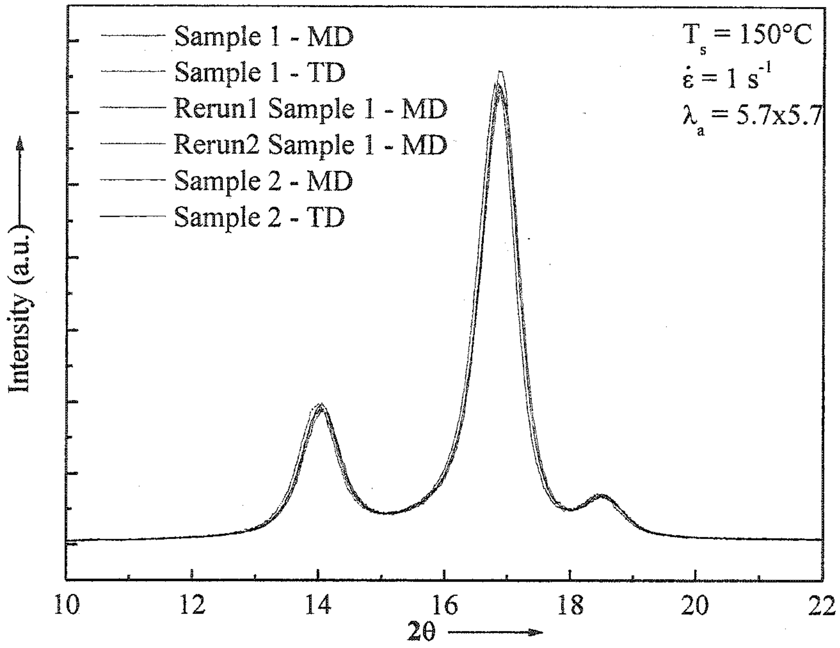

Figure A-11 *Measurement reproducibility of the WAXD patterns for a film equibiaxially stretched at 150°C up to a 5.7x5.7 area stretching ratio*

run#		1	2	3	4	5	6	7	**Average**	**Std. dev.**	**Error$_{max}$**
D_{110}	**[Å]**	134	139	134	135	133	133	133	134	2	5
D_{040}	**[Å]**	130	134	130	129	128	129	128	130	2	4
In-Plane	**[-]**	0.741	0.745	0.742	0.745	0.741	0.745	0.748	0.744	0.002	0.004
d_{110}	**[Å]**	6.33	6.30	6.30	6.31	6.30	6.30	6.29	6.31	0.01	0.02
d_{040}	**[Å]**	5.27	5.25	5.25	5.25	5.25	5.25	5.25	5.25	0.01	0.02

Table A-1 *Measurement reproducibility of the different parameters for a film equibiaxially stretched at 150°C up to a 5.7x5.7 area stretching ratio*

A.2 - Wide Angle X-Ray Diffraction Pole Figures

To characterize the orientation of the various crystallographic axes *a*, *b*, and *c* with respect to the sample axes, the study of the orientation distribution of certain crystallographic (*hkl*) planes with respect to the sample axes must be carried out. The most useful and complete method to obtain this information is the pole figure technique.

The study of orientation in polypropylene films using the X-ray pole figure method has been first carried out by Wilchinsky (20-22). The author first showed that the average *c* axis orientation could be obtained by determination of orientation of two planes, (110) and (040) containing the *c* axis. More recently, other studies have investigated orientation for iPP using X-ray pole figures (23-25). It was found that rolling (22), hydrostatic uniaxial compression (26), or tentering (24, 27) produced chain axis *c* orientation nearly parallel to the drawing plane or direction and *b* axis orientation perpendicular to the drawing plane. This is equivalent to having the (040) plane oriented parallel to the drawing plane.

WAXD pole figure experiments in this work were carried out to obtain information about the type of texture obtained under various modes of stretching, such as uniaxial, planar, and biaxial. The orientation distribution functions for the distinctly textured samples were also evaluated.

A.2.1 - Principle

The diffracted intensity distribution over a whole sphere can be obtained by rotating the sample over two perpendicular axes. Diffraction data may be used to determine the Hermans orientation functions in the form of eq.(2-2), where the average square cosines of the average angles that the normal of the set of (*hkl*) planes make with some sample axes (MD, TD, or ND). If $I(\alpha, \beta)$ is the diffracted intensity representing the relative amount of material having (*hkl*) plane normals in the direction (α, β) the following relationships can be written:

$$<\cos^2\theta_{hkl,N}>=\frac{\int_0^{2\pi}\int_0^{\pi/2} I(\alpha,\beta)\cos^2\alpha\sin\alpha\,d\alpha\,d\beta}{\int_0^{2\pi}\int_0^{\pi/2} I(\alpha,\beta)\sin\alpha\,d\alpha\,d\beta} \qquad eq.(A\text{-}8)$$

[Refs. on p. A27]

$$< \cos^2 \theta_{hkl,MD} >= \frac{\int_0^{2\pi}\int_0^{\pi/2} I(\alpha,\beta)\sin^3\alpha\cos^2\alpha\, d\alpha\, d\beta}{\int_0^{2\pi}\int_0^{\pi/2} I(\alpha,\beta)\sin\alpha\, d\alpha\, d\beta} \qquad eq.(A\text{-}9)$$

$$< \cos^2 \theta_{hkl,TD} >= \frac{\int_0^{2\pi}\int_0^{\pi/2} < I(\alpha,\beta)\sin^3\alpha\sin^2\alpha\, d\alpha\, d\beta}{\int_0^{2\pi}\int_0^{\pi/2} < I(\alpha,\beta)\sin\alpha\, d\alpha\, d\beta} \qquad eq.(A\text{-}10)$$

where the two angles, α and β, describe the orientation of the normals to a given crystallographic plane; α is the tilt angle between the sample transverse direction and a fixed direction, and β is the rotation angle about the sample normal, as shown in Figure A-12.

A.2.2 - Pole Figure Measurements

X-ray pole figure measurements were carried out with a D500 diffractometer equipped with a pole figure attachment employing CoK_α radiation. The voltage and the current of the X-ray source were set to 35 kV and 14 mA, respectively. The tube length was 100 mm with an aperture of 1°, the secondary aperture diaphragm was 2°-4° and the detector diaphragm was 0.6°.

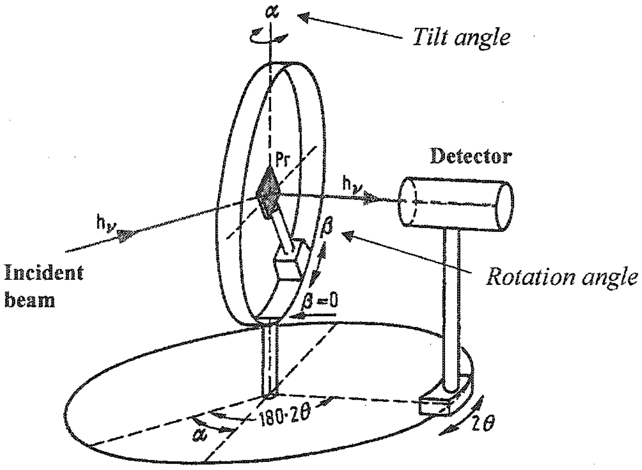

Figure A-12 Schematic of the pole figure X-ray measurement technique (α = tilt angle and β = rotation angle)

A.2.2.1 - Pole Figure Attachment

The pole figure attachment was a computer-controlled, full-circle Eulerian cradle, which provided two complete circular motions of the sample about two axes while the diffraction angle is fixed, as illustrated in Figure A-12. The diffracted intensity distribution over a whole sphere can be then recorded. Orientation measurements can be presented in terms of pole figures, which are the stereographic projections of the diffracted intensities of the normals to the crystallographic planes.

A.2.2.2 - Experimental Procedure

The preparation of the specimens was the same as for the WAXD experiments in reflection, as described in section 5.1.3.2. Samples were approximately 30 mm x 20 mm. A specially designed sample holder was employed in order to ensure perfect planarity of the sample. Each sample was scanned to measure the intensity as a function of α and β in both transmission and reflection modes, since neither mode can cover the whole range of tilt angle from 0 to 90°. The position of the detector was set at the 2θ angle corresponding to the *(hk0)* reflection, while the sample was rotated about its own axis to record the intensities of the diffracting planes in space. The intensities were recorded with full circular scans at different tilt angles, from 0 to 90° by 2.5° steps. The circular scans were performed in reflection from 0° to 60° and in transmission from 60° to 90°, with a 5° step. For the circular scan, a speed of 1s/1° was utilized. Only the (110) and (040) pole figures were performed for all the investigated samples.

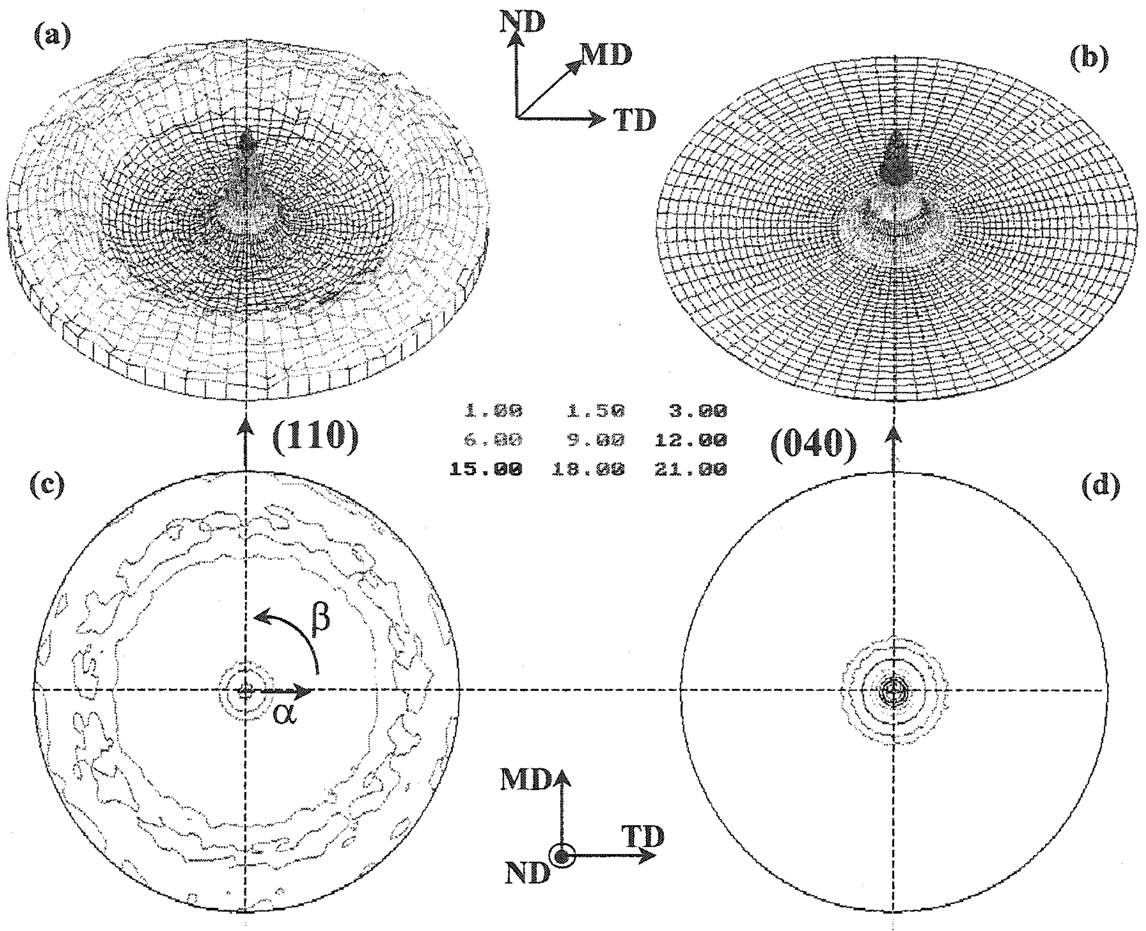

Figure A-13 *Example of the three and two dimensional representation of the (110) and (040) pole figures for a biaxially oriented iPP sample. (a) and (c) correspond to the (110) pole figure while (b) and (d) to the (040) pole figure; in (c) and (d) the contours are isointensity lines*

A.2.3 - Pole Figure Data Analysis

A.2.3.1 - Intensity Corrections

The intensity data were corrected for background, defocusing and absorption effects. Background scatter was measured as a function of α and β at $2\theta = 35°$, a position off the peak in reflection and in transmission modes. Defocusing and absorption in the reflection mode were performed using an isotropic iPP sample of the same

[Refs. on p. A27]

thickness as the investigated sample (9). Absorption corrections in transmission were calculated by the Siemens TEX_AT software, according to the procedure developed by Decker et al. (11). The integrated software scaled the intensities obtained from the measurements in reflection and transmission to the same level and allowed the plotting of the pole figures in three dimensions, as illustrated in Figure A-13.

A.2.3.2 - Representation of Orientation

Orientation measurements can always be presented as pole figures, which are the stereographic projections of the diffracted intensities, as illustrated in Figure A-13. Three- (3D) and two-dimensional (2D) representations show intensities as function of α and β, either on the z-axis for the 3D representation, or as isointensity contours for the 2D representation. The diffracted intensities are correlated with the orientation of the normal of (*khl*) planes. High intensities will indicate a high concentration of these planes and define a type of texture.

For example, the (040) pole figure shown in Figure A-13 exhibits an intensity maximum in the center that indicates that the (040) crystal plane normals are oriented towards ND, and hence that the (040) crystal planes are oriented in the MD-TD plane, i.e. parallel to the film surface. This type of plane orientation can be referred to as a uniplanar texture, as defined in Chapter 2. The (110) pole figure exhibits two high intensity regions: one in the center and one with radial symmetry at $\alpha = 72.5°$. The former indicates that some (110) planes are also oriented in the MD-TD plane, while the latter indicates that the (110) plane normals are inclined with a 72.5° angle to ND. This last feature is a direct consequence of the main uniplanar texture, i.e. (040) planes being oriented in the MD-TD plane, that requires that the (110) planes be oriented at an angle of 17.5° (90 – 72.5) to the MD-TD plane.

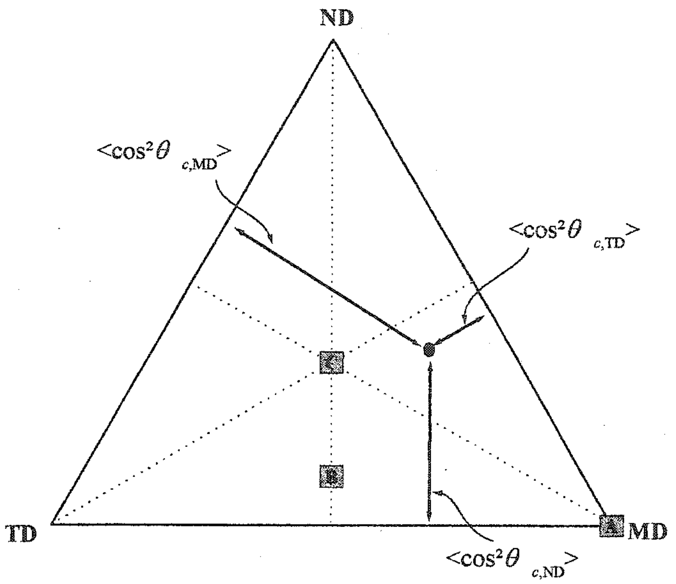

Figure A-14 *Hypothetical orientation diagram of the* $\langle\cos^2\theta_{c,J}\rangle$ *values.* ● = *hypothetical diagram point; (A) ideal uniaxial orientation; (B) uniplanar orientation; (C) random orientation*

An orientation diagram that uses the Hermans-orientation factors may be plotted in the form of equilateral triangle, as shown in Figure A-14. The three bisectors have a length of unity and can be related to the values of $\langle\cos^2\theta_{i,J}\rangle$, the average square cosines calculated from the diffracted intensities. A given point on such a triangular plot defines the second moment orientation parameters of a given crystal axis or plane with respect to the three sample axes. For example, each of the points (A) to (C) represents a particular orientation of the *c* crystal axis with respect to MD, TD, and ND. Point (A) refers to the case where there is perfect alignment of the c axis along the MD axis, corresponding to the ideal case of uniaxial orientation. Point (B) represents also the preferential orientation of the c axis in the plane MD-TD, with uniform distribution in MD and TD. Finally, point (C) refers to random orientation.

A.3 - Measurement of the Isotacticity Index

A.3.1 - Principle

In addition to the complex ^{13}C NMR investigation to characterize the structure of the chain, IR spectroscopy offers a good alternative to carry out a quantitative analysis of structure and conformation of polymer chains. From the first attempt to quantify isotactic content, various absorption bands at 809, 841, 900, 998, 1168, and 1220 cm^{-1} have been associated with isotactic helices(28). More recently, Kissin et al.(29, 30) observed that specific absorption bands are related to the critical length of isotactic sequences: 975 cm^{-1} for at least 5 units, 998 cm^{-1} for 11-12 units, and 841 cm^{-1} for 13-15 units. The bands at 841 and 998 cm-1 have been used as standards for calibration curves, which suppose a direct relationship between absorption intensity and isotactic content. This view is not realistic since highly tactic parts of chain are also present in the amorphous phase. Nevertheless, for the standardized method, for which the samples are annealed in the temperature range close to the melting point for at least 15 min (31, 32), a reasonable direct correlation is found between the absorption intensity ratios, A_{998}/A_{973} and A_{841}/A_{973} and the isotacticity index deduced from NMR measurements (31).

Consequently, the different PP resins were also characterized by IR spectroscopy in order to confirm the results of isotactic content obtained from the room temperature xylene solubility experiments. In this method five grams of PP resin were dissolved in 250 ml xylene and then precipitated at low temperature. Since atactic polypropylene is soluble in xylene at room temperature, after filtering the precipitated isotactic part and drying out xylene only the xylene soluble (*XS*) part remained and could be assessed. The isotacticity index (II) was calculated as follows: II = 100% - XS.

A.3.2 - Experimental Procedure

The experimental procedure described here is the one based on a standard method discussed in (31). A very thin of about 10μm was prepared by compression molding, annealed for 10 min at approximately 5°C below its melting point, and then cooled down slowly to room temperature. The film sample was then scanned. After correction for the

[Refs. on p. A27]

baseline and overlapping peaks, the absorption intensities of the peak at 973 cm^{-1} and 998 cm^{-1} were used to compute the absorption intensity ratio. In this case the isotacticity index is proportional to this ratio ($II \propto A_{998}/A_{973}$).

References

1 - C. G. Vonk, *J. Appl. Cryst.,* **6**, pp148-152 (1973).

2 - W. Ruland, *Acta Cryst.,* **14**, 1180-1185 (1961).

3 - N. S. Murthy and H. Minor, *Polymer,* **31**, 996-1002 (1990).

4 - P. Riello, G. Fagherazzi, P. Canton, D. Clemente and M. Signoretto, *J. Appl. Cryst.,* **28**, 121-126 (1995).

5 - A. Weidinger and P. H. Hermans, *Makromol. Chem.,* **50**, p98-115 (1961).

6 - R. Gehrke and H. G. Zachmann, *Makromol. Chem.,* **182**, 627-635 (1981).

7 - P. Scherrer, *Nachr. ges. Wiss. Gottingen,* **2**, 96-100 (1918).

8 - B. E. Warren, *J. Appl. Phys.,* **12**, 375-383 (1941).

9 - L. E. Alexander, *X-Ray Diffraction Methods in Polymer Science*, Wiley, New York, (1969).

10 - T. Nishino, T. Matsumoto and K. Nakame, *Polym. Eng. Sci.,* **40**, 336-343 (2000).

11 - D. Geiss and D. Hoffman, *Prog. Polym. Sci.,* **15**, 1-101 (1990).

12 - W. J. O'Kane, R. J. Young and A. J. Ryan, *J. Macromol. Sci.-Phys.,* **B34**, 427-458 (1995).

13 - L. Poussin, Y. A. BErtin, J. Parisot and C. Brassy, *Polymer,* **39**, pp4261-4265 (1998).

14 - Y. R. Wang, F. E. Teng, N. Zhang and Y. M. Wang, *J. Macromol. Sci.-Phys.,* **B34**, 78-93 (1995).

15 - S. Krumm, *Acta Geoligica,* **38**, 253-261 (1994).

16 - A. Turner-Jones, J. M. Aizlewood and D. R. Beckett, *Makromol. Chem.,* **75**, 134-158 (1964).

17 - R. Zannetti, G. Celoti, A. Fichera and R. Francesconi, *Makrom. Chem.,* **128**, 137-142 (1969).

[Refs. on p. A27]

18 - A. Martorana, S. Piccarolo and F. Sciclilone, *Macromol. Chem. Phys.,* **198**, 597-604 (1997).

19 - H. Tanaka, T. Masuko and S. Okajima, *J. Polym. Sci. Part A1,* 7, 3351-3361 (1969).

20 - Z. W. Wilchinsky, *J. Appl. Phys.,* **31**, 1969-1972 (1960).

21 - Z. W. Wilchinsky, *Adv. X-ray Anal.,* **6**, 231-241 (1962).

22 - Z. W. Wilchinsky, *J. Appl. Polym. Sci.,* **7**, 923-933 (1963).

23 - A. J. d. Vries, *Pure and Appl. Chem.,* **53**, 1011-1037 (1981).

24 - H. Uejo and S. Hoshino, *J. Appl. Polym. Sci.,* **14**, 317-328 (1970).

25 - I. Karacan, A. K. Taraiya, D. I. Bower and I. M. Ward, *Polymer,* **34**, 2691-2701 (1993).

26 - R. F. Saraf, *Polymer,* **35**, 1359-1368 (1994).

27 - Z. Bartczack and E. Martuscelli, *Polymer,* **38**, 4139-4149 (1997).

28 - H. Tadokoro, M. Kobayashi, M. Ukita, K. Yasufuku, S. Murahashi and T. Torii, *J. Chem. Phys.,* **42**, pp1432-1449 (1965).

29 - Y. V. Kissin and V. I. Tsvetkova, *Euro. Polym. J.,* **8**, 529-46 (1972).

30 - Y. V. Kissin and L. A. Rishina, *Euro. Polym. J.,* **12**, 757-9 (1976).

31 - D. R. Burfield and P. S. T. Loi, *J. Appl. Polym. Sci.,* **36**, 279-293 (1988).

32 - D. R. Burfield, P. S. T. Loi, Y. Doi and J. Mejzik, *J. Appl. Polym. Sci.,* **41**, 1095-1114 (1990).

[Refs. on p. A27]

APPENDIX B

COMPLEMENT OF CHAPTER 5

SURFACE MORPHOLOGY OF THE CAST FILMS

The asymmetric morphology along the thickness of the cast films is also discussed. For this reason, the terms "CR side" and "water side" are introduced. The former will refer to the film surface that was solidified in contact with the chill roll and the latter term will refer to the film surface solidified first in air and then into water, except for the PP4-CF4 cast film that was only cooled by air.

The WAXD patterns of both surfaces for the series of melt-crystallized cast films, the PP4-CFx cast films, showed differences in peak intensity and amorphous halo. This suggests that the proportion of the different phase content was varying from one surface to another.

			Water Side			Chill Roll Side		
Code	**WB [°C]**	**CR [°C]**	**CI [%]**	**k_{sm}**	**k_β**	**CI [%]**	**k_{sm}**	**k_β**
PP4-CF1	**20**	**20**	34.1	0.46	0	37.2	0.33	0
PP4-CF2	**55**	**55**	40.5	0.13	0	50.4	0	<0.01
PP4-CF3	**80**	**80**	48.1	0	0	56.6	0	0.03
PP4-CF4	**-**	**85**	58.1	0	0.03	59.0	0	0.15

Table B-1 Crystallinity index and the smectic (k_{sm}) and β-index (k_β) calculated from the WAXD patterns for both sides of the four CF_x films

The degree of crystallinity and the smectic and β-form indices for each side of the four CF_x films are tabulated in Table B-1. First, it was concluded that the crystalline phase content increased from CF1 to CF4 and was always higher for the chill roll side than that for the air side. The latter difference was rather pronounced for CF2 and CF3 (~10%), but almost vanished for CF4 (~1%). This can be explained in terms of cooling efficiency, which is greater for water due to convection, than that for the stainless steel.

Moreover, with increasing temperature, the water conductivity will increase while that of steel will remain constant, inducing thus a higher difference between both sides. Finally, the almost identical crystallinity for both sides might be explained by similar cooling efficiency for air and stainless steel at 85°C.

Micrographs from polarized light microscopy were in agreement with the X-ray diffraction data, as shown in Figure B-3. The micrographs revealed that there is a morphology gradient along the thickness. Two distinct skin structures of approximately 150 μm in depth with a more or less homogeneous core structure of 700-800 μm in size. For the skin layers, larger spherulites could be observed in the micrographs for the CR side that those for the water side. Furthermore, the spherulite size was found to increase from the surface to the core on each side, with the exception of the air side of CF4. In this case, the surface was only cooled by air, resulting in a poor nucleation at the surface. However, a transcrystallized morphology was observed for CF3 and CF4 at the surface that solidified in contact with the chill roll. The chill roll favored heterogeneous nucleation at its surface.

It was thus found that the side of the specimen cooled in air and then water was more rapidly crystallized than the other side in contact with the chill roll. The uniqueness of these measurements could reveal that up to a 10% difference in crystallinity may exist between the two sides of cast sheet of 1 mm in thickness. Moreover, differences in the amount of smectic or β crystal form can also vary significantly from one side to another.

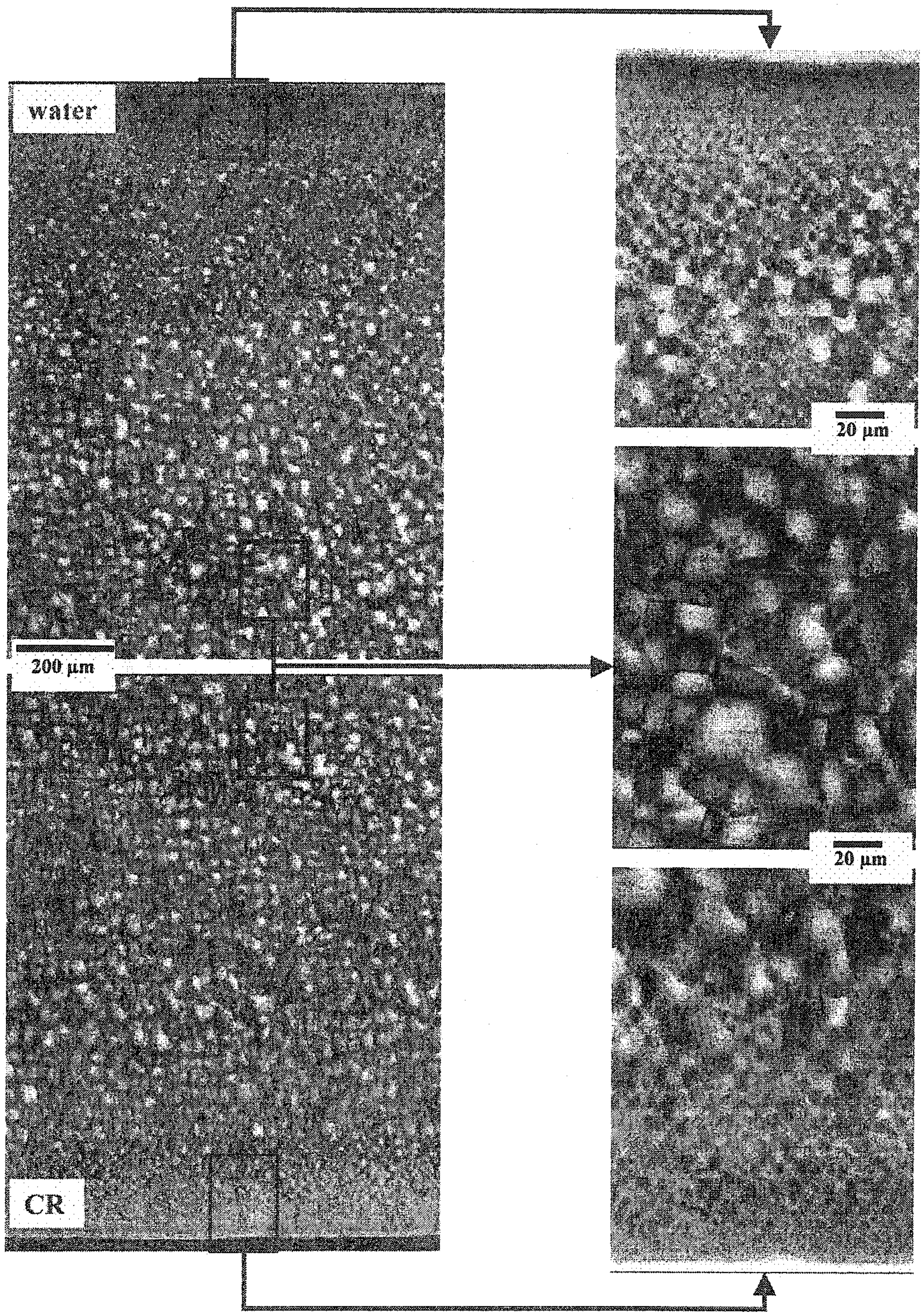

Figure B-1 PLM micrographs of the CF1 film

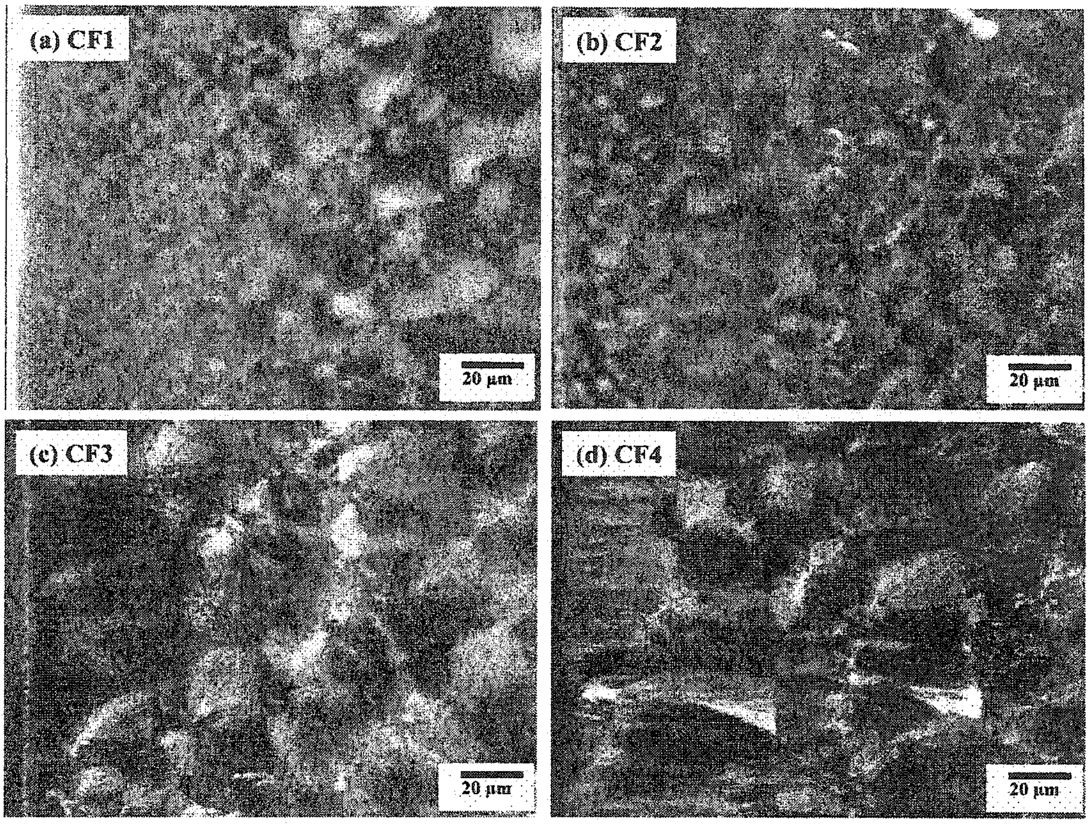

Figure B-2 PLM micrographs of the chill roll side of the (a) CF1, (b) CF2, (c) CF3, and (d) CF4 films

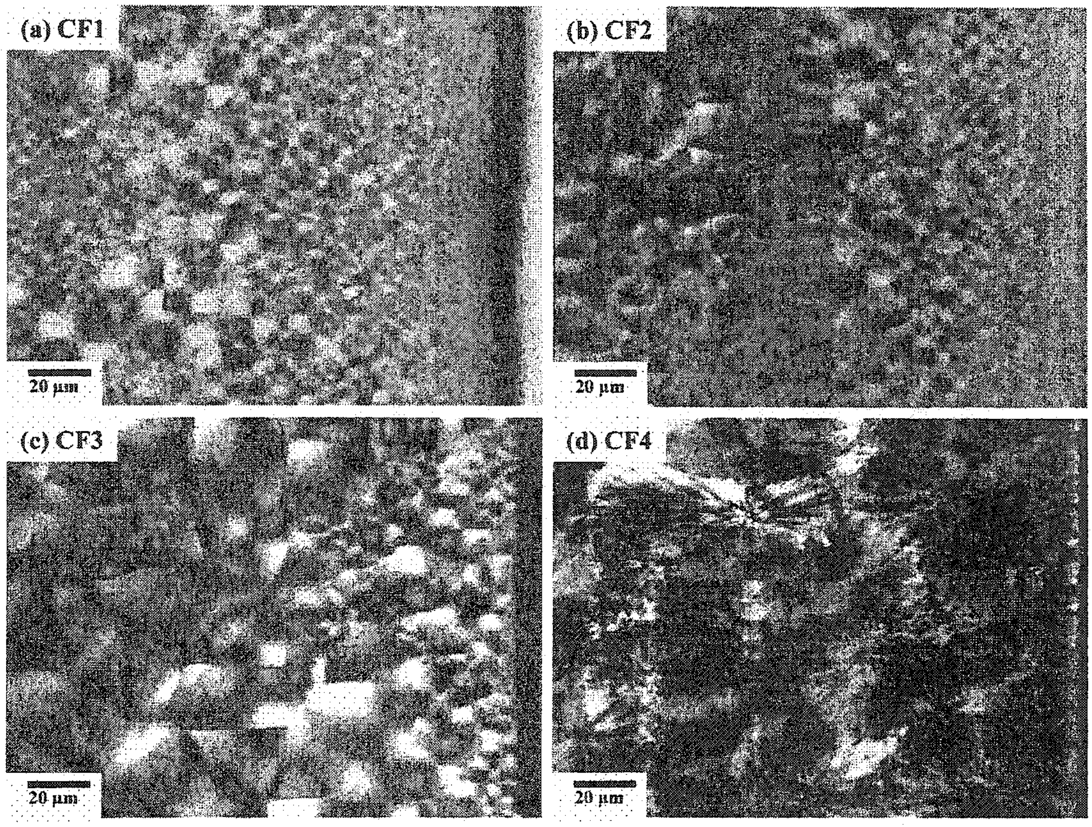

Figure B-3 PLM micrographs of the water side of the (a) CF1, (b) CF2, (c) CF3, and (d) CF4 films

APPENDIX C

COMPLEMENT OF CHAPTER 7

C.1 - Effect of Stretching Conditions on Biaxially Stretched Morphology

C.1.1 - *Effect of Stretching Temperature and Strain Ratio on Stretched Morphology*

Temp. [°C]	**Strain Rate** [s-1]	λ_a [-]	CI_{DSC} [-]	**Tm** [°C]	D_{110} [Å]	D_{040} [Å]	IPO_{040} [-]	$IP0_{110}$ [-]
140	1	2 x 2	-	-	152	168	0.362	0.242
140	1	3 x 3	-	-	138	139	0.556	0.256
140	1	4 x 4	-	-	132	142	0.673	0.203
145	1	1 x 1			201	199	0.240	0.301
145	1	2 x 2	-	-	164	180	0.421	0.226
145	1	3 x 3	-	-	151	150	0.604	0.238
145	1	4 x 4	-	-	138	136	0.725	0.208
145	1	4.9 x 4.9	0.4835	166.4	129	128	0.787	0.174
150	1	1 x 1	0.5160	163.6	211	204	0.215	0.301
150	1	2 x 2	0.4904	163.2	189	189	0.480	0.231
150	1	3 x 3	0.5043	165.3	168	159	0.604	0.242
150	1	4 x 4	0.5077	167.0	155	149	0.710	0.211
150	1	4.9 x 4.9	0.4952	167.2	141	139	0.766	0.183
150	1	5.7 x 5.7	0.5134	167.4	137	133	0.801	0.167
155	1	1 x 1	0.5447	165.7	242	222	0.217	0.306
155	1	2 x 2	-	-	185	203	0.485	0.189
155	1	3 x 3	0.5098	167.1	177	172	0.605	0.220
155	1	4 x 4	0.5228	167.6	171	161	0.673	0.219
155	1	4.9 x 4.9	0.5096	168.7	158	150	0.732	0.205
155	1	5.7 x 5.7	0.5206	168.9	146	139	0.766	0.191
155	1	7 x 7	0.5359	167.7	141	135	0.809	0.173
160	1	1 x 1	0.5662	167.2	255	233	0.224	0.294
160	1	2 x 2	-	-	244	229	0.525	0.207
160	1	3 x 3	0.5190	168.9	192	185	0.619	0.211
160	1	4 x 4	-	-	191	180	0.655	0.220
160	1	4.9 x 4.9	0.5392	170.2	177	164	0.684	0.223
160	1	5.7 x 5.7	0.5308	170.0	169	160	0.719	0.215
160	1	8 x 8	0.5175	169.3	161	151	0.764	0.208

Table C-1 *Morphological characteristics of the PP2 films simultaneously equibiaxially stretched at different drawing temperatures and area stretching ratios*

[Refs. on p. C-16]

C.1.2 - Effect of Stain Rate on Equibiaxially Stretched Morphology

Temp.	Strain Rate	CI_{DSC}	Tm	D_{110}	D_{040}	IPO_{040}	IPO_{110}
[°C]	[s-1]	[-]	[°C]	[Å]	[Å]	[-]	[-]
	Hencky	± 0.01	± 0.2	± 3	± 3	± 0.005	± 0.005
150	0.0	0.491	167.2	138	130	0.800	0.147
150	0.5	0.499	167.2	144	138	0.772	0.179
150	1.0	0.495	167.2	141	139	0.766	0.183
150	1.5	0.486	166.7	144	138	0.756	0.195
	Cauchy						
150	0.23	0.519	167.6	144	134	0.795	0.143
150	0.68	0.518	167.3	144	138	0.779	0.163
150	1.35	0.504	167.2	146	141	0.770	0.175
150	4.05	0.509	167.1	148	143	0.748	0.201

Table C-2 *Morphological characteristics of the PP2 films simultaneously equibiaxially stretched at 150°C up to a 4.9x4.9 stretching ratio at different strain rates and deformation profiles*

Figure C-1 illustrates the effect of strain rate on the degree of crystallinity for films equibiaxially stretched at 150°C. It can be observed that, in this strain rate range, the final degree of crystallinity was not affected by the strain rate or the strain rate profile.

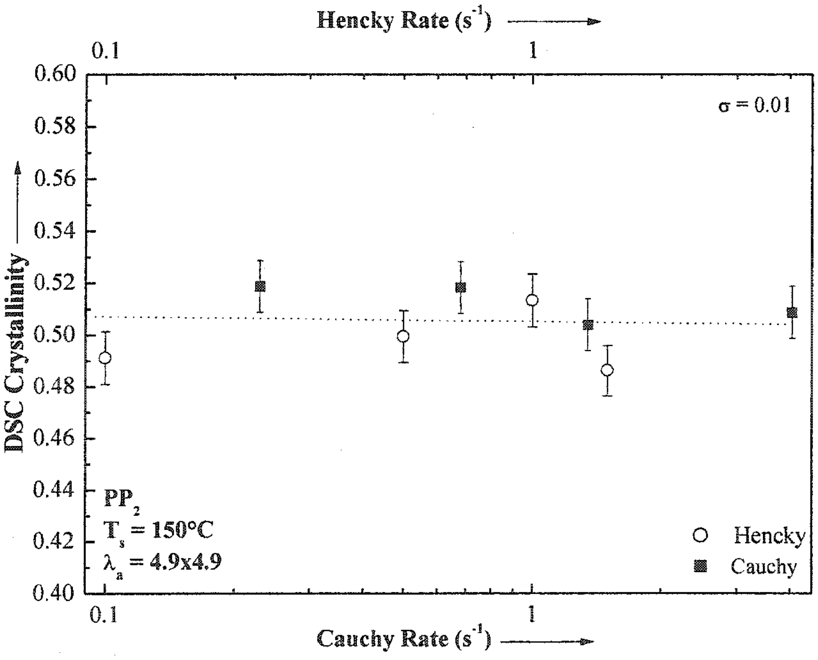

Figure C-1 *Effect of strain rate on the DSC crystallinity for PP2 films equibiaxially stretched at 150°C up to a 4.9x4.9 area stretching ratio*

C.2 - Effect of Initial Morphology on Biaxially Stretched Morphology

Figure C-2 shows the effect of the initial morphology on the final degree of crystallinity for the PP4 and PP2 melt-crystallized cast films equibiaxially stretched at 150°C and 160°C. Figure C-3 presents also the effect of the initial morphology on crystallinity but for the annealed morphologies equibiaxially stretched at 150°C up to a 4x4 stretching ratio. In both figures, the final degree of crystallinity increase slightly with increasing the initial degree of crystallinity. The tendency is clearer for the annealed morphologies, which contained only the stable monoclinic crystal form.

Cast Film	**Temp.**	**CI_{DSC}**	**Tm**	**D_{110}**	**D_{040}**	**IPO_{040}**	**IPO_{110}**
	[°C]	[-]	[°C]	[Å]	[Å]	[-]	[-]
		± 0.01	± 0.2	± 3	± 3	± 0.005	± 0.005
PP4-CF1	150	0.487	166.6	137	132	0.772	0.189
PP4-CF2	150	0.485	166.9	143	138	0.760	0.190
PP4-CF3	150	0.499	167.2	141	138	0.757	0.192
PP4-CF4	150	0.500	167.5	149	145	0.733	0.204
PP2	150	0.495	167.2	141	139	0.766	0.183
PP4-CF1	160	0.525	169.3	176	160	0.692	0.237
PP4-CF2	160	0.519	170.0	183	165	0.690	0.231
PP4-CF3	160	0.504	169.8	181	162	0.689	0.229
PP4-CF4	160	0.512	169.7	183	166	0.693	0.217
PP2	160	0.539	170.2	177	164	0.684	0.223

Table C-3 *Morphological characteristics of the PP4 and PP2 films simultaneously equibiaxially stretched up to a 4.9x4.9 area stretching ratio with a Hencky strain rate of 1s*$^{-1}$

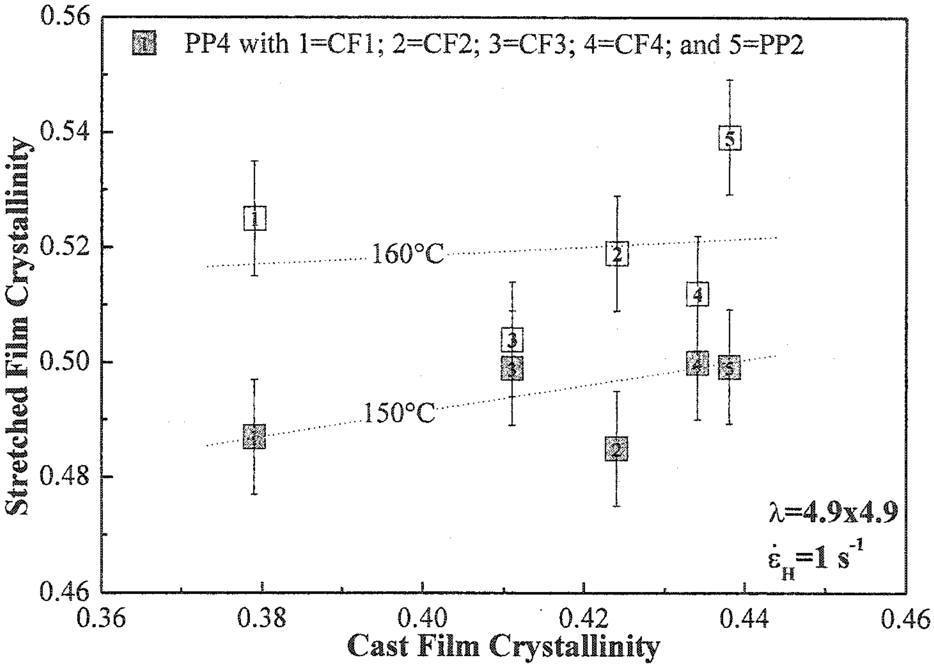

Figure C-2 *Effect of the initial melt-crystallized morphology on the final crystallinity for equibiaxially stretched films at 150°C and 160°C*

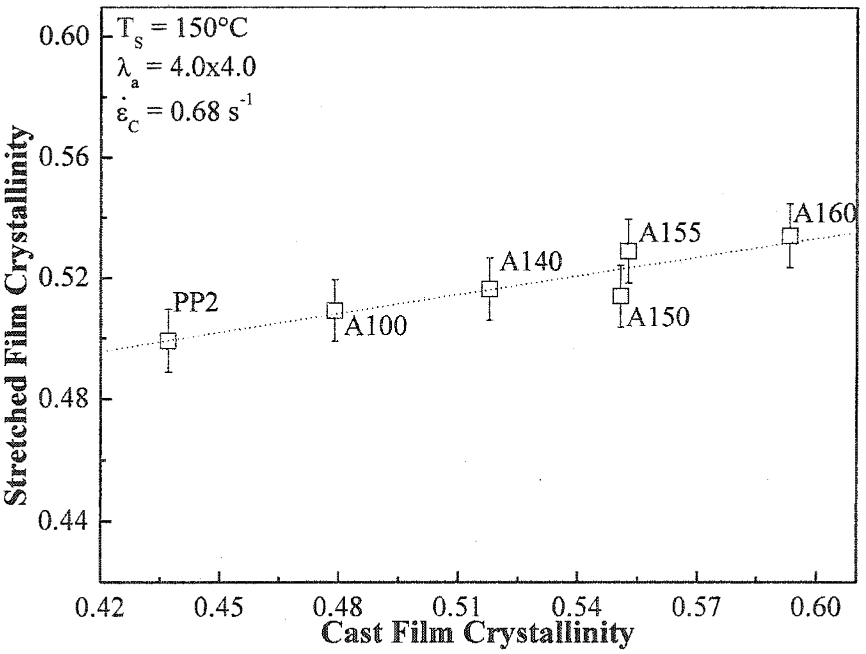

Figure C-3 *Effect of the initial annealed morphology on the degree of crystallinity of equibiaxially stretched films at 150°C*

C.3 - Effect of Chain Tacticity on Equibiaxially Stretched Morphology

Temp.	**λa**	**CI_{DSC}**	**Tm**	**D_{110}**	**D_{040}**	**IPO_{040}**
[°C]	[-]	[-]	[°C]	[Å]	[Å]	[-]
		± 0.01	± 0.2	± 3	± 3	± 0.005
155	2 x 2	0.481	162.7	239	225	0.542
155	3 x 3	0.474	164.9	217	197	0.625
155	4 x 4	0.487	165.2	187	176	0.675
155	4.9 x 4.9	0.493	163.9	178	166	0.703
155	5.7 x 5.7	0.494	164.3	168	158	0.732
145	4.9 x 4.9	0.465	162.5	140	137	0.759
150	4.9 x 4.9	0.489	163.4	156	150	0.730
155	4.9 x 4.9	0.493	164.1	178	166	0.703

Table C-4 *Morphological characteristics of the PP1 films simultaneously equibiaxially stretched under various conditions with a Hencky strain rate of 1s^{-1}*

Temp.	**λa**	**CI_{DSC}**	**Tm**	**D_{110}**	**D_{040}**	**IPO_{040}**
[°C]	[-]	[-]	[°C]	[Å]	[Å]	[-]
		± 0.01	± 0.2	± 3	± 3	± 0.005
150	4.9 x 4.9	0.564	169.6	141	139	0.778
153	4.9 x 4.9	0.562	170.3	148	144	0.767
155	4.9 x 4.9	0.564	170.4	157	151	0.757
158	4.9 x 4.9	0.572	171.0	165	158	0.744
163	4.9 x 4.9	0.613	172.0	195	181	0.712
155	2.0 x 2.0	0.590	166.6	188	188	0.516
155	3.0 x 3.0	0.568	169.3	182	172	0.656
155	4.0 x 4.0	0.590	170.5	162	156	0.721
155	4.9 x 4.9	0.564	170.4	157	151	0.757
155	5.7 x 5.7	0.577	170.8	-	-	-

Table C-5 *Morphological characteristics of the PP3 films simultaneously equibiaxially stretched under various conditions with a Hencky strain rate of 1s^{-1}*

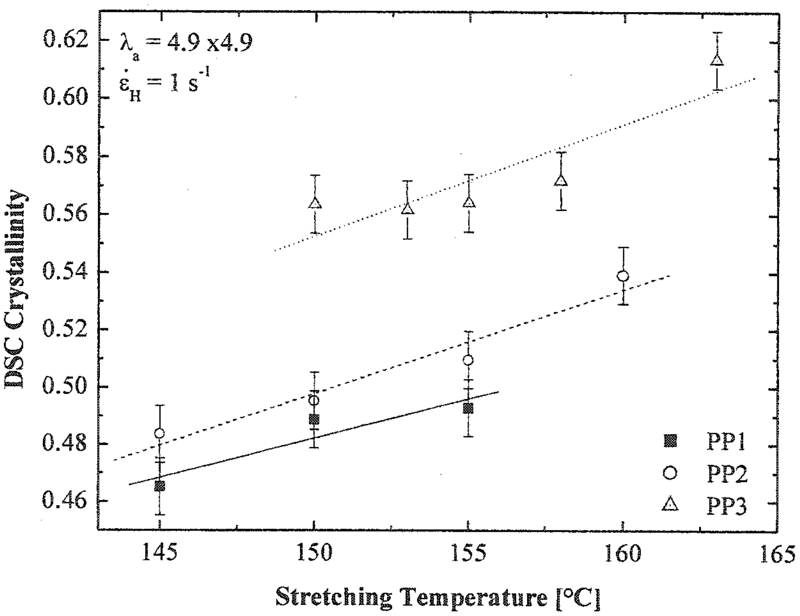

Figure C-4 *Effect of stretching temperature on the degree of crystallinity of 4.9x4.9 equibiaxially stretched films for the PP1, PP2, and PP3 resins*

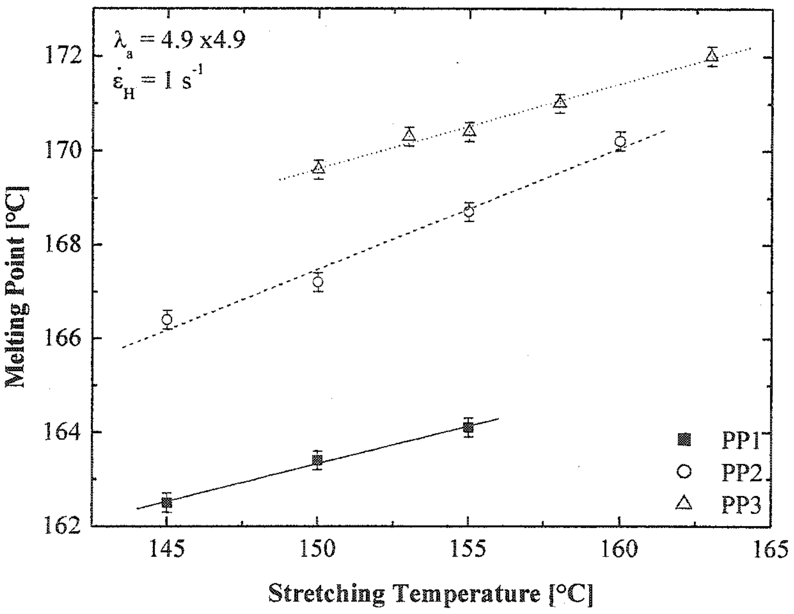

Figure C-5 *Effect of stretching temperature on the melting point of 4.9x4.9 equibiaxially stretched films for the PP1, PP2, and PP3 resins*

C.4 - Effect of Deformation Type on the Equibiaxially Stretched Film Morphology

The effect of the type of deformation on stretched film morphology was investigated by drawing samples under uniaxial, planar, non-equibiaxial, and equibiaxial deformation. Non-equibiaxial stretching corresponds to deformation in which a specimen was simultaneously biaxially stretched up to different stretching ratios in the MD and TD directions. It was ensured that the stretching time was identical in both directions for non-equibiaxial stretching. Thus, the strain rate was reduced in the direction of the lowest stretching ratio (here always TD). A biaxiality factor, as defined by Sweeney et al.(1) : $\phi = (\lambda_{TD} - 1)/(\lambda_{MD} - 1)$ was utilized. Given that λ_{MD} is greater than λ_{TD}, the biaxiality is equal to one when the deformation is equibiaxial and zero for a planar deformation in MD.

C.4.1 - Effect on Crystalline Texture - Results and Discussion

Figure C-6 illustrates the two- and three-dimensional (3D) representation of the (110) and (040) X-Ray pole figures for the samples, biaxially stretched up to the same area stretching ratio of 24 (except for (d)) but with a different biaxiality. The sample shown in Figure C-6(d) corresponds to the case for which biaxiality equals zero, i.e. planar deformation. The 3D representation of the pole figures is included for better visualization of the positions of the intensity maxima. High intensities in a (*hkl*) pole figure indicate a high concentration of the (*hkl*) crystal planes and that the normals of these planes are oriented towards the maxima positions. The contours in the 2D representation represent isointensity lines of the 3D pole figure. More information and references about the interpretation of pole figures and X-ray pole figure measurements can be found in Chapter 4.

Figure C-6(a) shows that, for a biaxiality of one (equibiaxial deformation), the (040) and (110) pole figures have a symmetrical intensity distribution about the central axis that represents the normal direction (ND) to the sample film surface. Moreover, an intensity maximum can be observed in the center for both (040) and (110) pole figures. These maxima indicate that the normals to the (040) and (110) crystal planes are preferentially oriented towards ND. Furthermore, the (110) pole figure exhibits one extra broad maximum with radial symmetry at a tilt angle of around 72.5°. The latter indicates that the (110) plane normals are inclined with a 72.5° angle to ND. This last feature is a direct consequence of the main uniplanar texture, i.e. (040) planes being oriented in the MD-TD plane, that impose that the (110) planes be oriented at an angle of 17.5° (90 – 72.5) to the MD-TD plane (2, 3).

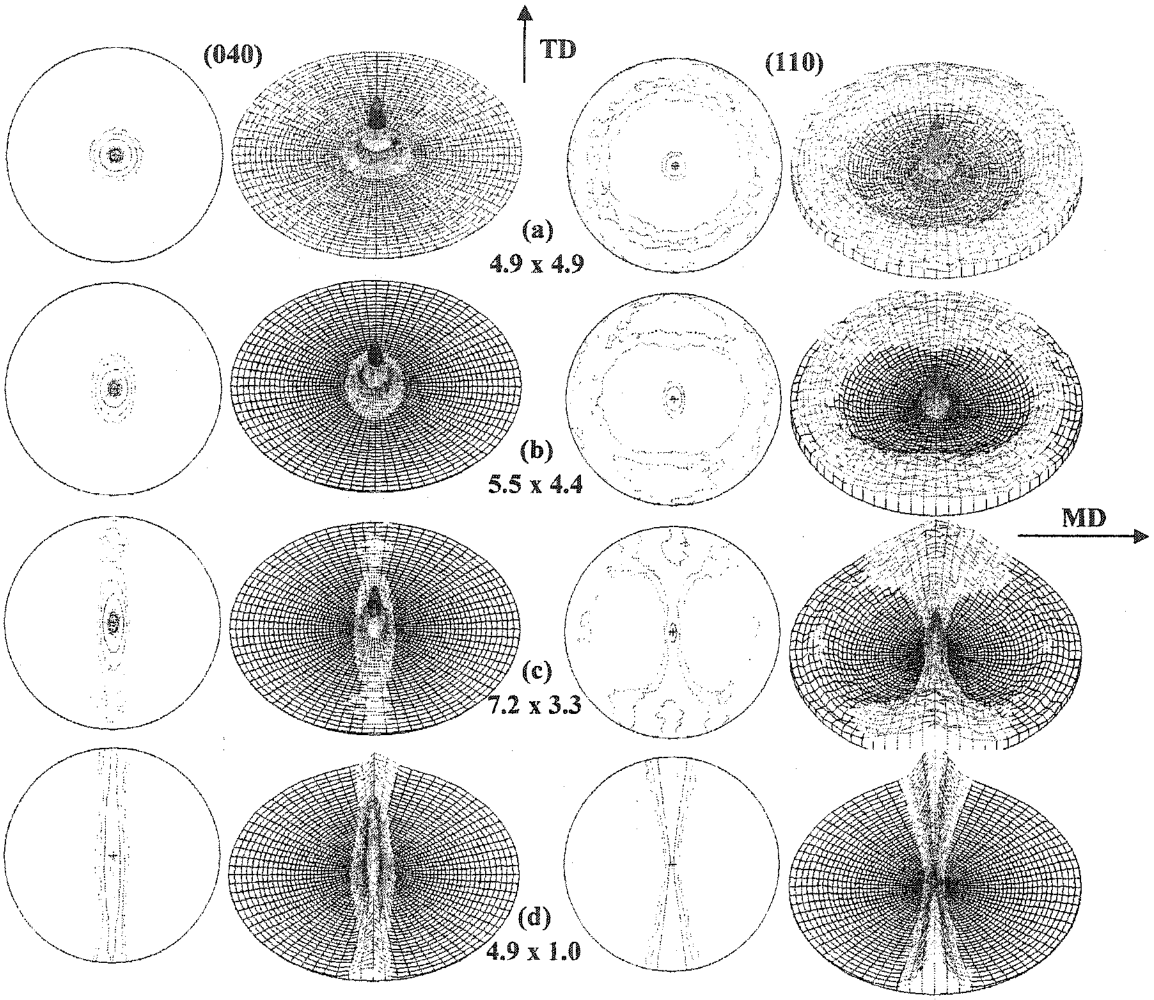

Figure C-6 Effect of deformation type on the (040) and (110) pole figures of PP2 films stretched at 150°C up to the same area ratio (except (d)) but different biaxiality factor (the left image is the 2D representation of the right image, the 3D representation)

The maxima in the center of the (040) pole figure and the maxima at 72.5° in the (110) pole figure are the characteristics of the (010) [001] texture, while the maxima in the center for the (110) pole figure are the characteristics of the (110) [001] texture. The pole figure measurements confirmed the previous conclusion that simultaneous equibiaxial deformation generates a crystalline texture with two components: the (010) [001] and (110) [001] uniplanar textures (4). This also confirmed that the (010) [001] texture dominates the (110) [001] texture in the equibiaxially stretched samples.

Figure C-6(a), (b) and (c) show that, for non-equibiaxial deformation, the intensity distribution of the (040) pole figures tends to be displaced from around ND to the TD-ND plane with decreasing biaxiality. Meanwhile, the maximum of the (040) pole figures remains in the center. The latter observations indicate that the normals to the (040) planes remain preferentially oriented perpendicular to the film surface as well as being partly oriented in the TD direction with decreasing biaxiality. Two broad, symmetrical intensity maxima can be distinguished at a tilt angle of 72.5° in the TD direction of the (110) pole figure in Figure C-6(c). The two maxima increased in intensity with decreasing biaxiality, to become higher than the central maximum for planar deformation, as seen in Figure C-6(d). Finally, the (040) pole figure still exhibited a maximum in the center for planar deformation.

Non-equibiaxial deformation disrupts the symmetry of the orientation of the (*hk0*) crystal planes around the normal direction, as expected. The normals to the (040) and (110) planes tend to be preferentially aligned perpendicular to MD with decreasing biaxiality. The results for the planar deformation showed that the normals to the (040) and (110) crystal planes are oriented in the TD-ND plane. However, a majority of the normals to the (040) planes are pointing in ND, while the majority of the normals to the (110) planes are oriented in TD. All these components have in common that the *c*-axis is oriented in MD. The pole figures of the uniaxially and planarly stretched films were almost identical. These two types of deformation generate a texture composed of several components: the (010) [001], (100) [001], and (110) [001], as already reported in the literature (4).

The interpretation of the results from the pole figure measurements can also be made by plotting the average squared cosines $<\cos^2\theta_{i,J}>$ in an orientation diagram (cf. Chapter 4). The average cosines $<\cos^2\theta_{i,J}>$ were plotted in Figure C-7 for the three crystallographic axes *a**, *b*, and *c* with respect to the three sample directions. The center of the equilateral triangle represent random orientation. It can be seen that the *c*-axis orientation goes from preferentially parallel to MD to uniformly oriented in the MD-TD plane with decreasing biaxiality or going from uniaxial to equibiaxial. The *b*-axis is almost randomly oriented in the TD-ND plane after uniaxial deformation, but is preferentially oriented towards ND after equibiaxial deformation . Finally, the *a** axis is almost oriented uniformly around MD after uniaxial deformation and becomes oriented uniformly around ND, i.e. in the MD-TD plane with increasing biaxiality.

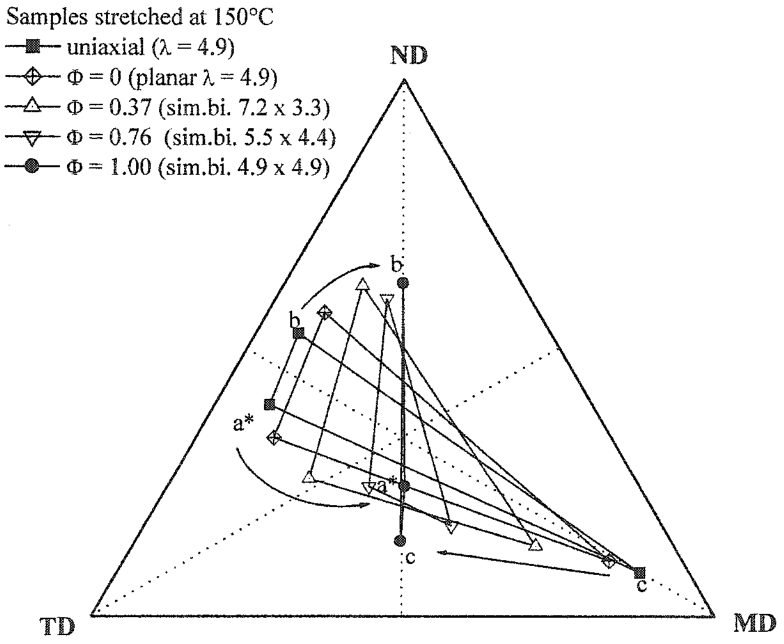

Figure C-7 *Orientation diagram of the PP2 films stretched at 150°C with different biaxiality (a*, b, and c are the crystallographic axes; the arrows indicate the direction from uniaxial to equibiaxial)*

The orientation diagram of Figure C-7 indicates that the orientation of the *c*-axis tends always towards the main stretching directions, i.e. MD for planar, the MD-TD plane for equibiaxial, and in between for non-equibiaxial deformation. The orientation of the *b*-axis is towards ND for equibiaxial deformation and in the ND-TD plane for the planar deformation. This is in agreement with other published studies (4, 5).

C.4.2 - Effect on Film Morphology - Results and Discussion

Figure C-8 compares the DSC melting curves of samples stretched up to the same MD stretching ratio (λ_{MD}) but different TD stretching ratio (λ_{TD}). Uniaxial, planar, and equibiaxial deformation are compared in Figure C-8. First of all, it can be seen that the melting peaks differ in shape and intensity. The melting behavior of the planarly deformed sample is similar to that of the uniaxially stretched sample. Both curves exhibited a weak double-peak melting behavior: a low-temperature shoulder at around 165°C and a high-temperature peak at about 168°C. The low-temperature melting shoulder is more pronounced for the uniaxially than for the planarly stretched sample. For the equibiaxially stretched sample, the lower temperature shoulder has almost vanished and the high-temperature peak is around 167°C. The onset of melting of the equibiaxially stretched film morphology appears at much lower temperatures than for the other two samples. Nevertheless, the curves for the three deformation types overlapped each other in the region of the end of melting.

The evolution of the high temperature melting peak was then investigated as function of λ_{MD} for the three deformation types, as shown in Figure C-9. The dependence of the melting point on λ_{MD} was similar for all three deformation types. The melting point was observed to increase with λ_{MD} and to start leveling off at $\lambda_{MD} \sim 6$, for stretching at 150°C. No clear observation could be made about the degree of crystallinity due to large scatter of the enthalpy of fusion. Nevertheless, the crystallinity of the stretched samples was found not to vary by more than 2%.

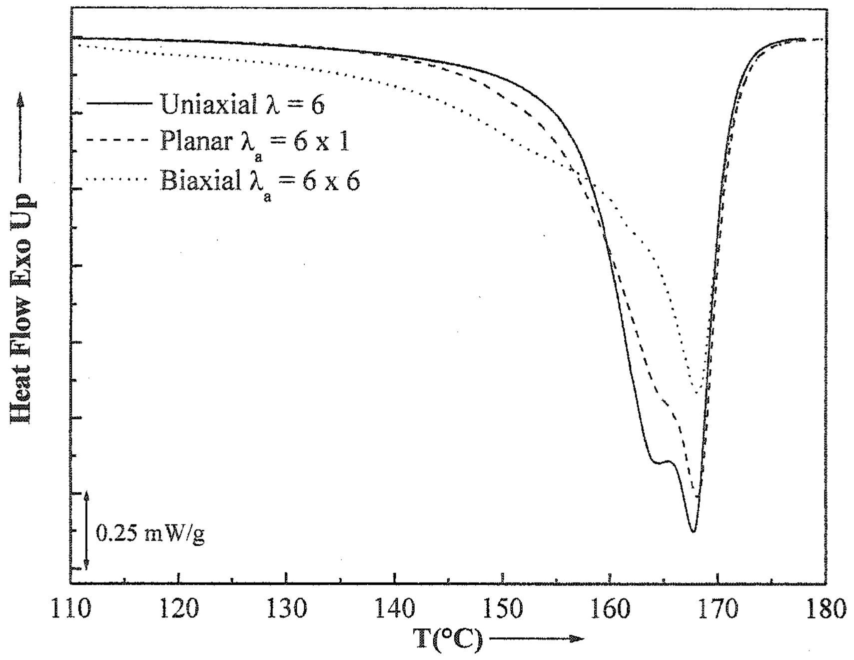

Figure C-8 *Effect of deformation type on the DSC melting curve of PP2 films stretched at 150°C*

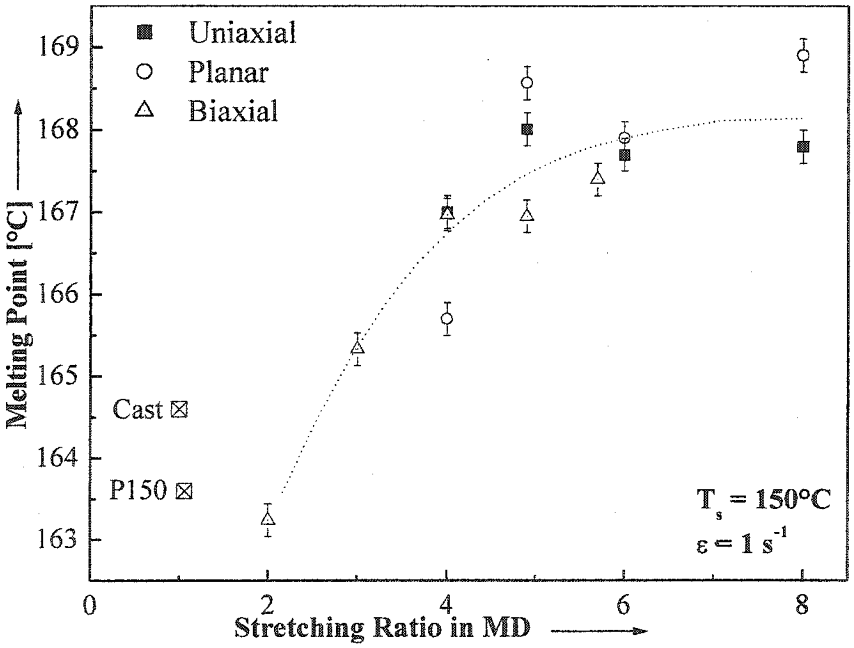

Figure C-9 *Effect of deformation type on the high temperature melting point of PP2 films stretched at 150°C*

[Refs. on p. C-16]

It has been reported that highly uniaxially deformed polypropylene shows two separate peaks in the DSC melting curves, which indicates the presence of two structures of differing thermal stabilities (6). Yan et al. (7) concluded that the high temperature peak corresponds to the melting of the lamellar crystals within fibrils, and the low temperature peak to an extended structure. The exact form of the latter remains unclear. Tarayia et al. (6) suggested that it may arise from either small crystallites connected by taut tie molecules or from a disordered crystal form whose chain ends are constrained and/or which is an extended form.

The above suggests that uniaxial and planar deformations contribute to formation of a greater amount of extended, non-crystalline structure than for equibiaxial deformation. Because the deformation takes place in a plane rather than in a direction with freedom to contraction, molecular rearrangements are easier due to less directional constraints in uniaxial and planar stretching. This should be evident in the stress-strain curves. Indeed, the yield stress was observed to increase from the uniaxial, to planar, to equibiaxial deformation (8).

Figure C-10 compares the WAXD patterns of samples that were stretched uniaxially, planarly, and equibiaxially up to the same MD stretching ratio of 4.9. The three patterns exhibited only the characteristic peaks of the α-form of iPP. The patterns differ only in peak intensity, especially for the (110), (040), and (130) peaks. The highest peak intensity was found for the (110) peak in the case of the uniaxially stretched sample and for the (040) peak in the case of the planar and equibiaxially stretched samples. The disappearance of the $(111)/(041)(\bar{1}31)$ peak doublet at 21° – 22° was observed for all three deformation types at this stretching ratio. The WAXD pattern of the planar stretched film morphology is similar to the uniaxially stretched film morphology. The equibiaxially stretched sample exhibits the highest (040) peak intensity and the lowest (110) and (130) peak intensities of all three samples. All these differences in WAXD patterns indicate that the three samples have a different crystalline texture, as already indicated by the X-ray pole figure measurements (cf. discussion).

[Refs. on p. C-16]

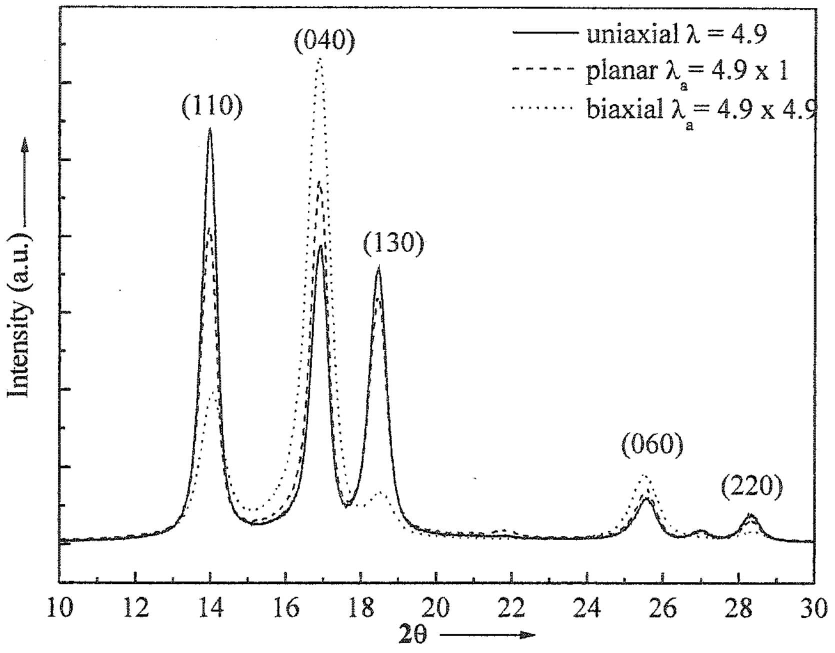

Figure C-10 Effect of deformation type on the WAXD patterns measured in the MD direction for PP2 films stretched at 150°C

Figure C-11 shows the evolution of the apparent crystallite size on stretching for the three main deformation types. The stretched film samples were characterized in both MD and TD directions. The TD values were found to be always greater than the MD ones for the non-equibiaxial deformations, given that λ_{MD} was greater than λ_{TD}. For comparison and clarity purposes, only the D_{040} apparent crystallite size measured in MD was plotted versus λ_{MD} in Figure C-11. The apparent crystallite size was found to decrease upon stretching for the three deformation types. The values for the planar and uniaxial deformation were identical within experimental accuracy, whereas those for the equibiaxial deformation were found to be significantly smaller for constant λ_{MD}.

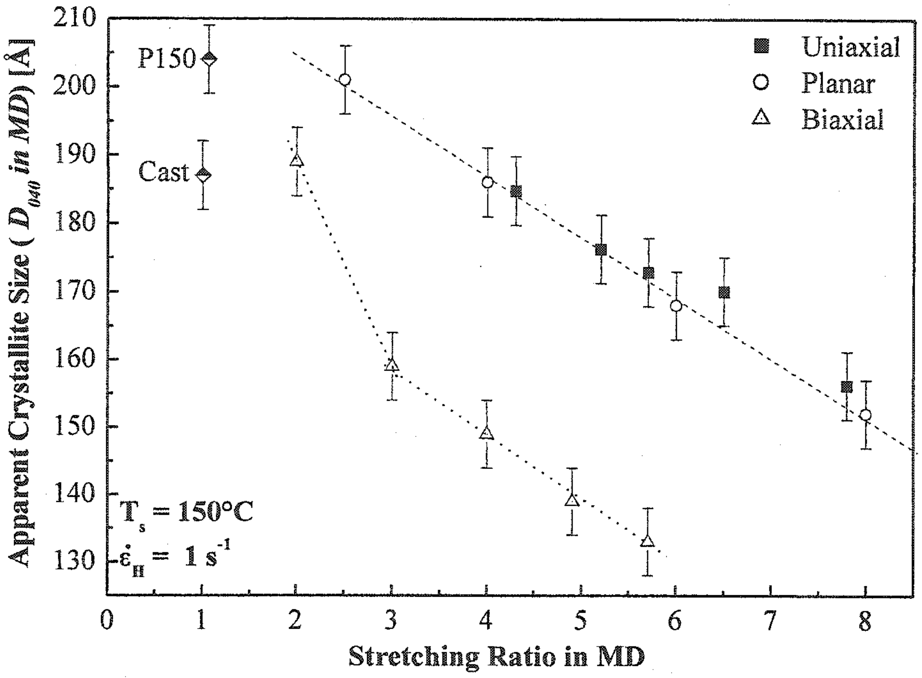

Figure C-11 *Effect of deformation type on the apparent crystallite size (measured in MD) of PP2 films stretched at 150°C*

The smaller crystallite sizes obtained for equibiaxial deformation compared to those obtained for uniaxial and planar deformation can be explained by the fact that comparison was made at equal MD stretching ratio. The actual area stretching ratios differed significantly. Nevertheless, this can be also partly explained by considering the alignment of the crystallites towards the stretching directions. On one hand, the crystallites that have their (040) and (110) slip planes already favorably oriented in the MD-TD plane will undergo lamellar fragmentation under equibiaxial stretching. On the other hand, the crystallites that are not aligned in the drawing direction or plane must be first finely sheared and rotated towards the drawing direction before lamellar fragmentation occurs. The latter case has a higher probability of occurring during uniaxial and planar deformation, since there is only one drawing direction, more mobility freedom. It should also be noticed

[Refs. on p. C-16]

C.4.3 - Conclusions

The deformation type influences the crystalline texture and orientation distribution along the sample directions. Equibiaxial stretching produces a uniform morphology and orientation in the deformation plane. Decreasing the biaxiality led to a preferential orientation of the chain axis in the direction of the main stretching direction, while keeping the *b*-axis preferentially oriented in ND and in the minor stretching direction. Uniaxial and planar deformation were found to have similar crystalline textures.

The other major effect of deformation type is on the lamellar morphology. Equibiaxial stretching led to a much larger decrease in crystallite size and lower melting point than uniaxial and planar deformation, at a given stretching ratio in the major deformation direction. This may be attributed to increased lamellar fragmentation due to the reduced mobility of the lamellar crystals, when subjected to plane deformation compared to axial deformation. The differences in actual stretching ratio may also explain the differences in lamellar morphology.

References

1 - J. Sweeney, I. M. Ward, T. L. D. Collins and P. D. Coates, *Polymer,* **38**, 5991 - 5999 (1997).

2 - Z. W. Wilchinsky, *J. Appl. Polym. Sci.,* **7**, 923-933 (1963).

3 - R. F. Saraf, *Polymer,* **35**, 1359-1368 (1994).

4 - Z. Bartczack and E. Martuscelli, *Polymer,* **38**, 4139-4149 (1997).

5 - C. E. Chaffey, A. K. Taraiya and I. M. Ward, *Polym. Eng. Sci.,* **37**, 1774-1784 (1997).

6 - A. K. Taraiya, I. M. Ward and A. P. Unwin, *J. Polym. Sci.: Polym. Phys.,* **26**, 817-838 (1988).

7 - R. J. Yan and B. Jiang, *J. Polym. Sci. Polym. Phys. Ed.,* **31**, 1089-1094 (1993).

8 - L. Capt, M. R. Kamal, S. Rettenberger and H. Münstedt, *Polym. Eng. Sic.,* **in Press,** (2003).

APPENDIX D

COMPLEMENT OF CHAPTER 8

This appendix presents in table form the mechanical and optical properties of the film samples investigated in this work.

D.1 - Effect of Stretching Ratio on The End-Film Properties for the PP2 Cast Film

Drawing Ratio	**Tensile Strength** [N/mm²]		**Force** [N]		**Elongation at Break** [%]		**Young Modulus** [N/mm²]		**Shrink-age** [%]	
					Average					
		±		±		±		±		±
4.0 x 4.0	163	3	121	4	142	6	2614	22	2.7	0.1
4.9 x 4.9	188	3	103	2	118	6	2815	26	1.9	0.2
5.7 x 5.7	203	5	85	3	98	6	2948	14	2.3	0.4
7.0 x 7.0	227	6	69	2	71	6	3315	45	3.2	0.1
					MD					
		±		±		±		±		±
4.0 x 4.0	164	3	127	5.3	143	6	2600	25	2.7	0.1
4.9 x 4.9	190	3	104	2	115	6	2839	35	1.9	0.2
5.7 x 5.7	205	5	86	2.8	89	5	2987	11	2.0	0.6
7.0 x 7.0	233	7	70	1.9	70	6	3383	72	3.2	0.0
					TD					
		±		±		±		±		±
4.0 x 4.0	163	3	115	3	141	7	2628	19	2.7	0.2
4.9 x 4.9	186	4	101	3	120	7	2791	18	2.0	0.1
5.7 x 5.7	201	5	84	3	107	8	2909	17	2.7	0.1
7.0 x 7.0	221	6	67	2	72	6	3247	17	3.1	0.1

Table D-1 *Effect of stretching ratio on the mechanical properties for the PP2 films simultaneously equibiaxially stretched at 155°C*

Drawing Ratio	**Thickness** [μm]		**Gloss** [-]		**Haze** [%]	
		±		±		±
4.0 x 4.0	51.6	1.4	96.5	1	0.75	0.11
4.9 x 4.9	36.4	0.5	97.7	0.8	0.41	0.04
5.7 x 5.7	27.8	0.3	99.0	0.6	0.30	0.04
7.0 x 7.0	20.2	0.1	99.0	0.6	0.27	0.03

Table D-2 *Effect of stretching ratio on the optical properties for the PP2 films simultaneously equibiaxially stretched at 155°C*

D.2 - Effect of Drawing Temperature on the End-Film Properties for the PP1 Cast Film

Drawing Temp. [°C]	Tensile Strength [N/mm²]	±	Force [N]	±	Elongation at Break [%]	±	Young Modulus [N/mm²]	±	Shrink-age [%]	±
Average										
140	195	9	127	7	112	12	2145	20	7.4	0.3
145	198	5	122	3	117	7	2289	16	5.4	0.4
150	185	4	106	3	119	6	2357	30	3.8	0.1
155	161	5	70	2	135	13	2369	67	2.0	0.1
160	84	3	18	3	194	22	2122	52	0.2	0.2
MD										
140	192	7	128	6	115	9	2120	30	7.3	0.4
145	198	3	124	2	121	4	2277	19	5.5	0.4
150	185	5	106	3	122	6	2378	41	3.9	0.1
155	160	3	70	2	132	8	2403	56	2.1	0.1
160	85	2	19	2	179	10	2166	49	0.3	0.2
TD										
140	198	12	126	8	110	15	2169	10	7.4	0.2
145	197	6	119	4	114	10	2302	13	5.4	0.4
150	185	4	107	3	116	6	2336	19	3.8	0.2
155	162	7	69	2	138	17	2335	78	2.0	0.0
160	82	4	17	2	210	33	2078	56	0.1	0.1

Table D-3 *Effect of drawing temperature on the mechanical properties for the PP1 films simultaneously equibiaxially stretched up to 4.9 x 4.9*

Drawing Temp. [°C]	Thickness [µm]	±	Gloss [-]	±	Haze [%]	±
140	43.4	0.9	96.0	1.0	0.49	0.03
145	41.0	0.6	97.1	0.4	0.55	0.03
150	38.3	0.9	93.1	1.0	0.86	0.04
155	28.9	0.5	84.8	1.6	2.14	0.04
160	14.4	1.2	74.9	1.6	5.20	0.14

Table D-4 *Effect of drawing temperature on the optical properties for the PP1 films simultaneously equibiaxially stretched up to 4.9 x 4.9*

D.3 - Effect of Drawing Temperature on the End-Film Properties for the PP2 Cast Film

Drawing Temp. [°C]	Tensile Strength [N/mm²]	±	Force [N]	±	Elongation at Break [%]	±	Young Modulus [N/mm²]	±	Shrink-age [%]	±
					Average					
145	206	8	129	5	106	9	2682	19	5.3	0.3
150	204	6	115	4	105	7	2750	45	3.2	0.2
155	188	3	103	2	118	6	2815	26	1.9	0.2
160	164	4	72	2	130	10	2963	33	1.0	0.1
					MD					
145	212	5	135	4	106	6	2701	20	5.2	0.3
150	210	8	117	5	114	10	2745	37	3.2	0.2
155	190	3	104	2	115	6	2839	35	1.9	0.2
160	166	3	75	2	130	7	3012	32	0.9	0.1
					TD					
145	200	10	122	6	107	12	2663	19	5.4	0.3
150	198	5	113	3	96	5	2756	54	3.2	0.2
155	186	4	101	3	120	7	2791	18	2.0	0.1

Table D-5 *Effect of drawing temperature on the mechanical properties for the PP2 films simultaneously equibiaxially stretched up to 4.9 x 4.9*

Drawing Temp. [°C]	Thickness [μm]	±	Gloss [-]	±	Haze [%]	±
145	42.5	0.9	98.7	0.8	0.26	0.00
150	38.1	0.7	99.3	0.8	0.28	0.04
155	36.4	0.2	97.7	0.8	0.41	0.04
160	29.9	0.4	88.9	1.0	1.37	0.04

Table D-6 *Effect of drawing temperature on the optical properties for the PP2 films simultaneously equibiaxially stretched up to 4.9 x 4.9*

D.4 - Effect of Drawing Temperature on the End-Film Properties for the PP3 Cast Film

Drawing Temp. [°C]	Tensile Strength [N/mm^2]	±	Force [N]	±	Elongation at Break [%]	±	Young Modulus [N/mm^2]	±	Shrinkage [%]	±
Average										
150	219	6	127	3	100	7	3450	52	2.9	0.2
155	203	8	113	4	102	12	3368	24	1.9	0.2
160	174	6	86	5	113	13	3488	48	1.0	0.2
MD										
150	224	7	131	3	99	7	3479	47	2.8	
155	205	8	115	5	99	11	3406	16	1.8	0.0
160	177	7	87	4	117	12	3519	37	1.0	0.0
TD										
150	213	5	123	3	102	7	3421	57	3.0	0.3
155	201	8	111	4	105	13	3330	33	2.0	0.1
160	171	6	86	6	109	14	3457	58	1.0	0.0

Table D-7 *Effect of drawing temperature on the mechanical properties for the PP3 films simultaneously equibiaxially stretched up to 4.9 x 4.9*

Drawing Temp. [°C]	Thickness [μm]	±	Gloss [-]	±	Haze [%]	±
150	38.8	0.8	96.3	1.0	0.73	0.10
155	37.1	0.7	97.8	0.2	0.57	0.11
160	33.2	1.3	95.8	0.4	0.83	0.05

Table D-8 *Effect of drawing temperature on the optical properties for the PP3 films simultaneously equibiaxially stretched up to 4.9 x 4.9*

D.5 - Effect of Strain Rate on the End-Film Properties for the PP2 Cast Film

Strain Rate $[s^{-1}]$	Tensile Strength $[N/mm^2]$	±	Force [N]	±	Elongation at Break [%]	±	Young Modulus $[N/mm^2]$	±	Shrinkage [%]	±
					Average					
1.5	182	5	102	4	117	8	2651	20	1.8	0.2
1.0	187	4	102	3	118	6	2850	23	2.1	0.1
0.5	192	5	104	2	113	7	2830	32	2.1	0.1
0.1	202	5	106	4	105	5	2990	32	3.7	0.4
					MD					
1.5	185	5	104	3	114	9	2711	21	1.9	0.1
1.0	190	3	104	2	116	6	2868	27	2.0	0.1
0.5	190	5	103	2	108	10	2842	24	2.1	0.1
0.1	202	5	108	6	99	6	2984	23	3.8	0.6
					TD					
1.5	179	5	101	4	120	7	2591	20	1.6	0.3
1.0	185	4	101	3	121	7	2832	18	2.1	0.1
0.5	193	4	104	2	119	5	2818	39	2.1	0.1
0.1	202	4	104	2	110	5	2995	41	3.6	0.2

Table D-9 *Effect of strain rate on the mechanical properties for the PP2 films simultaneously equibiaxially stretched at 155°C up to 4.9 x 4.9*

Strain Rate $[s^{-1}]$	Thickness [µm]	±	Gloss [-]	±	Haze [%]	±
1.5	39.2	0.5	97.0	0.6	0.48	0.03
1.0	37.6	0.5	96.8	0.8	0.45	0.05
0.5	36.9	1.2	96.5	0.4	0.50	0.03
0.1	35.7	1.2	97.0	0.6	0.39	0.03

Table D-10 *Effect of strain rate on the optical properties for the PP2 films simultaneously equibiaxially stretched at 155°C up to 4.9 x 4.9*

D.6 - Effect of Initial Morphology on the End-Film Properties for the PP2 Cast Film

Cast Film	Tensile Strength [N/mm²]		Force [N]		Elongation at Break [%]		Young Modulus [N/mm²]		Shrink-age [%]	
Average										
		±		±		±		±		±
PP4-CF1	198	5	135	3.8	108	6	2555	18	3.7	0.1
PP4-CF2	197	4	128	2.9	112	7	2579	18	3.0	0.1
PP4-CF3	192	7	125	5.3	108	10	2589	18	3.0	0.1
PP4-CF4	186	2	119	3.0	100	4	2616	18	2.9	0.1
PP2	204	6	115	4	105	7	2750	45	3.2	0.2
MD										
		±		±		±		±		±
PP4-CF1	198	6	137	5	107	8	2583	19	3.6	0.4
PP4-CF2	199	5	131	3	113	6	2602	18	3.0	0.1
PP4-CF3	197	5	129	4	110	8	2665	24	3.0	0.1
PP4-CF4	186	3	120	3	97	4	2623	24	2.9	0.1
PP2	210	8	117	5	114	10	2745	37	3.2	0.2
TD										
		±		±		±		±		±
PP4-CF1	198	4	134	3	109	4	2526	17	3.8	0.4
PP4-CF2	194	3	125	2	110	8	2555	25	3.0	0.1
PP4-CF3	188	10	121	7	106	12	2512	24	3.1	0.1
PP4-CF4	187	2	119	3	102	5	2609	20	2.9	0.1
PP2	198	5	113	3	96	5	2756	54	3.2	0.2

Table D-11 *Effect of initial morphology on the mechanical properties for the PP4 and PP2 films simultaneously equibiaxially stretched at 150°C up to 4.9 x 4.9*

Cast Film	Thickness [µm]		Gloss [-]		Haze [%]	
		±		±		±
PP4-CF1	45.6	0.7	100.5	0.6	0.39	0.06
PP4-CF2	43.3	0.4	101.2	0.8	0.34	0.06
PP4-CF3	43.4	0.6	101.5	0.4	0.41	0.04
PP4-CF4	42.7	0.9	97.1	0.6	0.68	0.05
PP2	38.1	0.7	99.3	0.8	0.28	0.04

Table D-12 *Effect of initial morphology on the optical properties for the PP4 and PP2 films simultaneously equibiaxially stretched at 150°C up to 4.9 x 4.9*

Cast Film	Tensile Strength [N/mm²]		Force [N]		Elongation at Break [%]		Young Modulus [N/mm²]		Shrink-age [%]	
					Average					
		±		±		±		±		±
PP4-CF1	166	4	73	3	126	8	2817	39	2.0	0.1
PP4-CF2	160	5	76	4	135	10	2730	35	2.0	0.1
PP4-CF3	167	4	86	6	142	10	2690	27	2.0	0.1
PP4-CF4	131	7	68	4	110	6	2695	63	1.1	0.1
PP2	164	2	72	2	130	10	2963	33	1.0	0.1
					MD					
		±		±		±		±		±
PP4-CF1	165	2	73	2	122	6	2854	53	1.0	0.1
PP4-CF2	159	3	76	2	133	7	2746	52	0.8	0.2
PP4-CF3	167	4	86	3	143	8	2708	26	1.0	0.1
PP4-CF4	131	2	69	4	107	6	2732	58	0.8	0.1
PP2	166	3	75	2	130	7	3012	32	0.9	0.1
					TD					
		±		±		±		±		±
PP4-CF1	167	5	73	4	129	9.4	2780	25	1.0	0.1
PP4-CF2	161	7	75	5	138	11.8	2715	18	1.0	0.1
PP4-CF3	166	6	86	8	141	12	2671	28	1.0	0.1
PP4-CF4	132	3	68	5	112	6.7	2658	68	0.9	0.1
PP2	161	5	70	2	131	13	2913	34	1.0	0.0

Table D-13 *Effect of initial morphology on the mechanical properties for the PP4 and PP2 films simultaneously equibiaxially stretched at 160°C up to 4.9 x 4.9*

Cast Film	Thickness [µm]		Gloss [-]		Haze [%]	
		±		±		±
PP4-CF1	29.3	0.9	94.1	0.8	1.06	0.05
PP4-CF2	31.6	0.9	92.9	0.8	1.15	0.04
PP4-CF3	34.4	1.7	94.9	0.8	1.07	0.04
PP4-CF4	34.7	2.1	82.6	1.2	2.74	0.16
PP2	29.9	0.4	88.9	1.0	1.37	0.04

Table D-14 *Effect of initial morphology on the optical properties for the PP4 and PP2 films simultaneously equibiaxially stretched at 160°C up to 4.9 x 4.9*